Lappeenranta
University of Technology

Vesa Tanskanen

CFD MODELLING OF DIRECT CONTACT CONDENSATION IN SUPPRESSION POOLS BY APPLYING CONDENSATION MODELS OF SEPARATED FLOW

Thesis for the degree of Doctor of Science (Technology) to be presented with due permission for public examination and criticism in the Auditorium 1381 at Lappeenranta University of Technology, Lappeenranta, Finland on the 13th of April, 2012 at noon.

Acta Universitatis
Lappeenrantaensis 472

Supervisor Professor Riitta Kyrki-Rajamäki
Laboratory of Nuclear Engineering
Faculty of Technology
Lappeenranta University of Technology
Finland

Reviewers Assoc. Professor Walter Ambrosini
Faculty of Engineering
Department of Mechanical, Nuclear and Production Engineering
University of Pisa
Italy

D.Sc. Mikko Lemmetty
Teollisuuden Voima Oyj
Olkiluoto, Eurajoki
Finland

Opponent Assoc. Professor Walter Ambrosini
Faculty of Engineering
Department of Mechanical, Nuclear and Production Engineering
University of Pisa
Italy

ISBN 978-952-265-221-8
ISBN 978-952-265-222-5 (PDF)
ISSN 1456-4491
Lappeenrannan teknillinen yliopisto
Digipaino 2012

Abstract

Vesa Tanskanen
CFD Modelling of Direct Contact Condensation in Suppression Pools by Applying Condensation Models of Separated Flow
Lappeenranta 2012
184 pages
Acta Universitatis Lappeenrantaensis 472
Diss. Lappeenranta University of Technology
ISBN 978-952-265-221-8, ISBN 978-952-265-222-5 (PDF), ISSN 1456-4491

The condensation rate has to be high in the safety pressure suppression pool systems of Boiling Water Reactors (BWR) in order to fulfill their safety function. The phenomena due to such a high direct contact condensation (DCC) rate turn out to be very challenging to be analysed either with experiments or numerical simulations. In this thesis, the suppression pool experiments carried out in the POOLEX facility of Lappeenranta University of Technology were simulated. Two different condensation modes were modelled by using the 2-phase CFD codes NEPTUNE_CFD and TransAT. The DCC models applied were the typical ones to be used for separated flows in channels, and their applicability to the rapidly condensing flow in the condensation pool context had not been tested earlier.

A low Reynolds number case was the first to be simulated. The POOLEX experiment STB-31 was operated near the conditions between the 'quasi-steady oscillatory interface condensation' mode and the 'condensation within the blowdown pipe' mode. The condensation models of Lakehal et al. and Coste & Laviéville predicted the condensation rate quite accurately, while the other tested ones overestimated it. It was possible to get the direct phase change solution to settle near to the measured values, but a very high resolution of calculation grid was needed.

Secondly, a high Reynolds number case corresponding to the 'chugging' mode was simulated. The POOLEX experiment STB-28 was chosen, because various standard and high-speed video samples of bubbles were recorded during it. In order to extract numerical information from the video material, a pattern recognition procedure was programmed. The bubble size distributions and the frequencies of chugging were calculated with this procedure. With the statistical data of the bubble sizes and temporal data of the bubble/jet appearance, it was possible to compare the condensation rates between the experiment and the CFD simulations.

In the chugging simulations, a spherically curvilinear calculation grid at the blowdown pipe exit improved the convergence and decreased the required cell count. The compressible flow solver with complete steam-tables was beneficial for the numerical success of the simulations. The Hughes-Duffey model and, to some extent, the Coste & Laviéville model produced realistic chugging behavior. The initial level of the steam/water interface was an important factor to determine the initiation of the chugging. If the interface was initialized with a water level high enough inside the blowdown pipe, the vigorous

penetration of a water plug into the pool created a turbulent wake which invoked the chugging that was self-sustaining. A 3D simulation with a suitable DCC model produced qualitatively very realistic shapes of the chugging bubbles and jets. The comparative FFT analysis of the bubble size data and the pool bottom pressure data gave useful information to distinguish the eigenmodes of chugging, bubbling, and pool structure oscillations.

Keywords: Condensation, CFD, Suppression Pool, Pattern Recognition, Chugging, POOLEX
UDC 621.039:51.001.57:004.93’1:532.5

Acknowledgements

This work was carried out in the LUT Institute of Energy Technology at Lappeenranta University of Technology (LUT), Finland, between 2005 and 2012. The research conducted in this study has received funding from the NURESIM and NURISP projects of the 6th and 7th EURATOM Framework Programme of European Commission; from the Finnish Research Programmes on Nuclear Power Plant Safety: SAFIR, SAFIR2010, and SAFIR2014; and from the Academy of Finland by the Graduate School of Computational Fluid Dynamics and the SusEn/NETNUC project.

I express my deepest gratitude to my supervisor Professor Riitta Kyrki-Rajamäki for all the support she provided during this work, especially including the work done during the last sleepless months.

I humbly thank my reviewers, Professor Walter Ambrosini and Dr Mikko Lemmetty, for their valuable comments and suggestions. They deserve exceptional thanks for their fast, but very careful review processes.

The CFD modelling work in this study was supported by the model and code developers of EDF (Électricité de France), CEA (Commissariat à l'énergie atomique), and ASCOMP GmbH. I would especially like to thank Dr Pierre Coste and Dr Dominique Bestion from CEA, Dr Jerome Laviéville from EDF, and Dr Djamel Lakehal and Dr Mathieu Labois from ASCOMP GmbH.

I express my deep gratitude to the whole personnel in the Laboratory of Nuclear Engineering and in the Nuclear Safety Research Unit of LUT. Especially I wish to thank Mrs Anne Jordan, a lady who laughs too much while being still uncompromisingly efficient in her work, and Mr Juhani Vihavainen who takes care of the major part of the bureaucracy related to the projects. Their assistance was of great help during the whole research period related to this work. I would also like to thank Mr Markku Puustinen, the father of the P/POOLEX facility, as well as Dr Heikki Purhonen. There would not have been this thesis without the POOLEX experiments. Concerning the technical issues that appeared during this work, I also wish to thank Mr Ville Rintala, Mr Jani Laine, and Mr Antti Räsänen whose professional help was invaluable and available whenever it was needed. Many thanks also to Ms Sari Silventoinen for her assistance.

I also wish to thank my former supervisor Professor Piroz Zamankhan. He was the one who led me to the murky world of the CFD modelling of multiple phases.

Finally, I express my heartfelt appreciation to my family, to Eveliina, and to the other loved ones for the support and motivation during my researcher career.

Vesa Tanskanen
March 2012
Lappeenranta, Finland

Or who shut up the sea with doors,
when it brake forth, as if it had issued out of the womb?
When I made the cloud the garment thereof,
and thick darkness a swaddlingband for it,
And brake up for it my decreed place, and set bars and doors,
And said, Hitherto shalt thou come, but no further:
and here shall thy proud waves be stayed?

Job 38: 8-11

Contents

Nomenclature

Latin letters

$\mathbb{G}$	stratification attenuation of kinetic energy	$\mathrm{m^2/s^3}$
$\mathbb{P}$	production of kinetic energy due to velocity gradients	$\mathrm{m^2/s^3}$
$\overline{H}$	modified Heaviside function	–
A	area	$\mathrm{m^2}$
a_i	interfacial area	$1/\mathrm{m}$
B	constant	–
C	constant	–
C_A	added mass coefficient	$\mathrm{kg/m^3}$
C_D	drag coefficient	–
c_p	specific heat at constant pressure	$\mathrm{J/(kg\,K)}$
C_μ	turbulent viscosity constant in $k-\varepsilon$ model	–
$C_{\varepsilon 1}$	constant in $k-\varepsilon$ model	–
$C_{\varepsilon 2}$	constant in $k-\varepsilon$ model	–
$C_{\varepsilon 4}$	constant in $k-\varepsilon$ model	–
D	diameter	m
D_α	thermal diffusivity	$\mathrm{m^2/s}$
E	Young's modulus	Pa
F_D	drag coefficient	$\mathrm{kg/(m^3\,s)}$
G	mass flux	$\mathrm{kg/(m^2\,s)}$
g	gravitational acceleration	$\mathrm{m/s^2}$
Gr	Grashof number	–
H	total enthalpy	$\mathrm{J/kg}$
h	heat transfer coefficient	$\mathrm{W/(m^2\,K)}$
h_m	mass transfer coefficient	$\mathrm{m/s}$
I	interfacial momentum transfer rate	$\mathrm{kg/(m^2\,s^2)}$
K	mass transfer velocity	$\mathrm{m/s}$
k	turbulence kinetic energy	$\mathrm{m^2/s^2}$
K^+	dimensionless mass transfer velocity	–
L	length	m
Le	Lewis number	–
M	molar mass	$\mathrm{kg/kmol}$
m	mass fraction	–
Nu	Nusselt number	–
P	mean pressure	Pa
q	covariance of velocity fluctuations	$\mathrm{m^2/s^2}$
q''	heat flux	$\mathrm{W/m^2}$
q_m	mass flow rate	$\mathrm{kg/s}$
Ra	Rayleigh number	–
Re	Reynolds number	–
S_H	source term of heat	$\mathrm{J/(m^3\,s)}$

S_{M}	source term of momentum	$\mathrm{kg}/(\mathrm{m}^2\,\mathrm{s}^2)$
t	time	s
U	velocity	m/s
u	velocity	m/s
u^*	friction velocity	m/s
u^+	dimensionless velocity	$-$
V_{r}	relative velocity	m/s
V_d	drift velocity	m/s
X	molar fraction	$-$
x_{eq}	equilibrium quality	$-$
y^+	dimensionless distance from wall or interface	$-$

Greek letters

α	volume fraction	$-$
β	volumetric thermal expansion coefficient	$1/\mathrm{K}$
δ	interface thickness	m
δ_{I}	interfacially centered smoothed dirac delta function	$1/\mathrm{m}$
δ_{ij}	Kronecker delta tensor	$-$
ϵ_E	strain	ε or $-$
η	Kolmogorov length scale	m
Γ	interfacial mass transfer rate	$\mathrm{kg}/(\mathrm{m}^3\,\mathrm{s})$
κ	constant	$-$
κ_σ	surface curvature	$1/\mathrm{m}$
λ	thermal conductivity	$\mathrm{W}/(\mathrm{m}\,\mathrm{K})$
μ	dynamic viscosity	$\mathrm{Pa}\,\mathrm{s}$
ν	kinematic viscosity	m^2/s
ϕ	Level Set distance function	m
Π	bulk interfacial heat transfer rate	W/m^3
Π_q	production/destruction of kinetic energy due to other phases	$\mathrm{kg}/(\mathrm{m}\,\mathrm{s}^3)$
ρ	density	kg/m^3
σ^{t}	turbulent Prandtl number	$-$
σ_ε	turbulent Prandtl number for dissipation	$-$
σ_k	turbulent Prandtl number for kinetic energy	$-$
τ	time scale, time constant	s
$\tau_{k,ij}$	viscous stress strain tensor	Pa
$\tau^{\mathrm{t}}_{k,ij}$	turbulent stress strain tensor	Pa
ε	turbulence dissipation rate	$\mathrm{m}^2/\mathrm{s}^3$

Superscripts

c	contribution
l	laminar
t	turbulent

$\mathrm{w/s}$	water/steam system
$''$	flux
$'$	independent of mass transfer
σ	jump of enthalpy (mass transfer)

Subscripts

1	liquid phase
2	gas phase
η	Kolmogorov scale
I	interface of phases
norm	on the normal direction
n	non-condensable
P	perimeter
sat	saturation
s	surface
tang	on the tangential direction
v	vapor
$\mathrm{w/oNC}$	without non-condensable gases
wallc	condensation on walls
$*$	shear
i	on the direction i
j	on the direction j
k	phase 'k'
p	phase 'p'
x	location

Abbreviations

BWR	Boiling Water Reactor
CFD	Computational Fluid Dynamics
CFL	Courant number of flow, denotes also to other transported parameters
DCC	Direct Contact Condensation
DNS	Direct Numerical Simulation
ECCS	Emergency Core Cooling System
FE	Finite Element
FFT	Fast Fourier Transform
FSI	Fluid Structure Interaction
HTC	Heat Transfer Coefficient
IAEA	International Atomic Energy Agency
KTH	Kungliga Tekniska Högskolan
LI3C	3 Cell Large Interface model
LI	Large Interface
LOCA	Loss of Coolant Accident

LUT	Lappeenranta University of Technology
NC	Non-Condensable Gas
NPP	Nuclear Power Plant
NURESIM	Nuclear Reactor Simulations
NURISP	The Nuclear Reactor Integrated Simulation Project
PACTEL	Parallel Channel Test Loop
PIV	Particle Image Velocimetry
PSI	Paul Scherrer Institute
PSTF	The General Electric Pressure Suppression Test Facility
PTS	Pressurized Thermal Shock
(U)RANS	(Unsteady) Reynolds Averaged Navier-Stokes
ROI	Region of Interest
SRV	Safety/Relief Valve
STUK	Radiation and Nuclear Safety Authority of Finland
VOF	Volume Of Fluid method

1 Introduction

Safety is in a key position whenever the sustainable use of nuclear power is being evaluated. Nuclear power plant (NPP) constructors, NPP operating energy companies, and national regulators of nuclear technologies are usually well-aware of the importance of the safety aspect, which leads to a continuous need of safety related research. Considering from an engineering point of view, this research is usually related to various passive and active safety systems of NPPs and their functionality in different circumstances. As the safety system related experiments with real NPPs are unacceptable or difficult, this research is done in research institutes and universities.

The experimental part of the research is carried out by using suitable experimental facilities scaling from robust integral scale test facilities modelling the whole NPP primary circuit to separate effect test facilities trying to capture a single phenomenon of nature. The analytical and computational parts of the research aim to reveal the physics behind the experimental results, to model it and to simulate it as accurately as possible. As an outcome, new scientific models and computational tools, i.e. computer codes are developed and validated for NPP designers, operators, and regulating authorities. These models and codes can be used in the best-estimate analysis of certain components of NPPs or they can be used to find out flaws in conservative safety tools as well.

In this thesis, efforts have been made to increase the capability of Computational Fluid Dynamics (CFD) codes to successfully model and predict rapid Direct Contact Condensation (DCC) in the safety pressure suppression pool systems of Boiling Water Reactors (BWR). Although the DCC as a physical phenomenon is somewhat understood and it can be modelled satisfactorily in many applications, it has proven challenging to be modelled in systems where the level of turbulence is high and the sub-cooling of the liquid phase is remarkable. In addition to the challenges in modelling, these DCC phenomena of suppression pools are difficult and expensive to capture with desirable accuracy in the experiments even with academic measurement instrumentation.

1.1 Objective of the study

In pressure suppression pools, the conditions can change significantly during such accidents that require sustained suppression of releasing steam. A number of different DCC modes can be passed through as the boundary conditions for the condensation change. For example, during the initial phase of steam blowdown, non-condensable gases (NC) (i.e. nitrogen in BWR containment) may decrease the condensation rates remarkably or even prevent it. When the amount of NCs has decreased enough in the drywell and in the vent pipes of the suppression pool system, the chugging condensation mode initiates. During the chugging mode, the average steam bubble sizes, their lifetimes and resulting loads to the pool structures increase gradually as the sub-cooling of the pool water decreases. At the late phase of blowdown, the steam mass flow rate can be low enough to end the chugging mode and stabilize the water/steam-interface somewhere inside the vent pipes.

During the quasi-steady phase, the thermal stratification of the liquid phase controls the condensation rate, and therefore the stability of the interface.

During steam blowdown, the resulting loads against structures change according to the current condensation mode, and exceptionally strong pressure pulses may occasionally occur. The characteristics and magnitudes of such loads must be known, and a detailed analysis of the pressure response of the suppression system must be carried out in order to confirm that the containment structural design withstands these loads. Empirical data from air/steam discharge through large-diameter pipes is needed also for the validation of numerical simulation tools. Such validation efforts will lead to improved estimation of condensation rates during bubble formation and break-up and to more precise modelling of fluid structure interactions.

In this study, two of the abovementioned DCC modes are modelled using 2-phase CFD codes NEPTUNE_CFD and TransAT. The condensation models used in this study are mostly the same ones that are currently being validated for Pressurized Thermal Shock (PTS) cases in the NURESIM and NURISP EU projects. These DCC models are typically used for stratified flows, and their applicability for condensation pools has not been tested yet. The objectives of this study are the following:

- To simulate a low-Reynolds number DCC case (POOLEX STB-31 experiment) using stratified flow condensation models. Such a case corresponds to the quasi-steady water/steam-interface conditions in the suppression pools.
- To compare the condensation mass flow rates from CFD simulations to the measurements in the STB-31 experiment and to find out the most suitable DCC model for the low-Re condensation cases.
- To simulate a high-Reynolds number DCC case (POOLEX STB-28 experiment) using stratified flow condensation models. Such a case corresponds to the chugging condensation regime in the suppression pools.
- To find comparable qualities between the STB-28 experiment and CFD simulations, as the value of condensation rate was not measured directly in the experiment. To use these qualities in the validation of condensation models against the experiment.
- To find out how much the non-measured phenomena affected the measured results in the STB-28 and STB-31 experiments.
  - NC gases may have affected the results in the STB-31 experiment.
  - Wall condensation may have affected the results in the STB-28 experiment.
- To present the factors found to be important for the success of these CFD simulations.
- To find out, as far as possible, the sensitivities to the computational grid resolution and modelling approach.

- To give suggestions for the future experimental and numerical modelling work in order to achieve the final goal to reliably determine the critical BWR containment loads.

1.2 Author's contribution to present thesis

The author of this thesis has made an effort to extract more data from the former lightly instrumented suppression pool experiments of Nuclear Safety Research Unit of Lappeenranta University of Technology (LUT) to use the data for validation purposes of CFD codes. The author has validated some of the stratified flow condensation models against two different condensation pool experiments. The author presents also a number of findings that may ease the challenging simulations of DCC and a number of considerations for future experimental work. Concerning the validity of stratified flow condensation models to suppression pool cases, the author has co-operated with the computational code and model developers and has had an impact on the development and model implementation work of the codes.

2 Background and recent developments

Systematic ways to ensure the safety of nuclear power reactors have been developed both nationally and internationally. The International Atomic Energy Agency (IAEA) establishes its safety standards and measures in the IAEA Safety Standard Series, where the safety fundamentals, the safety requirements and the safety guides are given. The main requirements for the design of nuclear power plants are given in IAEA (2000). The fundamental safety functions to be performed in operational and accident states are the control of reactivity, the removal of heat from the core, the confinement of radioactive materials, and the control of operational discharges, as well as the limitation of accident releases. These safety functions can be met by having structures, systems and components performing more detailed safety functions. These safety functions differ for different reactor types. However, for water cooled reactors, IAEA has given 19 safety functions, three of which refer to the maintaining of the integrity of the principal physical barriers against the discharge or the release of radioactive materials, i.e. the fuel cladding, the reactor coolant pressure boundary, and the reactor containment. High pressures and temperatures can lead to ruptures of these barriers.

The reactor coolant system can be shielded against the intolerable pressure increases by using the pressure relief valves, though other means are preferably utilized. However, as the containment is the outermost barrier, the overpressure control shall be done there by other means. Due to the expensiveness of constructing large containments, different systems to reduce the pressure loads to the containment have been created already since the early stages of the nuclear reactor development era (Moody, 1984).

2.1 Containment pressure suppression

In BWRs, the cooling circuit containing the primary water is small, and thus the containment can be constructed to be compact if effective ways to control the pressure increase in the loss of coolant accident situations (LOCA) can be developed. The main solution to construct a BWR containment has been a containment including a condensation pool (Lahey and Moody, 1993). Figure 2.1 shows the schematic of the ASEA-Atom type BWR containment of the Olkiluoto 1&2 NPP units.

Large scale studies to guarantee the effectiveness of this system have been carried out in the USA (see e.g. Lahey and Moody (1993) for references), in Germany (e.g. Aust and Seeliger (1982)), and in the Marviken facility in Sweden (Wikdahl, 2007). In the condensation pool containment, the pressure increase due to steam blowdown is prevented by the condensation in the pool. However, the condensation, or more accurately, the direct contact condensation is a double-edged phenomenon that can help to control the pressure level or cause further threats by strong pressure oscillations (see Yue (1982) and Wikdahl (2007)). The direct contact condensation (DCC) of steam in sub-cooled water may occur in a rapid and unsteady manner and induce hydrodynamic loads against the submerged structures of the suppression pool. It is important to know the characteristics and the

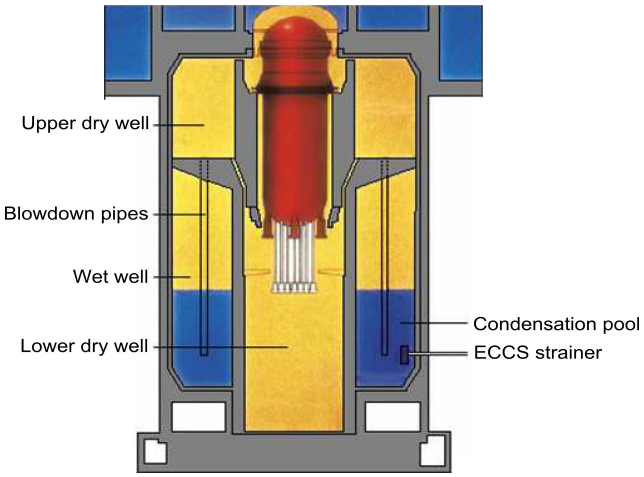

Figure 2.1. Schematic of the Olkiluoto type BWR containment (TVO, 2007).

magnitudes of such loads, and an analysis of the pressure response of the suppression system has to be carried out in order to confirm that the containment structural design withstands these loads.

2.2 A brief review of experimental studies

Plenty of work has been done in the past on various aspects of air/steam discharge into sub-cooled water (see e.g. Ylikauppila et al. (2009) and Lahey and Moody (1993) for references). Due to that, several test facilities modelling different containment/suppression pool designs have been constructed and utilized. This chapter summarizes some of the test facilities used in the air/steam discharge studies related to the hydrodynamics, condensation processes and structural loads in the pressure suppression systems of the BWR type nuclear power plants.

The most active period in the experiments of suppression pools was during the 1970s and 1980s. Depending on the type of a BWR pressure suppression pool system (e.g. MARK I, MARK II and MARK III containment designs), these experimental facilities include systems with vertical blowdown pipes, horizontal blowdown pipes and different injector nozzles connected to them. Figure 2.2 shows the sketches of the MARK I-III containment designs.

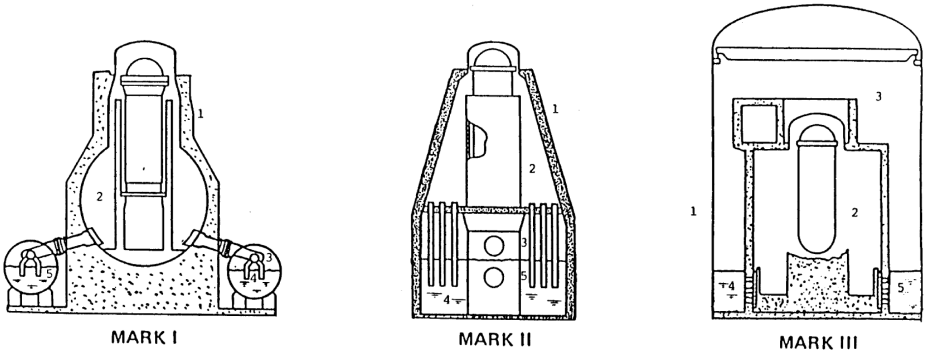

Figure 2.2. General Electric pressure suppression system designs. Here 1 is the primary containment, 2 is the drywell, 3 is the wetwell, 4 is the suppression pool, and 5 is the vent system (Karwat et al., 1986).

2.2.1 Horizontal steam injection

Kerney et al. (1972) made experiments with horizontal steam injector using high steam mass fluxes. High mass fluxes prevented the operation in the chugging mode, and thus they observed the quasi-steady condensation mode. Many of the experiments with horizontal injectors were motivated by the MARK III containment design in which the blowdown pipes are horizontal. McIntyre et al. (1975) conducted experiments with air blowdown in a facility in 1/3 scale of 8 degree sector of the MARK III containment. Their experiment gave evidence of the effect of hydrostatic pressure on the penetration depth of bubbles. Also different pool swelling velocities and pressure pulses between air and steam blowdowns were observed.

The General Electric Pressure Suppression Test Facility (PSTF) was in a great role in the MARK III research. Varzaly et al. (1977) gathered results of PSTF experiments with different MSLB break sizes, suppression pool temperatures and saturated liquid/vapor blowdowns with particular emphasis on the pool dynamic response during a LOCA. Varzaly (1977) also applied flow visualization using high speed video recording to qualitatively investigate fluid interface motion and steam bubble formation and collapse during the chugging mode. Chuang (1977) used the PSTF facility to test loads on the submerged structures during LOCA conditions.

The most of the later condensation pool experiments with horizontal blowdown have been conducted in Asia, particularly by Korean research institutes. Chun et al. (1996) did experiments with different injector nozzle diameters, pool temperatures and steam mass fluxes producing a condensation mode map of their results. Some of their experiments were done by using vertical nozzles as well. Youn et al. (2003) conducted experiments in the chugging mode, and obtained results of pressure pulse generation with various experimental parameters, e.g. nozzle diameters. Wu et al. (2007b) studied experimentally

the geometry of the injected steam plume, and found it dependent on the injector exit pressure.

2.2.2 Vertical steam injection

The blowdown experiments with vertical blowdown pipes with relatively large diameters are of more interest in this thesis. Although the DCC phenomena have similar modes in horizontal and vertical steam injections (e.g. chugging and quasi-steady condensation), the nozzle type injectors like spargers make the steam/water-interface structures in horizontal cases much different from the large diameter vertical blowdown pipe cases of this study.

As mentioned earlier, various large scale studies concerning the suppression pools have been carried out in the USA since the studies of Robbins (1960). A list of references has been gathered e.g. by Lahey and Moody (1993). Remarkable experimental work has been carried out also in Germany (e.g. Aust and Seeliger (1982)) and in the Marviken facility in Sweden (Wikdahl, 2007). In general, many of the reports produced are not freely available. Summarizing the past research in the USA in this light, many of the reports and articles concern the MARK I and MARK II containment designs and have been published by the General Electric Company. For example, in the MARK I suppression pool swell test program, Kennedy et al. (1978) made experiments with 1/4 scale facility (Galyardt et al., 1978). They tested the effect of the rigidity of blowdown pipe header to the pressure impact loads. Flexible header reduced the magnitude of the peak impact loads. Later, Shimegi and Suzuki (1988) studied the effect of non-condensable gases in 1/5 and 1/12 scaled facilities of MARK I type geometries.

Various MARK II experiments were conducted in the 1970s-1980s. The German and Swedish research is related mostly to the performance of the MARK II type containment. The specific experiments concerning the MARK II type containments became topical in connection with the startup of a boiling water reactor in Würgassen in Germany. It was discovered that at steam blowout through the safety valves, there were large loads on structures in the wetwell of the reactor containment. After the events in Würgassen, there was a need to verify that the pressure suppression principle was functional. Thus, a large number of containment experiments was conducted in Marviken during the years 1972 to 1981 (Wikdahl, 2007). O. Sandervåg summarizes the Marviken experiments in Appendix 2 in Wikdahl (2007). During the first series of experiments, 16 simulated pipe ruptures were conducted. A lot of information was obtained about the ruptures in the containments in the experiments, such as the effects of the break size, distribution of energy in the containment, loads from the water level changes, the temperature distribution in the condensation pool, the transport of iodine, and the behavior of different types of electrical components and instrumentation. Even various types of paints and thermal properties of concrete were tested. The experiments proofed that the pressure suppression principle works. It was discovered that standing pressure waves occurred in the containment and that these could be influenced by various things. Condensation of steam in the pool gave

rise to strong dynamic processes. It was considered that the topical problem of dynamic loads due to the venting of steam to the condensation pool could be addressed through the development and installation of devices to better distribute the steam flow to the pool.

The second series of the Marviken experiments focused on the dynamic processes of condensation, and they were aimed to generate data that could shed light on the fundamental properties associated with the condensation process. This series comprised eight simulated pipe ruptures, and they were conducted during the years 1975 to 1976. One of the tests was used as an international standard problem which means that researchers from different countries got to test their own models for calculating the processes. During this series, the improved instrumentation and the faster recording equipment had been put in place. One of the aims was to investigate dynamic processes called condensations oscillations and chugging that could lead to large hydraulic loads. The results showed that the loads from the blowdown through a large number of blowdown pipes gave loads that could be handled better.

In Germany, Aust and Seeliger (1982) and Aust et al. (1983) started their suppression pool studies with nuclear ship propulsion systems, concentrating later on MARK II and German KWU containment pressure suppression systems. In their test facility, three large (0.6 m) diameter blowdown pipes were used, and steam was produced with a flash boiler. An important aspect of their program was to study the mitigation of dynamic loads by pipe design. As mitigators they tested a round collar at the pipe exit and a 45-degree diagonal cut of the pipe exit. Both of the designs were successful in the mitigation purposes. No chugging was detected in the modified pipe exit, whereas in the the non-modified neighboring pipes it was detected. They also used strain-gauges to measure lateral loads on the pipes and recorded high-speed and standard speed video data from the experiments.

McIntyre et al. (1976) and Grafton et al. (1977) performed tests in the Mark II Pressure Suppression Test Program, where they applied the PSTF steam generator to suppression pool experiments with a single vertical pipe. Their emphasis was on the pool responses in LOCA situations. Kukita et al. (1984, 1987) conducted experiments with a multiple blowdown pipe facility modelling a 20 degree sector of annular wetwell. Their blowdowns included air, steam, and saturated water. They used strain-gauge pressure transducers and recorded video material from the top of the wetwell.

Experiments with the vertical steam injection have been conducted also outside the sole interest of suppression pool design validation. Chen and Dhir (1982) did vertical blowdown pipe experiments with air in order to develop a theoretical model for bubble growth at the pipe exit. They observed the bubble oscillations at the pipe exit and noticed that they were caused by the low gas flow rate against the inertia of expanding bubble. They also used fully active strain-gauge type transducers in pressure measurements and recorded high speed video material.
Chan and Lee (1982) studied condensation modes by varying steam mass fluxes and suppression pool temperatures in their single-pipe experimental facility. They used high speed video data to distinguish the bubble and jet types during the experiment. As the

result, they developed a condensation regime map presented in Figure 3.3 later in this thesis. Simpson and Chan (1982) also studied condensation processes and pressure oscillations. They found significant differences between the injected sonic and subsonic steam jets. They distinguished three intervals (i.e. bubble growth, bubble translation, and bubble separation) of the interfacial motion of subsonic jet and proposed that the condensation rates during these intervals are governed by different processes. They also noticed that the pool sub-cooling has a large influence on the dynamic behavior and that the pressure pulse intensity correlates with the Jacob and Reynolds numbers.

Concerning the recent suppression pool experiments, the large PANDA and LINX experimental facilities have to be mentioned. Initially they were used in the ALPHA project of Paul Scherrer Institute (PSI) (Smith, 2007). The goal of the project was to study passive containment cooling systems and the interaction between the various system components during long-term cooling. The PANDA facility is a large integral scale test facility to study such topics. The facility has 1:1 height, 1:25 volume and 1:25 power scaling to the General Electrics Simplified BWR design concept. The LINX facility has been used to study condensation, mixing, effect of non-condensable gases and stratification in suppression pools (Hart et al., 2001).

Also in PSI, Meier et al. (1998) and Meier (1999) conducted smaller scale blowdown experiments with transparent tank using steam and non-condensables. They observed that the length of pipe and compressibility of the gas in piping affects the bubble size, shape and frequency at low flow rates. With high flow rates instead, the effect of compressibility became insignificant.

2.3 A brief review of theoretical studies and modelling

Almost as far as experiments with the condensation pool facilities have been conducted, theoretical work and modelling efforts related to them have been performed as well. Most of this work has been done in order to develop potential flow models to predict pressure distributions that collapsing bubbles cause. In some later studies, CFD has been applied to solve the pressure field as well, but rarely with real phase-change modelling. CFD is also used with FSI in order to solve the pool loads more comprehensively. In this chapter, some of these studies are briefly summarized. Also in this chapter, the background of DCC models used in this study is presented. These models are used usually for separated flows in channels, and they have not generally been applied to suppression pool studies.

2.3.1 Modelling of suppression pools

Before the first nuclear reactors and their safety systems were even considered, rapid condensation processes caused risks for structures elsewhere, particularly in the form of cavitation in pumps and on the surfaces of any kind of fluid moving propellers. Concerning the problem of cavitation, Lord Rayleigh published equations for collapsing cavity (Rayleigh, 1917). Decades later, the bubble equations of Rayleigh had been expanded

for the BWR suppression pool purposes. Giencke (1981) expanded the equations for a finite rigid pool and calculated the pressure time history and bubble radius during a collapse of steam bubble. By calculating also the spatial pressure distribution based on the stationary point source, he presented the flow potential as the product of time-dependent and location dependent parts. Refined Rayleigh bubble analysis with finite pool size, compressibility, vertical bubble motion and gravity was reported also in General Electric reports (McCready et al., 1973). The potential field theory, method-of-images and electric field analogies have been applied to solve the pressure field after the bubble pressure behavior was resolved (Moody, 1977; Karwat et al., 1986).

Lahey and Moody (1993) have presented an analytical model based on the Rayleigh bubble equation and the energy balance equation. They proposed that with a suitable heat transfer coefficient, a mode with damped bubble radius oscillation is reached and it resembles the typical pressure trace of a chugging cycle. Furthermore they extended their model to contain the effect of thermal damping due to bubbly water/gas mixture in the pool.

The use of CFD methods has become increasingly popular during the 1990s and 2000s. Pättikangas et al. (2000) simulated the water hammer due to a steam bubble collapse by using 2D-axisymmetric CFD. They reviewed the Rayleigh equations for the collapse of spherical cavity in an infinite pool. They found out that the mass sink, i.e. the condensation rate has its maximum value when the bubble volume is 1/4 of the fully inflated bubble. During the 2000s, much work has been carried out in VTT concerning the simulations of POOLEX and PPOOLEX experiments at LUT.

A major part of the reported work in VTT has been done with air blowdown and fluid structure interaction modelling (Tuomainen, 2001; Pättikangas and Pokela, 2003; Timperi et al., 2006). During the last years the researchers in VTT have worked on the DCC model development using the PPOOLEX geometry. They have successfully implemented DCC models into Eulerian-Eulerian two-phase solver ANSYS FLUENT. However, the DCC rates, by the Mayinger and Chen (1986) correlation they used, were low compared to the experiments (Pättikangas et al., 2010). Recently, they applied the Hughes-Duffey DCC model tested by Tanskanen and Jordan (2011) and obtained higher DCC rates (Pättikangas et al., 2011). Although the DCC rates were much higher with the Hughes-Duffey DCC model, there remained still hints, e.g. rising bubbles, that the condensation rate would be too weak. They concluded that the condensation models should still be improved, as well as the models for the interfacial area.

Simulations by using lumped-parameter codes have been considered as one option to model suppression pools (Karwat et al., 1986). Concerning the latest simulation with lumped-parameter codes, the GOTHIC simulations in KTH can be mentioned. Li et al. (2010) simulated POOLEX/PPOOLEX experiments using GOTHIC lumped-parameter and FLUENT CFD codes. They did not model DCC, but they used effective heat and momentum sources due to chugging to study the stratification-mixing issue in suppression pools. They also applied the GOTHIC code to resolve missing boundary conditions for

more detailed simulations, e.g. heat losses due to conduction were estimated. The idea of using system codes or lumped-parameter codes for solving missing boundary conditions for POOLEX simulations has also been applied in Tanskanen and Jordan (2009) in which the APROS and TRACE system codes were used to solve some boundary conditions for the POOLEX STB-28 CFD simulations. In VTT, APROS has also been used to study the stratification issue which Li et al. (2010) studied with GOTHIC (Poikolainen and Silde, 2008).

Following the experiments conducted with the PANDA facility of PSI, Yadigaroglu and Lakehal (2003) included the injection of steam/air-mixture from a vertical blowdown pipe into a water pool as one of the challenges in their list of future challenges in thermal hydraulics modelling. They proposed that a coarser-level interfacial tracking, e.g. Volume Of Fluid method (VOF) CFD simulation would receive the necessary exchange rates for DCC heat and mass transfer from a finer-level DNS simulation during a cascade simulation process.

In KTH, Thiele (2010) made an effort to simulate DCC with the VOF model of OpenFOAM code. Energy equation was not available in his simulations, but DCC mass transfer was modelled using $T_{\mathrm{sat}} - T_{\mathrm{bulk}}$ as temperature difference and combustion-like approach (time-scale or 'combustion' frequency) to determine the amount of condensate per unit time or a flat plate condensation correlation for Nu obtained from Bejan (1995).

2.3.2 Direct contact condensation modelling

The heat transfer models for direct contact condensation used in this study were formulated originally based on the separated (or stratified) flows in cases where a film of liquid is subjected under zero or moderate shear conditions. These cases can be falling condensate films or stratified horizontal flows, in which the interfacial shear is formed from the velocity difference between the flowing liquid and vapor phases. Because the liquid phase is in a form of film in many of such cases, there has often been the presence of a wall assumed at a certain distance from the phase interface. Due to the shear also on the wall, the wall has naturally an effect on the turbulence generation in the liquid phase. Because of this, the stratified film flow cases may seem to be an inappropriate basis for the model development for suppression pool cases in which the wall effects on the steam/water-interface are generally negligible. However, in a great part of the model development workarounds, the turbulence near the interface has been considered as a major contributor in the heat transfer mechanisms. Because of that, the parameters, i.e. dimensionless numbers of those models are defined with the local or bulk parameters, like turbulence intensity, eddy size, eddy period, turbulence kinetic energy and dissipation rate, instead of coarser characteristic parameters, like film thickness or average velocity.

As a good starting point, the work of Banerjee et al. (1968) can be mentioned. They detected that very little is known about the effect of a free interface on the turbulent flow. They saw two possible approaches for solving the mass transfer to turbulent liquid. In the first approach, a semiempirical or empirical correlation for eddy diffusivity should

be used, and in the second approach, a physical model based on idealized turbulence structure could be used instead. They discarded the first approach because of the lack of empirical data on the velocity fields. The knowledge of average velocity field would not be sufficient because in high Prandtl or Schmidt number flows, very small scale fluctuations have a significant effect on turbulent heat or mass transfer. Considering the second approach, they developed a model based on the surface renewal theory of Higbie (1935). The surface renewal model is based on the rate, i.e. the time scale with which the very small eddies just beneath the phase interface transport mass, heat or any scalar quantity from the diffusion layer into the larger eddies of bulk flow. Figure 2.3 shows a diagram of the phenomenon.

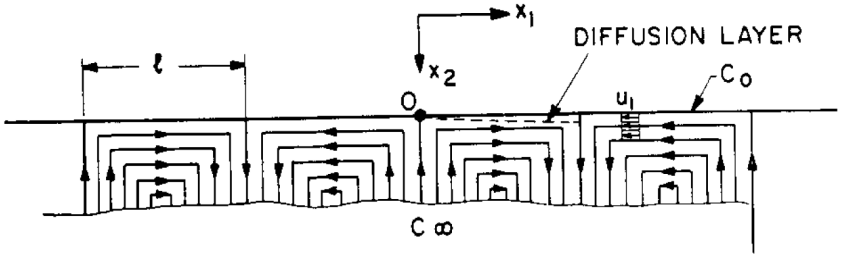

Figure 2.3. Idealized diagram of small eddy structure near interface. Figure from Banerjee et al. (1968).

In the model of Banerjee et al. (1968) and in later models (e.g. Lamont and Scott (1970)), the eddy length and velocity scales are related to parameters such as dissipation of turbulence. Banerjee continued his work on proposing a surface renewal based heat and mass transfer model for a transient two-phase flow Banerjee (1978).

Before Banerjee et al. (1968), Fortescue and Pearson (1967) assumed that the mass transfer across the phase interface can be defined by relatively large scale eddies, and they developed a model that was later called the 'Large Eddy' model. Lamont and Scott (1970) found out that the small eddies control, i.e. the surface renewal rate controls the mass transfer instead and proposed a model called the 'Small Eddy' model. Theofanous et al. (1976) combined these theories by proposing that the 'Large Eddy' model is valid with low (turbulent) Reynolds numbers and the 'Small Eddy' model with the high ones.

In the 1980s, various experiments were conducted and correlations proposed for condensation in separated flows. As examples of these experiments, the studies of Jensen and Yuen (1982), McCready and Hanratty (1984), Lim et al. (1984), Kim and Bankoff (1983), Kim et al. (1985), Sonin et al. (1986) and Banerjee (1990) can be mentioned. Most of these models, summarized also in Lakehal and Labois (2011), can be presented as functions of interfacial shear, i.e. friction velocity u^*.

Hughes and Duffey (1991) reviewed and applied the surface renewal theory to liquid films taking into account the turbulence generated by both the interfacial and wall shear.

They obtained the surface renewal period from the Kolmogorov scales and turbulence dissipation rates. Coste (2004) proposed also a surface renewal model where the surface renewal rate is obtained from the ratio of turbulent velocity and the Kolmogorov length scale.

There are observations that the interfacial shear due to vapor mass flow rate may have a more significant effect on the condensation rate than the flow rate on the liquid side (Lim et al., 1984). With increasing vapor mass flow rates, the appearance of waves increases also the condensation rates further (Lu and Suryanarayana, 1995). Concerning the case without shear of vapor flow, Banerjee (1990) and Banerjee et al. (2004) developed a scalar (heat, mass) exchange model called the 'surface divergence model'. In the surface divergence model, the divergence of tangential velocity fluctuations (streamwise and spanwise fluctuations) at the phase interface is considered as a signature of surface convergence or divergence. The convergence or divergence is also a signature of the surface renewal caused by the eddies that "sweep" the interface bringing bulk fluid on to it and taking interfacial fluid away from it. The main advantage of surface divergence models, according to Banerjee et al. (2004), is that the surface divergence term is easier to measure than the renewal time scale in surface renewal models.

To predict the surface divergence, Banerjee (1990) applied the blocking theory of Hunt and Graham (1978) to relate it to the bulk (homogenous and isotropic region) turbulence characteristics. Applying the results of Brumley and Jirka (1987), he obtained the spectrum of surface divergence and integrated it from the integral scale to the Kolmogorov scale. Eventually, the surface divergence function was formulated which is in use also in the Lakehal 2008b DCC model of this study (Lakehal et al., 2008b).

Although the surface divergence model of Banerjee (1990) and Banerjee et al. (2004) was designed for the unsheared interfaces only, they found out that it applies surprisingly well to the sheared interfaces as well. Particularly for that reason, Lakehal and Labois (2011) continued the development work and proposed an adapted version of the model which borrows the idea of Theofanous et al. (1976) to adjust the model depending on the turbulent Reynolds number.

Coste and Laviéville (2009) observed that the surface renewal models of Hughes and Duffey (1991) and Coste (2004) tend to overestimate the condensation rates in low turbulent (or smooth steam/water interface) cases of Lim et al. (1984) and Tanskanen et al. (2008a), while the model of Lakehal et al. (2008b) and Lakehal (2007) predicts the condensation rate there better. In the high turbulent (rough interface) cases the situation is the opposite. Thus, they presented a model that applies the model of Coste (2004) when the interface is rough and the model of Lakehal et al. (2008b) and Lakehal (2007) when it is smooth. To determine the needed interface agitation information, they applied the diagram of Brocchini and Peregrine (2001a).

In this study, the main comparisons are made between the surface renewal model of Hughes and Duffey (1991) and the surface divergence model of Lakehal et al. (2008b). Also, the hybrid model of Coste and Laviéville (2009) is tested.

3 POOLEX experiments

The main objective of the POOLEX and CONDEX projects was to improve the understanding and increase the fidelity in the quantification of different phenomena inside the dry and wet well compartments of a BWR containment during steam discharge. These phenomena could be connected, for example, to bubble dynamics issues, thermal stratification and mixing, wall condensation, direct contact condensation (DCC), and interaction of parallel blowdown pipes. In such a system, steam bubbles interact with pool water by heat transfer, condensation and momentum exchange via buoyancy and drag forces, and therefore, pressure oscillations due to rapid condensation can occur frequently.

In this chapter, the POOLEX facility and the POOLEX STB-28 and STB-31 experiments are briefly introduced, and their locations in the condensation mode maps are shown.

3.1 POOLEX and PPOOLEX suppression pool experiments

The phenomena taking place in the condensation pool after an internal pipe rupture in the containment have been investigated originally at LUT in the FINNUS/TOKE project, where the effect of non-condensable gas (air) bubbles on the performance of an ECCS strainer and pump was studied (Laine, 2002). The condensation pool test facility used for the experiments of the second generation Nordic BWRs consisted of the following main parts: a condensation pool, two pressure tanks, two blowdown pipes, an ECCS strainer, a pump with piping, and a pressurized air injection system (Riikonen, 2011). After a few modifications the facility was also used for the experiments of the first generation Nordic BWRs. After the steam line from PACTEL steam generators was built, the facility was renamed POOLEX according to the project name in SAFIR. The SAFIR/POOLEX project focused on experiments where steam is discharged into a water pool. Figure 3.1 shows the main characteristics of the POOLEX and the later PPOOLEX test facilities.

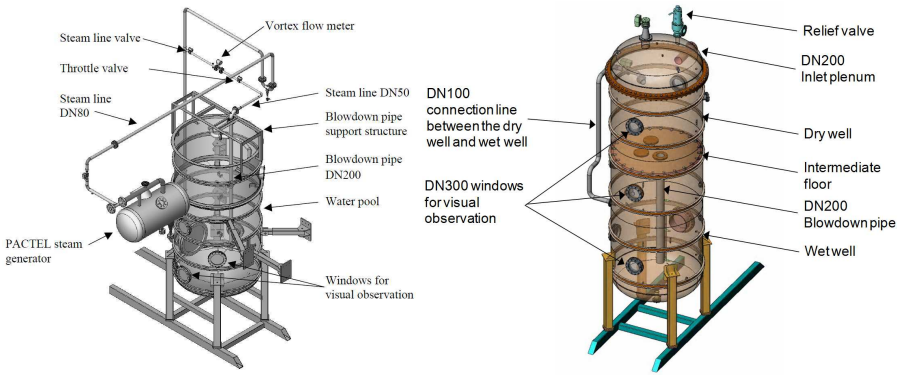

Figure 3.1. POOLEX (left) and PPOOLEX (right) test facilities.

The pool of POOLEX was a cylinder shaped stainless steel pool with open top. The inner diameter of the pool was $2.4\,\mathrm{m}$, the cross-sectional area $4.5\,\mathrm{m}^2$ and the height $5.0\,\mathrm{m}$. There were five circular windows in the pool wall for the visual observation of the interior. Measurement instrumentation included temperature, pressure, flow rate, strain-gauge and valve position measurements. During the experiments, the events in the pool could also be recorded with video cameras through the windows on the pool walls and below the pool level with an underwater camera.

The maximum operating pressures on the primary and secondary sides of the PACTEL facility were $8.0\,\mathrm{MPa}$ and $4.6\,\mathrm{MPa}$, respectively. The maximum electrical heating power of the PACTEL core simulator available for steam production was $1\,\mathrm{MW}$. The steam line from PACTEL steam generators was made of standard DN80 and DN50 steel pipes. The line was thermally insulated with mineral wool to prevent steam from condensing before reaching the blowdown pipe. DN200 (inner diameter $214.1\,\mathrm{mm}$), DN100 (inner diameter $110.3\,\mathrm{mm}$) and DN80 (inner diameter $84.9\,\mathrm{mm}$) stainless steel pipes were used separately as blowdown pipes in the early experiments. Later, the DN200 pipe was the mostly used one. The blowdown pipe is located to a non-axisymmetric location from the pool vertical axis.

After the SAFIR/POOLEX project experiments, the POOLEX facility was replaced with the closed-pool PPOOLEX facility to be used in the SAFIR/CONDEX project (Riikonen, 2011). The PPOOLEX pressure vessel includes a wet well compartment (condensation pool) and a dry well compartment with connections to the inlet plenum with air/steam line piping. An intermediate floor separates the compartments from each other, but a route for gas/steam flow from the dry well to the wet well is created by a vertical blowdown pipe attached underneath the floor.

The main component of the PPOOLEX facility is the $31\,\mathrm{m}^3$ cylindrical test vessel, $7.45\,\mathrm{m}$ in height and $2.4\,\mathrm{m}$ in diameter. The test facility is able to withstand considerable structural loads caused by rapid condensation of steam ($4\,\mathrm{bar}$ overpressure, $0.5\,\mathrm{bar}$ underpressure). The vessel sections modelling dry well and wet well are volumetrically scaled

according to the compartment volumes of the Olkiluoto containment buildings by using the scaling factor circa 1:320. Like in the POOLEX facility, the DN200 blowdown pipe is positioned inside the pool in a non-axisymmetric location, i.e. $300\,\mathrm{mm}$ away from the centre of the condensation pool. As in the case of the POOLEX facility, the steam needed in the experiments is produced with the PACTEL steam generators, and the accumulators connected to the compressed air network of the lab can be used for providing an additional non-condensable gas injection. The steam lines are thermally insulated.

The POOLEX objectives and results

The main objective during the POOLEX steam discharge experiments was the production of measurement data to be used for different verification purposes. Load estimation, structural analysis, modelling of fluid-structure interactions and thermal stratification are, for example, research areas where the data produced in the POOLEX project could be utilized.

With low steam mass fluxes, high sub-cooling of pool water and large blowdown pipe, condensation inside the blowdown pipe and water-hammer with strong pressure oscillations inside the pipe were observed. With higher steam mass fluxes, the chugging mode was reached with DCC occurring mostly on bubbles outside of the pipe. The dynamic loads on the pool bottom were measured. For example, the maximum dynamic loads of $54\,\mathrm{MPa}$ were recorded, which with $58\,\mathrm{MPa}$ hydrostatic load of pool water yields $112\,\mathrm{MPa}$ total stress. The most severe loads were observed during lower sub-cooling, and their occurrence was occasional among the series of lower amplitude loads.

The bubbles at the exit of the blowdown pipe were recorded with high-speed and standard speed video cameras. Typical bubble sizes and their collapse rates were obtained visually from the video material recorded at different pool water temperatures.

Thermal stratification in the pool water was observed in the long term experiments. Strong temperature stratification of pool water developed in conditions where the DCC occurs mainly inside the blowdown pipe. This was due to the weak mixing of water as the bubbles and their collapses were not mixing the pool water.

The PPOOLEX objectives and results

The main objectives of experiments with the PPOOLEX facility have been the same as with the POOLEX facility, but with the PPOOLEX, also the phenomena in the dry well compartment and their effect on the whole system can be observed.

The drywell was filled initially by air in the PPOOLEX experiments at the beginning of steam injection. Condensation oscillations and chugging phenomenon were encountered in the tests where the fraction of non-condensables had time to decrease significantly. A radical change from smooth condensation behavior to oscillating one with pressure pulses occurred quite abruptly when the air fraction of the blowdown pipe flow dropped close to zero. The experiments demonstrated the strong diminishing effect that non-condensable gases mixed in the flow have on dynamic unsteady loadings experienced by submerged pool structures.

Concerning the drywell compartment, a number of experiments were conducted in which the wall condensation in the dry well was measured by a condensate collecting system. Later the whole PPOOLEX facility was thermally insulated.

The thermal stratification of pool water and dynamic loads due to the chugging were investigated in the same way as in the POOLEX experiments. Concerning the studies of dynamic loads, bubble formation and break up, the effect of blowdown pipe exit collar and two parallel blowdown pipes were studied. Also, a transparent plexiglass blowdown pipe was tested to get some hint of water/steam-interface motion inside the blowdown pipe.

The condensation pool experiments still continue at LUT with the PPOOLEX facility. The recent upgrades to the instrumentation include particle image velocimetry system (PIV) and high speed video camera at the pool bottom below the blowdown pipe. With PIV, the velocity field of pool water near the blowdown pipe is measured, and with multiple high speed cameras, the geometry and collapse of bubbles can be better evaluated.

3.2 Condensation mode maps of suppression pools

The handbook of thermal hydraulics of BWRs (Lahey and Moody, 1993), presents a map of the condensation modes that have been observed during either Loss-of-Coolant Accident (LOCA) or Safety/Relief Valve (SRV) steam discharge, see Figure 3.2. Another condensation mode map proposed by Chan and Lee (1982) is presented in Figure 3.3. The map of Lahey and Moody (1993) labels clearly the main condensation modes, whereas the map ofChan and Lee (1982) describes more clearly the types of observable bubbles and jets.

With low steam mass flux and cold pool water temperature, condensation takes place within vents or blowdown pipes. A sharp drop in local steam pressure occurs as steam condenses rapidly when interacting with cold pool water. Because the condensation process is very rapid, an underpressure develops inside the blowdown pipe. Immediately after that, a condensation-induced water hammer is initiated as the pipe begins to fill with water. At the end of the collapse, a high pressure pulse occurs inside the pipe when it is filled with water. In this condensation mode, steam/water interface moves strongly up and down in the blowdown pipe.

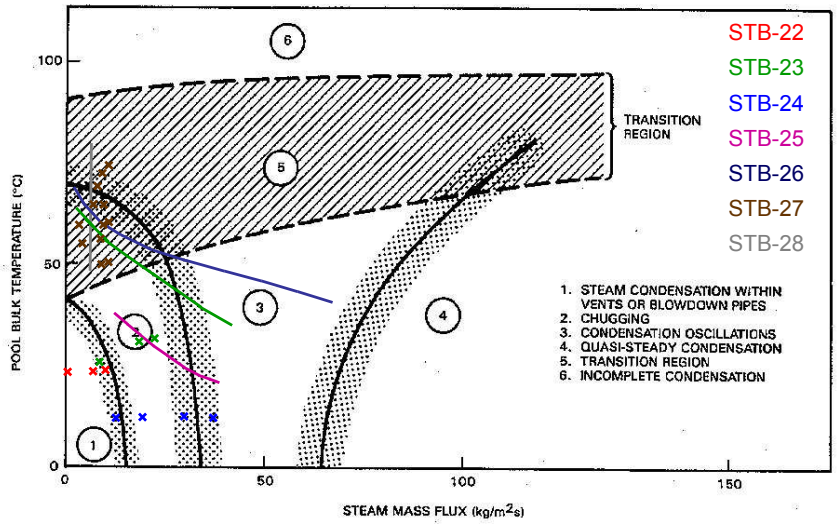

Figure 3.2. Condensation mode map for pure steam discharge (Lahey and Moody, 1993). Crosses and lines of different colors illustrate separate blowdowns during STB-22, STB-23, STB-24, STB-25, STB-26, STB-27 and STB-28 experiments in the POOLEX facility.

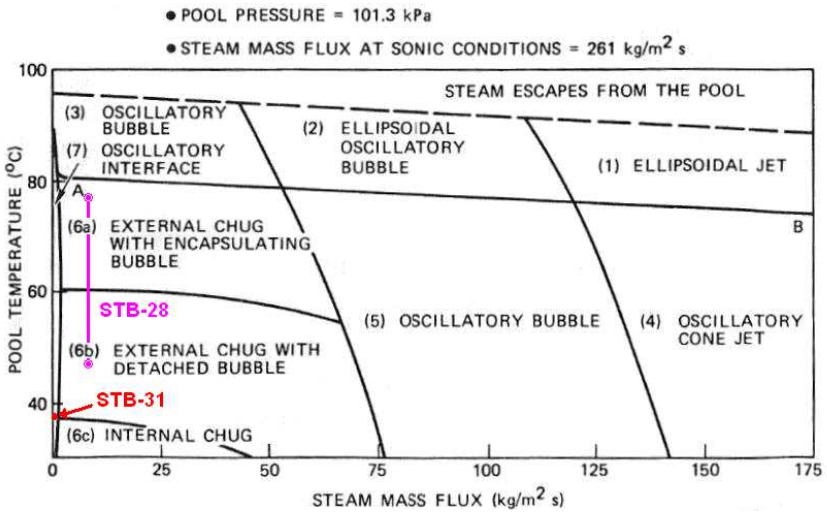

Figure 3.3. Condensation regime map of Chan and Lee (1982). POOLEX STB-31 and STB-28 experiments marked with colors.

As the steam mass flux increases, chugging or random condensation phenomena will commence. In the chugging, the steam/water interface moves downwards inside the blowdown pipe and a steam bubble is formed at the pipe outlet (see steps 1−5 in Figure 3.4). The bubble condenses rapidly, and an underpressure is generated (step 6). The steam/water interface begins to move upwards inside the pipe (steps 7−9) until the steam pressure is high enough to stop the interface and start again to push it downward (step 10). Chugging imposes dynamic loads on submerged pool structures (Lahey and Moody, 1993).

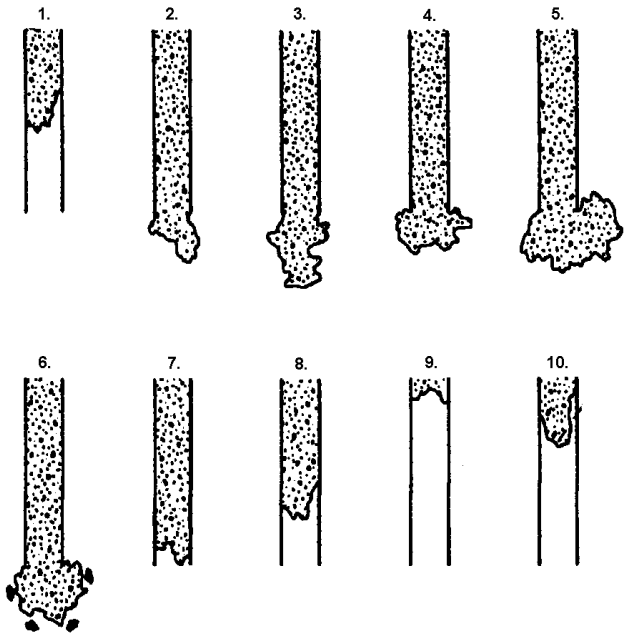

Figure 3.4. Sketch of the chugging phenomena. Sargis et al. (1978)

Increasing the steam mass flux further leads to condensation oscillations. In this case, the steam/water interface undergoes a condensation event entirely in the pool. Steam bubble forms at the pipe outlet and begins to collapse. However, the high steam flow rate prevents water from re-entering into the blowdown pipe. The next bubble is formed, leading to a condensation event and the cycle is repeated. Condensation oscillations cause unsteady loads on submerged pool structures (Lahey and Moody, 1993).

With very high steam flows, quasi-steady condensation is the dominating condensation mode. Condensation can be quasi-steady also with low steam mass flow rates if non-condensable gases mitigate condensation, sub-cooling of water is low and/or the blowdown pipe is insulated to prevent wall condensation. In this mode, high steam mass flux or low condensation rate keeps the steam/water interface on the pipe outlet. Because the steam condenses steadily, no large loads are imposed on submerged pool structures.

3.3 The STB-31 experiment: Direct contact condensation on stable interface

The earlier steam discharge experiments with the facility (i.e. the STB-29 and the experiments before it) were considered too challenging as initial validation cases for the CFD codes due to very rapid direct contact condensation phenomena and unknown amount of condensation on the pipe walls. Therefore, it was decided to carry out an experiment series aimed at producing data of more stable nature. One experiment (labeled as STB-31) in the POOLEX series was conducted for the validation of the NEPTUNE_CFD condensation models. In the STB-31 experiment, the vertical blowdown pipe (inner diameter $214.1\,\mathrm{mm}$) was thermally insulated to prevent condensation on the pipe inner wall. The nearby PACTEL test facility was used as a steam source. Figure 3.5 presents the POOLEX test facility and the locations of the steam line measurements. Figure 3.6 shows the measurements in the pool, and Figure 3.7 in the vicinity of the pipe exit.

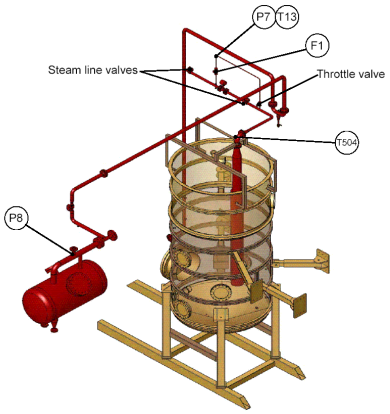

Figure 3.5. POOLEX test facility and the locations of the steam line measurements.

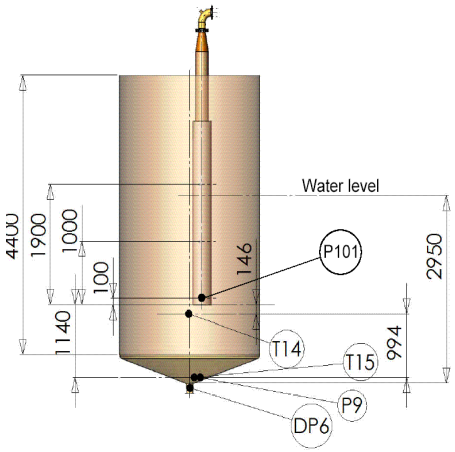

Figure 3.6. Measurements in the pool.

Before starting the measurements, the pool was filled with isothermal water ($32\,^{\circ}\mathrm{C} \pm 3\,^{\circ}\mathrm{C}$) to a level of $2.95\,\mathrm{m}$, i.e. the total volume of water was approximately $12\,\mathrm{m}^3$ and the blowdown pipe was submerged by $1.81\,\mathrm{m}$. The duration of the experiment was about $6000\,\mathrm{s}$. The steam mass flow rate ($0.5 \ldots 1.5\,\mathrm{g/s}$) was controlled through the experiment to prevent steam bubble formation and to keep the steam/water interface as close as possible to the pipe outlet. As the interface was stationary, it could be assumed that the injected steam mass flow rate was equal to the condensation mass flow rate. Several such quasi-steady state intervals can be found from the experiment data. Due to the known condensation rate, these intervals from the experiment are suitable for the validation of direct contact condensation models. Figure 3.8 shows the desired stable steam/water interface in the pipe outlet and Figure 3.9 shows the mass flow rate, temperature and pressure of steam during the STB-31 experiment. For further information of the STB-31 experiment,

see Laine and Puustinen (2006a). The measurement instrumentation of the POOLEX facility is described in detail in APPENDIX 1.

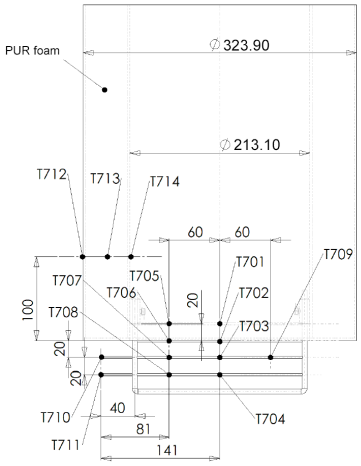

Figure 3.7. Measurements in the vicinity of the pipe mouth.

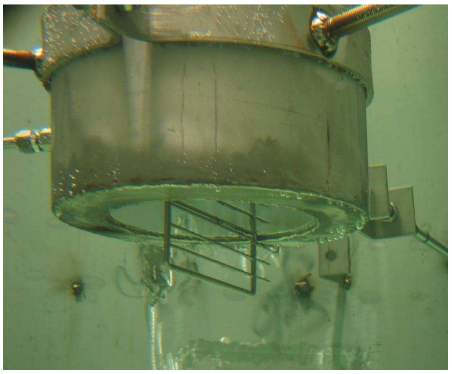

Figure 3.8. The stable steam/water interface in the pipe outlet.

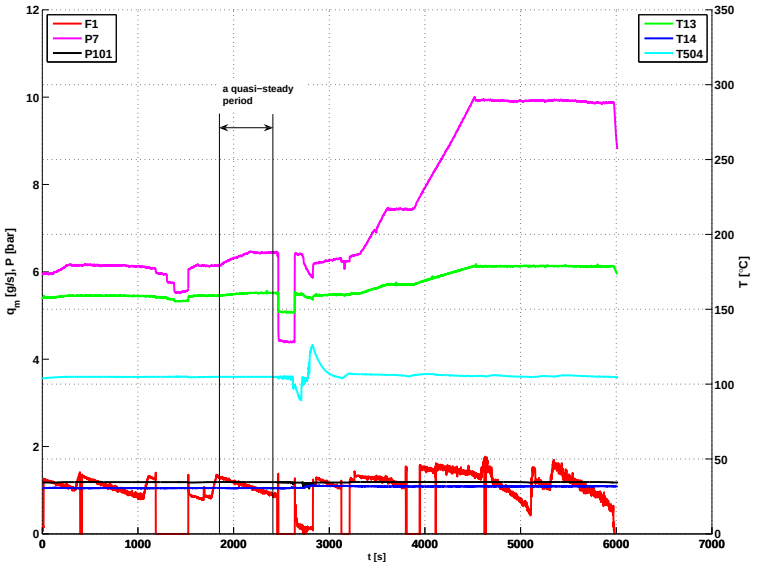

Figure 3.9. Steam mass flow rate (F1), steam line temperature (T13), steam line pressure (P7), blowdown pipe temperature (T504) and blowdown pipe pressure (P101) in the STB-31 experiment. T14 is the water temperature in the pool.

3.4 The STB-28 experiment: Direct contact condensation in chugging regime

A sketch of the pre STB-31 POOLEX test rig and the instrumentation inside its pipeline and pool are presented in Figure 3.10.

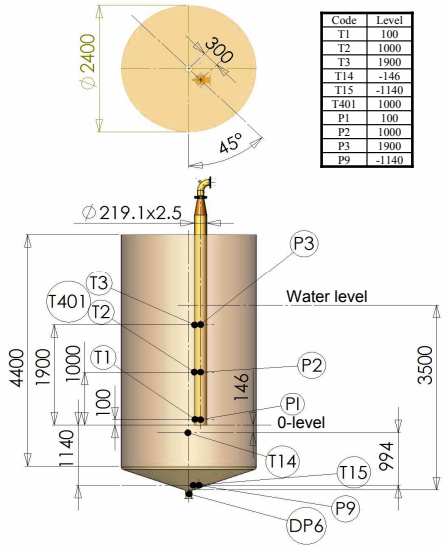

Code	Level
T1	100
T2	1000
T3	1900
T14	-146
T15	-1140
T401	1000
P1	100
P2	1000
P3	1900
P9	-1140

Figure 3.10. Instrumentation inside the blowdown pipe and at the pool bottom.

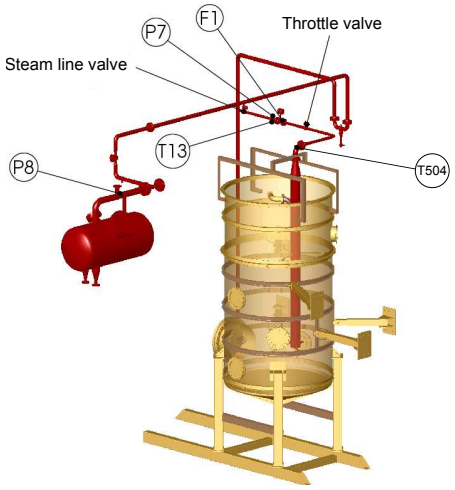

Figure 3.11. Flow rate (F1), temperature (T13, T504) and pressure (P7, P8) of steam.

One of the test programmes in the project consisted of seven tests labeled from STB-22 to STB-28. Each test included three to sixteen separate blowdowns. All tests were performed by using the DN200 blowdown pipe. Steam generators of the PACTEL test facility were used as a steam source during the experiments (Tuunanen et al., 1998). Before each experiment, the pool was filled with water to the level of approximately $3.5\,\mathrm{m}$, i.e. the blowdown pipe outlet was submerged by $2\,\mathrm{m}$. The position of the throttle valve (located just after the flow meter in the steam line) was adjusted before the blows to have the steam flow rate inside the measurement range ($0 \ldots 285\,\mathrm{l/s}$). During the pressure build-up phase and between the individual tests, the steam line was heated with a small bypass flow. After the desired pressure in the steam generators had been achieved, the remote controlled shut-off valve in the steam line was opened. As a result, the blowdown pipe was filled with steam that immediately pushed its way to the pool. The steam flow may have contained a small amount of air, depending on the on-going state of the experiment. During the experiments, all three PACTEL steam generators were used to generate steam. The measurement instrumentation of the POOLEX facility is described in detail in APPENDIX 1.

The STB-28 experiment consisted of one long-running steam blowdown (duration $3195\,\mathrm{s}$). The purpose of this test was to study the formation and condensation of steam bubbles at the blowdown pipe outlet as a function of pool water temperature. During the blowdown, seven short time intervals (duration $12 \ldots 30\,\mathrm{s}$) were recorded by using LabView software (labeled from STB-28-1 to STB-28-7). The initial steam generator pressure was $0.3\,\mathrm{MPa}$. The pool water temperature rose from $47\,^{\circ}\mathrm{C}$ to $77\,^{\circ}\mathrm{C}$ during the test. The steam mass flux stayed at the level of $8\,\mathrm{kg}/(\mathrm{m}^2\,\mathrm{s})$ during the whole blowdown. Figure 3.12 shows the mass flow rate, temperature and pressure of steam during the STB-28 experiment.

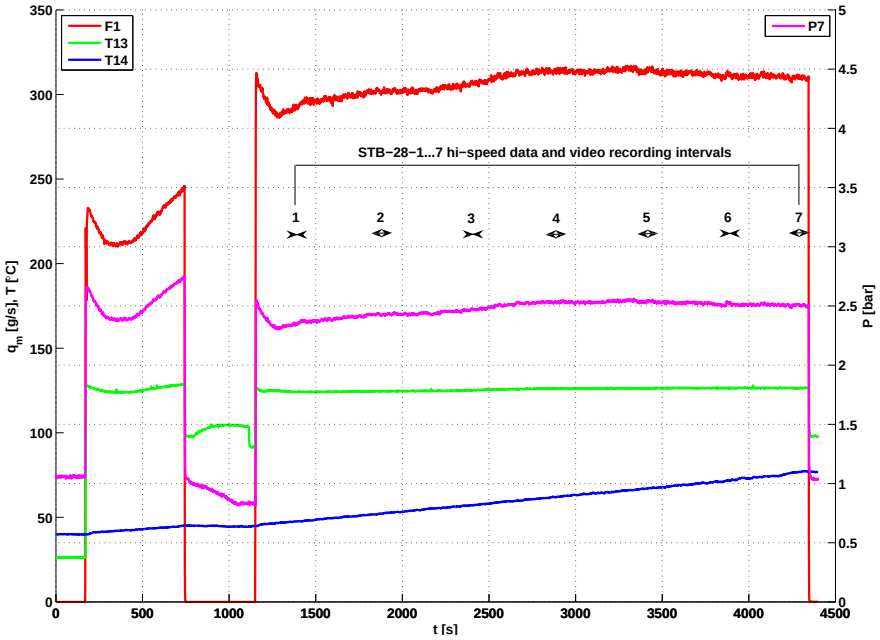

Figure 3.12. Steam mass flow rate (F1), temperature (T13) and pressure (P7) in the STB-28 experiment. T14 is the water temperature in the pool. The actual steam blowdown was initiated at $1150\,\mathrm{s}$.

During the blowdown, the chugging phenomenon was the dominating condensation mode. For this reason, steam bubbles of different sizes formed at the blowdown pipe outlet. The bubbles were quite small in the early phase of the test. As the pool water temperature rose, still larger and larger bubbles formed at the pipe outlet. Figure 3.13 shows some typical steam bubbles that formed during the STB-28 experiment. The collapse times and diameters of the steam bubbles (see Table 3.1) were estimated by observing the high-speed videos. The collapse times presented in Table 3.1 represent the time which is required for a fully expanded steam bubble to collapse to approximately zero void at the mouth of the blowdown pipe.

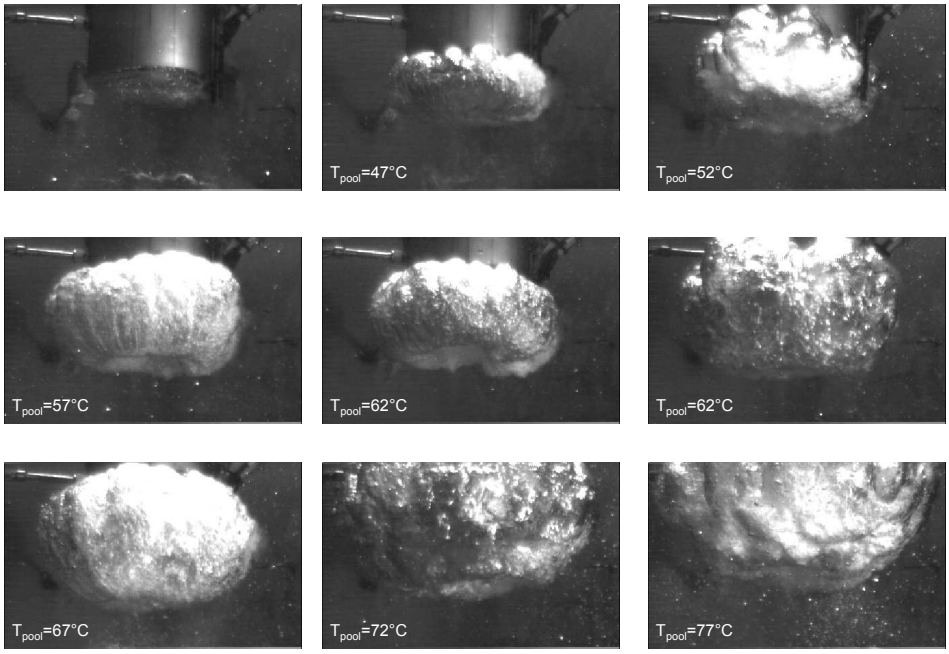

Figure 3.13. Frame captures from STB-28.

Table 3.1. Collapse times and diameters of the steam bubbles presented in Figure 3.13.

Experiment part n:o	**Pool water temperature** [°C]	**Steam mass flux** [kg/(m^2 s)]	**Collapse time** [m s]	**Bubble diameter** [mm]	**Collapse speed** [m/s]
STB-28-1	47	8	35	270	3.8
STB-28-2	52	8	45	300	3.4
STB-28-3	57	8	40	350	4.6
STB-28-4	62	8	80	380	3.0
STB-28-5	67	8	90	400	2.2
STB-28-6	72	8	110	450	2.1
STB-28-7	77	8	130	500	2.0

Chugging caused loads to the pool structures during the experiment STB-28. Figure 3.14 shows the measured pressures at the pool bottom.

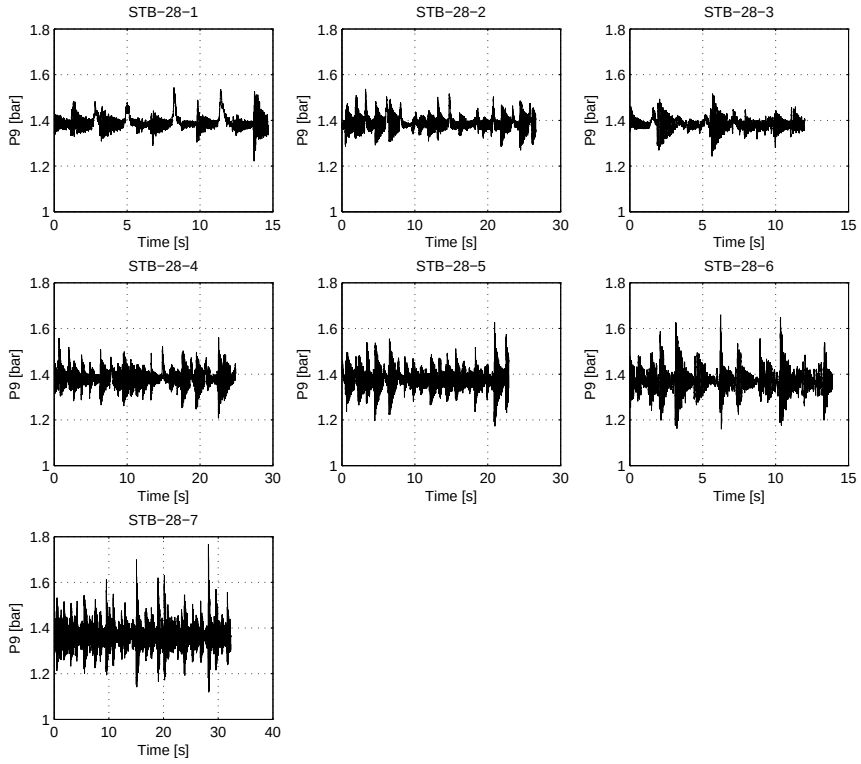

Figure 3.14. Pressure (P9) at the pool bottom in the STB-28 experiment.

Pressure loads (max. $1.1\,\mathrm{MPa}$) were registered inside the blowdown pipe after a low-pressure void was filled with water hammer. Strain gauges on the pool outer wall registered oscillations with the maximum amplitude of $270\,\mu\varepsilon$ (measured by ST5 during STB-28-7). The strain is a dimensionless length defined as

$$\epsilon_E = \frac{\Delta L}{L}, \tag{3.1}$$

where ΔL is the displacement and L is the original length. Although the strain is dimensionless, it is generally marked with some notation of unit e.g. [ε] or [S] to be capable of speaking $\mu\varepsilon$ - micro strains. The stresses can be calculated from the strain by using Hooke's law:

$$\sigma_E = E\epsilon, \tag{3.2}$$

where E is the Young's modulus. The highest pressure load at the pool bottom was $40\,\mathrm{kPa}$. The load was caused by condensation-induced water hammer during the end part of the experiment (see STB-28-7 in Figure 3.14). The load caused by a water plug hit to the pool bottom in the beginning of the blowdown was not measured. Figure 3.2 shows a

condensation mode map, where the STB-28 blowdown is marked as a continuous vertical gray line in the overlapping chugging and transition regions.

The end part of the continuous blowdown in the STB-28-4 (see Table 3.1) was selected as the first case to be simulated using CFD. After simulating this case in a satisfactory manner, other parts of the experiment would be simulated as well.

4 Physical models

In this chapter, the governing equations of NEPTUNE_CFD and TransAT are shown and the stratified flow condensation models to be applied in the simulations are described. The $k-\varepsilon$ turbulence model of NEPTUNE_CFD is presented as well. The specified models like closure models, i.e. drag models are described in the extent that is reasonable. At the end, the methods used in the estimations of non-condensable gas and wall condensation effects are presented. Concerning the governing equations and closure laws of the NEPTUNE_CFD code, the theory manual of Laviéville et al. (2006) is used as the reference documentation. The references for the condensation models and other special models are mentioned separately. Concerning all the TransAT equations and models, the theory manual of multiphase flow modelling with TransAT (Ascomp, 2011) is used as the reference.

4.1 Eulerian-Eulerian approach of 2-phase flow modelling

According to NEPTUNE_CFD theory manual of Laviéville et al. (2006), the multi-field mass balance equation for the field k is written

$$\frac{\partial}{\partial t}\left(\alpha_k \rho_k\right) + \frac{\partial}{\partial x_i}\left(\alpha_k \rho_k U_{k,\,i}\right) \;=\; \Gamma_k, \tag{4.1}$$

where α_k is the volume fraction, ρ_k is the density and U_k is the mean velocity of phase k. Γ_k is the interfacial mass transfer rate of phase k, and it is the sum of all other phase contributions.

The conservation of momentum equation in NEPTUNE_CFD has the form

$$\begin{aligned}\rho_k \frac{\partial}{\partial t} U_{k,i} - U_{k,i}\frac{1}{\alpha_k}\frac{\partial}{\partial x_j}\left(\alpha_k \rho_k U_{k,j}\right) + \frac{1}{\alpha_k}\frac{\partial}{\partial x_j}\left(\alpha_k \rho_k U_{k,i} U_{k,j}\right) = \\ \frac{1}{\alpha_k}\frac{\partial}{\partial x_j}\left(\alpha_k\left(\tau_{k,ij} + \tau^{\mathrm{t}}_{k,ij}\right)\right) - \frac{\partial P}{\partial x_i} + \rho_k g_i + \sum_{p\neq k}\frac{I'_{(p\to k),i}}{\alpha_k} + S_{\mathrm{M},k,i},\end{aligned} \tag{4.2}$$

where P is the mean pressure, g_i is the acceleration due to gravity, $\tau_{k,ij}$ is the viscous stress strain tensor, $\tau^{\mathrm{t}}_{k,ij}$ is the turbulent stress strain tensor, S_{M} is the external source term of momentum, and $I'_{(p\to k),i}$ is the interfacial momentum transfer rate without the mass transfer contribution. The effect of mass transfer in the momentum equation is considered negligible and it is left out from the equation. The viscous and turbulent stress strain tensors are defined as follows:

$$\tau_{k,ij} = \mu_k\left(\frac{\partial U_i}{\partial x_j} + \frac{\partial U_j}{\partial x_i} - \frac{2}{3}\left(\nabla\cdot U\right)\delta_{i,j}\right) \tag{4.3}$$

$$\tau^{\mathrm{t}}_{k,ij} = -\rho_k \langle U'_{k,i} U'_{k,j}\rangle_k \tag{4.4}$$

The energy equation of NEPTUNE_CFD is

$$\rho_k \frac{\partial H_k}{\partial t} - H_k \frac{1}{\alpha_k}\frac{\partial}{\partial x_j}\left(\alpha_k \rho_k U_{k,j}\right) + \frac{1}{\alpha_k}\frac{\partial}{\partial x_j}\left(\alpha_k \rho_k H_k U_{k,j}\right) = \tag{4.5}$$
$$-\frac{1}{\alpha_k}\frac{\partial}{\partial x_j}\left(\alpha_k q''_{k,j}\right) + \frac{\partial P}{\partial t} + \rho_k U_{k,i} g_i + \frac{q''_{(\text{wall}\to k)}}{\alpha_k}$$
$$+\frac{1}{\alpha_k}\sum_{p\neq k}\left[\Pi'_{(p\to k)} + \Gamma^{\text{c}}_{(p\to k)} H^{\sigma}_{(p\to k)}\right] - \frac{\Gamma_k H_k}{\alpha_k},$$

where H is the total enthalpy, q'' is the conductive thermal flux, $q''_{(\text{wall}\to k)}$ represents the heat exchanges with wall boundaries and is described by the nucleate boiling model in NEPTUNE_CFD, Π' is the interfacial heat transfer rate independent of the mass transfer, $H^{\sigma}_{(p\to k)}$ is the jump of enthalpy associated with mass transfer from phase p to phase k, and $\Gamma^{\text{c}}_{(p\to k)}$ is the mass transfer rate contribution from phase p to phase k. For the $\Gamma^{\text{c}}_{(p\to k)}$, the following relation must be verified

$$\Gamma^{\text{c}}_{(p\to k)} = -\frac{\Pi'_{(p\to k)} + \Pi'_{(k\to p)}}{H^{\sigma}_{(p\to k)} - H^{\sigma}_{(k\to p)}}. \tag{4.6}$$

In two-phase water/steam cases, these notations can be simplified, so for example for water phase, Equation 4.6 is presented as

$$\Gamma^{\text{c}}_{1} = \frac{\Pi_1^{'\text{w/s}} + \Pi_2^{'\text{w/s}}}{H_2 - H_1}. \tag{4.7}$$

Thus in the two-phase case, if nucleate mass transfer does not exist, the last term and the mass transfer contribution in the previous term in the energy equation (Equation 4.5) can be neglected. In the case with saturated vapor, the $\Pi_2^{'\text{w/s}}$ contribution is negligible in Equation 4.7. The heat transfer rate $\Pi_1^{'\text{w/s}}$ has to be solved by using a suitable condensation model. It can be noticed that the effects of surface tension and other possible energy sources like the entropy of mixing are not explicitly present or are neglected in the conservation equations. The effect of surface tension is not generally present in the Eulerian-Eulerian conservation equations due to its complicated calculation, which is not often easy to implement into the code. The effect of the surface tension can be simulated by using a suitable drag model or a separate source term. Due to the presence of phase change, the other energy sources like the entropy of mixing can be considered negligible, and can therefore be omitted from the energy equation.

4.2 Interface tracking method for 2-phase flow modelling

In interface tracking methods, a single set of transport equations is solved for the whole computational (fluid) domain and the two phases of fluid are solved as a single fluid with variable material properties. The location of the interface determines the location where

the material properties change. The interface location in the Level Set method is solved by advecting the Level Set function

$$\frac{\partial \phi}{\partial t} + U_i \frac{\partial \phi}{x_i} \quad = \quad 0, \tag{4.8}$$

which is rewritten in the case of phase change in TransAT (Ascomp, 2011) as

$$\frac{\partial \phi}{\partial t} + U_i \frac{\partial \phi}{x_i} \quad = \quad -\frac{\rho q_{\mathrm{m}}^{''}}{\rho_1 \, \rho_2} | \frac{\partial \phi}{\partial x_i} |. \tag{4.9}$$

In these equations, $\phi \left[\mathbf{x}, t \right]$ is a smooth signed-distance function referring to the shortest distance to the interface. The sign of ϕ determines in which of the two phases the location $\mathbf{x}$ is. The ϕ function has its zero level at the interface. The material properties across the interface are updated in the Level Set by using a Heaviside function, which is zero when $\phi < 0$ and one elsewhere. In TransAT, a modified version of the Heaviside function is used, which is

$$\overline{H} \left[\phi \right] \quad = \quad \tanh \left[2\phi / \delta \right], \tag{4.10}$$

where δ is the interface thickness. Figure 4.1 shows the presumable average temperature profiles near a liquid/vapor interface (Ghiaasiaan, 2008).

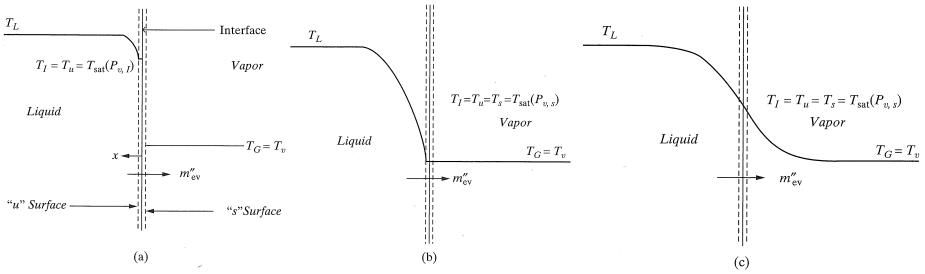

Figure 4.1. The temperature distribution near the liquid-vapor interphase: (a) early, during a very fast transient evaporation; (b) quasi-steady conditions with pure vapor; (c) quasi-steady conditions with a vapor-noncondensable mixture (Ghiaasiaan, 2008).

Taking into account the shape of the temperature profile and also its analogy with the concentration profile, the Heaviside function of Eq. 4.10 is a good approximation, as can be seen in Figure 4.2.

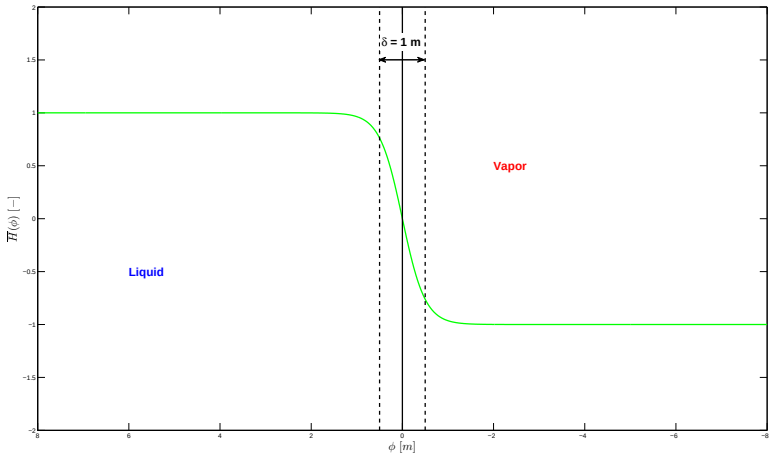

Figure 4.2. The modified Heaviside function across the interface defined by a Level Set function. Interface thickness δ set to unity.

By refining the calculation grid, the Heaviside function approaches a step function if δ is bound to the cell size. If necessary, δ can be adjusted to a looser value. In any case, the material properties can be updated by multiplying them by the value of the Heaviside function. For example, the density values are then updated with

$$\rho\left[\phi,t\right] \;=\; \sum_{k}\rho_k\overline{H}\left[\phi\right], \tag{4.11}$$

where 'k' indicates phase 1 or 2. The other material properties like μ, c_p and λ are updated in the same way.

If phase change is assumed, the incompressible mass conservation equation of TransAT can be presented in the form

$$\frac{\partial U_i}{\partial x_i} \;=\; q''_{\mathrm{m}}\left(\frac{1}{\rho_2}-\frac{1}{\rho_1}\right)\delta_{\mathrm{I}}\left[\phi\right]\left|\frac{\partial\phi}{\partial x_i}\right|, \tag{4.12}$$

where δ_{I} is a smoothed dirac delta function centered at the interface. The incompressible momentum equation in TransAT has the form

$$\frac{\partial\rho U_i}{\partial t}+\frac{\partial}{\partial x_j}\left(\rho U_iU_j\right) \;=\; \frac{\partial}{\partial x_j}\left(-P\delta_{ij}+\tau_{ij}\right)+\rho g_i+\sigma\kappa_\sigma\delta_{\mathrm{I}}\left[\phi\right]n_i, \tag{4.13}$$

where σ is the surface tension, κ_σ is the interface curvature, n_i is the i component of unit normal vector to the interface, and δ_{ij} is the Kronecker delta tensor. The heat (enthalpy)

equation in TransAT has the form

$$\frac{\partial \rho c_p T}{\partial t} + \frac{\partial}{\partial x_j}\left(\rho c_p T U_j\right) = \frac{\partial}{\partial x_j}\left(\lambda \frac{\partial T}{\partial x_j}\right) + S_{\mathrm{H}} - q''_{\mathrm{m}} \delta_I \left[\phi\right]\left(\Delta h_2 + T_{\mathrm{sat}} \Delta c_p\right) \quad (4.14)$$

where c_p , λ is the specific heat at constant pressure and S_{H} is the (additional) volumetric heat source term.

4.3 Turbulence models

The most of the simulations presented in this study have been performed using the Reynolds (Unsteady) Averaged Navier-Stokes ((U)RANS) approach, i.e. the $k-\varepsilon$ model in NEPTUNE_CFD. A few TransAT simulations have been simulated using Direct Numerical Simulation (DNS), i.e. without averaging of velocity field in time or space. The equations of $k-\varepsilon$ model of TransAT are not presented here due to their relative similarity with the NEPTUNE_CFD formulations, and due to the small number of RANS simulations done using TransAT in this study.

The $k-\varepsilon$ model of NEPTUNE_CFD is a classical one, which is extended for multiphase purposes. It can be used to simulate the turbulence of a single continuous phase, a continuous phase with dispersed phase contribution or the turbulence of two continuous phases. In the simulations of this study, both of the phases are considered as continuous phases, i.e. both phases have their own equations for turbulent kinetic energy k and dissipation rate ε;

$$\rho_k \left(\frac{\partial k_k}{\partial t} + U_{k,i}\frac{\partial k_k}{\partial x_i}\right) = \frac{1}{\alpha_k}\frac{\partial}{\partial x_j}\left(\alpha_k \frac{\mu_k^{\mathrm{t}}}{\sigma_k}\frac{\partial k_k}{\partial x_j}\right) + \rho_k\left(\mathbb{P}_k + \mathbb{G}_k - \varepsilon_k\right) + \Pi_{qk} \quad (4.15)$$

$$\begin{aligned}\rho_k \left(\frac{\partial \varepsilon_k}{\partial t} + U_{k,i}\frac{\partial \varepsilon_k}{\partial x_i}\right) =& \frac{1}{\alpha_k}\frac{\partial}{\partial x_j}\left(\alpha_k \frac{\mu_k^{\mathrm{t}}}{\sigma_\varepsilon}\frac{\partial \varepsilon_k}{\partial x_j}\right) + \rho_k \frac{\varepsilon_k}{k_k}\left(C_{\varepsilon 1}\mathbb{P}_k + C_{\varepsilon 1}\max\left(\mathbb{G}_k, 0\right) - C_{\varepsilon 2}\varepsilon_k\right) \\ &+ C_{\varepsilon 4}\frac{\varepsilon_k}{k_k}\Pi_{qk},\end{aligned} \quad (4.16)$$

where μ^{t} is the turbulent viscosity, σ_k and σ_ε are the turbulent Prandtl numbers for k and ε, $\mathbb{P}$ is the positive production of k due to the mean velocity gradients, $\mathbb{G}$ is the stratification attenuation term, and Π_q is the production or destruction of k due to the influence of the other phases. Constants $C_{\varepsilon 1}$,$C_{\varepsilon 2}$ and $C_{\varepsilon 4}$ are the model constants of the $k-\varepsilon$ model, having values 1.44, 1.92, and 1.2, respectively. The turbulent viscosity μ^{t} is defined in the $k-\varepsilon$ model as

$$\mu_k^{\mathrm{t}} = C_\mu \rho_k \frac{k^2}{\varepsilon_k}, \quad (4.17)$$

where $C_\mu = 0.09$ is the turbulent viscosity constant of the $k-\varepsilon$ model. $\mathbb{P}$ can be calculated

from the velocity fluctuations and velocity gradients:

$$\mathbb{P}_k = -\langle U'_{k,i} U'_{k,j} \rangle \frac{\partial U_{k,i}}{\partial x_j}. \tag{4.18}$$

The stratification attenuation term $\mathbb{G}$ models the correlation between the fluctuating density and velocity

$$\mathbb{G}_k = -\frac{\nu_k^{\mathrm{t}}}{\sigma^{\mathrm{t}}} \frac{1}{\rho_k} \frac{\partial \rho_k}{\partial x_i} g_i, \tag{4.19}$$

where σ^{t} is the turbulent Prandtl number with a constant value of 0.9. The source term Π_q contains the production and attenuation of the turbulence due to other phases, and it is described by drag and added mass forces,

$$\begin{aligned} \Pi_{qk} &= \sum_{p \neq k} \Pi_{q(p \to k)} \\ \Pi_{q(p \to k)} &= \alpha_p F_{\mathrm{D}}^{kp} \frac{\rho_p}{\rho_p + \alpha_k C_{\mathrm{A}}^{kp}} \left(q_{kp} - 2k_k \right) + \alpha_p F_{\mathrm{D}}^{kp} V_{d,i}^{kp} \left(U_{p,i} - U_{k,i} - V_{\mathrm{d},i}^{kp} \right), \end{aligned} \tag{4.20}$$

where F_{D} is the drag coefficient, C_{A} is the added mass coefficient, V_d is the drift velocity, and $q_{kp} = \langle U'_{k,i} U'_{p,i} \rangle$ is the covariance of velocity fluctuations between the phases.

4.4 Large interface modelling

In basic Eulerian 2-phase modelling, the interface between the phases is not necessarily sharpened, because the existence of separate conservation equations closed with volume fractions does not require that. Also, the effect of the surface tension does not appear in the equations as default. Thus, the gas-liquid ”interface” can be smeared into various control volumes when looking from a continuous phase to another. In the interface tracking methodologies instead, both phases share the same conservation equations, and the location of the interface determines the border where the material properties change. Thus, the gas-liquid interface is intrinsically solved as accurately as possible in the interface tracking methods, and the phases are considered immiscible to each other. As a result, the Eulerian 2-phase model needs closure laws to deal with the smeared interface, e.g. laws for drag and added mass forces for the bubbles in the liquid phase and for the droplets in the gas phase. In the interface tracking methods instead, there are no sub-grid scale bubbles or droplets to be modelled and the grid resolution determines the level of interfacial details to be solved.

Closure laws for NEPTUNE_CFD simulations without enhanced interface modelling

In the NEPTUNE_CFD interfacial momentum transfer, the closure laws are included in the $\mathbf{I}'_{(p \to k)}$ term as laminar and turbulent contributions

$$\mathbf{I}'_{(p \to k)} = \mathbf{I}'^{,\mathrm{l}}_{(p \to k)} + \mathbf{I}'^{,\mathrm{t}}_{(p \to k)}. \tag{4.21}$$

The turbulent contribution is only taken into account for the cases with the turbulence of continuous phase modelled with $k-\varepsilon$ turbulence model and the turbulence of other (dispersed) phase modelled with Tchen's local equilibrium model (Tchen, 1947; Hinze, 1975). In the cases of this study, both phases are considered continuous, separated phases, and their turbulence is modelled with $k-\varepsilon$ when the turbulence has to be modeled. Thus, the turbulent contribution term is now neglected. The laminar contribution term is the sum of drag, added mass, lift, and other forces

$$\mathbf{I}^{',\mathrm{l}}_{(p\to k)} = \mathbf{I}^{',\mathrm{D}}_{(p\to k)} + \mathbf{I}^{',\mathrm{A}}_{(p\to k)} + \mathbf{I}^{',\mathrm{L}}_{(p\to k)}. \tag{4.22}$$

The added mass force is a virtual force due to a particle motion within the carrier fluid. In the large interface cases, its applicability is not very well validated. The added mass force is considered negligible in the STB-31 case, and for simplification reasons, it has been neglected also in the STB-28 simulations because it is possible that a poorly posed added mass force term would smear the interface further. The effect of the lift force is considered small compared to the drag force, and therefore it is omitted as well. Thus, only the drag force is applied in this study. The laminar contribution term between the phases '1' and '2' gains then the form

$$\mathbf{I}^{',\mathrm{l}}_{(1\to 2)} = \mathbf{I}^{',\mathrm{D}}_{(1\to 2)} = -\left(\alpha_1\alpha_2\right) F^{12}_{\mathrm{D}}\mathbf{V}^{12}_{\mathrm{r}}, \tag{4.23}$$

where F_{D} is the drag coefficient and V_{r} is the averaged local relative velocity. In the simulations of separated flows, bubbles and droplets can coexist in the same case as the interface between the phases tends to smear. The drag model in NEPTUNE_CFD for such cases is called the SIMMER model referring to the code SIMMER-III (Kondo et al., 1992). In this model, the drag coefficient is related to the volume fractions of the phases

- Bubbles in liquid if $\alpha_2 < 0.3$:

$$F^{12}_{\mathrm{D}} = F^{\mathrm{bubb}}_{\mathrm{D}}\left[\alpha_2\right] = \frac{\rho_2}{\alpha_1}\frac{1}{\tau^{\mathrm{D}}_2}$$

- Droplets in gas if $\alpha_2 > 0.7$:

$$F^{12}_{\mathrm{D}} = F^{\mathrm{drop}}_{\mathrm{D}}\left[\alpha_2\right] = \frac{\rho_1}{\alpha_2}\frac{1}{\tau^{\mathrm{D}}_1} \tag{4.24}$$

- Mixed if $0.3 < \alpha_2 < 0.7$:

$$F^{12}_{\mathrm{D}} = \left(\frac{0.7-\alpha_2}{0.7-0.3}\right) F^{\mathrm{bubb}}_{\mathrm{D}}\left[0.3\right] + \left(\frac{\alpha_2-0.3}{0.7-0.3}\right) F^{\mathrm{drop}}_{\mathrm{D}}\left[0.7\right],$$

where τ^{D} is the particle relaxation time for the drag. The particle relaxation time for the

phase '2' has the form

$$\frac{1}{\tau_2^{\mathrm{D}}} = \frac{\rho_1}{\rho_2}\frac{3}{4}\frac{C_{\mathrm{D}}}{d_2}\langle|V_{\mathrm{r}}^{12}|\rangle_2, \tag{4.25}$$

where the drag coefficient C_{D} is

$$C_{\mathrm{D}} = \frac{24}{\mathrm{Re}_2}\left(1+0.15\mathrm{Re}_2^{0.687}\right). \tag{4.26}$$

The particle (droplet, bubble) Reynolds number is based on its characteristic diameter and on the relative velocity taking into account the turbulence;

$$\mathrm{Re}_2 = \frac{\rho_1|\mathbf{V}_{\mathrm{r}}^{12}|d_2}{\mu_1} \qquad |\mathbf{V}_{\mathrm{r}}^{12}| = \sqrt{\left(\mathbf{U}_2-\mathbf{U}_1-\mathbf{V}_{\mathrm{d}}^{12}\right)^2+2k_1-q_{12}+2k_2}. \tag{4.27}$$

Closure laws for NEPTUNE_CFD simulations with enhanced interface modeling

During the NURESIM project, an improvement for the Eulerian interface modelling was proposed by Coste et al. (2008). They considered the fact that the closure laws are different on the large interface (LI) and in the dilute region around it. In order to improve the applicability of closure laws, they included an interface position location method in NEPTUNE_CFD. This kind of approach in Eulerian 2-phase modelling differs from the interface tracking modelling in that it only locates the interface, but it does not try to reconstruct it to sharp interface. When the interface location and direction is known, it is possible to solve tangential velocities, friction and boundary layers on the interface, which enables more advanced closure laws and heat transfer models, i.e. DCC models. The interface detection method of Coste et al. (2008) is based on the gradient of liquid volume fraction $\nabla\alpha_1$. Intending to capture the fronts, a refined volume fraction gradient is calculated by using interpolated face values between the cells. The components of this gradient are then compared to the corresponding maximum gradient based on the grid geometry. If any of the components satisfies

$$\left(\frac{\partial\alpha_1}{\partial x_i}\right)_{\mathrm{refined}} > C_1\left(\frac{\partial\alpha_1}{\partial x_i}\right)_{\mathrm{geometry}}, \tag{4.28}$$

its cell will be selected for the LI. After that the interface is refined in order to ensure that only one cell locally represents the LI in its normal direction. By analyzing the interface normals in neighboring cells 'I' and 'J', the dual representatives can be found by the criterion

$$\left|\left((\nabla\alpha_1^I)_{\mathrm{refined}}+(\nabla\alpha_1^J)_{\mathrm{refined}}\right)\cdot\overline{IJ}\right| > C_2\|(\nabla\alpha_1^I)_{\mathrm{refined}}+(\nabla\alpha_1^J)_{\mathrm{refined}}\|\|\overline{IJ}\|. \tag{4.29}$$

When two cells are found to represent the LI in the normal direction, the cell with lower α_1 is removed from the LI. According to Coste et al. (2008), the values $C_1 = 0.2$ and $C_2 = 0.7$ for the criteria seem to detect the interface best in many conditions, e.g. in the context of PTS simulations.

Concerning the LI model specific closure laws implemented in the NEPTUNE_CFD, Coste et al. introduced the use of three cell thick interfacial sheet around the LI; one cell in the liquid side normal to the LI, one cell in the gas side normal to the LI and one cell containing the LI itself. This method is called LI3C. As the closure laws are based on the three cells instead of the interfacial cell only, they are less affected by the interface location in the grid and the grid resolution. Of the closure laws, the drag closure law is the most relevant one in this study.

The LI3C modelling offers a possibility to solve tangential velocities near LI. As the SIMMER model of Equation 4.24 considers the drag only in the normal direction of LI, with LI3C it is possible to include the tangential friction into the drag model as well, completing the drag model to a more general friction model of Coste et al. (2008)

$$\mathbf{I}^{',\mathrm{D}}_{(1\to 2)} \;=\; -\alpha_1 \left(F^{12}_{\mathrm{D,norm}} \mathbf{V}^{12}_{\mathrm{r,norm}} + F^{12}_{\mathrm{D,tang}} \mathbf{V}^{12}_{\mathrm{r,tang}} \right), \tag{4.30}$$

where 'norm' denotes to the normal and 'tang' tangential to the interface (LI). The relative velocity is

$$\mathbf{V}^{12}_{\mathrm{r}} \;=\; \mathbf{U_2} - \mathbf{U_1} = \mathbf{V}^{12}_{\mathrm{r,norm}} + \mathbf{V}^{12}_{\mathrm{r,tang}}. \tag{4.31}$$

In this model, the normal drag coefficient $F^{12}_{\mathrm{D,norm}}$ is the same as in the SIMMER model in Eqs. 4.24 - 4.27. Considering the tangential friction, the hypothesis of this model is that the free surface is a wall for the gas phase and it is moving at the interface velocity $\mathbf{u_{int}}$. The $\mathbf{u_{int}}$ in the earlier NEPTUNE_CFD versions is considered the same as the liquid velocity in the LI3C liquid cell, but later it was improved by solving the friction velocity u^* for the liquid side from the gas side with the relation of tangential shears $\rho_1 u_1^{*^2} = \rho_2 u_2^{*^2}$. The friction velocity of the gas phase is solved by using the wall law and damping function of Driest (1956)

$$u^+ \;=\; \int_0^{y^+} \frac{2dy'}{1 + \sqrt{1 + 4\kappa^2 y^{+^2} \left(1 - \exp\left(-y'/A\right)\right)^2}}, \tag{4.32}$$

where the constants κ and A are 0.42 and 25.6, respectively. The dimensionless velocity u^+, the dimensionless distance y^+ and the friction velocity have the forms

$$u^+ \;=\; \frac{u}{u^*}, \qquad y^+ = \frac{y u^*}{\nu}, \qquad u^* = \sqrt{\frac{\tau_{\mathrm{LI}}}{\rho}}. \tag{4.33}$$

By applying $|\mathbf{V}_{\mathrm{r,tang}}|$ of the gas side cell and its distance from interface 'y' to Eqs. 4.33 and 4.32, the friction velocity can be solved, and therefore also the shear stress τ_{w}. The shear stress leads to the solution of the tangential drag force and the drag coefficient. However, instead of using just one interfacial cell to determine that, the LI3C uses three cells. Also, the internal momentum exchange is taken into account within the three cell layer, as well as the turbulence production. More details of the three cell model can be found from Coste et al. (2007).

4.5 Phase change models for condensation

The phase change models used in this study are listed in this chapter. At first, the basic Nu correlations used in NEPTUNE_CFD are presented. Then, the TransAT formulations and Coste-Laviéville model of NEPTUNE_CFD are shown in terms of dimensionless mass transfer velocity K^+.

Basic phase change models in NEPTUNE_CFD

For the turbulent stratified flows in NEPTUNE_CFD, the heat transfer rate to water phase has the equation

$$\Pi_1^{'\mathrm{w/s}} = a_\mathrm{i} h_1 \left(T_\mathrm{sat} - T_1\right), \tag{4.34}$$

where $a_\mathrm{i} = |\nabla \alpha_1|$ is the interfacial area in units $[\mathrm{m}^{-1}]$. T_sat is the saturation temperature and T_1 is the temperature of water. The heat transfer coefficient h_1 is defined as

$$h_1 = \frac{\lambda_1}{L_\mathrm{t}} \mathrm{Nu}, \tag{4.35}$$

where λ_1 is the thermal conductivity and L_t is the characteristic length. In the modified **Hughes and Duffey (1991) model**, Nu is defined as

$$\mathrm{Nu} = \frac{2}{\sqrt{\pi}} \mathrm{Re}_\mathrm{t}\, \mathrm{Pr}^{1/2}, \tag{4.36}$$

where Re_t is

$$\mathrm{Re}_\mathrm{t} = \frac{u_\mathrm{t}\, L_\mathrm{t}}{\nu}. \tag{4.37}$$

The length and velocity parameters are defined as

$$L_t = C_\mu \frac{k_1^{3/2}}{\varepsilon_1} \tag{4.38}$$

and

$$u_\mathrm{t} = \min\left(|U_1|, C_\mu^{1/4} k_1^{1/2}\right) \text{ in } '\mathrm{nept.}' \qquad u_\mathrm{t} = (\nu_1 \varepsilon_1)^{1/4} \text{ in } '\mathrm{orig.}'. \tag{4.39}$$

The notation $'\mathrm{nept.}'$ in Eq. 4.39 means the version implemented in standard NEPTUNE_CFD and $'\mathrm{orig.}'$ is the version of Hughes and Duffey (1991). In the **Coste ICMF'04 model** (Coste, 2004; Coste and Laviéville, 2009), Nu has the form

$$\mathrm{Nu} = \mathrm{Re_t}^{7/8}\, \mathrm{Pr}^{1/2}. \tag{4.40}$$

The turbulent Reynolds number of Coste ICMF'04 model is the same as in Equation 4.37. In the **Lakehal et al. (2008b) model** (see also Banerjee et al. (2004); Lakehal (2007)),

Nu has the form

$$\mathrm{Nu} \;=\; B\, f\left[{\mathrm{Re_t}}^{m}\right]\, \mathrm{Re_t}\, \mathrm{Pr}^{1/2}. \tag{4.41}$$

In this equation, B is a model constant (i.e. $B = 0.35$ for $\mathrm{Pr} \approx 1$ and 0.45 for $\mathrm{Pr} \gg 1$) and $f\left(\mathrm{Re_t}\right)$ has the form

$$f\left[{\mathrm{Re_t}}^{m}\right] \;=\; \left[0.3\left(2.83\,{\mathrm{Re_t}}^{3/4} - 2.14\,{\mathrm{Re_t}}^{2/3}\right)\right]^{1/4} {\mathrm{Re_t}}^{-1/2}. \tag{4.42}$$

The turbulent Reynolds number in this model is

$$\mathrm{Re_t} \;=\; \frac{k_1^2}{\nu\,\varepsilon_1}. \tag{4.43}$$

The heat transfer coefficient is the same as in Equation 4.35. As the length scale L_t does not cancel out in this model, it is calculated using Equation 4.37 yielding

$$L_\mathrm{t} \;=\; \frac{\nu}{u_\mathrm{t}}\mathrm{Re_t}, \tag{4.44}$$

where u_t is calculated using Equation 4.39.

Phase change models in TransAT and the Coste-Laviéville model

The phase change can be solved directly due to the thermal conduction if the grid resolution is high enough to capture eddies small enough and temperature gradients high enough,

$$\mathbf{m} \;=\; \frac{\lambda \nabla T}{h_\mathrm{fg}}, \tag{4.45}$$

where $\mathbf{m}$ is an evaporation/condensation rate vector. This is particularly the case in the DNS cases. For the direct solution of phase change, the local conductive heat flux $q^{''}$ from a phase to another in TransAT is given by formula

$$q^{''} \;=\; \mathbf{q}\cdot\mathbf{n} = 2\lambda\left(T - T_\mathrm{sat}\right)\delta\left[\phi\right]. \tag{4.46}$$

The mass flux is then obtained from the heat flux by

$$q^{''}_\mathrm{m} \;=\; \frac{q^{''}}{h_\mathrm{fg}}. \tag{4.47}$$

The TransAT solver available in this study was an incompressible flow solver without the availability of variable material properties in terms of pressure, i.e. steam tables or compressible ideal gas. Thus, Eq. 4.46 does not take into account the possibly varying saturation conditions. In the case of simulations of the STB-31 experiment, the pressure conditions are practically constant and the temperature changes are modest, making the assumption of ideal fluids acceptable. In TransAT, the effect of interface curvature can be

taken into account by adjusting the saturation temperature,

$$T_{\mathrm{sat}}[\mathbf{x}] = T_{sat}\left(1 + \frac{\left(\rho_2^{-1} + \rho_1^{-1}\right)\kappa_\sigma[\mathbf{x}]\sigma[\mathbf{x}]}{2h_{\mathrm{fg}}}\right). \tag{4.48}$$

In addition to the direct solution of phase change, a number of heat transfer models is available in the later TransAT versions (Ascomp, 2011). These models are documented in a general dimensionless form

$$K^+ \;=\; \frac{K}{u_{\mathrm{t}}} = \frac{h}{\rho\, c_p\, u_{\mathrm{t}}} = \frac{\mathrm{Nu}}{\mathrm{Re}\,\mathrm{Pr}} = f\left(\mathrm{Pr},\, \mathrm{Re}\right), \tag{4.49}$$

where the mass transfer velocity K is

$$K \;=\; \frac{q_{\mathrm{m}}''}{\rho}. \tag{4.50}$$

The surface divergence model of the **Lakehal et al. 2008b** can be written as

$$K^+ \;=\; C\,\mathrm{Sc}^{-1/2}\left(0.3\left(2.83{\mathrm{Re_t}}^{3/4} - 2.14{\mathrm{Re_t}}^{2/3}\right)\right)^{1/4}{\mathrm{Re_t}}^{-n}, \tag{4.51}$$

where $n = 1/2$ and $C = 0.35$ if Sc (or Pr) < 4, being 0.45 otherwise. This model is adapted for the low Reynolds numbers. By changing the exponent $n \to 1/4$, the model is better suited for the high Reynolds number cases. The high Reynolds number variant of the Eq. 4.51 model is called the Small Eddy model which should not be confused with the small eddy model of Banerjee et al. (1968) and Theofanous et al. (1976). By combining the surface divergence model and its Small Eddy variant, it is possible to formulate a model for a large Reynolds number range called the Adaptive surface divergence model:

$$\begin{aligned}
&K^+ = C\,\mathrm{Sc}^{-1/2}\left(0.3\left(2.83{\mathrm{Re_t}}^{3/4} - 2.14{\mathrm{Re_t}}^{2/3}\right)\right)^{1/4}{\mathrm{Re_t}}^{-n},\ \text{where}\\
&n = 0.5 \qquad\qquad \text{if} \quad \mathrm{Re}_{\mathrm{t,int}} < 3000\\
&n = -1.89\cdot 10^{-5}\mathrm{Re}_{\mathrm{t,int}} + 0.56 \quad \text{if} \quad 3000 < \mathrm{Re}_{\mathrm{t,int}} < 16\,000\\
&n = 0.25 \qquad\qquad \text{if} \quad \mathrm{Re}_{\mathrm{t,int}} > 16\,000,
\end{aligned} \tag{4.52}$$

where $\mathrm{Re}_{\mathrm{t,int}}$ is the turbulent Reynolds number at the interface.

The small eddy model of **Banerjee et al. (1968) and Theofanous et al. (1976)** available in TransAT is

$$K^+ \;=\; 0.25\mathrm{Sc}^{-1/2}{\mathrm{Re_t}}^{-1/4}. \tag{4.53}$$

The **Hughes-Duffey model** in TransAT has the form

$$K^+ \;=\; \frac{2}{\sqrt{\pi}}\mathrm{Sc}^{-1/2}, \tag{4.54}$$

and the **Coste ICMF'04 model** is

$$K^+ = \mathrm{Sc}^{-1/2}\mathrm{Re_t}^{-1/8}. \tag{4.55}$$

The last of TransAT models, the surface renewal model of **Lakehal et al. (2008a)**, has the form

$$K^+ = C\,\mathrm{Sc}^{-1/2}\mathrm{Re}_*^{-1/2}, \tag{4.56}$$

where Re_* is the shear Reynolds number. Re_* has the form

$$\mathrm{Re}_* = \frac{u^*|\phi|}{\nu_1}, \tag{4.57}$$

where C has the following expression

$$C = 1.45 \cdot 10^{-6}\mathrm{Pr}^2 + 6.6 \cdot 10^{-5}\mathrm{Pr} + 0.0789. \tag{4.58}$$

If the LI3C interface modelling is enabled in NEPTUNE_CFD, it is possible to use the condensation model of **Coste and Laviéville (2009)**. This model differs from the other models presented here in that it tries two major improvements: a wall function type heat transfer modelling on the liquid side and a turbulence level dependent selection of a DCC correlation. The wall function type model is based on Magnaudet and Calmet analysis (Magnaudet and Calmet, 2006) in which the zones of boundary layers on the liquid side can be presented with dimensionless numbers y^+, T^+, and $\mathrm{Re}_{\mathrm{t,MC}}$

$$T^+ = \frac{\rho_1 c_{p,1} u_t}{h_1} \qquad \mathrm{Re}_{\mathrm{t,MC}} = \frac{2u_\mathrm{t}L_\mathrm{t}}{\nu_1}. \tag{4.59}$$

Depending on $\mathrm{Re}_{\mathrm{t,MC}}$, three zones are separated

- Sub-layer region if $y_1^+ \leq \mathrm{Re_{t,MC}}^{1/4}\mathrm{Pr}^{-1/2}$:

$$T^+ = \mathrm{Pr}\, y_1^+$$

- Logarithmic region if $\mathrm{Re_{t,MC}}^{1/4}\mathrm{Pr}^{-1/2} \leq y_1^+ \leq 10\mathrm{Re_{t,MC}}^{1/2}$:

$$T^+ = A\ln\left(y_1^+\right) + B, \qquad A = \frac{\frac{u_\mathrm{t}}{K} - \mathrm{Re_t}^{\frac{1}{4}}\mathrm{Pr}^{\frac{1}{2}}}{\ln\left(10\mathrm{Re_t}^{\frac{1}{4}}\mathrm{Pr}^{\frac{1}{2}}\right)} \qquad B = \frac{u_\mathrm{t}}{K} - A\ln\left(10\mathrm{Re_t}^{\frac{1}{2}}\right) \tag{4.60}$$

- Outer region if $10\mathrm{Re_{t,MC}}^{1/2} \leq y_1^+$:

$$T^+ = \frac{u_\mathrm{t}}{K},$$

where u_t/K is the inverse of the dimensionless heat transfer coefficient K^+ presented in Eq. 4.49. A DCC correlation can be used for K^+. In the Coste-Laviéville model, this correlation is selected depending on the level of turbulence, i.e. Coste ICMF'04 correlation for strongly turbulent flow and Lakehal correlation for weakly turbulent flow. The criterion for the selection is obtained from the L-q-diagram of Brocchini and Peregrine (Brocchini and Peregrine, 2001a,b). In the diagram, L presents the size scale of the blobs, coherent discrete volumes of fluid ascending towards the interface. The turbulence velocity q can be obtained from k. The bounding criterion between the strong and weak turbulence is

$$q^2 \;=\; 2k = 7.7 \times 10^{-4} gL + 0.22\frac{\sigma}{\rho L}. \tag{4.61}$$

The area above the bounding criterion is the strongly turbulent region and the area below is the weakly turbulent region.

4.6 Non-condensable gases

The effect of non-condensable gases (air) in the STB-31 experiment has been estimated by using the Couette flow film model of Ghiaasiaan (2008). In this model, the energy balance equation across the steam/water interface is written as

$$h_{2I}\left(T_2 - T_{\mathrm{I}}\right) - h_1^{'}\left(T_{\mathrm{I}} - T_{1,\mathrm{bulk}}\right) + G h_{\mathrm{fg}}\left[T_{\mathrm{I}}\right] = 0, \tag{4.62}$$

where the subscript 'I' refers to the value at the interface and G is the mass flux. It can be assumed that the vapor-side heat transfer coefficient h_{2I} can be dependent on mass transfer, whereas on the liquid side such an effect can be neglected. With saturated steam and without non-condensable gases the steam side heat transfer can be neglected and $T_{\mathrm{I}} = T_{\mathrm{sat}}$. Thus, the mass transfer rates in cases with and without non-condensable gases can be compared by using

$$\frac{G_{\mathrm{w/oNC}}}{G} = \frac{h_1^{'}\left(T_{\mathrm{sat}} - T_{1,\mathrm{bulk}}\right) h_{\mathrm{fg}}\left[T_{\mathrm{I}}\right]}{\left(h_1^{'}\left(T_{\mathrm{I}} - T_{1,\mathrm{bulk}}\right) - h_{2\mathrm{I}}\left(T_2 - T_{\mathrm{I}}\right)\right) h_{\mathrm{fg}}\left[T_{\mathrm{sat}}\right]}, \tag{4.63}$$

where $G_{\mathrm{w/oNC}}$ is the mass flux without the presence of non-condensable gases. For the Equation 4.63, T_{sat}, $T_{1,\mathrm{bulk}}$, and G can be obtained from the measurement data. Liquid side heat transfer Nusselt number can be roughly approximated by using the McAdams correlation for a lower surface of a heated plate (Incropera and Dewitt, 2002; McAdams, 1954):

$$\overline{\mathrm{Nu}}_1 = 0.27\mathrm{Ra}_1^{1/4} \qquad \left(10^5 \lesssim \mathrm{Ra}_1 \lesssim 10^{10}\right), \tag{4.64}$$

where Ra_1 is

$$\mathrm{Ra}_1 = \mathrm{Gr}_1\mathrm{Pr} = \frac{g\beta\left(T_{\mathrm{sat}} - T_{1,\mathrm{bulk}}\right) L^3}{\nu D_\alpha}. \tag{4.65}$$

Here, β is the volumetric thermal expansion coefficient and D_α is the thermal diffusivity. For the characteristic length L, it is recommendable to use the following (Incropera and Dewitt, 2002; Goldstein et al., 1973; Lloyd and Moran, 1974):

$$L \equiv \frac{A_\mathrm{s}}{L_\mathrm{P}}, \tag{4.66}$$

where A_s is the surface area and L_P is the perimeter. By using Eqs. 4.64-4.66, the heat transfer coefficient for the liquid-side can be calculated as

$$h_1^{'} = \frac{\overline{\mathrm{Nu}}_1 \lambda}{L}. \tag{4.67}$$

According to the Couette flow film model of Ghiaasiaan (2008), $h_{2\mathrm{I}}$ can be solved by using the vapor side heat transfer coefficient independent of mass transfer $h_{2\mathrm{I}}^{'}$:

$$h_{2\mathrm{I}} = \frac{G c_{p2} h_{2\mathrm{I}}^{'}}{1 - \exp\left(\frac{-G c_{p2}}{h_{2\mathrm{I}}^{'}}\right)}. \tag{4.68}$$

The heat transfer coefficient $h_{2\mathrm{I}}^{'}$ can be evaluated by the Reynolds analogy of heat and mass transfer:

$$\frac{h_{2\mathrm{I}}^{'}}{h_{\mathrm{m2I}}} = \rho_2 c_{p2} \mathrm{Le}^{1-n} \qquad \text{where} \qquad n = \frac{1}{3} \qquad \text{and} \qquad \mathrm{Le} = \frac{D_{\alpha 2}}{D_{12}}. \tag{4.69}$$

The mass transfer coefficient h_{m2I} can be calculated from the condensation mass flux and the mass fractions of vapor on the steam/water interface ($m_{\mathrm{v,I}}$) and in the bulk steam ($m_{\mathrm{v},2}$):

$$h_{\mathrm{m2I}} = \frac{-G}{\rho_2 \ln\left(\frac{1-m_{\mathrm{v},2}}{1-m_{\mathrm{v,I}}}\right)}. \tag{4.70}$$

The mass fractions can be obtained from the molar fractions and vice versa;

$$m_{\mathrm{v},x} = \frac{X_{\mathrm{v},x} M_\mathrm{v}}{X_{\mathrm{v},x} M_\mathrm{v} + (1 - X_{\mathrm{v},x}) M_\mathrm{n}} \qquad X_{\mathrm{v},x} = \frac{-m_{\mathrm{v},x} M_\mathrm{n}}{m_{\mathrm{v},x} (M_\mathrm{v} - M_\mathrm{n}) - M_\mathrm{v}}, \tag{4.71}$$

where x denotes the distance from the steam/water interface, and M_v and M_n are the vapor and air molar masses, i.e. $18.0153\,\mathrm{kg/kmol}$ and $28.9647\,\mathrm{kg/kmol}$, respectively. Saturation conditions of steam are assumed in the STB-31 case. Thus, the molar fractions of vapor are assumed to be

$$X_{\mathrm{v},x} = \frac{p_\mathrm{sat}\,[T_x]}{p}. \tag{4.72}$$

The absolute pressure p and the local temperatures T_x are measured. If the molar fractions at two (or more) distances from the surface are known, it is possible to fit a logarithmic curve between them and extrapolate it onto the steam/water interface. In the STB-31 experiment, the temperatures $T_{20\,\mathrm{mm}}$, $T_{100\,\mathrm{mm}}$ and $T_{0\,\mathrm{mm}}$ are measured. However, the measured temperature $T_{0\,\mathrm{mm}}$ is considered to be too unreliable to be used as interfacial temperature, because the steam/water interface fluctuates slightly. Due to that it is not exactly known in which phase the measurement probes very near the interface locate temporarily. Figure 4.3 shows the instantaneous logarithmic vapor molar fraction profile in the STB-31 experiment at $t = 2100\,\mathrm{s}$.

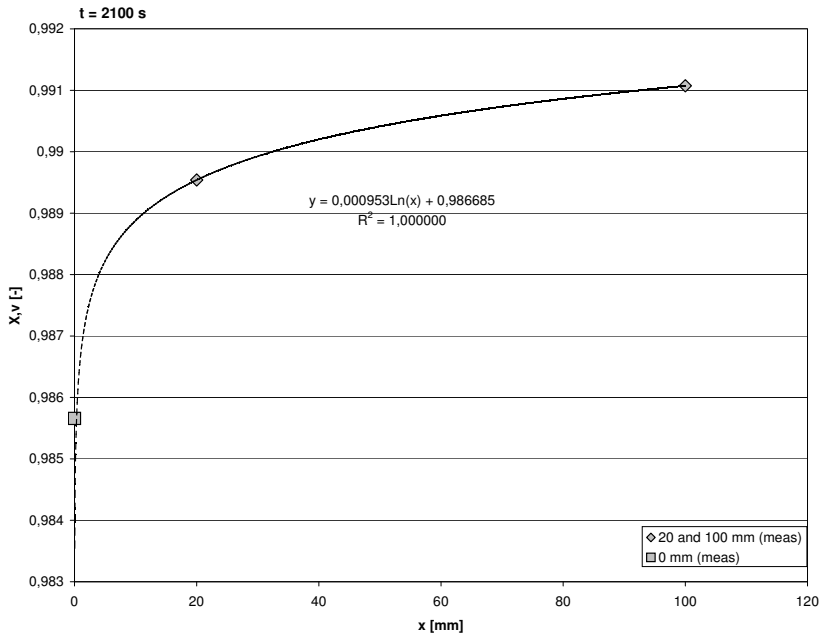

Figure 4.3. Vapor molar fraction in the vicinity of the steam/water interface in the STB-31 experiment at $t = 2100\,\mathrm{s}$. Logarithmic fit using points $x = 20\,\mathrm{mm}$ and $100\,\mathrm{mm}$.

The instantaneous $X_{\mathrm{v},x}$ profiles for the all measured $T_{20\,\mathrm{mm}}, T_{100\,\mathrm{mm}}$ pairs can be fitted similarly, yielding the values for $X_{v,0\,\mathrm{mm}}$. With $X_{\mathrm{v},0\,\mathrm{mm}}$, it is possible to obtain T_{I} ($= T_{0\,\mathrm{mm}}$):

$$T_{\mathrm{I}} = T_{\mathrm{sat}}\left[X_{\mathrm{v},0\,\mathrm{mm}} p\right]. \tag{4.73}$$

The interfacial mass fraction of vapour $m_{\mathrm{v,I}}$ ($= m_{\mathrm{v},0\,\mathrm{mm}}$) can be solved from $X_{\mathrm{v},0\,\mathrm{mm}}$ using Eq. 4.71. By assuming that $m_{\mathrm{v},2} \approx m_{v,100\,\mathrm{mm}}$, also Eq. 4.70 can be solved, which leads to the solution of Equations 4.69, 4.68, and 4.63.

4.7 Wall condensation

Condensation on pipe walls cannot be neglected in the cases where the submerged part of the blowdown pipe is not thermally insulated, i.e. in the case of the STB-28 experiment. Although the major part of condensation occurs as direct contact condensation between the pool water and injected steam, the condensation on the pipe walls may decrease the steam flux enough to change the dynamics of the steam portion that reaches the pool water. The CFD modelling of wall condensation, however, is left outside of this thesis, because it would need special treatment in the boundary cells at walls which may produce additional instabilities to the simulations. In this study, the portion of wall condensation is estimated by hand calculation of the wall condensation rate using the correlation of Chen et al. (1987) (Chen et al., 1987; Ghiaasiaan, 2008). The effect of non-condensable gases is assumed negligible in the STB-28 case of this study, hence it is omitted from this wall condensation analysis.

The conductive heat flux through the pipe wall is

$$q_{\mathrm{w}}^{''} = \frac{2\pi L \lambda_{\mathrm{s}} \left(T_{\mathrm{wall}} - T_{\mathrm{pool}}\right)}{A_{\mathrm{wall}} \ln\left(r_2/r_1\right)} = \frac{\lambda_{\mathrm{s}} \left(T_{\mathrm{wall}} - T_{\mathrm{pool}}\right)}{r_1 \ln\left(r_2/r_1\right)}, \tag{4.74}$$

where L is the length of submerged pipe, A_{wall} is the area of its wall, λ_{s} is the heat conductivity of the pipe material, and r_1 and r_2 are the inner and outer radii of the pipe, respectively. Assuming saturated pure steam to be injected, the heat transported by conduction can be obtained also from the condensed steam proportion

$$q_{\mathrm{w}}^{''} = \frac{q_{\mathrm{m}}}{A_{\mathrm{wall}}} \left(1 - x_{\mathrm{eq}}\right) h_{\mathrm{fg}}, \tag{4.75}$$

where q_{m} is the mass flow rate of injected steam and x_{eq} is the equilibrium quality of steam. The third way to present the heat flux is in terms of Nusselt number of Chen et al. (1987):

$$q_{\mathrm{w}}^{''} = h_1 \left(T_{\mathrm{sat}} - T_{\mathrm{wall}}\right) = \frac{\lambda_1}{\left(\nu_1^2/g\right)^{1/3}} \mathrm{Nu} \left(T_{\mathrm{sat}} - T_{\mathrm{wall}}\right), \tag{4.76}$$

where Nu is

$$\mathrm{Nu} = h_1 \frac{\left(\nu_1^2/g\right)^{1/3}}{\lambda_1} = \left[\left(0.31 \mathrm{Re}_1^{-1.32} + \frac{\mathrm{Re}_1^{2.4} \mathrm{Pr}_1^{3.9}}{2.37 \cdot 10^{14}} \right)^{1/3} + \frac{A_D \mathrm{Pr}_1^{1.3}}{771.6} \left(\mathrm{Re}_{1,0} - \mathrm{Re}_1\right)^{1.4} \mathrm{Re}_1^{0.4} \right]^{1/2}, \tag{4.77}$$

where

$$\mathrm{Re}_{1,0} = \frac{GD}{\mu_1}, \tag{4.78}$$

$$\mathrm{Re}_1 = \frac{G\,(1 - x_{\mathrm{eq}})\,D}{\mu_1}, \tag{4.79}$$

$$A_D = \frac{0.252\mu_1^{1.177}\mu_2^{0.156}}{D^2 g^{2/3}\rho_1^{0.553}\rho_2^{0.78}}, \tag{4.80}$$

and D is the inner diameter of the pipe. By combining Eqs. 4.74 and 4.75 and Eqs. 4.74 and 4.76, a pair of equations can be formed:

$$\begin{aligned} f\left[x_{\mathrm{eq}}, T_{\mathrm{wall}}\right] &= q_{\mathrm{m}}\,(1 - x_{\mathrm{eq}})\,h_{\mathrm{fg}} - \frac{2\pi L\lambda_{\mathrm{s}}\,(T_{\mathrm{wall}} - T_{\mathrm{pool}})}{\ln\,(r_2/r_1)} = 0 \\ g\left[x_{\mathrm{eq}}, T_{\mathrm{wall}}\right] &= -\frac{\lambda_{\mathrm{s}}\,(T_{\mathrm{wall}} - T_{\mathrm{pool}})}{r_1 \ln\,(r_2/r_1)} + \frac{\lambda_1}{\left(\nu_1^2/g\right)^{1/3}}\mathrm{Nu}\left[x_{\mathrm{eq}}\right](T_{\mathrm{sat}} - T_{\mathrm{wall}}) = 0. \end{aligned} \tag{4.81}$$

This pair of equations can be solved e.g. by the Newton-Raphson method yielding values for x_{eq} and T_{wall}. When these values are solved for the first time, they can be used to update the values of material properties for further iterations. These material properties are the liquid properties of the condensate film dependent on the mean temperature $T_1 = (T_{\mathrm{wall}} + T_{\mathrm{sat}})\,/2$. After the converged solution of Eq.4.81, the wall condensation rate can be obtained from the following equation:

$$q_{\mathrm{m,wallc}} = \frac{\pi}{4}D^2 G\,(1 - x_{\mathrm{eq}})\,. \tag{4.82}$$

5 CFD modelling of the low-Re STB-31 experiment

The STB-31 experiment was the starting point for the simulations reported in this study, and it was simulated comprehensively using the NEPTUNE_CFD Eulerian code and TransAT interface tracking code. Some processing of the experimental results was needed to make an estimation of the amount of non-condensable gases affecting the results. The results of this analysis are presented in this chapter, as well as the solver settings for the CFD codes.

5.1 Analysis of the effect of non-condensable gases in the experiment

For the CFD simulations, a $300\,\mathrm{s}$ period (from $2040\,\mathrm{s}$ to $2340\,\mathrm{s}$) from the STB-31 experiment was selected. The injected steam was in saturated conditions, the pressure in the blowdown pipe was almost constant ($1.19\,\mathrm{bar} \pm 0.04\,\mathrm{bar}$) during the selected period, and the time average value of mass flow rate in this period was $1.1\,\mathrm{g/s} \pm 1.3\,\mathrm{g/s}$. Within the period, the mass flow rate decreases slowly and almost linearly in time. This slight decrease in the mass flow rate occurs due to the decreasing condensation rate caused both by the water heat up near the steam/water interface and by the possible accumulation of an air layer to the steam/water interface. Such an air layer could be developed from the dissolved gas that was released from the coolant during the blowdown because the steam/water interface was stable, and the convection was probably weak on the steam side. Reliable modelling of non-condensable gases was challenging with the CFD codes used in this work. Thus it was omitted from the simulations, and the effect of non-condensable gases was estimated on the experimental results only. An effort to evaluate the amount of non-condensable gases in the vicinity of the steam/water interface during the selected period of the experiment was carried out.

On the basis of air and steam partial pressures derived from the measured temperatures and the total pressure at the outlet of the pipe, the Couette flow film model of Ghiaasiaan (2008) was applied to produce an estimate of the non-condensables' effect on the condensation rate. The result obtained by the model is a modified condensation rate for each measured mass flow rate value. These modified values should correspond to the optimal condensation rates without the presence of non-condensable gases. These values indicate approximately 3–$50\,\%$ higher condensation rates without the presence of non-condensable gases (Figure 5.1). The estimate obtained with this method should be assumed to be coarse and sensitive to the inaccuracies in certain measurement values due to the assumption of a logarithmic concentration profile of the non-condensable gases near the interface.

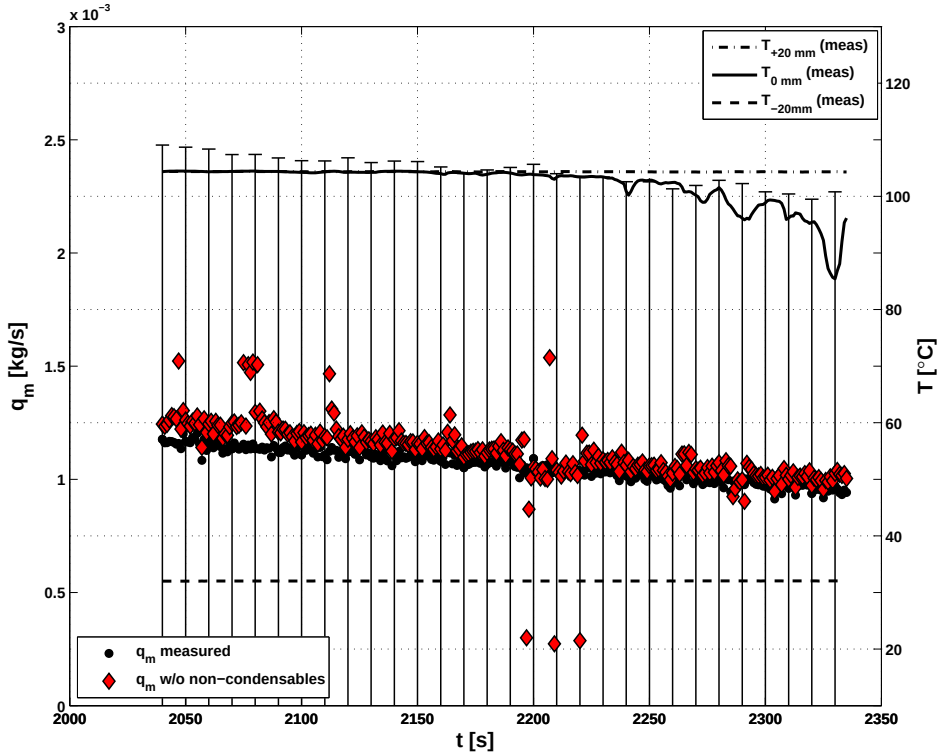

Figure 5.1. Temperatures in the vicinity of the pipe outlet, measured steam mass flow rate, and modified mass flow rate.

In Figure 5.1, the temperature values at the pipe outlet and $\pm 20\,\mathrm{mm}$ above and below it are presented during the selected $300\,\mathrm{s}$ period. As the steam/water interface was very steady at the outlet of the pipe, the values of $T_{0\,\mathrm{mm}}$ and $T_{20\,\mathrm{mm}}$ indicate initially steam temperatures. Later, the steam/water interface started to retreat into the pipe after $2200\,\mathrm{s}$, wetting the thermocouples at that level. In Figure 5.1, the measured mass flow rate with a $\pm 1.3\,\mathrm{g/s}$ error is shown as well. As can be seen, the estimated measurement error in the mass flow rate exceeds the estimated non-condensable gas effect. The liquid side heat transfer coefficient used in the non-condensable gas analysis seemed to be slightly too small. However, the accurate heat transfer coefficient was not known, and the error estimation had to be carried out with the cooled-flat-plate correlation of Equation 4.64. It is likely that a greater liquid side heat transfer coefficient would mitigate the non-condensable gas effects further in the Couette flow film model analysis. Figure 5.2 shows the sensitivity of the non-condensable gas estimation to the errors in the measurements.

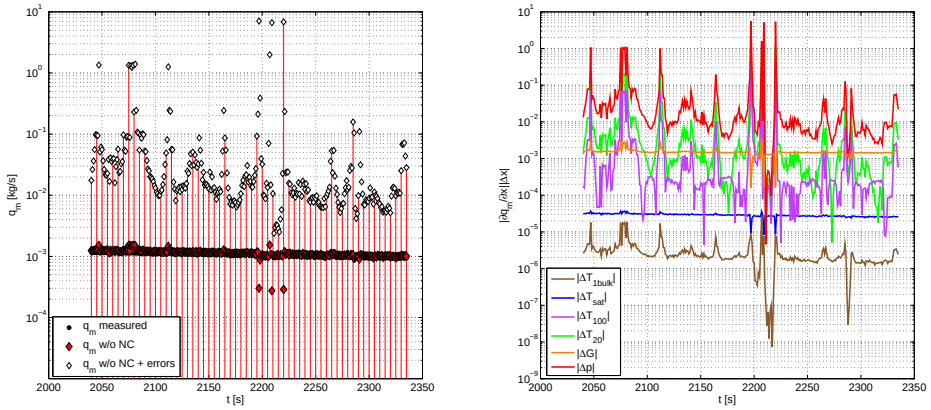

Figure 5.2. Sensitivity of the non-condensable gas estimation to the errors in the measurements.

In the error estimation in Figure 5.2, a total derivative was calculated by using $\pm 2.25\,^{\circ}\mathrm{C}$ error for the $T_{1\mathrm{bulk}}$, $\pm 1.8\,^{\circ}\mathrm{C}$ error for the other temperatures, $\pm 0.04\,\mathrm{bar}$ error for the total pressure, and $\pm 1.3\,\mathrm{g/s}$ error for the mass flow rate. These values are conservative, and the total derivative maximizes the error in the amount of non-condensable gases. The total derivative of Couette flow film model (Equations 4.63 - 4.73) can be written as follows:

$$\begin{aligned} |\Delta G_{\mathrm{w/oNC}}| = &|\frac{\partial G_{\mathrm{w/oNC}}}{\partial T_{\mathrm{sat}}}||\Delta T_{\mathrm{sat}}| + |\frac{\partial G_{\mathrm{w/oNC}}}{\partial T_{1\mathrm{bulk}}}||\Delta T_{1\mathrm{bulk}}| + |\frac{\partial G_{\mathrm{w/oNC}}}{\partial T_{20\,\mathrm{mm}}}||\Delta T_{20\,\mathrm{mm}}| \\ &+ |\frac{\partial G_{\mathrm{w/oNC}}}{\partial T_{100\,\mathrm{mm}}}||\Delta T_{100\,\mathrm{mm}}| + |\frac{\partial G_{\mathrm{w/oNC}}}{\partial p}||\Delta p| + |\frac{\partial G_{\mathrm{w/oNC}}}{\partial G}||\Delta G|. \end{aligned} \tag{5.1}$$

The calculation procedure of the derivatives in Equation 5.1 is complicated due to the various sub-functions dependent on the measurements. The MATLAB code for the calculation procedure is presented in APPENDIX 2. Figure 5.1 shows that the most severe errors are caused by the inaccuracies in the pressure, $T_{20\,\mathrm{mm}}$, and massflow rate measurements. One should recall that the experiment was operated by using saturated steam with very low massflow rates. Errors in the interdependent p, T values can lead even to the misprediction of the prevailing phase in such circumstances, i.e. the measurement errors of p and T could not be at the same time maximally co-directional or contra-directional in all occasions. Therefore, it would be possible to obtain a more realistic error estimation by using more sophisticated methods.

Also the heat up of water below the steam/water interface decreased the condensation rate during the experiment. This warmer water rose freely towards the pool surface along the blowdown pipe outer wall due to the buoyancy forces. The measurement grid in this experiment was not dense enough to produce an accurate initial temperature profile for the simulations. Regarding the temperatures, bulk $30\,^{\circ}\mathrm{C}$ for water and $104\,^{\circ}\mathrm{C}$ for steam were selected as the initial values in the CFD simulations.

5.2 Models for NEPTUNE_CFD solver

The NEPTUNE_CFD simulation cases of the STB-31 experiment were initialized to conditions where the steam/water interface was exactly at the outlet of the blowdown pipe. The main simulation boundary and initial conditions are presented in Table 5.1.

Table 5.1. NEPTUNE_CFD initial and boundary conditions for the STB-31 case.

		Phase 1	**Phase 2**
Fluid		Water	Steam
Initial conditions			
ρ_0	$[\mathrm{kg/m^3}]$	995.6	0.6892
T_0	[K]	303.2	377.5
H_0	[J/kg]	at $[T_0, P_0]$	at $H_{\mathrm{sat}}\,[P_0]$
μ_0	[Pa s]	$7.96{\cdot}10^{-4}$	$1.24{\cdot}10^{-5}$
$c_{p,0}$	$[\mathrm{J/(kg\,K)}]$	4180	2095
α_0	$[-]$	1 outside pipe	1 inside pipe
P_0	[Pa]	hydrostatic	119 435
Boundary conditions			
Inlet type		P inlet/outlet	
Inlet P	[Pa]	119 435 (120 433)	
Inlet α	$[-]$	0	1
Inlet q_{m}	[kg/s]	0	$(1.0594{\cdot}10^{-3})$
Inlet k; ε	$[\mathrm{m^2/s^2}]$; $[\mathrm{m^2/s^3}]$	$(1{\cdot}10^{-4};1{\cdot}10^{-3})$	N/A
Inlet H condition		0-flux	fixed T
Inlet T	[K]	N/A	377.5
Outlet type		P inlet/outlet	
Outlet P	[Pa]	102 870	
Outlet α	$[-]$	1	0
Outlet k; ε	$[\mathrm{m^2/s^2}]$; $[\mathrm{m^2/s^3}]$	$1{\cdot}10^{-4};1{\cdot}10^{-3}$	N/A
Outlet H condition		fixed T	fixed T
Outlet T	[K]	303.2	(303.2)
Other		Symmetry BCs and walls: 0-flux H conditions	

In these simulations, constant pressure boundary conditions were used in order to keep the steam/water interface just at the pipe outlet. Due to the short simulation period and long quasi-steady period to be simulated, steady boundary conditions were sufficient for the STB-31 case. The initial field for α_2 in the vicinity of the pipe outlet is shown in Figure 5.3.

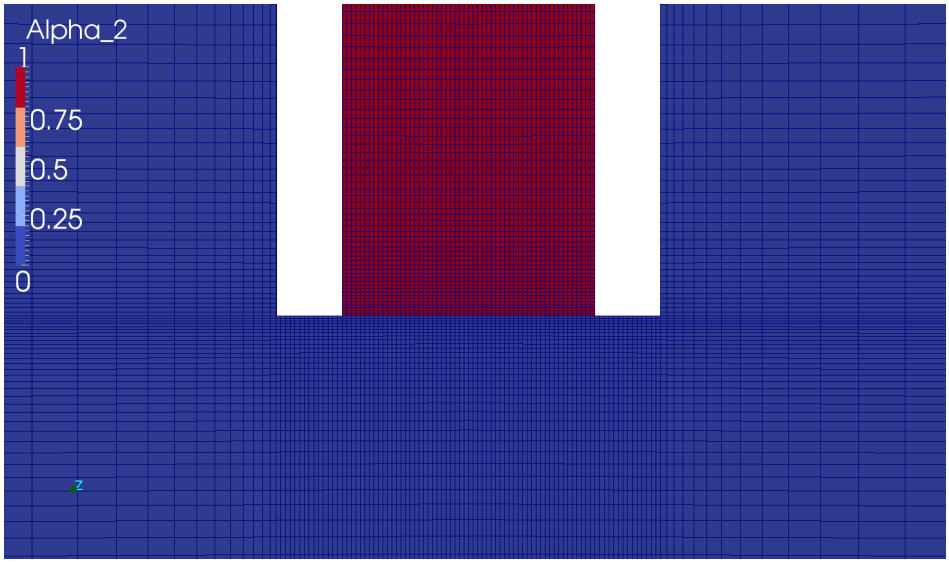

Figure 5.3. Initial steam volume fraction field at the blowdown pipe outlet in the STB-31 NEPTUNE_CFD simulations with Grid 1.

The solver settings and models for the STB-31 simulations are presented in Table 5.2. The steam tables of CATHARE code built in NEPTUNE_CFD were enabled, and the enthalpy scalars were initialized by using the initial temperature and pressure. The condensation model to be tested was selected for the water phase. As the steam phase was in the saturation conditions, no heat transfer models e.g. for superheating were needed for that phase.

Table 5.2. NEPTUNE_CFD solver settings for the STB-31 case.

General settings	
Compressible	Phase 1: No, Phase 2: Yes
Turbulence	Phase 1: $k-\varepsilon$, Phase 2: None
Turb. couplings to Phase 1	Yes, "Separated phase"
Drag model	"SIMMER" or "LI"
Added mass; Lift model	No; No
Interfacial ∇P_{hyd} correction	Yes, "Refined gradient method"
Reference P; σ	$102\,870\,\mathrm{Pa}$; $(0.058\,\mathrm{N/m})$
Gravity	On
Heat transfer settings	
Steam tables	Yes, CATHARE Water Std rev6 ext.
Steam table limits	H-P clipping, physical values
Non-condensables	None
Phase 1 HTC models	Hughes-Duffey or Lakehal'08b or Coste ICMF'04 or Coste-Laviéville
Phase 2 HTC models	None
Numerical scheme settings	
Time stepping	Adaptive
Max CFL; Fou; CFL_α; CFL_Γ	1;10;1000;1000
Solver cycles Navier-Stokes; $\alpha - P$	1;10
Max $\lvert 1-\alpha_1+\alpha_2\rvert$	$1{\cdot}10^{-6}$
Pressure solver	"gradco", multigrid
$\alpha - P$ coupling	"Reacal"

Two grid resolutions were tested in the NEPTUNE_CFD simulations of the STB-31 experiment. The Grid 1 is presented in Figure 5.4. The Grid 1 is a 2D-axisymmetric grid containing 8200 hexahedral cells, and it is refined in the outlet region of the pipe. In the refined region, the minimum cell dimensions are approximately $4\,\mathrm{mm}$ and $2.5\,\mathrm{mm}$ in horizontal and vertical directions, respectively. The Grid 2 is a refined version of Grid 1 and it is shown in Figure 5.5. The Grid 2 contains $28\,150$ hexahedral cells, and it is further refined in the outlet region of the pipe. In the refined region of Grid 2, the minimum cell dimensions are circa $2\,\mathrm{mm}$ and $1\,\mathrm{mm}$ in horizontal and vertical directions, respectively.

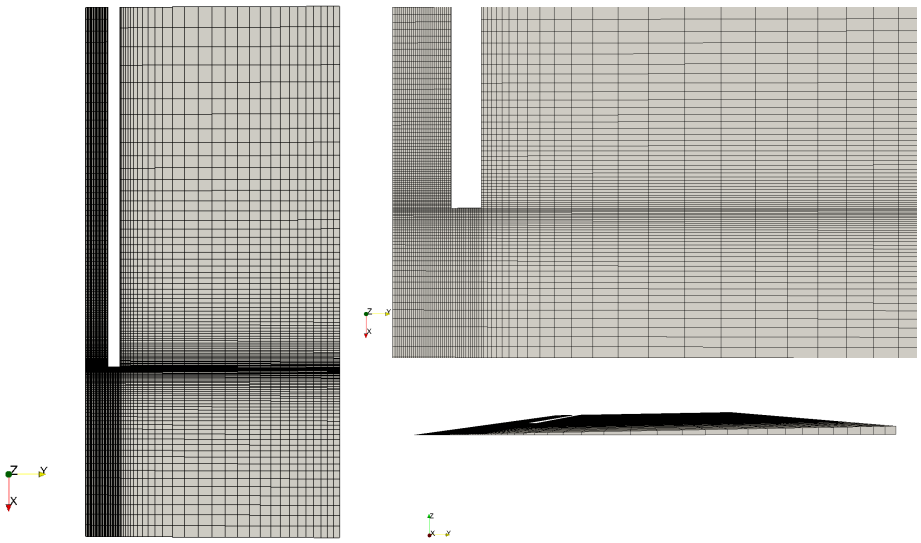

Figure 5.4. 2D-axisymmetric grid ’1’ in the NEPTUNE_CFD simulations.

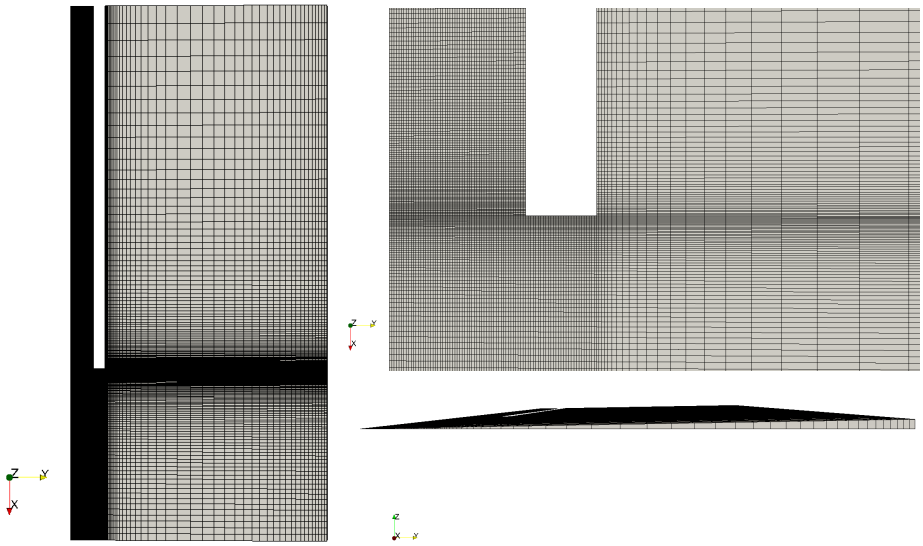

Figure 5.5. 2D-axisymmetric grid ’2’ in the NEPTUNE_CFD simulations.

5.3 Models for TransAT solver

Like in the NEPTUNE_CFD cases, the TransAT simulation cases were initialized to conditions where the steam/water interface was set exactly at the mouth of the blowdown pipe or very slightly ($0.5\,\mathrm{mm}$) inside the pipe. The boundary conditions and initial conditions are the same as in the NEPTUNE_CFD simulations. The main simulation parameters needed for TransAT are presented in Table 5.3.

Table 5.3. TransAT solver settings for the STB-31 case.

General settings	
Compressible	No, not available for 2-phase case
Turbulence	None or $k-\varepsilon$
σ	$0.072\,\mathrm{N/m}$
Contact angle	$130\,^{\circ}$
Gravity, hydrostatic	On, On
Heat transfer settings	
Steam tables	Not available
Phase change HTC models	Energy eq. or Lakehal'08a or Lakehal'08b or Banerjee'68
h_{fg}	$2245\,\mathrm{kJ/kg}$
T_{sat}	$377.45\,\mathrm{K}$
Numerical scheme settings	
Time stepping	Adaptive
Expl. CFL; Fou; CFL$_\mu$; CFL$_\sigma$	$0.2-0.3$; $0.2-0.3$; $0.2-0.3$; $0.2-0.3$
Impl. CFL; Fou; CFL$_\mu$; CFL$_\sigma$	$0.5-0.6$; $0.5-0.6$; $0.5-0.6$; $0.5-0.6$
Expl. residual ϵ; ϵ_p	$1{\cdot}10^{-5}$; $1{\cdot}10^{-6}$
Impl. residual ϵ; ϵ_p	$2{\cdot}10^{-4}$; $1{\cdot}10^{-2}$
Pressure solver	"gmres"
Time scheme	3^{rd} order R-K (expl.) or 1^{st} order Eulerian (impl.)
Convection scheme	QUICK for Level Set, HLPA for others
Default solver; preconditioner	"sip"; "sip"

In these simulations, constant pressure boundary conditions were used in order to keep the steam/water -interface just at the pipe outlet. In the TransAT version used in this study, the compressible flow solver, steam tables or correlations for material properties were not yet available. Therefore, constant values for material properties were used. However, the Boussinesq approximation was included in the code as default, but its functionally was not checked in these simulations. For the phase-change modelling, the earlier TransAT versions offered the Hiemenz flow correlation (Davis and Yadigaroglu, 2003), a fixed value condensation/evaporation rate, and the direct solution of phase-change (see e.g. Wu et al. (2007a)). The later versions of TransAT offer various condensation rate correlations in addition to the abovementioned.

TransATMesh code was used as the grid generator to generate cartesian, immersed body grids for TransAT solver. So far, three grid types with a few different resolutions have been tested. The full 3D calculation grid is presented in Figure 5.6.

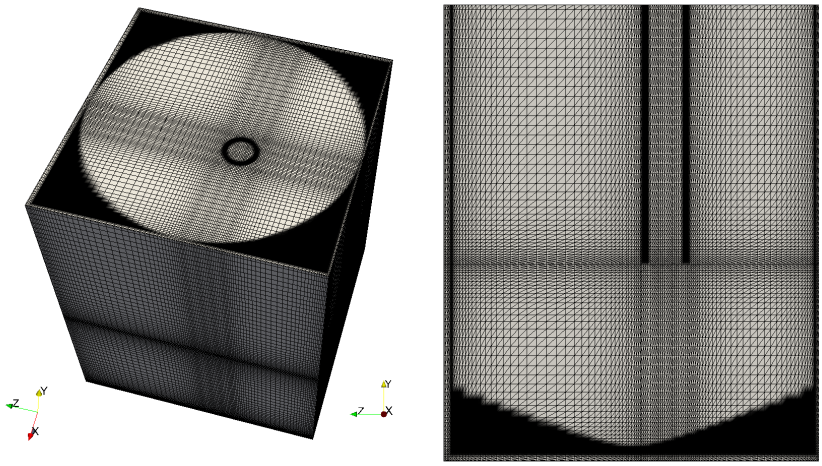

Figure 5.6. Full 3D geometry and mesh for the TransAT simulations of the STB-31 experiment.

This grid contains 784 080 hexahedral cells and it is refined near the pipe outlet and pipe walls. The clipped version of this 3D grid is presented in Figure 5.7 and—with a stronger refinement near the pipe outlet—in Figure 5.8.

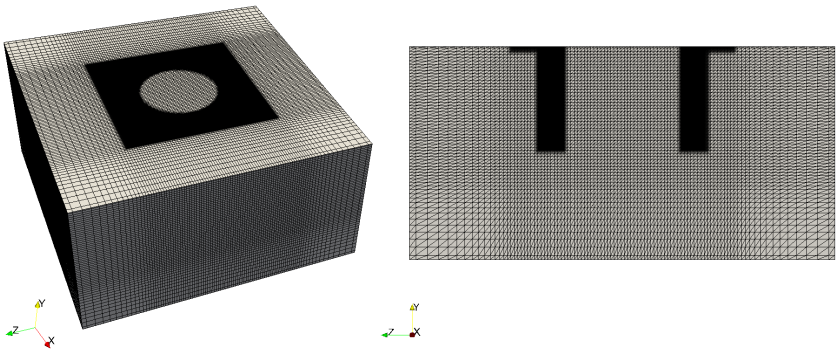

Figure 5.7. Clipped 3D geometry and mesh for the TransAT simulations of the STB-31 experiment.

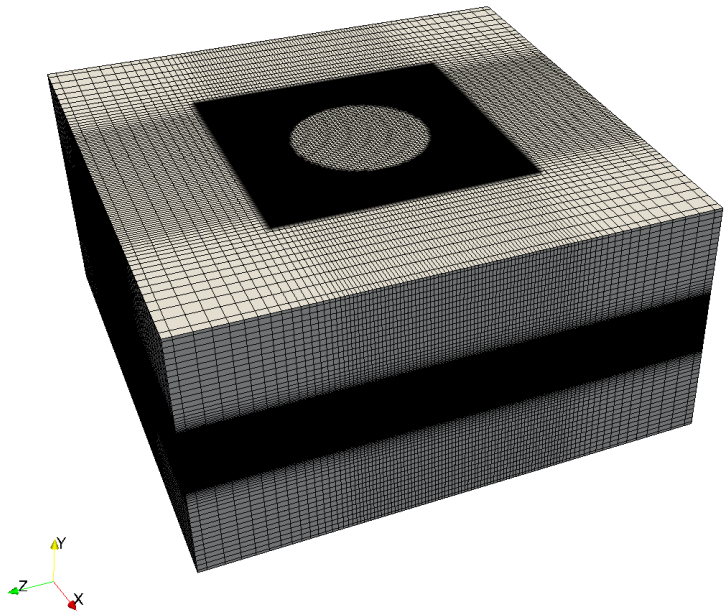

Figure 5.8. Clipped 3D geometry and refined mesh for the TransAT simulations of the STB-31 experiment.

The grids of Figures 5.7 and 5.8 contain $516\,096$ and $1\,474\,560$ hexahedral cells, respectively. The finest grid resolutions were reached by using 2D axisymmetric grids. Some details of a 2D axisymmetric grid are shown in Figure 5.9.

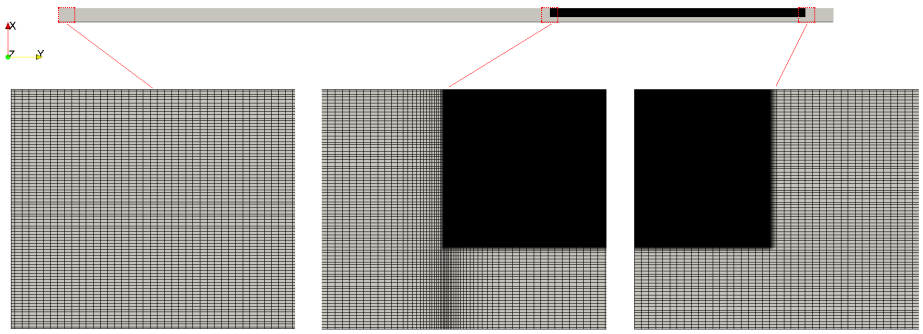

Figure 5.9. 2D-axisymmetrical grid for TransAT simulations.

The grid in Figure 5.9 contains $152\,320$ hexahedral cells. In this grid, only a $3\,\mathrm{mm}$ high and $168\,\mathrm{mm}$ wide section at the pipe outlet was modelled. In the axial ($3\,\mathrm{mm}$) dimension, the grid contains a $1.5\,\mathrm{mm}$ high initial region for each phase. The radial ($168\,\mathrm{mm}$) dimension covers the pipe inner radius $107\,\mathrm{mm}$, a piece of insulated wall of the pipe ($55.4\,\mathrm{mm}$), and a $5.6\,\mathrm{mm}$ section outside the pipe. A coarser 2D-axisymmetric grid with larger dimensions was also developed. This latest grid contains $43\,520$ hexahedral cells and is being used for longer simulations. The minimum cell dimensions in these grids are presented in Table 5.4.

Table 5.4. Cell dimensions of the TransAT simulation meshes.

Grid	**Cells**	Δx **or** Δr $[\mathrm{m}]$	Δy **or** Δh $[\mathrm{m}]$	Δz $[\mathrm{m}]$
Full 3D	784 080	$1.1{\cdot}10^{-2}$	$1.2{\cdot}10^{-2}$	$1.2{\cdot}10^{-2}$
Limited 3D I	516 096	$6.27{\cdot}10^{-3}$	$5.99{\cdot}10^{-3}$	$6.27{\cdot}10^{-3}$
Limited 3D III	1 474 560	$5.302{\cdot}10^{-3}$	$9{\cdot}10^{-4}$	$5.302{\cdot}10^{-3}$
2D-axi $[\mathrm{m}]$	43 520	$1.044{\cdot}10^{-3}$	$9.4{\cdot}10^{-4}$	–
2D-axi $[\mu]$	152 320	$8.9{\cdot}10^{-5}$	$3.75{\cdot}10^{-5}$	–

6 CFD modelling of the high-Re STB-28 experiment

The chugging simulations of STB-28 in this study were conducted using the Eulerian-Eulerian NEPTUNE_CFD code, although the work with TransAT has been initiated as well. Unlike in the STB-31 case, the effects of non-condensable gases were neglected in the study of the STB-28 experimental data. Their effect was small in the STB-31 case and it could be assumed that their effect is even smaller in the STB-28 case because of their stronger mixing in the steam due to vigorous chugging. As the pool water and steam generator set-up was similar to the STB-31 case, the amount of available NC gases could not be significantly higher in the STB-28 case. However, the blowdown pipe was not thermally insulated in the STB-28 case while it was insulated in the STB-31 set-up. Thus, the effect of wall condensation had to be estimated in this case. Also the condensation rate could not been revealed directly from the inlet mass flow rate of steam as the steam/water interface was not stable due to the chugging. Therefore, the validity of the tested DCC models had to be analysed indirectly. For this purpose, the experimental video data was processed by simple pattern recognition methods. The bubble sizes, i.e. volumes and diameters and the frequency of their appearance to the pipe mouth were calculated by using pattern recognition. Also, the frequency pressure pulses onto the pool bottom were analysed.

In this chapter, the results of the wall condensation analysis and the main results of the pattern recognition from the experimental data are presented. The solver settings for the CFD codes are presented as well.

6.1 Analysis of the effect of wall condensation in the experiment

The condensation on the wall of the submerged blowdown pipe was estimated using the correlation of Chen et al. (1987) (Chen et al., 1987; Ghiaasiaan, 2008). The method for the calculation has been presented in Chapter 4.7. The calculated wall temperature and heat flux through the pipe wall in the STB-28 experiment are shown in Figure 6.1.

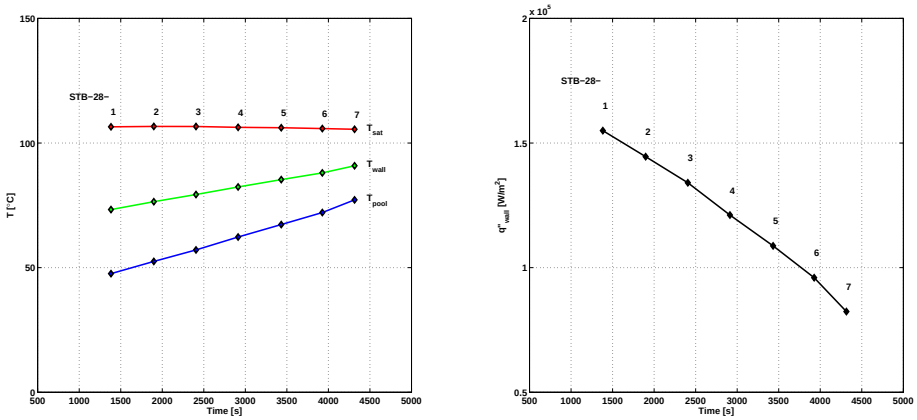

Figure 6.1. Estimated temperature and heat flux on the pipe wall in the STB-28 experiment.

As can be seen from Figure 6.1, the heat flux through the pipe wall decreases clearly during the experiment as the pool water heats up. The wall condensation rate corresponding the heat flux is shown in Figure 6.2.

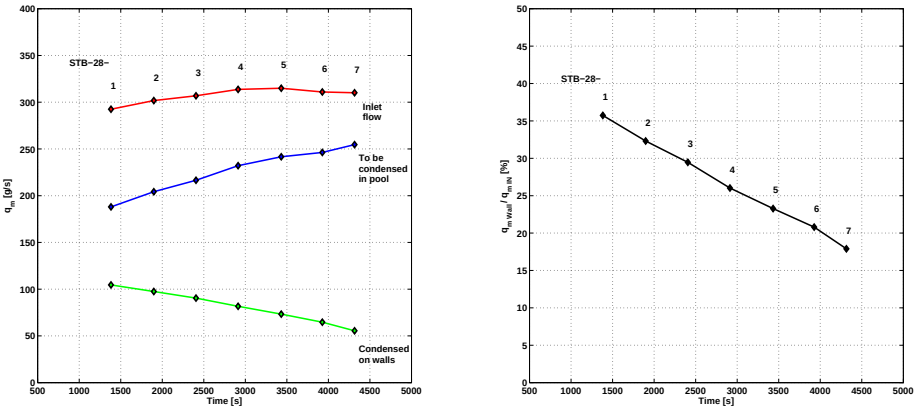

Figure 6.2. Estimation of wall condensation rate in the STB-28 experiment.

As a consequence of the pool water heat up, the wall condensation rate decreases during the experiment. However, as can be seen from Figure 6.2, the contribution of the wall condensation cannot be neglected in the POOLEX experiments with non-insulated blowdown pipes, and the effect of the wall condensation has to be taken into account in the CFD simulations. The CFD modelling of the wall condensation is not as straightforward as the bare modelling of the direct contact condensation on the free steam/water interface. The conduction through the walls and the conjugate heat transfer on the liquid side can be modelled with the CFD codes quite easily, but the phase change modelling on the steam

side requires additional models to be used with the typical DCC correlations. Particularly a model for the elementary condensate film on the walls is needed prior to the activation of a DCC model. The modelling of such a film requires modifications to the code and possibly to the grid discretizations near the walls. The development work of such a model was not conducted in this study. In the CFD simulations of DCC in this study, the effect of the wall condensation is taken into account by the simplest way available, just by removing the amount of wall condensate (15–$40\,\%$) from the inlet steam mass flow rate and assuming the blowdown pipe walls adiabatic. The feasibility of this approach can be considered good enough, because the volume of condensed water is small compared to the steam inside the pipe, and therefore, it does not have much effect to the flow inside the pipe, even if the wall condensation would be modelled. One benefit of this simplification is also that the possible numerical problems due to the wall condensation modelling can be avoided. The drawback of this simplification is that the possible dynamical effect of the varying wall condensation rate during the chugging is lost.

6.2 Pattern recognition analysis of the bubbles and jets

Clips of high-speed $(500\,\mathrm{fps})$ and standard speed $(25\,\mathrm{fps})$ video material were recorded during each blowdown. Figures 6.3 and 6.4 contain frame captures from the high speed video material of the STB-28-4 blowdown.

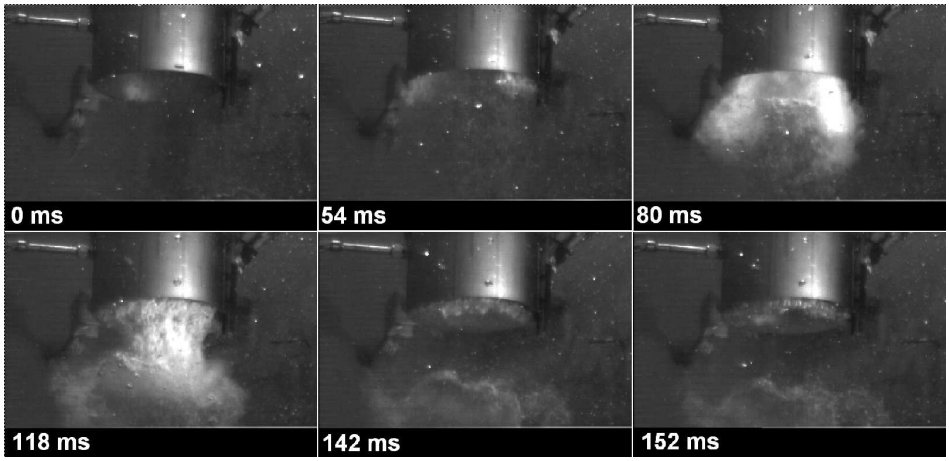

Figure 6.3. Penetration of a steam jet into the pool during the POOLEX STB-28-4 blowdown experiment.

In Figure 6.3, the steam/water interface is initially far inside the blowdown pipe from which it is pushed into the pool water. The first hints of a jet arrive into the pool along the inner pipe wall, then an elliptic hyperboloid jet is formed, after which this hyperboloid

collapses into two parts and a toroidal ring of steam is formed around the lip of the pipe mouth. Figure 6.4 shows the next steps.

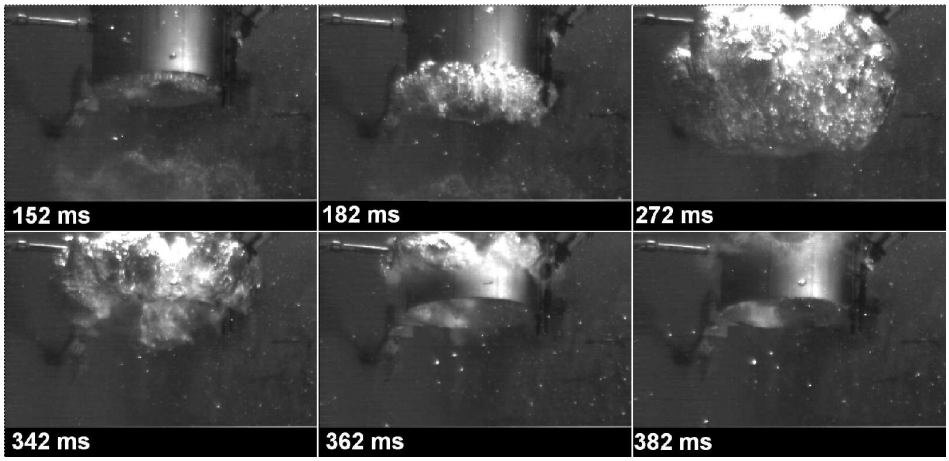

Figure 6.4. Steam bubble and its collapse during the POOLEX STB-28-4 blowdown experiment.

In Figure 6.4, the toroidal ring of steam inflates forming an ellipsoidal bubble, which may still have a vertical axial hole in the middle. After inflating enough, the bubble collapses with a relatively high speed, leaving a detached residual toroidal bubble rising upwards along the outer pipe wall. At the end, the steam/water interface has retreated deeply inside the blowdown pipe, and the residual bubbles have escaped from the video frame or condensed away. By assuming that the shapes of the major jets and bubbles and the behaviour of the jet-bubble cycles are somewhat regular and limited, a pattern recognition procedure was programmed to obtain some quantitative information of this chugging process. The programming was carried out by utilizing the image processing functions of the MATLAB software. The pseudo-code of the program algorithm is presented in APPENDIX 2. The MATLAB functions are introduced and the feasibility of the pattern recognition algorithm is briefly discussed in APPENDIX 2 as well.

The blowdown STB-28-4 was the main case to be simulated with the CFD codes in this study. Thus a pattern recognition algorithm was initially developed and adjusted to capture the bubble and the jet of the STB-28-4 high-speed video clip of Figures 6.3 and 6.4. Figure 6.5 shows two examples of the verification frames printed by the pattern recognition algorithm programmed for the MATLAB software.

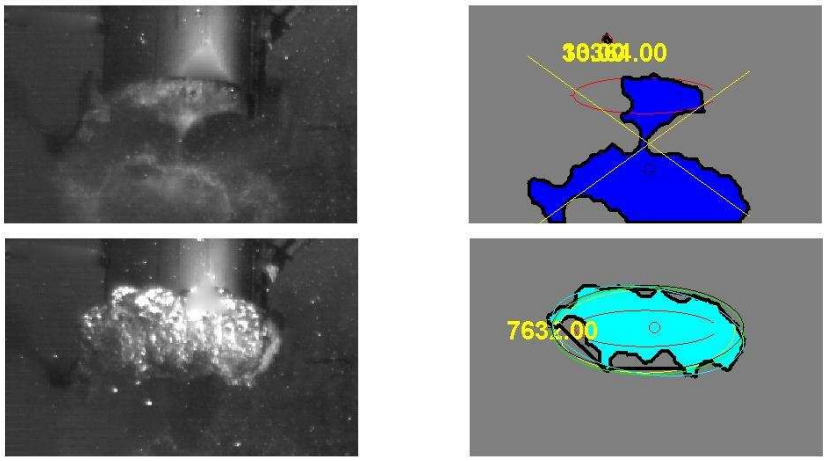

Figure 6.5. Two frames from the high-speed video material of the POOLEX STB-28-4 blow-down experiment and the corresponding pattern recognition verification frames from the automatic MATLAB output. The outlines of a jet and a bubble are detected and measured in pixels. An ellipse is fit around the bubble and the jet is recognized to be non-ellipsoidal.

The pattern recognition procedure obtains the coordinates, length and the enclosed area of the outline of a Region Of Interest (ROI), as shown in Figure 6.5. In the case of an elliptic shape, the script fits an ellipse around it. When an ellipse is fit, the characteristics of the ROI (i.e. the bubble) are calculated accordingly. In the case of other shapes of ROIs, the script will not try to fit an ellipse around them. Thus, in the cases of hyperboloid, conical and arbitrary shapes of jets, the characteristics are calculated by dividing the shape by its vertical axis and forming a body of rotation, the volume of which can be estimated by using the Guldin's rule. The simplified algorithm of the pattern recognition procedure is presented in Figure 6.6 as a flow diagram. A more detailed expression is presented as a pseudo-code in the APPENDIX 2.

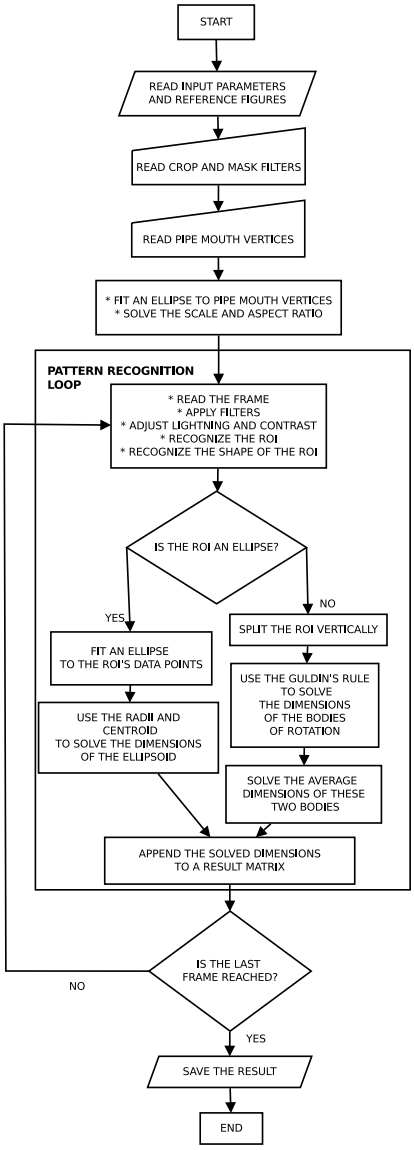

Figure 6.6. Simplified flow diagram of the pattern recognition procedure for the condensing bubbles and jets appearing at a blowdown pipe outlet.

The data from the ellipsoidal bubbles is considered to be more important in this study as their dimensions, like width or height, have less uncertainties than the corresponding information from the more arbitrary bodies like jets. However, the jets have to be somehow recorded and estimated as well because they are needed in the analysis of the chugging frequencies at the exit of the blowdown pipe.

Although the recorded high-speed video clips are good for the analysis of the inflation and collapse process of a single bubble, they are too short for the analysis of the chugging frequency and the statistics of the bubble sizes. For such an analysis, the standard speed video material is also analysed with the same pattern recognition procedure. In Figure 6.7, a few successive frames from the $25\,\mathrm{fps}$ video data of STB-28-4 are shown and analysed by using the pattern recognition procedure.

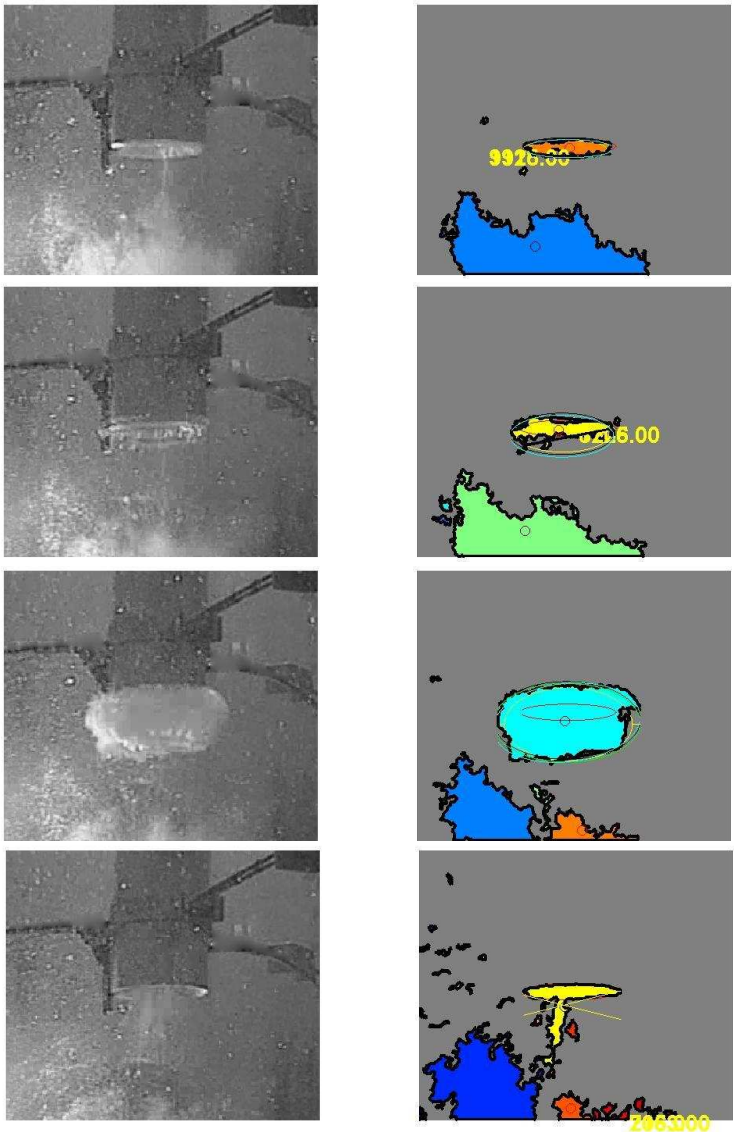

Figure 6.7. Five successive frames from the 25 fps video material of the POOLEX STB-28-4 blowdown experiment and the corresponding pattern recognition verification frames from the MATLAB output.

By comparing Figure 6.7 to Figures 6.3 and 6.4, it can be seen that the slow speed video recording loses many phases of the jet and bubble inflation/collapse processes. Fortunately, the frame rate is high enough to capture the jet/bubble appearance at the exit of the blowdown pipe and get at least some information from the bubble size. The obtained bubble volume distributions of the STB-28 experiment are shown in Figure 6.8.

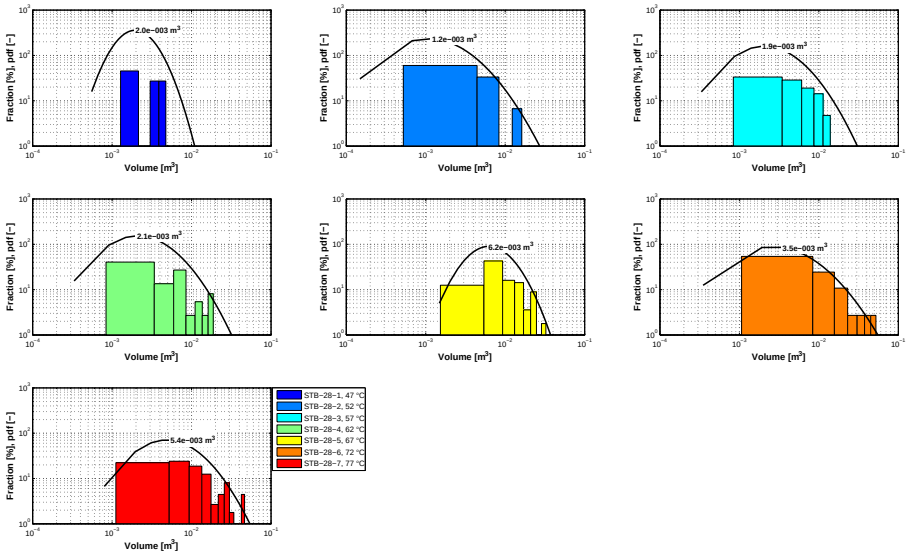

Figure 6.8. Bubble size distributions and the corresponding log-normal probability density functions for the fully inflated ellipsoidal bubbles in the STB-28 experiment.

The color coding in Figure 6.8 represents the pool water temperatures as well as the parts (1–7) of the blowdown experiment STB-28. As was shown earlier in Table 3.1, the temperature of the pool water rose linearly from the $47\,^{\circ}\mathrm{C}$ of STB-28-1 to $77\,^{\circ}\mathrm{C}$ of STB-28-7 during the experiment. In this light, the bubble volume distributions in Figure 6.8 represent well the statistically increasing bubble volumes due to the decreasing subcooling of the pool water.

The calculated volumes shown in Figure 6.8 are sensitive to errors because they are calculated from the 2D video material of a single camera, and the bubbles are assumed to form a pure ellipsoid without any asymmetries or the toroidal structures in every case. Thus, instead of using the recognized volumes, it is more convenient to use a one-dimensional metric as the quality of comparison. Figure 6.9 shows the distributions of the lateral diameter (width) of the fully expanded ellipsoidal bubbles in the STB-28 experiment.

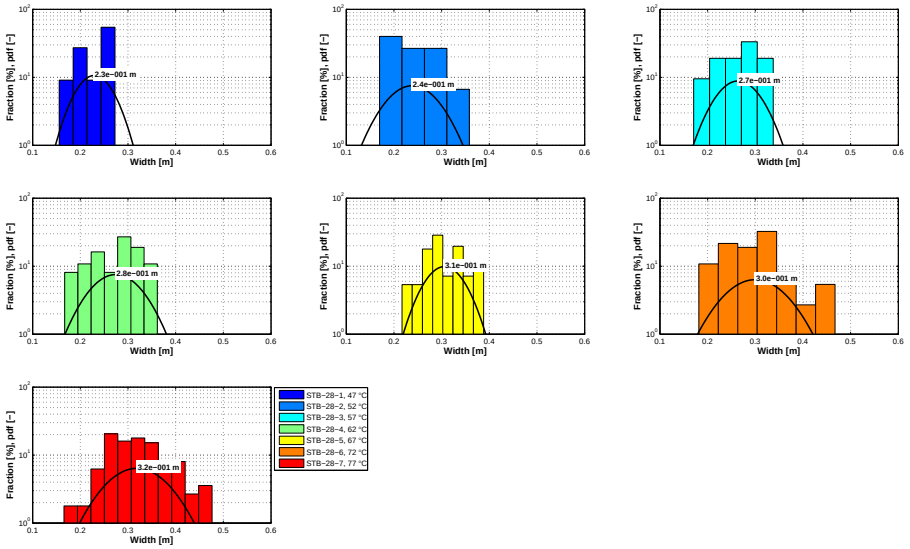

Figure 6.9. Bubble size distributions (maximum width) and the corresponding normal probability density functions for the fully inflated ellipsoidal bubbles in the STB-28 experiment.

It can be seen that the pattern recognition results of the bubble diameters present well the expected bubble size increase due to the heat up of the pool water.

Another useful parameter that can be obtained from the video material is the frequency of the steam jet or bubble penetrations, i.e. the frequency of the external chugging. The frequencies obtained for the STB-28-1. . . 7 partial experiments can be seen in the power spectrums of Figure 6.10.

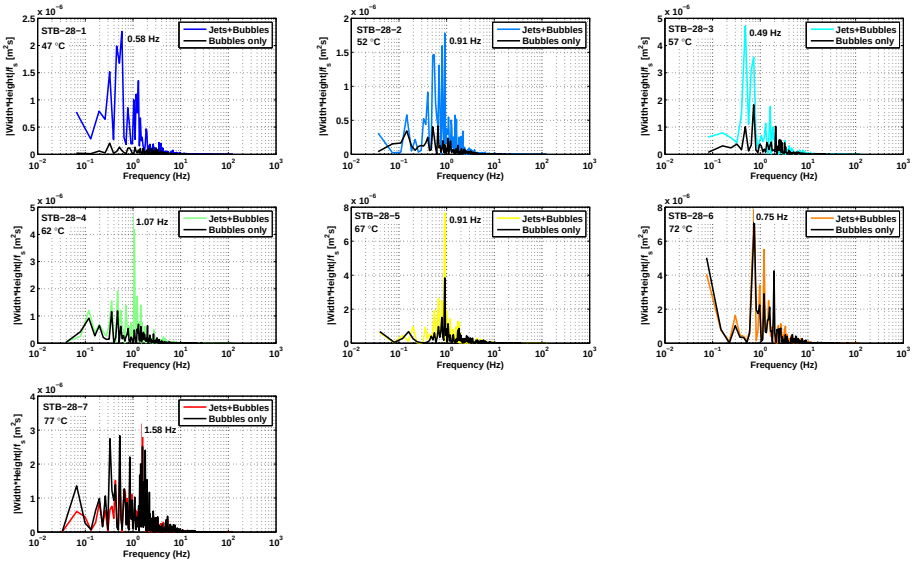

Figure 6.10. Power spectrums of the geometric mean of width and height $\sqrt{L_{\mathrm{Width}} L_{\mathrm{Height}}}$ of bubbles and jets in the STB-28 experiment.

The power spectrums of Figure 6.10 are obtained from the width and height data of bubbles/jets by using Fast Fourier Transform (FFT) in MATLAB. This FFT algorithm is presented in APPENDIX 2 and it is based on the method of Cooley and Tukey (1965). The volume data would be suitable for spectral analysis as well, but as the volume data of the jets may include a remarkable overestimation, the single dimensional data is a better option. It can be seen that the results are clearer in the cases of STB-28-2, 4, 5, and 7. This is due to the longer ($25\,\mathrm{s}$ or more) video sample length of those partial experiments. In the other cases, the recorded period was only $15\,\mathrm{s}$. If all the cases are summarized, the FFT data gives still a quite clear message that the chugging frequency and the nature of penetrations change due to the pool water heating. In the cold water, the external chugging occurs mainly with the frequencies $<1\,\mathrm{Hz}$, and it is dominated solely by the jets that condensate rapidly without occupying a large region. In the middle of the experiment, the main frequency is around $1\,\mathrm{Hz}$, and the proportion of ellipsoidal/toroidal bubbles is significant. In the end of the experiment, the main frequency is $1-2\,\mathrm{Hz}$, but other significant frequencies are present as well. The high peaks at low frequencies represent the occasional appearance of very large bubbles, and the peaks at higher frequencies represent the successive appearance of bubbles without a clear steam/water interface retreat back to the blowdown pipe.

The measurements with high sampling rates can be analysed with FFT as well. Concerning the suppression pool experiments, the pressure measurements are probably the most interesting ones. The pressure data on the pool bottom, just below the blowdown pipe, is compared to the results of the CFD simulations in this study as well. Figure 6.11 shows

the measured pool bottom 'P9' pressure during the STB-28-4 blowdown and the FFT power spectrum analysis of it.

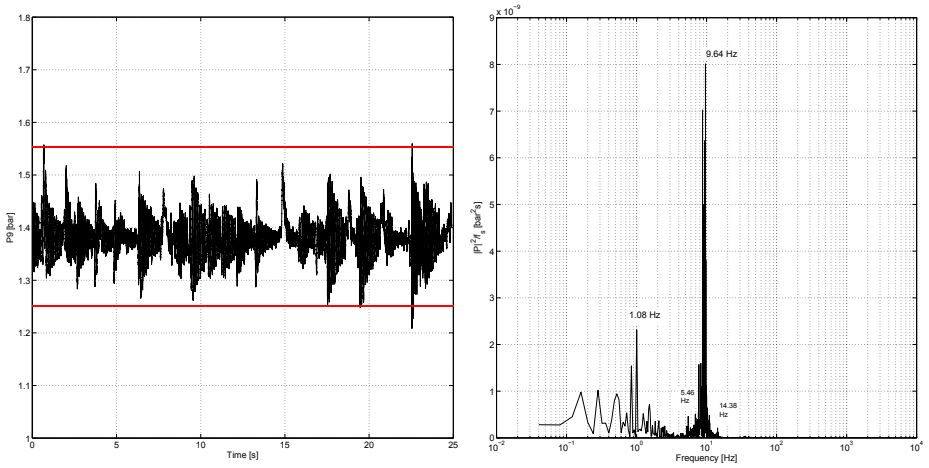

Figure 6.11. Pressure (P9) and the power spectrum of it on the suppression pool bottom in the STB-28-4 experiment.

The pressure measurements on the pool bottom show that the bottom receives pressure pulses with a certain frequency and those pulses are followed by oscillations that dampen with a higher frequency. The power spectrum in Figure 6.11 shows that the dominant pressure pulse frequency is near $10\,\mathrm{Hz}$ and there is another remarkable frequency near $1\,\mathrm{Hz}$. The $1\,\mathrm{Hz}$ frequency corresponds well with the frequency of the chugging seen in Figure 6.10. The $10\,\mathrm{Hz}$ frequency instead is not seen in the pattern recognition result at all. The explanation for this frequency can be found from the strain measurements of Laine and Puustinen (2005, 2006b) and from the Fluid Structure Interaction (FSI) analysis done for the POOLEX pool by Timperi et al. (2006). The strain measurements of Laine and Puustinen (2005, 2006b) indicated a $10\,\mathrm{Hz}$ fluctuation of strains on the pool bottom structures. Timperi et al. (2006) obtained $15.7\,\mathrm{Hz}$ for the eigenmode '4' of their study. According to them, that eigenmode corresponds well the deformation of the pool bottom, taking into account the vertical motion of the pool water mass. They noticed that their frequency is higher than the measured $10\,\mathrm{Hz}$, but they found out indications that their Finite Element (FE) model may contain too stiff structures (i.e. coarse mesh) for the pool bottom. Due to that, the response predicted by their model should yield higher frequencies than the measurements in the experiments. The power spectrums are shown for the measured strains of the STB-28-4 and STB-28-7 cases in Figure 6.12.

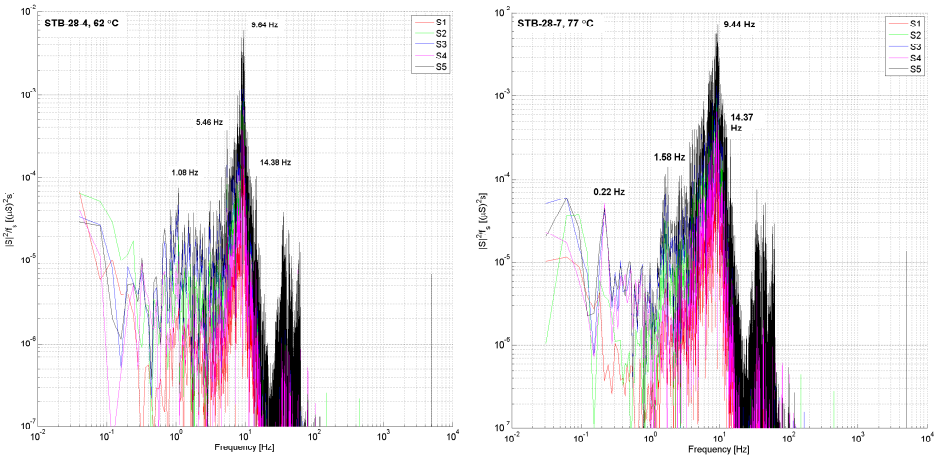

Figure 6.12. Power spectrums of strain rate sensor pulses on the suppression pool bottom in the STB-28-4 experiment.

Figure 6.12 shows that the $10\,\mathrm{Hz}$ frequency is very dominant in all measurement points, including the axial (ST2 and ST4) and torsional (ST1,ST3 and ST5) strain measurements. Such a strong bumping effect on the bottom is likely due to the axial movement of the whole water mass, and because it does not change due to the chugging frequency, it is likely an eigenmode of the POOLEX pool. In addition to the other eigenmodes of the pool, it is possible to see the effect of chugging also in the strain measurements. At least the dominant chugging rates shown in Figure 6.10 seem to have corresponding peaks in the strain power spectrums as well.

In the CFD simulations of this study, the FSI phenomena have not been modelled, i.e. the simulated pool is rigid. This should lead to the removal of the pool eigenmodes from the spectrums showing only the pressure fluctuations due to the steam volume changes, i.e. chugging and bubbling.

6.3 Models for NEPTUNE_CFD solver

The NEPTUNE_CFD simulation cases of the STB-28 experiment were initialized to conditions where the steam/water interface is either inside the blowdown pipe or exactly at the outlet of the blowdown pipe. Most of the cases were simulated with the initial interface inside the blowdown pipe. The main simulation boundary and initial conditions are presented in Table 6.1 for the STB-28-4 blowdown case.

Table 6.1. NEPTUNE_CFD initial and boundary conditions for the STB-28-4 case.

		Phase 1	**Phase 2**
Fluid		Water	Steam
Initial conditions			
ρ_0	$[\mathrm{kg/m^3}]$	979.2	0.7264
T_0	[K]	340.5	379.1
H_0	[J/kg]	at $[T_0, P_0]$	at $[T_0, P_0]$
μ_0	[Pa s]	$4.19{\cdot}10^{-4}$	$1.2{\cdot}10^{-5}$
$c_{p,0}$	[J/(kg K)]	4187	2102
α_0	$[-]$	1 - $\alpha_{0,\mathrm{steam}}$	in pipe at $y > 2.104\,\mathrm{m}$
P_0	[Pa]	hydrostatic	124 828
Boundary conditions			
Inlet type		Modified Velocity or mass flow inlet	
Inlet q_m	[kg/s]	0	0.314 or 0.238 w wcond
Inlet U	[m/s]	0	from q_m or BC fcn.
Inlet α	$[-]$	0	1
Inlet k; ε	$[\mathrm{m^2/s^2}]$; $[\mathrm{m^2/s^3}]$	$(1{\cdot}10^{-4}$; $1{\cdot}10^{-3})$	BC fcn.;BC fcn.
Inlet H condition		0-flux	fixed T
Inlet T	[K]	N/A	379.1
Outlet type		P inlet/outlet	
Outlet P	[Pa]	102 197	
Outlet α	$[-]$	1	0
Outlet k; ε	$[\mathrm{m^2/s^2}]$; $[\mathrm{m^2/s^3}]$	$1{\cdot}10^{-4}$; $1{\cdot}10^{-3}$	$1{\cdot}10^{-4}$; $1{\cdot}10^{-3}$
Outlet H condition		fixed T	fixed T
Outlet T	[K]	340.5	(340.5)
Other		Symmetry BCs and walls: 0-flux H conditions	

The two values for steam mass flow rate in Table 6.1 are the values with and without the removal of the steam fraction that is assumed to condense on the blowdown pipe walls. The notation 'BC fcn.' in Table 6.1 means that the value is calculated in a boundary condition script. The script contains a function for the velocity profile of turbulent pipe

flow (White, 1999)

$$U[r] = \left(\frac{1}{\kappa}\ln\frac{(R-r)\,u^*}{\nu}+B\right)u^*, \tag{6.1}$$

where $\kappa = 0.41$ and $B = 5$. By solving the average velocity from the q_{m} and assuming the average velocity at the axis of the pipe, the friction velocity u^* can be solved from the Equation 6.1 and it can be used to solve the whole profile. The turbulence quantities for the inlet are initialized by using the turbulence intensity for the pipe flow

$$I = 0.16\mathrm{Re}^{-1/8}, \qquad \text{where} \qquad \mathrm{Re} = \frac{UD}{\nu}. \tag{6.2}$$

By using this estimation for the turbulence intensity, k and ε can be calculated from equations

$$k = \frac{3}{2}(UI)^2, \qquad \varepsilon = \frac{C_\mu^{3/4}k^{3/2}}{L_c}, \qquad \text{where} \qquad L_c = 0.07D. \tag{6.3}$$

Due to the constant inlet steam mass flux during the experiment, steady boundary conditions were sufficient for STB-28 cases as well. The initial state of water/steam interface in the STB-28-4 was unknown. Concerning the long simulations in which multiple chugging cycles are simulated, one may consider the initial level of the interface quite unimportant and select an arbitrary location inside or outside the blowdown pipe. However, the author of this study found out that the proper selection of this initial interface may improve the results or at least reduce the time to reach a fully developed state of the turbulent velocity field. The initial level for the interface was estimated by using the high-speed video material of STB-28-4 blowdown and choosing the starting point of simulations accordingly. The high-speed video clip of STB-28-4 starts from a moment when the interface is inside the blowdown pipe. By observing the penetration speed of the steam jet and assuming it constant, the initial level of interface was calculated to be $0.76\,\mathrm{m}$ inside the blowdown pipe. The initial field for α_2 is shown in Figure 6.13.

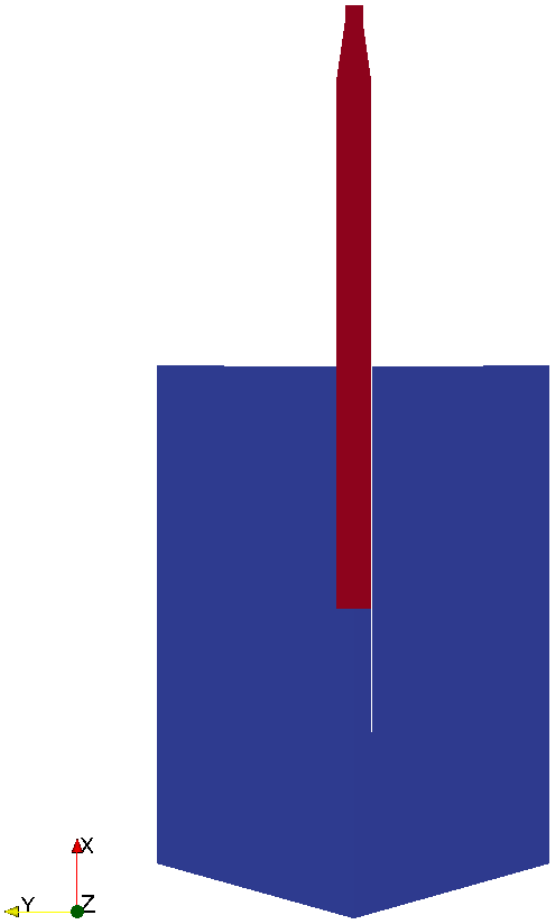

Figure 6.13. Initial steam volume fraction field in STB-28 NEPTUNE_CFD simulations.

The solver settings and models for STB-28 simulations are presented in Table 6.2. The steam tables of CATHARE code built in NEPTUNE_CFD were enabled and enthalpy scalars were initialized by using the initial state temperature and pressure. The condensation model to be tested was selected for the water phase. The steam phase was assumed to be approximately at the saturated state, due to which there was no need to add a heat transfer model on to the steam side. If the steam had for example been superheated, a convective heat transfer term could have been added to the model as the $\Pi_2^{'w/s}$ term in Equation 4.7.

Table 6.2. NEPTUNE_CFD solver settings for the (2D-axi.) STB-28 cases.

General settings	
Compressible	Phase 1: Yes, Phase 2: Yes
Turbulence	Phase 1: $k-\varepsilon$, Phase 2: $k-\varepsilon$
Turb. couplings to Phase 1	Yes, "Separated phase"
Drag model	"SIMMER" or "LI"
Added mass; Lift model	No; No
Interfacial ∇P_{hyd} correction	Yes, "Refined gradient method"
Reference P; σ	$102\,198\,\mathrm{Pa}$; $(0.058\,\mathrm{N/m})$
Gravity	On
Heat transfer settings	
Steam tables	Yes, CATHARE Water Std rev6 ext.
Steam table limits	H-P clipping, physical values
Non-condensables	None
Phase 1 HTC models	Hughes-Duffey or (Lakehal'08b) or Coste-Lavieville
Phase 2 HTC models	None
Numerical scheme settings	
Time stepping	Adaptive
Max CFL; Fou; CFL_α; CFL_Γ	1;10;1000;1000
Solver cycles Navier-Stokes; $\alpha - P$	$1-2$; $50-$
Max $\lvert 1-\alpha_1+\alpha_2\rvert$	$1{\cdot}10^{-6}$
Pressure solver	"gradco", w or w/o multigrid
$\alpha - P$ coupling	"Reacal"

The first grids generated for the STB-28 purposes were cartesian 2D-axisymmetric ones. The simulations with those grids suffered various numerical problems, however. One fundamental reason for the problems was the calculation grid, i.e. the practical meshing difficulty of avoiding too small grid cells and their too steep change to larger ones in the grid near the mouth of the blowdown pipe. The idea of the author was then to make an effort to develop a spherical curvilinear grid around the blowdown pipe exit. With this kind of an approach, the abrupt changes in grid cell sizes can be avoided and the amount of cells reduced. Furthermore, this kind of a grid structure conforms to the shape of the erupting ellipsoidal bubbles. Therefore, the numerical diffusion of the interface can be kept low, even though the amount of cells in the grid is small. A 2D-axisymmetric version of this grid is shown in Figure 6.14.

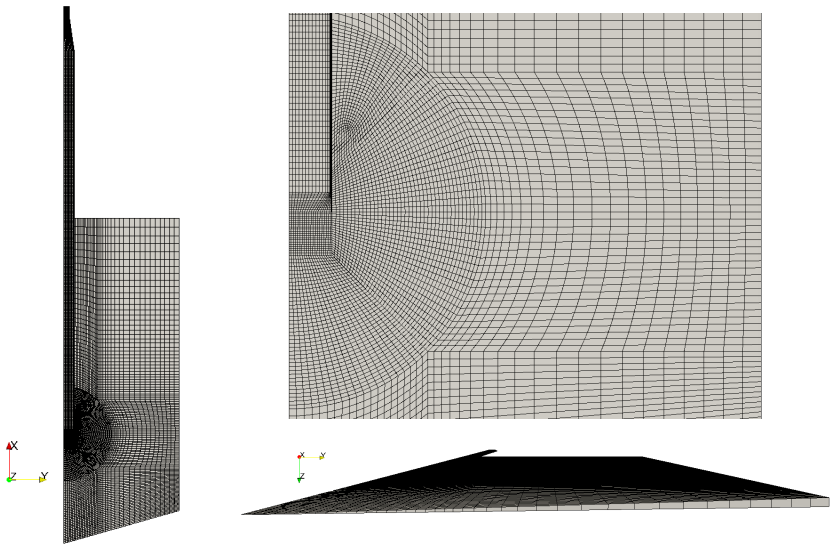

Figure 6.14. 2D-axisymmetric grid '1' in the STB-28 NEPTUNE_CFD simulations.

The grid shown in Figure 6.14 is an axisymmetric grid containing $12\,716$ hexahedral cells. The grid is refined towards the inner wall of the blowdown pipe to avoid too large y^+ values, although the standard wall functions of the k-ε-model should be in use. Apart from the wall region, the minimum cell size at the mouth of the blowdown pipe is approximately $5 \times 5\,\mathrm{mm}$.

In general, the 2D axisymmetric approach is too approximative for an accurate modelling of chugging, i.e. chugging is not exactly an axisymmetric phenomenon. The bubbles occurring during the chugging are rarely completely symmetric and the axial location of the blowdown pipe does not correspond exactly to the case in the experiment. Thus, a 3D grid was generated by applying the same spherical curvilinear design as in the axisymmetric case. Some cut-views of this grid are shown in Figures 6.15 and 6.16. This 3D grid contains $302\,796$ hexahedral cells with the minimum cell size of circa $5 \times 5\,\mathrm{mm}$ at the blowdown pipe exit.

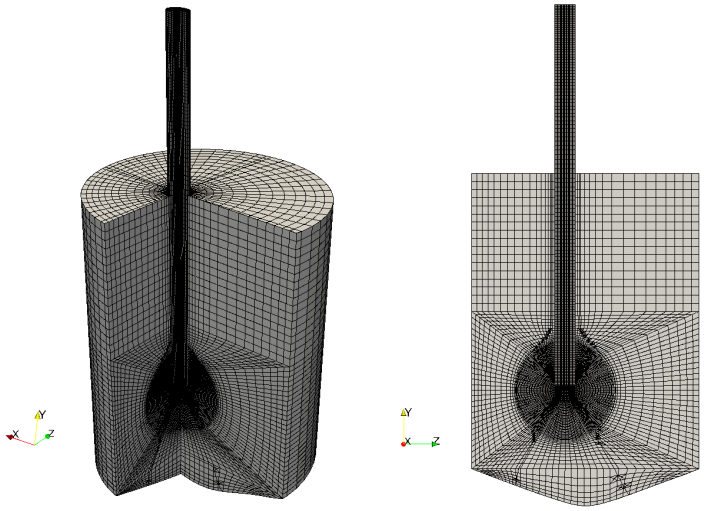

Figure 6.15. 3D grid in the STB-28 NEPTUNE_CFD simulations.

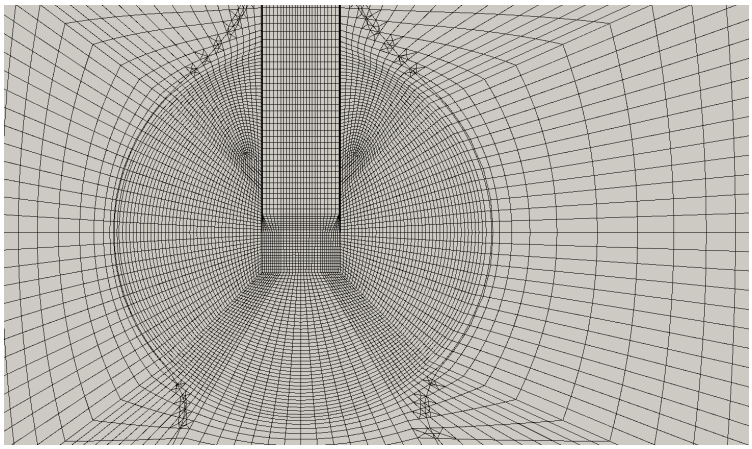

Figure 6.16. Clip of 3D grid in the STB-28 NEPTUNE_CFD simulations.

7 Results and discussions

In this chapter, the main simulation results are presented. The simulations of the low Reynolds number STB-31 experiment are presented first. The STB-31 experiment has been simulated using the NEPTUNE_CFD and TransAT CFD codes. Then, the results of high Reynolds number STB-28 simulations are presented. The STB-28 cases have been simulated using the NEPTUNE_CFD code.

The early STB-31 results have been published in Tanskanen et al. (2008a), in the research reports of SAFIR e.g. in Tanskanen and Jordan (2010a), and in the research reports of NURESIM and NURISP (Tanskanen et al., 2007, 2008b). Some of the STB-28 results have been presented in the research reports of SAFIR (Tanskanen and Jordan, 2009, 2011) and in the NURISP progress report (Tanskanen and Jordan, 2010b).

7.1 Simulation of a low Reynolds number condensation case

The STB-31 experiment has been simulated using the Eulerian-Eulerian two-phase solver of the NEPTUNE_CFD code and the interface tracking solver of the TransAT software. The stratified flow DCC models tested in this part are the following models: Hughes-Duffey of Hughes and Duffey (1991) (in NEPTUNE_CFD only), Lakehal '08b of Lakehal et al. (2008b), Coste '04 of Coste (2004) (in NEPTUNE_CFD only), Coste-Laviéville of Coste and Laviéville (2009) (in NEPTUNE_CFD only), Banerjee '68 of Banerjee et al. (1968) (in TransAT only), and Lakehal '08a of Lakehal et al. (2008a) (in TransAT only). The direct solution for phase change is tested by using the TransAT code.

In the NEPTUNE_CFD simulations, the 'SIMMER' and 'Large Interface' (LI) drag models of the solver have been tested in order to see their effect on the condensation rates. The 'LI' drag model also offers the capability to use the condensation model of Coste-Laviéville which is specifically designed to be used with the LI3C approach provided by this drag model. In order to reveal calculation grid dependencies, the NEPTUNE_CFD cases have been simulated with two different grid resolutions and the TransAT simulations with 2–4 grid resolutions.

7.1.1 Eulerian-Eulerian simulations of STB-31 experiment with NEPTUNE_CFD solver

The condensation mass flow rates predicted by the models of Hughes-Duffey, Lakehal '08b and Coste '04 by using the 2D-axisymmetric **'Grid 1'** and **'SIMMER'** drag model are presented in Figure 7.1. Concerning Figure 7.1 and other DCC mass flow rate and flux figures henceforward, the measurement uncertainty has been marked with dark grey area and the maximal uncertainty due to the NC gas effect estimation with light grey area. The 'STB-31 w/o non-condensables' denotes the measurement results from which the effect of NCs is removed. Such points should better correspond these simulations done without the NC modelling.

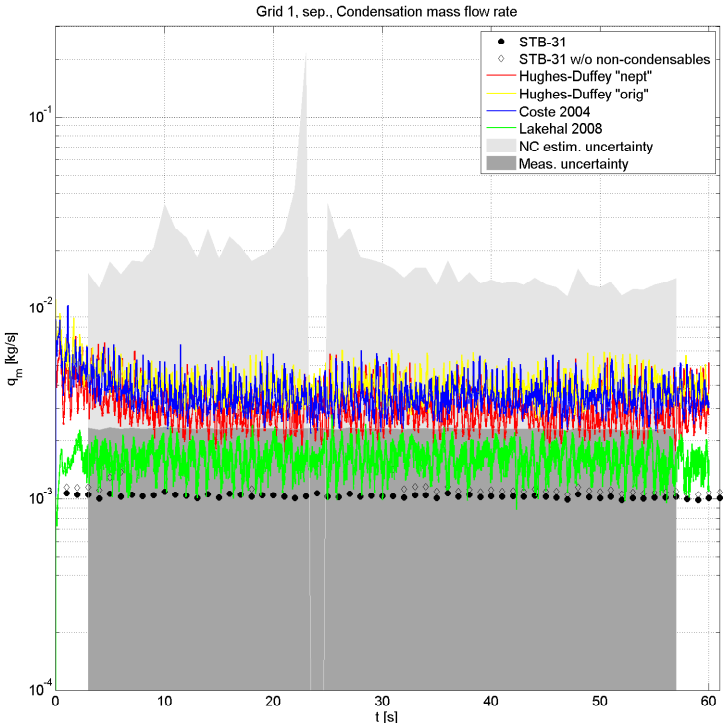

Figure 7.1. Condensation mass flow rate predictions of Hughes-Duffey, Coste '04 and Lakehal '08b models versus the STB-31 experimental data. Grid 1, 'SIMMER' drag model.

It can be seen from the results in Figure 7.1 that the DCC models of Hughes-Duffey and Coste '04 yield mostly similar results and overestimate significantly ($200\,\%$) the condensation mass flow rate, while the Lakehal '08b model seems to overestimate it by $50\,\%$. However, the condensation mass flow rate includes the effect of interface area fluctuations during the simulations. Because the interfacial area changes due to the fluctuation it may have an effect on the total condensation rate. Thus, the results are calculated also as interfacial DCC mass fluxes in this study, whenever it is possible or reasonable. The fluctuations of the interface have been considered negligible in the experiment. Figure 7.2 shows the results of Figure 7.1 in terms of the total interfacial mass flux.

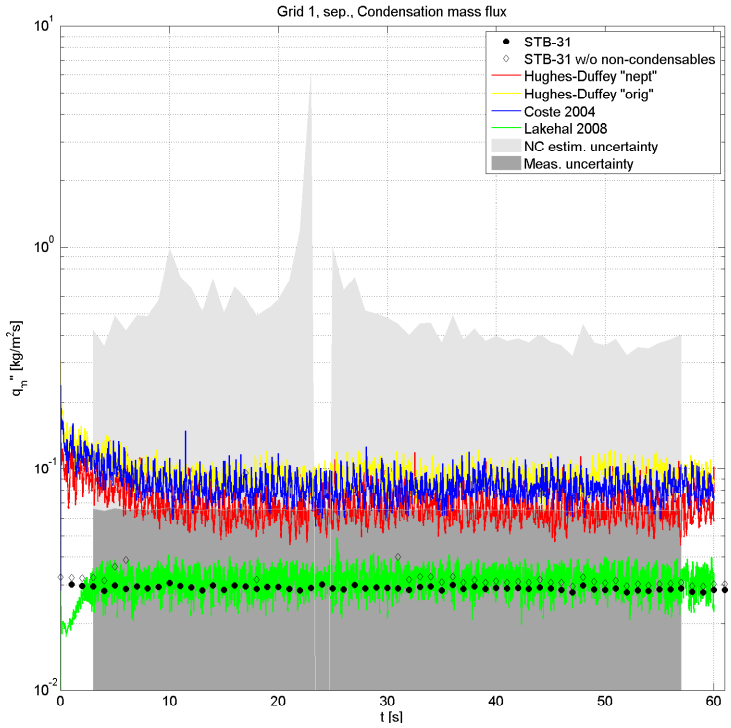

Figure 7.2. Condensation mass flux predictions of Hughes-Duffey, Coste '04 and Lakehal '08b models versus the STB-31 experimental data. Grid 1, 'SIMMER' drag model.

The condensation mass fluxes of Hughes-Duffey and Coste '04 models still indicate $100-200\,\%$ overestimation in the condensation rates meaning that the interface does not deform or fluctuate much in these simulations. The Lakehal '08b model predicts the DCC mass flux very close to the measured values, instead. This indicates that the fluctuation of the interface was with this model the only reason for the overpredictions of the condensation mass flow rates.

The condensation mass flow rates and mass fluxes for the 2D-axisymmetric **'Grid 2'** and **'SIMMER'** drag model cases are presented in Figures 7.3 and 7.4. Only the Hughes-Duffey $'\mathrm{nept.}'$ and Lakehal '08b models were tested in this case because the other models should predict results very similar to the Hughes-Duffey model.

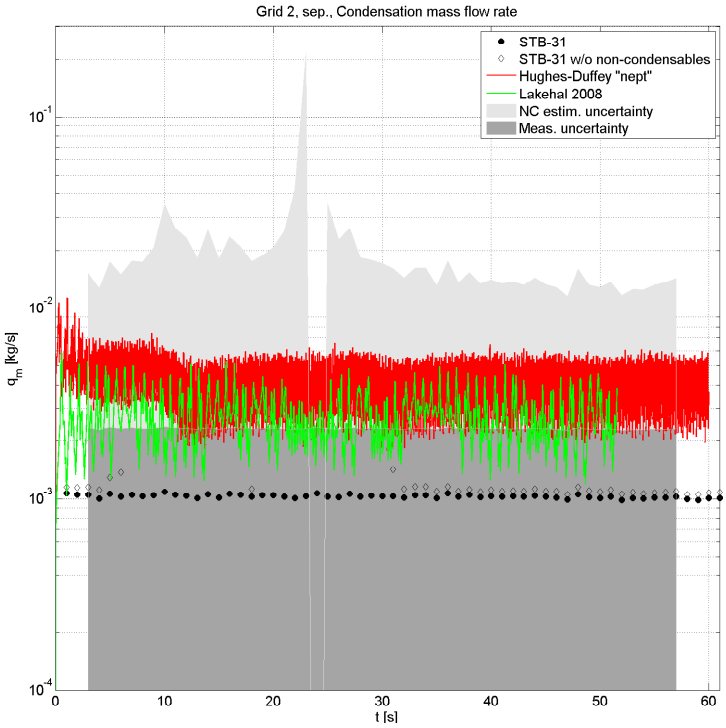

Figure 7.3. Condensation mass flow rate predictions of Hughes-Duffey, Coste '04 and Lakehal '08b models versus the STB-31 experimental data. Grid 2, 'SIMMER' drag model.

The DCC mass flow rate results with a finer grid indicate a moderate increase in the mass flow rates due to the grid refinement. The model of Hughes-Duffey overpredicts the mass flow rate now by $200-300\,\%$ and Lakehal '08b by $150\,\%$. The corresponding mass fluxes are shown in Figure 7.4.

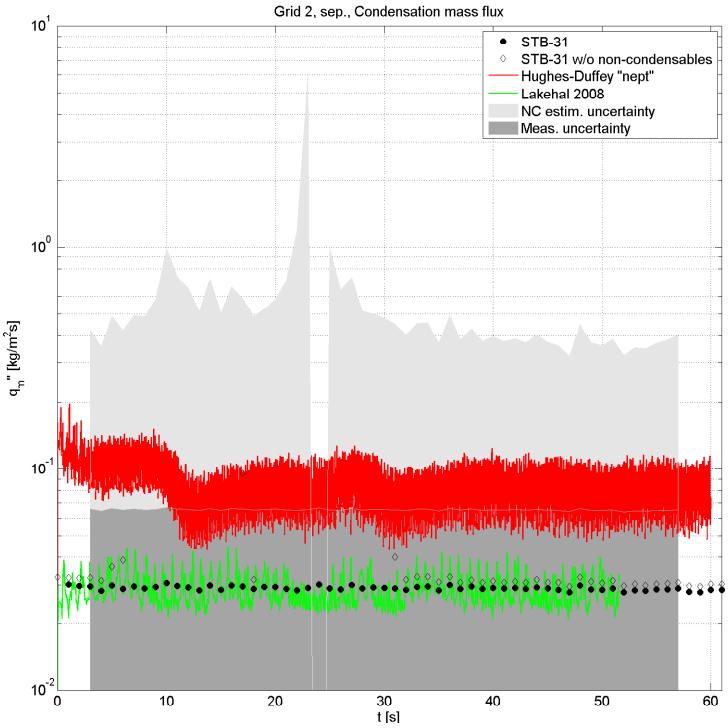

Figure 7.4. Condensation mass flux predictions of Hughes-Duffey, Coste '04 and Lakehal '08b models versus the STB-31 experimental data. Grid 2, 'SIMMER' drag model.

As can be seen in Figure 7.4, the DCC rate results seem to be more promising in terms of the interfacial mass flux. As was the case with the coarser grid, the Hughes-Duffey model overpredicts the condensation mass flux by $200 - 300\,\%$, while the Lakehal '08b model matches the measured values. Thus, there is no severe grid dependency concerning the DCC or heat transfer rates predicted by these models when using 'SIMMER' drag model.

Volume fraction fields in Figures 7.5 and 7.6 reveal the grid dependency due to interface movement in the simulation cases with the Lakehal '08b condensation model.

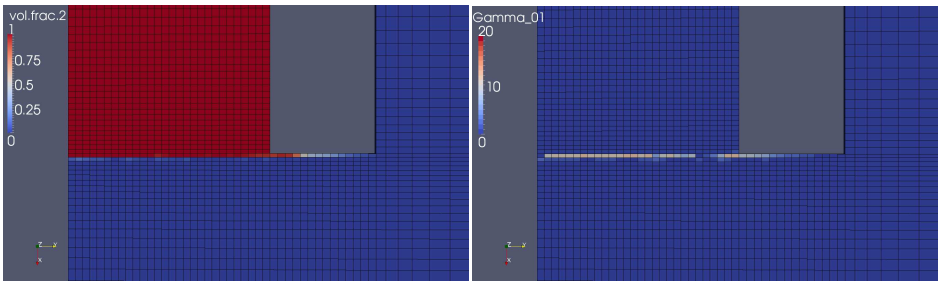

Figure 7.5. Volume fraction of steam and condensation mass flux in 2D-axisymmetric simulation (Grid 1, 'SIMMER', Lakehal '08b) of the STB-31 experiment.

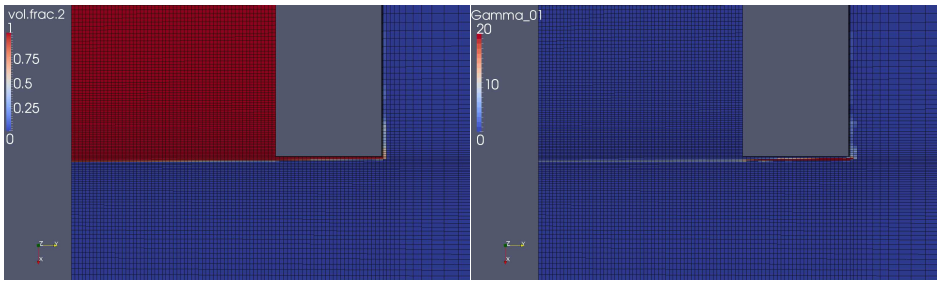

Figure 7.6. Volume fraction of steam and condensation mass flux in 2D-axisymmetric simulation (Grid 2, 'SIMMER', Lakehal '08b) of the STB-31 experiment.

Although the steam/water interface is 'forced' to stay at the mouth of the blowdown pipe by pressure boundary conditions, it is rarely completely calm in the computations. In the cases of Figures 7.5 and 7.6, the interface oscillated slightly particularly by the increasing/decreasing DCC rates. Because of the relatively low DCC rates at the large flat interface, the excess steam was capable of occupying cells on the pipe lip wall region. The condensation mass flow rate was higher near the walls due to higher turbulence kinetic energy and increasing interfacial area of the crawling steam tongue. Thus, the DCC was capable of collapsing the steam tongue with the help of locally high condensation rate values. After the condensation of the steam tongue, the cycle started again from the low DCC rates. The difference between the grid resolutions comes probably from the combination of slightly decreased DCC rate and increased number of cells; the steam has time to occupy more cells and form a buffering layer of interfacial steam cells around the core tongue. With that kind of a structure it can occupy a greater volume and create a larger interface before collapsing.

The total interfacial areas during the STB-31 ('SIMMER' Grid1 and Grid2) simulations are shown in Figure 7.7.

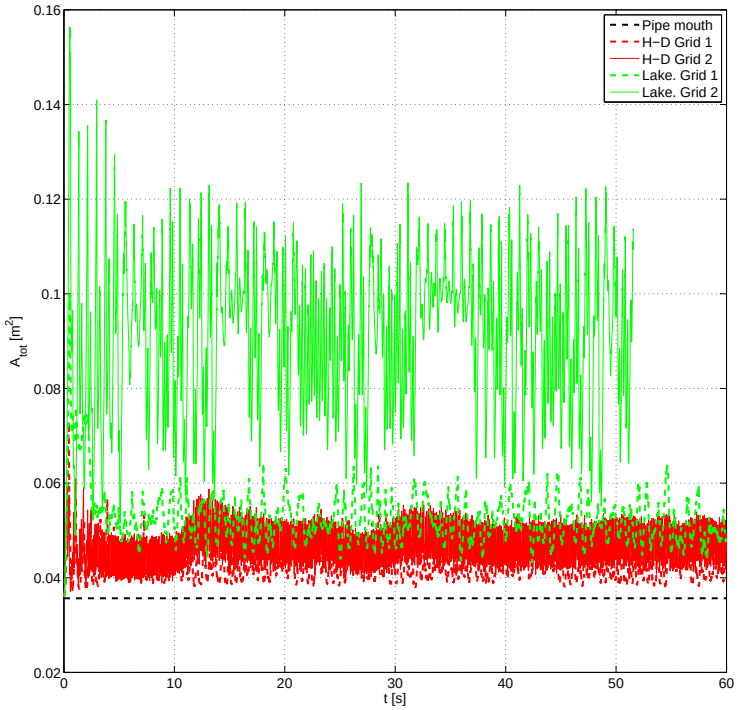

Figure 7.7. Total interfacial area in 2D-axisymmetric simulations of the STB-31 experiment using Hughes-Duffey and Lakehal '08b models. 'SIMMER' drag model.

Figure 7.7 shows clearly that in the case of the Lakehal '08b model the interfacial area is the main reason for the differences between the Grid 1 and Grid 2 results.

Heat transfer coefficients (h or HTC) have in CFD simulations different values in each cell. However, some information of them can be obtained by calculating the average heat transfer coefficient from all the cells where the correlation is activated, i.e. in the interfacial cells. The average HTCs for the 2D-axisymmetric cases with 'SIMMER' drag model are presented in Figures 7.8 and 7.9.

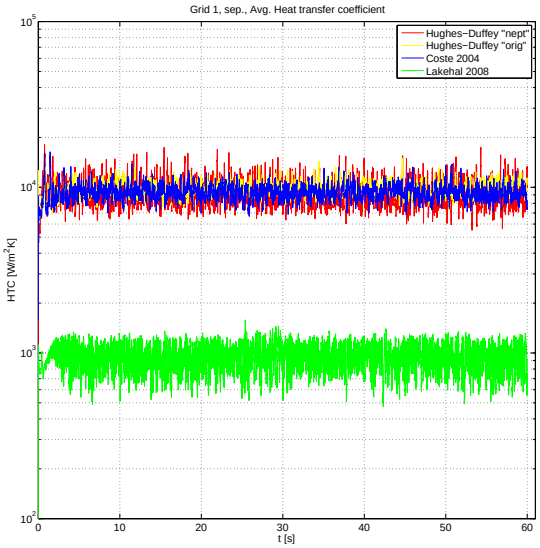

Figure 7.8. Average heat transfer coefficients of Hughes-Duffey, Coste ’04, and Lakehal ’08b models for Grid 1 and ’SIMMER’ drag model.

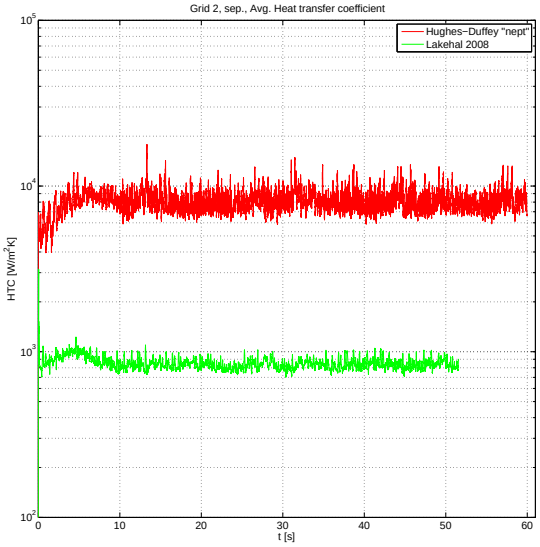

Figure 7.9. Average heat transfer coefficients of Hughes-Duffey and Lakehal ’08b models for Grid 2 and ’SIMMER’ drag model.

The average HTCs in Figures 7.8 and 7.9 show that the grid resolution does not have a significant effect on their magnitude. In comparison of the Lakehal '08b and the other models, there seems to be a difference of a single order of magnitude between the HTCs. The HTC by Lakehal '08b is around $1000\,\mathrm{W/(m^2\,K)}$ and the HTC by the others around $10\,000\,\mathrm{W/(m^2\,K)}$.

The condensation mass flow rates predicted by the models of Hughes-Duffey, Lakehal '08b and Coste '04 by using the 2D-axisymmetric **'Grid 1'** and **'Large Interface'** drag model are presented in Figure 7.10.

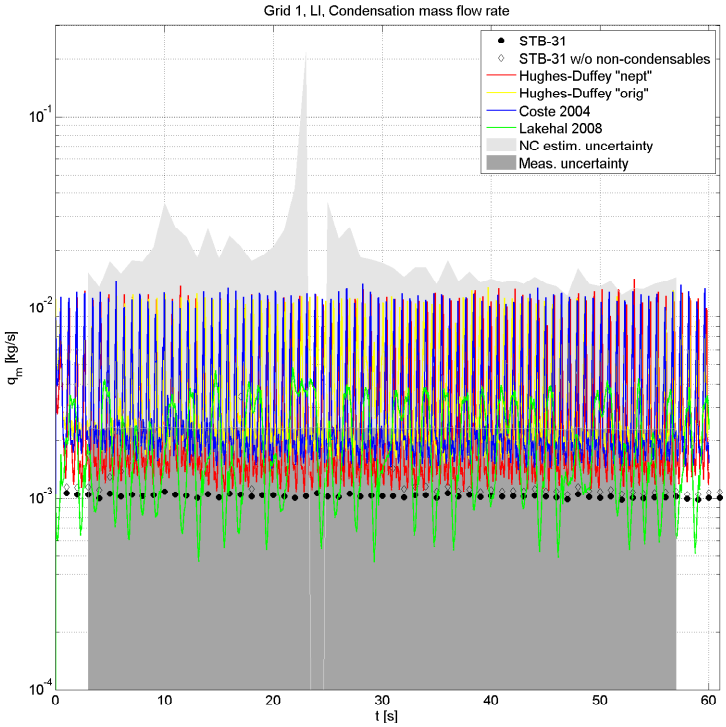

Figure 7.10. Condensation mass flow rate predictions of Hughes-Duffey, Coste '04, and Lakehal '08b models versus the STB-31 experimental data. Grid 1, 'Large interface' drag model.

The results of the condensation mass flow rate with the 'Large Interface' drag model are different from the ones obtained with the simpler 'SIMMER' drag model. It can be seen from Figure 7.10 that the condensation mass flow rates of each DCC model fluctuate with a larger amplitude than observed in the case of 'SIMMER' with Grid 1. The effective mass flow rates of all the models seem to be around values corresponding $50 - 100\,\%$ overprediction of the DCC rate. The corresponding DCC mass fluxes are shown in Figure 7.11.

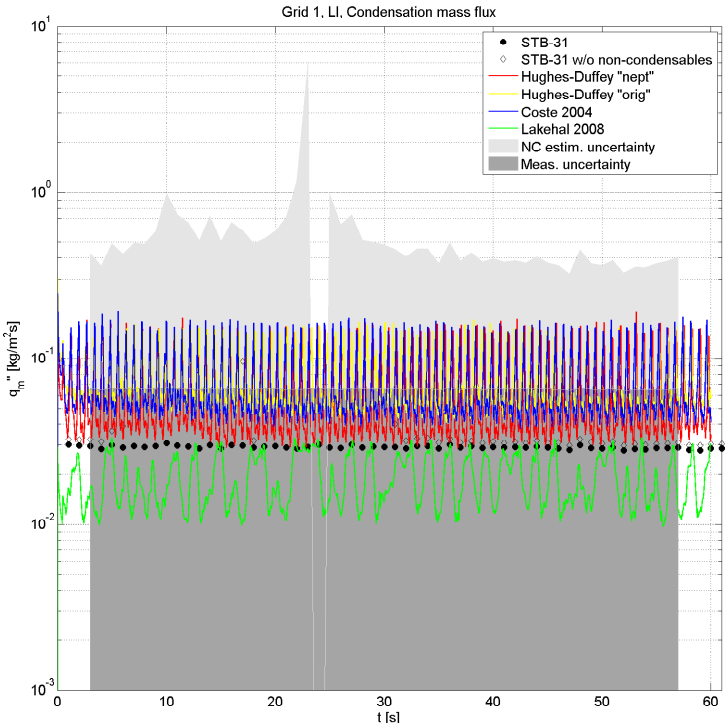

Figure 7.11. Condensation mass flux predictions of Hughes-Duffey, Coste '04 and Lakehal '08b models versus the STB-31 experimental data. Grid 1, 'Large interface' drag model.

The mass flux results in Figure 7.11 for 'Grid 1' and 'Large interface' drag model indicate that the interfacial area fluctuations are small for the Hughes-Duffey and Coste '04 models as their overpredictions of the DCC rates are still around $50 - 100\,\%$. Again, the Lakehal '08b model seems to suffer more of the interface fluctuations and underpredicts the mass flux by $0 - 66\,\%$. As the fluctuation of the Lakehal '08b results can be explained much by the interfacial area, the fluctuation seen in Hughes-Duffey and Coste '04 cases is more difficult to explain, since the source coding of the Large Interface model is not available to the author with all details. One likely explanation is that the tangential shear at the interface, obtained by the 'Large interface' drag model, varies when the interface fluctuates and it affects the turbulence field.

The condensation mass flow rates for the Coste-Laviéville condensation model with the 2D-axisymmetric 'Grid 1' and 'Large interface' drag model are presented in Figure 7.12

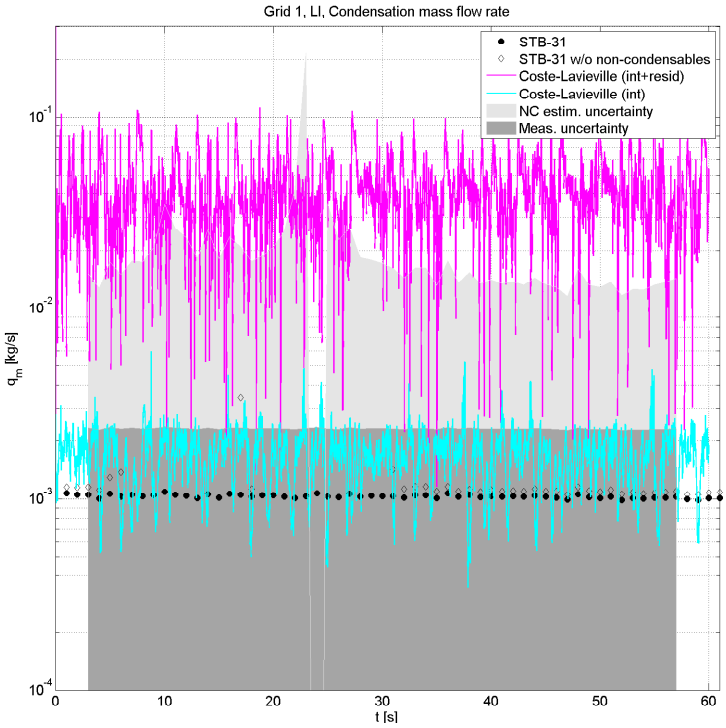

Figure 7.12. Condensation mass flow rate predictions using 'Large interface' drag model and the Coste-Laviéville condensation model versus the STB-31 experimental data. Grid 1.

The original implementation 'int+resid' of the Coste-Laviéville model shows an enormous overprediction of the DCC rate. This overprediction is due to the handling of the residual volume fractions outside of the LI3C region by using simple time-constant-based droplet/bubble condensation models. Such a model tends to dominate in the condensation when the DCC rate on the interface is low, particularly in the STB-31 case (Tanskanen et al., 2007). When the residual model was disabled, the DCC rates dropped to the values of Lakehal '08b model as they should, recalling that the Coste-Laviéville model employs the Lakehal '08b model in the low-Re cases.

Simulations with a denser grid were also conducted for the 'Large interface' drag model cases. The condensation mass flow rates predicted by the models of Hughes-Duffey, Lakehal '08b and Coste '04 by using the 2D-axisymmetric **'Grid 2'** and **'Large Interface'** drag model are presented in Figure 7.13.

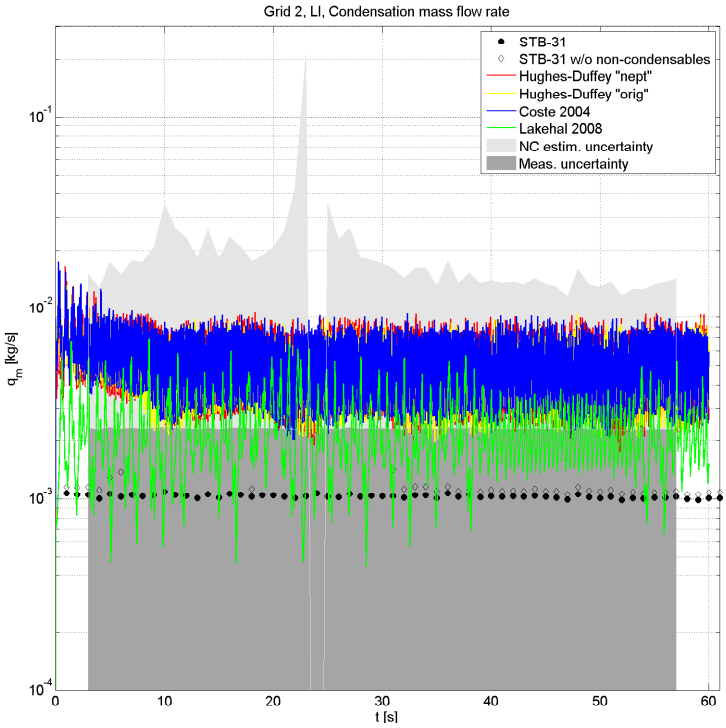

Figure 7.13. Condensation mass flow rate predictions using 'Large interface' drag model. Hughes-Duffey, Coste '04, and Lakehal '08b models versus the STB-31 experimental data. Grid 2.

According to Figure 7.13, the refined grid brings the result near the ones obtained with the 'SIMMER' drag model. Maybe due to the refinement, the tangential shear or boundary layer on the interface are better resolved. However, the DCC mass flow rates oscillate still with a higher amplitude than in the 'SIMMER' cases. The corresponding DCC mass fluxes are shown in Figure 7.14.

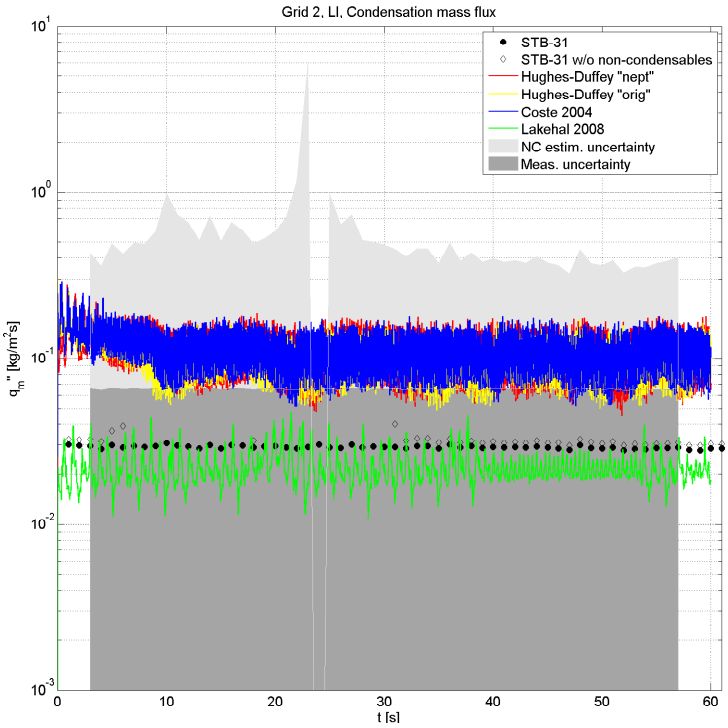

Figure 7.14. Condensation mass flux predictions using 'Large interface' drag model and Hughes-Duffey, Coste '04, and Lakehal '08b DCC models versus the STB-31 experimental data. Grid 2.

The condensation mass fluxes with the 'Large interface' drag model correspond well the results obtained with the 'SIMMER' drag model in the same grid resolution.

The condensation mass flow rates for the Coste-Laviéville condensation model with the 2D-axisymmetric 'Grid 2' and the 'Large interface' drag model are presented in Figure 7.15

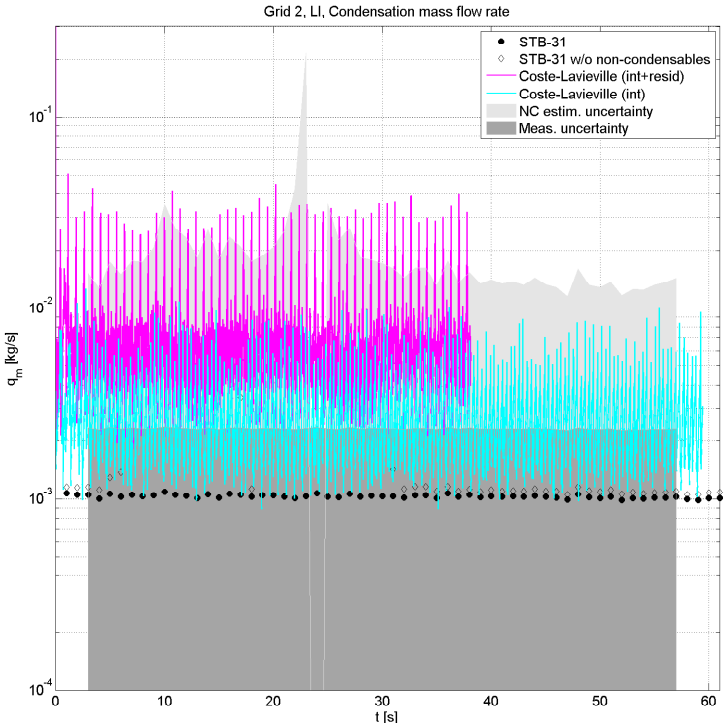

Figure 7.15. Condensation mass flow rate predictions using 'Large interface' drag model and Coste-Laviéville condensation model versus the STB-31 experimental data. Grid 2.

As an effect of the grid refinement, the proportion of diffuse residual phase around the LI3C decreases. This can be seen as a smaller prediction of DCC mass flow rate by the 'int+resid' version of the Coste-Laviéville model with this denser grid. However, the condensation rate predicted by it is still too high. The 'int.' version of the Coste-Laviéville model predicts the DCC rate near the Lakehal '08b model, as was also the case with the coarser grid.

The total interfacial areas during the STB-31 ('Large interface' Grid 1 and Grid 2) simulations are shown in Figure 7.16.

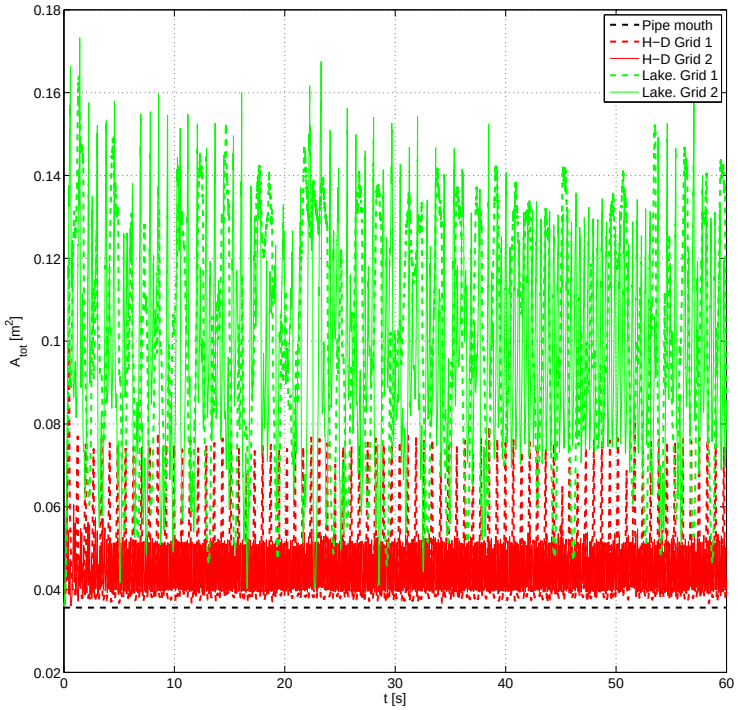

Figure 7.16. Total interfacial area in simulations with Hughes-Duffey and Lakehal '08b models by using 'Large interface' drag model.

Figure 7.16 shows that in the case of the Lakehal '08b model, the interfacial area is the main reason for the differences between the Grid 1 and Grid 2 results also when using the 'Large interface' drag model.

The average HTCs for the 2D-axisymmetric cases with the 'Large interface' drag model are presented in Figures 7.17 and 7.18. The HTCs with the 'Large interface' drag model correspond to the DCC mass flow rate and mass flux results presented earlier. With the denser grid, the HTCs are higher as was the case with the mass flow rates as well. However, the HTCs are lower than the ones seen in the cases of the 'SIMMER' drag model. As the DCC rates do not differ from the 'SIMMER' results, the condensation rate has to be enhanced by a larger interfacial area which can be seen by comparing Figures 7.7 and 7.16.

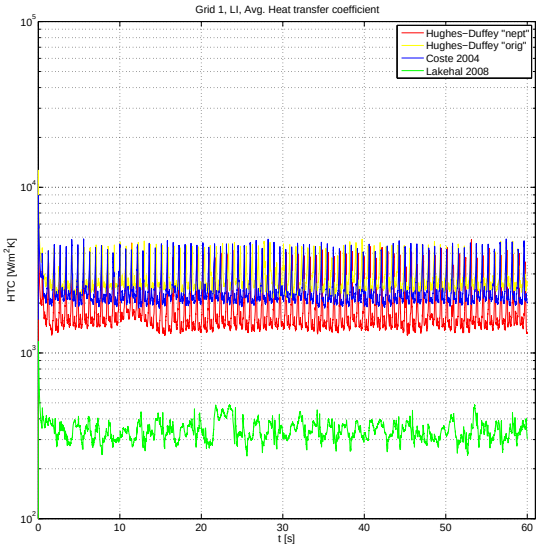

Figure 7.17. Average heat transfer coefficients of Hughes-Duffey, Coste ’04, and Lakehal ’08b models for Grid 1 and ’Large interface’ drag model.

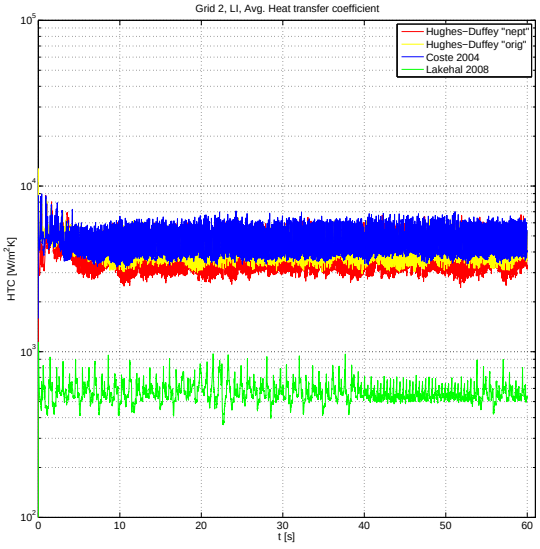

Figure 7.18. Average heat transfer coefficients of Hughes-Duffey, Coste ’04, and Lakehal ’08b models for Grid 2 and ’Large interface’ drag model.

7.1.2 Interface tracking method simulations of STB-31 experiment with TransAT solver

The TransAT simulations were started directly with the 3D geometry, as the TransAT uses cartesian grid and immersed body technique for surfaces making grid generation work quite straightforward. Also for the (DNS) simulation with the direct phase change solution, the 3D geometry is the only really reasonable one as the solved eddies are three dimensional. In these 3D simulations, the grid was refined to $900 - 1100\,\mu\mathrm{m}$ cell height in the blowdown pipe outlet region. Only the direct phase change solution was tested in these 3D simulations. Some results of the 3D simulations are presented in Figure 7.19.

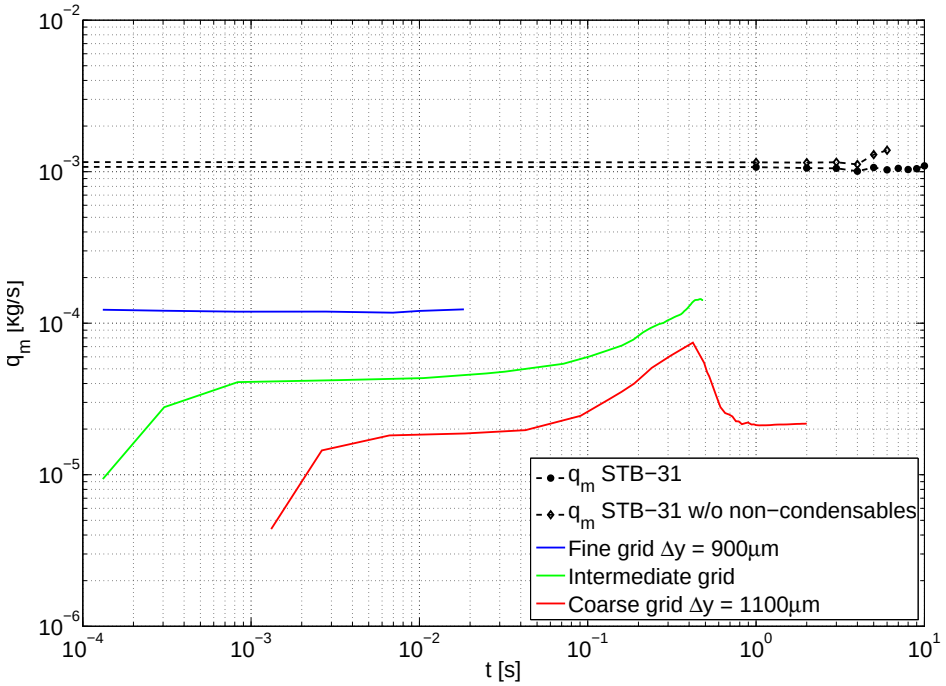

Figure 7.19. Condensation rates in 3D TransAT simulations of the STB-31 experiment with the direct phase change solution method.

The simulated time periods in the 3D TransAT calculations were left very short. This was mainly due to the strong grid refinements which lead to short time stepping. Because of the short simulation times, the results in Figure 7.19 are presented on a log-log-scale. The Figure 7.19 shows that the condensation rate was underestimated by 1 - 2 orders of magnitude in these 3D simulations. However, it shows also quite clearly that the condensation rate increases as a function of grid refinement. These kinds of high mesh requirements are presumable for the direct phase change solution. Thus, it was not feasible to continue 3D calculations further, and the work was directed to 2D-axisymmetric grids, although

the eddies cannot be solved then as 3D. A peak in the condensation rates can be seen in Figure 7.19 at $t = 0.1 - 1\,\mathrm{s}$. This peak is due to the bubble eruptions during that period of time. The formation of bubbles increased the interfacial area leading to a higher total condensation mass transfer rate. In these early 3D simulations, the pressure boundary conditions were not adjusted to keep the interface exactly at the outlet of the blowdown pipe. Thus, minor bubble formation occurred due to the inaccuracy of the measurement based pressure values. The formation of a bubble in the 3D case is presented in Figure 7.20.

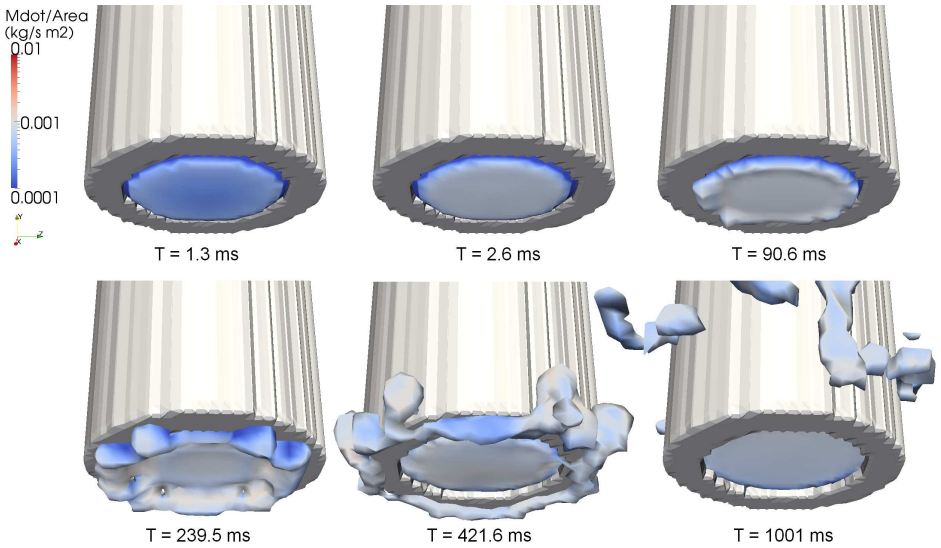

Figure 7.20. Formation of a bubble in the TransAT 3D simulation of the STB-31 experiment due to inaccuracies in the measurement-based pressure boundary conditions.

A 2D-axisymmetric geometry was developed after the 3D simulations. In this model, only a $3\,\mathrm{mm}$ high and $168\,\mathrm{mm}$ wide section at the pipe outlet was modeled. Various grid resolutions were tested in this geometry, and also the URANS simulations with the stratified DCC models were conducted in a 2D-axisymmetric grid. Concerning the direct phase change solution, the condensation rates seem to reach values that are stationarily very close to the measured steam mass flow rate values only with the denser grids. The condensation rates obtained by using the denser ($\Delta h = 37.5$ and $10\,\mu\mathrm{m}$) grids are presented in Figure 7.21.

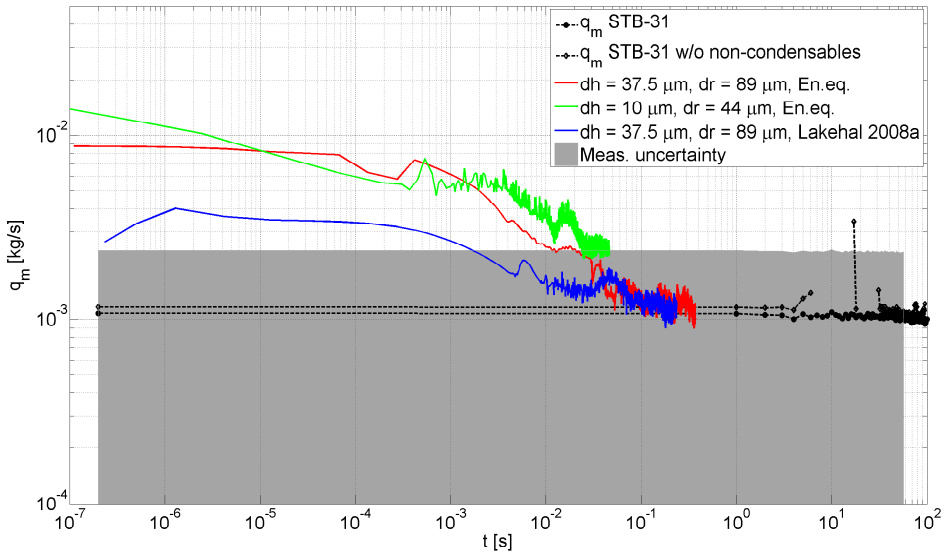

Figure 7.21. Condensation rates in 2D-axisymmetric TransAT simulations of the STB-31 experiment. Grid cell $\Delta h = 10$ or $37.5\,\mu\mathrm{m}$. Direct phase change solution and surface renewal model of Lakehal '08a used as phase change models.

The condensation rates shown in Figure 7.21 are the most promising ones achieved by the direct phase change solution and surface renewal model of Lakehal 2008a in TransAT simulations of the STB-31 experiment. After warming up the initial liquid surface, the condensation rates settle to values very close to the measured steam mass flow rates. The surface renewal model produces results similar to the results of the direct phase change solution. Due to the short time step size, simulations with the dense grid were computationally challenging for the current 4 node computer cluster used in these TransAT calculations. The computation times for the cases of Figure 7.21 were $1 - 1.5\,\mathrm{months}$. Another reason to interrupt the calculations after a few tenths of seconds was simply the small dimension of the calculation domain. After the warm water clusters pass the boundary of the domain, calculation could lose its predictivity as the warm water cannot freely return back from behind the boundary.

With the coarser grids, some temporary large scale ($L_{\mathrm{wave}} \approx 10 - 100\,\mu\mathrm{m}$) disturbances developed on the steam/water interface which increased condensation rates. When these disturbances settled down, the condensation rates fell below the measured mass flow rate values. With the denser grids such disturbances had a much smaller amplitude and the condensation rates were mostly dominated by local small scale ($r_{\mathrm{eddy}} < 1\,\mathrm{mm}$) heat transport phenomena inside the liquid phase. Figure 7.22 shows the temperature profiles with the different grid resolutions.

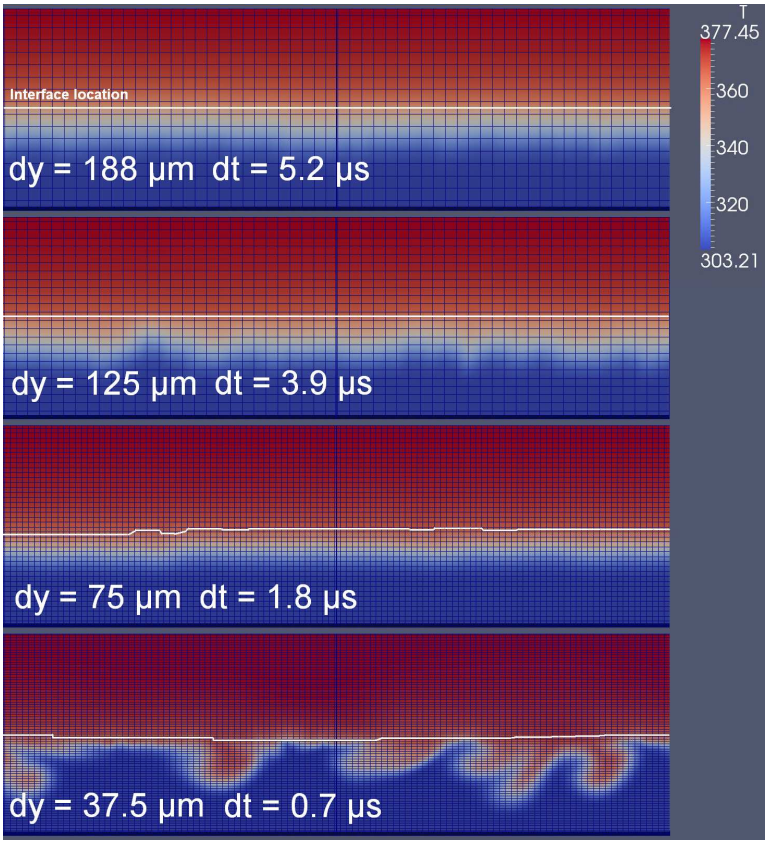

Figure 7.22. Samples of temperature fields at $t = 0.1\,\mathrm{s}$ in 2D axisymmetric TransAT simulations of the STB-31 experiment. Locations of the steam/water interface are marked with white lines.

As can be seen from Figure 7.22, the water just below the steam/water interface seems to heat up more homogenously in the coarser grid cases than in the very dense grid case. The effect of this on the condensation rates is shown in Figure 7.23. A sample of velocity vectors with temperature fields for the dense grid case is shown in Figure 7.24.

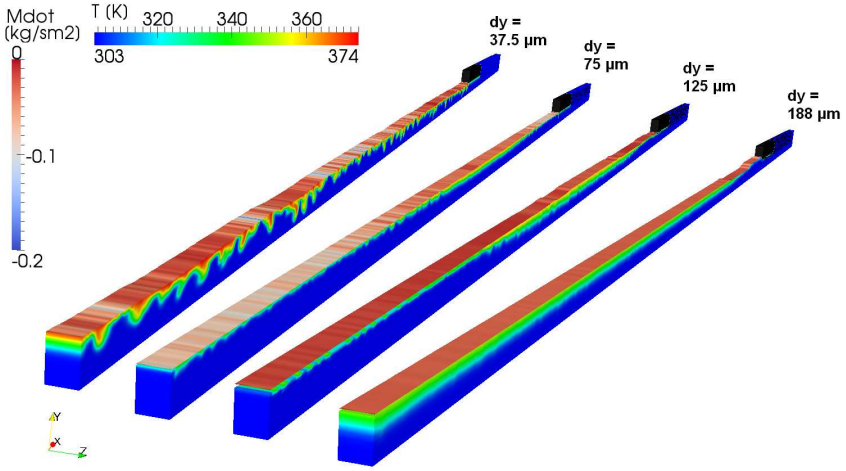

Figure 7.23. Samples of liquid temperature fields beneath the interface and interfacial condensation rates at $t = 0.1\,\mathrm{s}$ in 2D axisymmetric TransAT simulations of the STB-31 experiment. Negative mass flux denotes here condensation.

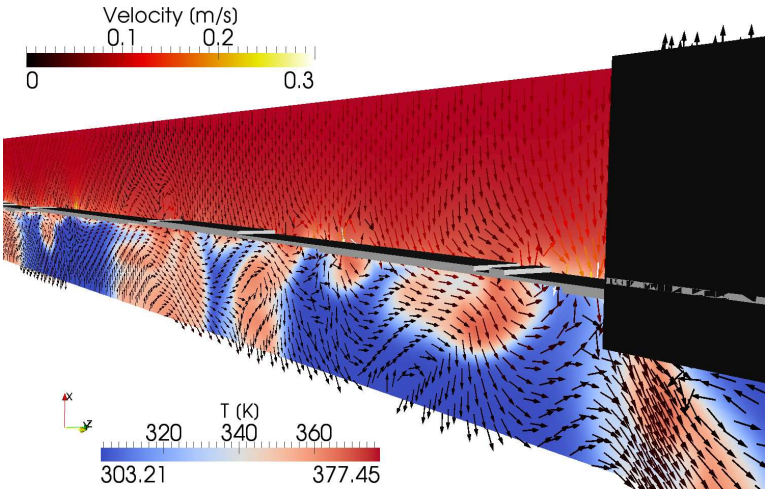

Figure 7.24. A sample of velocity and temperature fields in a dense-grid 2D axisymmetric TransAT simulation of the STB-31 experiment.

Figure 7.23 shows that the heat transfer mechanisms seem to be quite different with different grid resolutions in the direct phase change solution. The densest grid produces an eddy-looking temperature field on the liquid side, leading to high condensation rates in the local low-temperature points. For this dense grid case, Figure 7.24 shows also how the local condensation drains steam towards the interface and, on the water side, how the water near the interface is transported beneath that interface. In the case of the second densest grid in Figure 7.24, a larger scale wave can be seen in the temperature field, leading to a local large cool interface area preferable for the condensation. However, the condensation mass flux there is still not as high as in the densest grid case. In the coarser grid cases, the temperature fields on the liquid side are more homogenous and diffuse, leading to low condensation rates. Not even the local low-temperature regions seem to increase the condensation rates remarkably in these cases.

Due to the abovementioned results with the direct phase change modelling, it can be concluded that the direct solution is practically computationally too expensive for most of the DCC cases. However, the direct phase change solution can be used in 'numerical experiments' in order to get data that is difficult to measure. Considering the STB-31 case, the results of direct solution with increasing grid resolution converge to the values near the measured mass flow rates or to the values predicted by the model of Lakehal '08b. In this light, this can be considered as partial 'validation' of the measurements, as well as validation of the Lakehal '08a and '08b DCC models.

Few simulations were done also with a larger 2D-axisymmetric domain and coarser mesh ($\Delta h \approx 940\,\mu\mathrm{m}$) in order to reach longer simulation periods. The RANS DCC models of Lakehal '08b and Banerjee '68 were briefly tested with that grid, too. The results of the direct phase change solution and Lakehal '08a model with the coarse 2D-axisymmetric grid are presented in Figure 7.25.

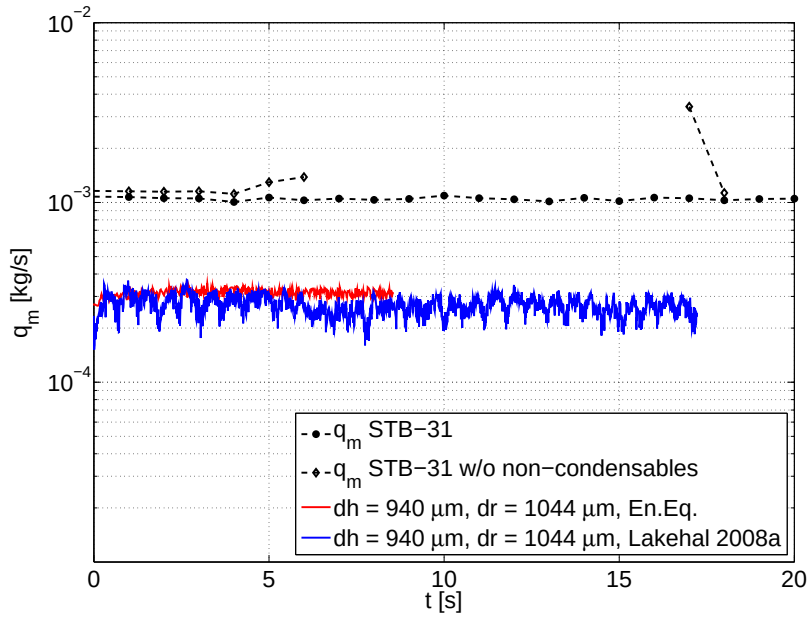

Figure 7.25. Condensation rates in 2D-axisymmetric TransAT simulations of the STB-31 experiment. Grid cell $\Delta h \approx 940\,\mu\mathrm{m}$. Direct phase change solution and Lakehal 2008a model used as phase change models.

The condensation rates shown in Figure 7.25 correspond to the results obtained from the 3D simulation with grid cell $\Delta h \approx 900\,\mu\mathrm{m}$ (Figure 7.19). However, notably longer simulation periods were possible with the 2D-axisymmetric grid. According to the results of these 2D-axisymmetric simulations, it seems likely that both of these phase change solution methods underestimate the condensation rates also in longer simulation runs if the grid resolution is too coarse for them.

The results of TransAT RANS ($k-\varepsilon$) simulations by using the Lakehal '08b and Banerjee '68 DCC models are presented in Figure 7.26.

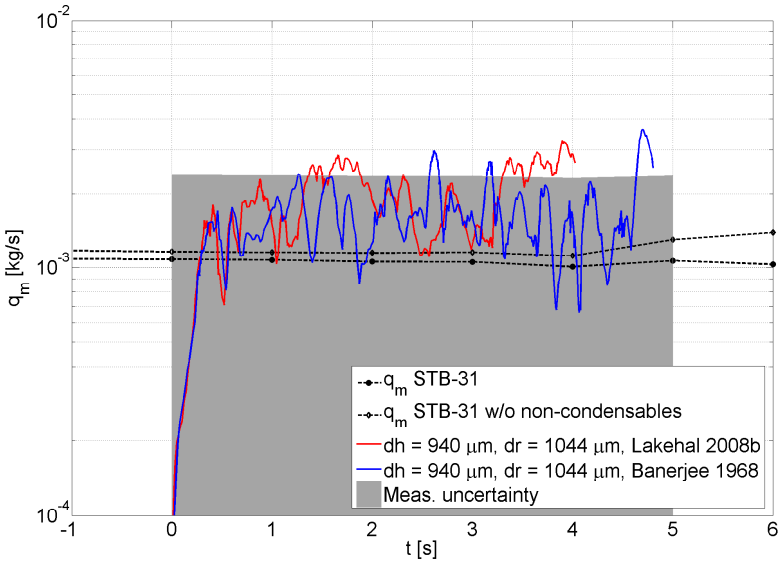

Figure 7.26. Condensation rates in 2D-axisymmetric TransAT simulations of the STB-31 experiment. Grid cell $\Delta h \approx 940\,\mu\mathrm{m}$. Lakehal '08b and Banerjee '68 DCC models used as phase change models.

As can be seen in Figure 7.26, the condensation mass flow rates of both models, Lakehal '08b and Banerjee '68, predict quite well the condensation mass flow rate. This result is in a good agreement with the results obtained using the Lakehal '08b model in NEPTUNE_CFD simulations. This result partially verifies the implementation of the model to the NEPTUNE_CFD carried out by the author. Unfortunately, the other DCC models, i.e. the ones tested with NEPTUNE_CFD, were not tested with TransAT in this study. The reason for this were the high condensation rates they tend to predict, causing convergence problems in the incompressible flow pressure solver of the TransAT version 2.3.0.

7.2 Simulation of a high Reynolds number condensation case

The STB-28-(4) experiment has been simulated using the Eulerian-Eulerian two-phase solver of the NEPTUNE_CFD code. The stratified flow DCC models tested in this part are the Hughes-Duffey, Lakehal '08b (to some extent) and Coste-Laviéville models. The 'Large interface' drag model is used in the simulations with the Coste-Laviéville model. Otherwise, the 'SIMMER' drag model is used. The 2D axisymmetric simulations are done by using a single grid, and a few of simulations are done by using a 3D grid.

7.2.1 Eulerian-Eulerian simulations of STB-28 experiment with NEPTUNE_CFD solver

The chugging simulation cases contain much of the qualitative information, the translation of which into the numerical form is challenging or laborous. In this study, such a translation work has been carried out for bubble diameters and frequencies. However, there are also some other phenomena of chugging that can be analysed qualitatively. Qualitative behaviours of chugging frequency, amplitude, jet/bubble shape, and DCC mass flow rate were used when choosing the models and methods to be examined further in this study.

Qualitative observations

At first, **the effect of initialization** of the steam/water interface level either inside or to the exit of blowdown pipe should be observed, as it determines the best setting for the rest of simulations. The simulations where the steam/water interface was initialized just at the exit of the blowdown pipe were a reasonable choice as the first cases to be simulated, because the earlier 2D-axisymmetric simulations with cartesian grids had showed that other approaches may be numerically challenging due to strong chugging (Tanskanen and Jordan, 2009). As assumed, the convergence was now better and various bubble eruptions were simulated. The Hughes-Duffey and Lakehal '08b condensation models were tested with this initialization. Figure 7.27 shows the volume fraction field during the simulation with that initialization and the Hughes-Duffey condensation model.

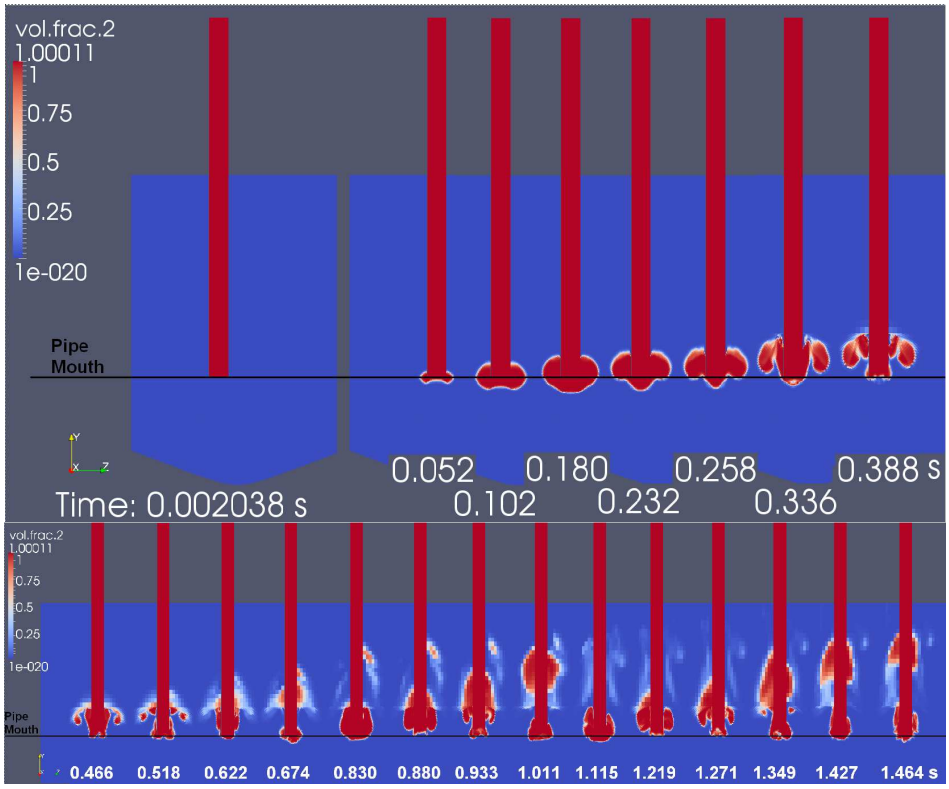

Figure 7.27. Volume fraction in a 3D NEPTUNE_CFD simulation of the STB-28 experiment. The Hughes-Duffey condensation model with initial surface set to the exit of the blowdown pipe.

The sizes of bubbles seen in Figure 7.27 are remarkably large and clearly larger than those seen in the STB-28 experiment. Furthermore, there is a notable amount of large residue bubbles capable of ascending to the upper parts of the pool. Although the condensation rates were not measured in the STB-28 experiment explicitly, these facts indicate that the condensation rate is strongly underpredicted in this simulation. The condensation model of Lakehal '08b produced almost an identical result with the one showed in Figure 7.27, and thus, the corresponding figure is not included here.

Figures 7.28 and 7.29 show the condensation rates at the steam/water interface during the first bubble eruption in the cases of Hughes-Duffey and Lakehal '08b models, respectively.

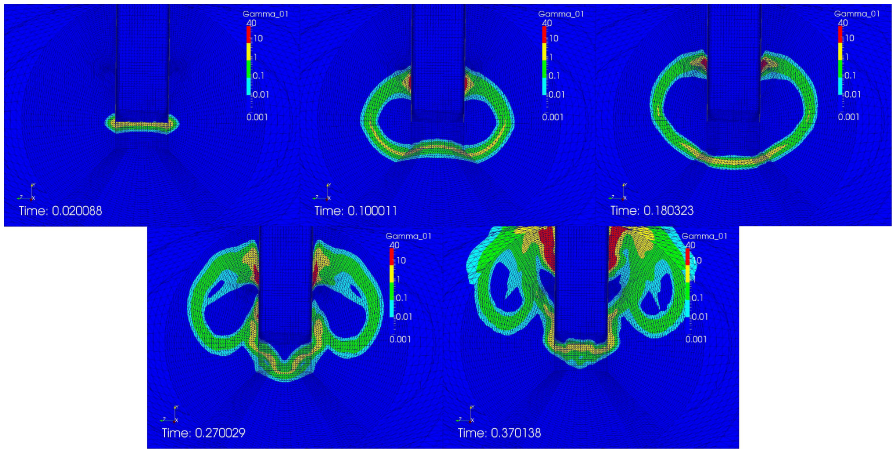

Figure 7.28. Local condensation rate [kg/m^{3}s] in a 3D NEPTUNE_CFD simulation of the STB-28 experiment. The Hughes-Duffey DCC model with initial surface set to mouth of the pipe.

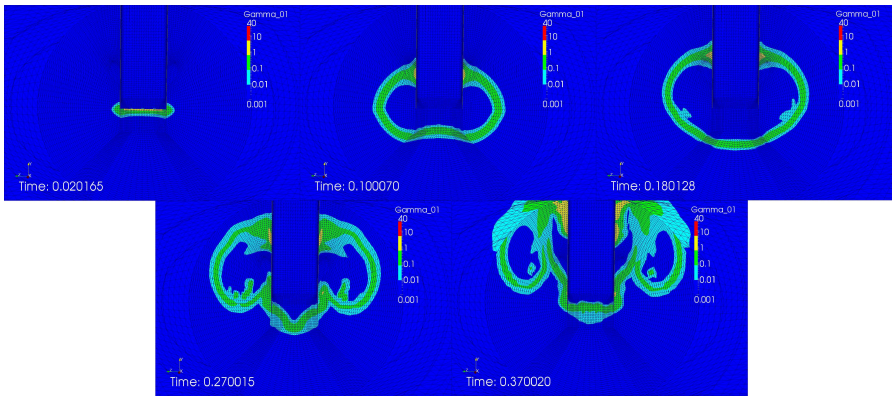

Figure 7.29. Local Condensation rate [kg/m^{3}s] in a 3D NEPTUNE_CFD simulation of the STB-28 experiment. The Lakehal '08b DCC model with initial surface set to mouth of the pipe.

Although the appearance of the bubbles was not seen to differ much between these two condensation models, Figures 7.28 and 7.29 show clear differences in their condensation rates. The condensation rate predicted by the Hughes-Duffey condensation model is much higher. Yet, it was not high enough to produce realistic chugging with this initial condition and length of simulation.

Despite the numerical problems in the earlier 2D-axisymmetric simulations, a 3D simulation with the initial steam/water interface inside the blowdown pipe was run (Tanskanen and Jordan, 2011). Figure 7.30 shows the main events of the volume fraction field during this simulation with the Hughes-Duffey condensation model.

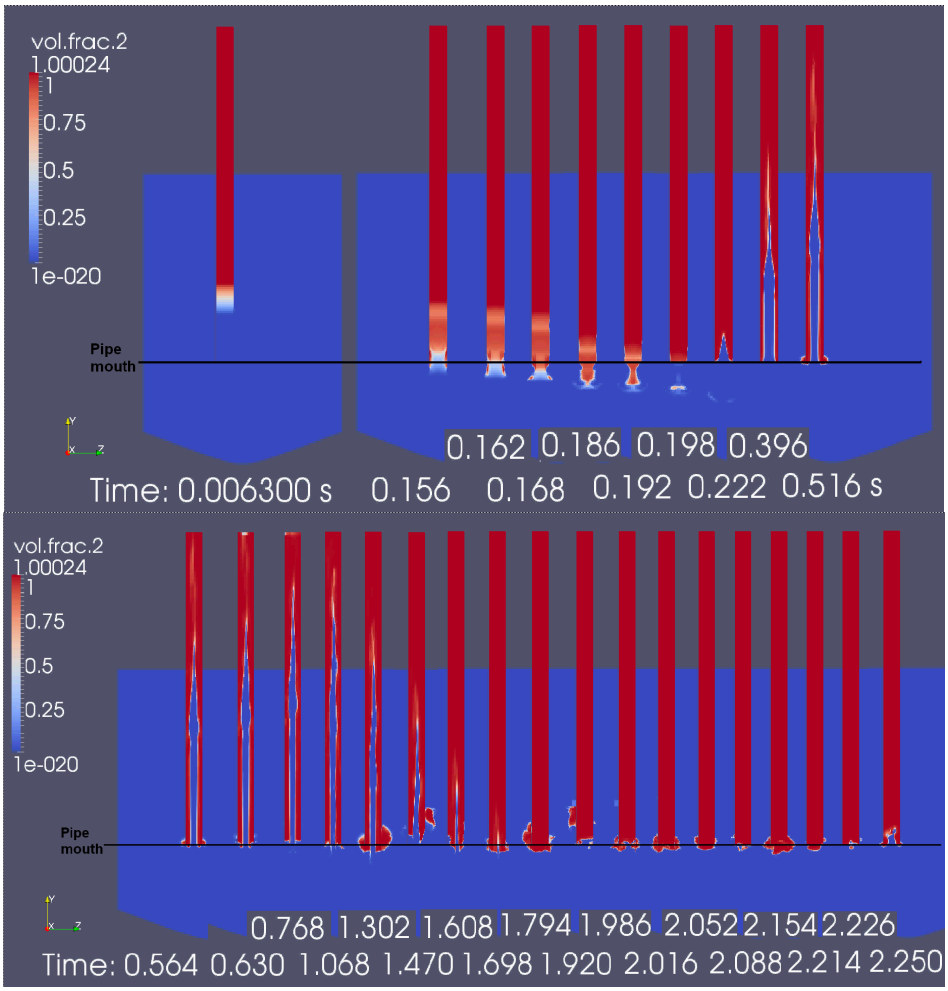

Figure 7.30. Volume fraction in a 3D NEPTUNE_CFD simulation of STB-28 experiment. The Hughes-Duffey condensation model with initial surface set inside the pipe.

In the earlier simulations, it was typical for the steam jet to penetrate into the pool and to condensate after that violently inside the blowdown pipe, leaving an annular steam volume on its walls. Numerical problems arose when the water core started to push upward inside the blowdown pipe. However, the 3D simulation shown in Figure 7.30 was capable of overcoming this initial collapse of the steam volume, and the simulation of a

few chugging cycles was possible. In addition to this, the condensation rates seem to be more realistic as no slowly condensing residual bubbles are detached, and the steam/water interface is also capable of retreating inside the blowdown pipe. This partial success is attributable to two important factors: the spherically curvilinear mesh at the pipe exit helped to mitigate numerical problems at the moment of bubble collapse, and the initialization of steam/water interface deeply inside the pipe invoked realistic chugging.

The explanation for enhanced chugging and DCC due to the initialization of interface inside the pipe can be obtained from Figure 7.31.

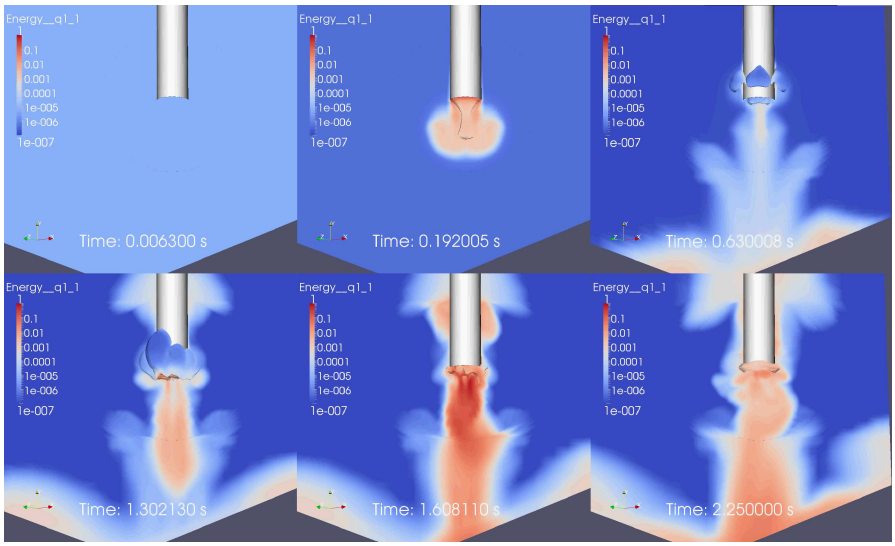

Figure 7.31. Turbulence kinetic energy in a 3D NEPTUNE_CFD simulation of STB-28 experiment. The Hughes-Duffey condensation model with the initial surface set inside the pipe.

As can be seen from Figure 7.31, the initial steam jet penetration pushes a water plug downward causing a highly turbulent trail towards the pool bottom. Later, when the pipe fills up again with steam, highly turbulent water is pushed from it to the pool. Furthermore, the early bubbles collapse slowly and are capable of rising a bit upward in the pool, increasing the mixing alongside the outer surface of the pipe as well. These phenomena increase the turbulent kinetic energy remarkably, thus leading to clearly higher condensation rates than in the case of the surface-at-mouth initialization.

To simulate longer periods of the chugging mode, a 2D axisymmetric grid was generated applying similar spherically curvilinear structure at the exit region of the blowdown pipe as used in the 3D grid. With longer simulation periods, it was possible to better compare different models and obtain some statistical data of the bubble sizes and frequencies. Figures 7.32 and 7.33 show **the qualitative differences between the results** of Hughes-Duffey and Lakehal ’08b models.

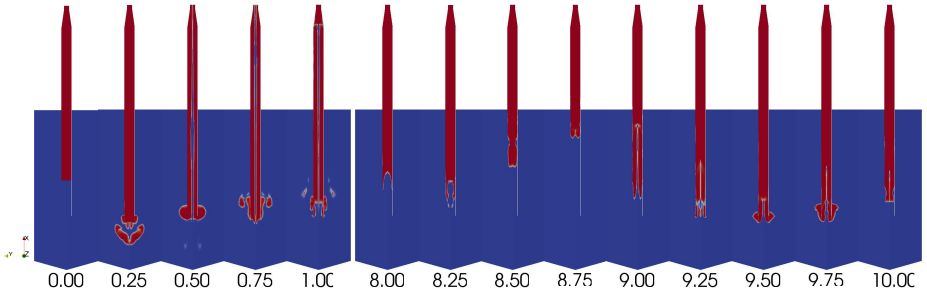

Figure 7.32. Volume fraction of steam during the first and last seconds of simulation in a 2D-axisymmetric NEPTUNE_CFD simulation of the STB-28-4 blowdown using Hughes-Duffey condensation model.

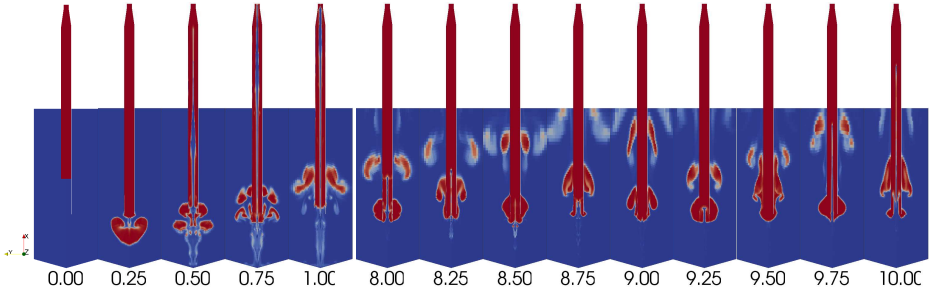

Figure 7.33. Volume fraction of steam during the first and last seconds of simulation in a 2D-axisymmetric NEPTUNE_CFD simulation of the STB-28-4 blowdown using Lakehal '08b condensation model.

It can be seen easily from Figures 7.32 and 7.33 that the DCC mass flow rate predictions of Hughes-Duffey and Lakehal '08b differ from each other remarkably also in high Reynolds number simulations. This time the Hughes-Duffey model provides realistic looking chugging phenomena, i.e. predicts the DCC rate near to the correct value. Lakehal '08b model instead underpredicts the DCC value significantly. Underprediction can be seen as large detaching slowly condensing bubbles, as constant presence of a bubble at the pipe exit and as minimal water penetration into the blowdown pipe. It seems that the Lakehal '08b model is more suitable for low-Re cases, while the models like Hughes-Duffey are more suitable for high-Re cases. Therefore the most STB-28 simulations in this study were conducted by using Hughes-Duffey or Coste-Laviéville models.

As the last qualitative property to be discussed, **the bubble and jet shapes** can be considered. A bubble in the STB-28-4 experiment and an example of a 3D bubble in a simulation with Hughes-Duffey DCC model are shown in Figures 7.34 and 7.35.

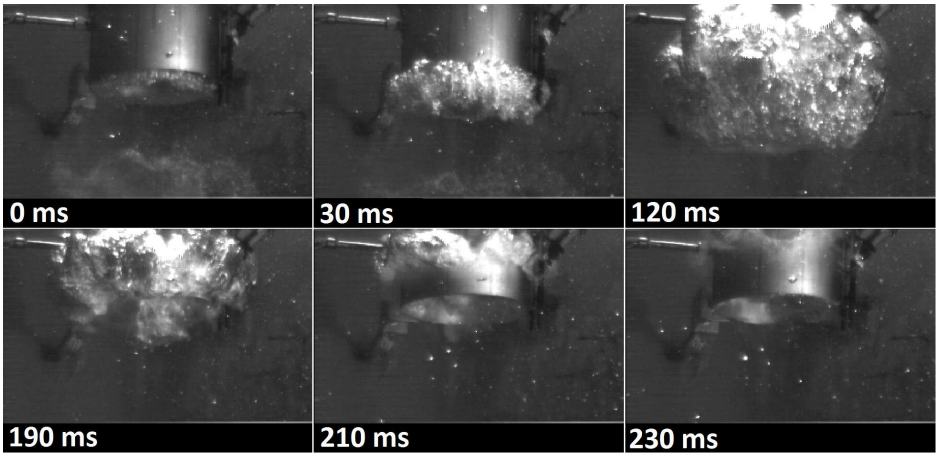

Figure 7.34. Inflation and collapse of a bubble during the STB-28-4 blowdown.

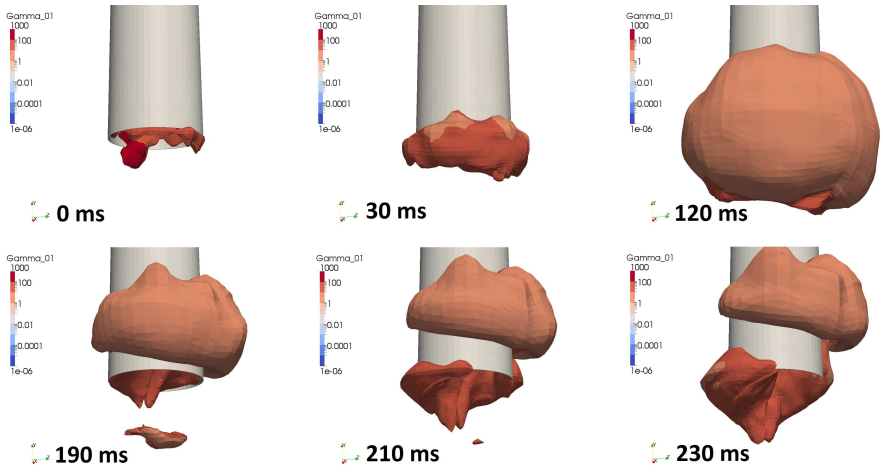

Figure 7.35. Inflation and collapse of a bubble in a 3D NEPTUNE_CFD simulation of the STB-28-4 blowdown. Hughes-Duffey condensation model, 'SIMMER' drag model.

Figure 7.35 shows that the condensation rate of the detaching bubble is quite realistic with the Hughes-Duffey DCC model. However, unlike in the example of the experiment, the total collapse of the steam/water interface into the blowdown pipe did not occur for that particular simulated bubble. Another example can be obtained from the simulation data as well. Figures 7.36 and 7.37 show a penetrating steam jet in the STB-28-4 experiment and in a simulation with Hughes-Duffey DCC model.

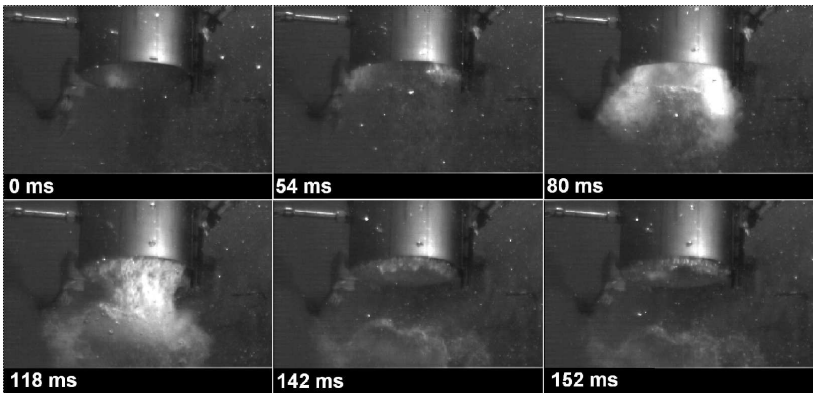

Figure 7.36. Penetration of a steam jet into the pool during the POOLEX STB-28-4 blowdown experiment.

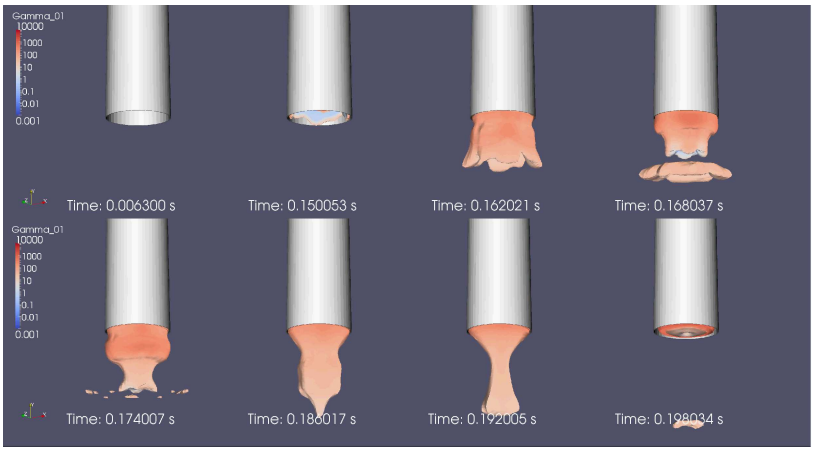

Figure 7.37. Penetration of the initial steam jet into the pool in a 3D NEPTUNE_CFD simulation of the STB-28 experiment. Hughes-Duffey DCC model.

In comparison to the experiment, it can be seen that there is an approximately $100\,\mathrm{ms}$ delay (error) in the arrival time of the jet, but the steam jet condenses away in the simulation circa $50\,\mathrm{ms}$ faster. Figure 7.38 presents the eruption and collapse of the first bubble after the jet is condensed.

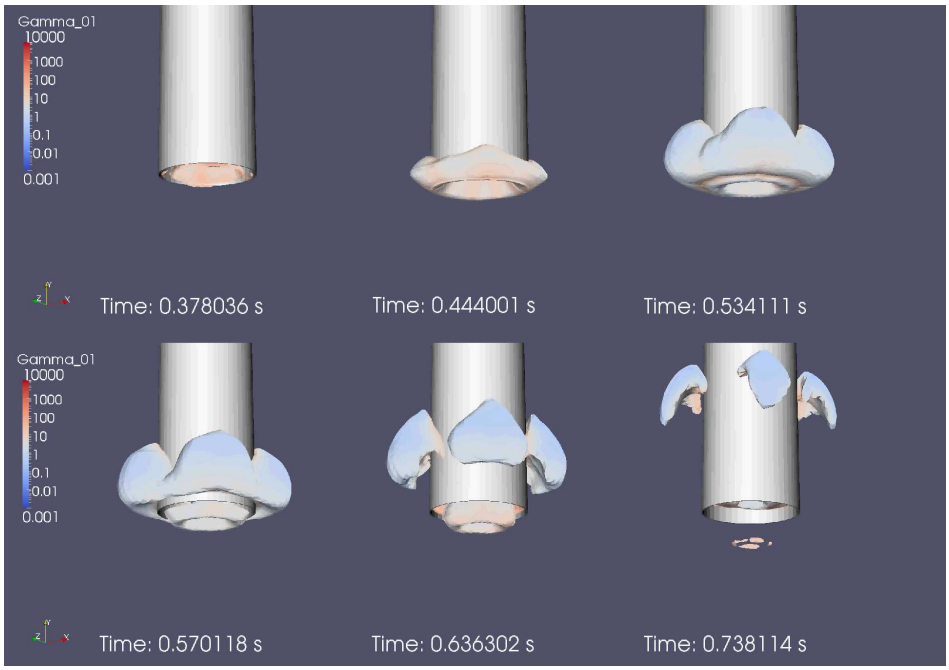

Figure 7.38. The first bubble and its collapse in a 3D NEPTUNE_CFD simulation of the STB-28 experiment. Hughes-Duffey DCC model.

When comparing Figure 7.38 of the first bubble to Figure 7.34 of the experiment, it can be seen that the bubble starts to form approximately $180\,\mathrm{ms}$ later than in the experiment and its lifetime is circa $130\,\mathrm{ms}$ longer than in the experiment. Figures 7.39 and 7.40 present the later bubbles in that simulation.

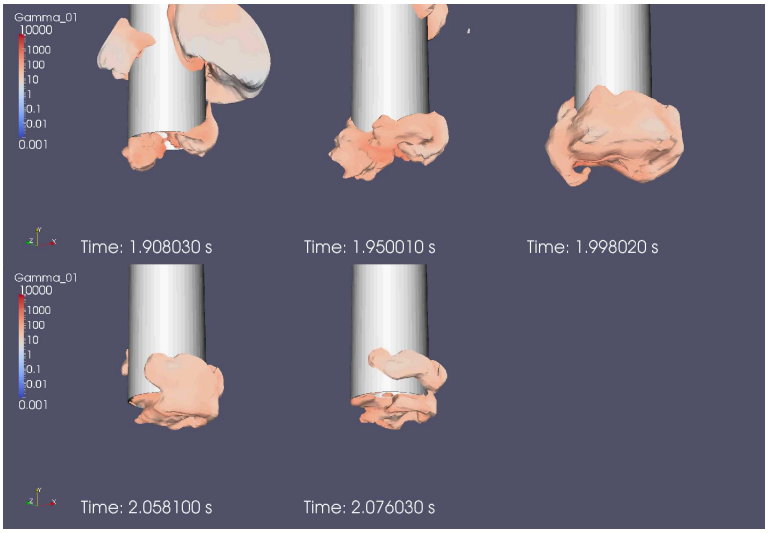

Figure 7.39. Late bubble (1) and its collapse in a 3D NEPTUNE_CFD simulation of the STB-28 experiment. Hughes-Duffey DCC model with the initial surface.

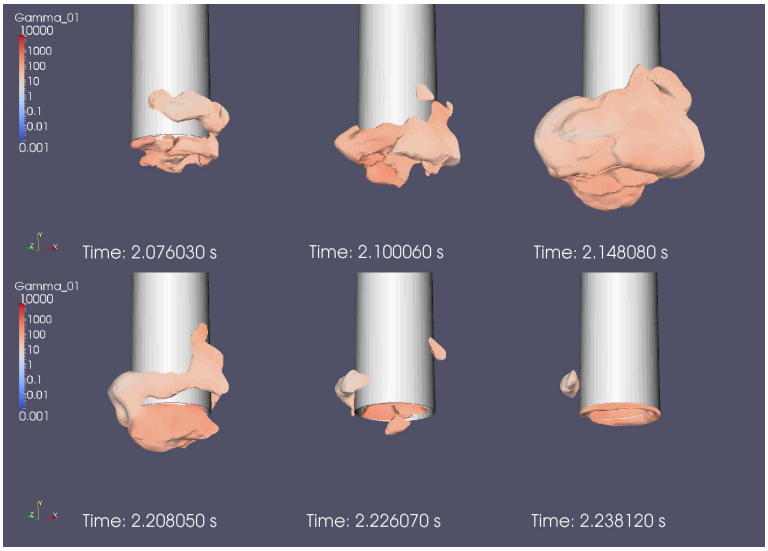

Figure 7.40. Late bubble (2) and its collapse in a 3D NEPTUNE_CFD simulation of the STB-28 experiment. Hughes-Duffey DCC model with the initial surface.

The behavior and type of bubbles in Figures 7.39 and 7.40 are somewhat different from those of the first bubble. Chugging is here faster, and the bubbles are not as symmetrically annular. The lifetime of the simulated bubbles is now $62 - 68\,\mathrm{ms}$ shorter than in the experiment, indicating that the Hughes-Duffey condensation model is capable of reaching the high condensation rates seen in the experiment.

In Table 7.1, the collapse times and bubble diameters for the abovementioned simulated bubbles are gathered. Also the collapse speed is calculated.

Table 7.1. Collapse times and diameters of the steam bubbles in a 3D NEPTUNE_CFD simulation of the STB-28 experiment. Hughes-Duffey DCC model with initial surface set inside the pipe.

Bubble	**Collapse time** $[\mathrm{ms}]$	**Bubble diameter** $[\mathrm{mm}]$	**Collapse speed** $[\mathrm{m/s}]$
First	215	375	0,9
Late 1	70	380	2,6
Late 2	85	450	2,7

The bubble diameters and collapse speeds are in a relatively good agreement with those derived from the experiment in Table 3.1.

Numerical results

By using pattern recognition, it was possible to obtain the distributions of bubble sizes from the experimental video clips and simulation volume fraction field results. Figure 7.41 shows the bubble size distribution in a $60\,\mathrm{s}$ long 2D-axisymmetric simulation case with the Hughes-Duffey DCC model and the 'SIMMER' drag model.

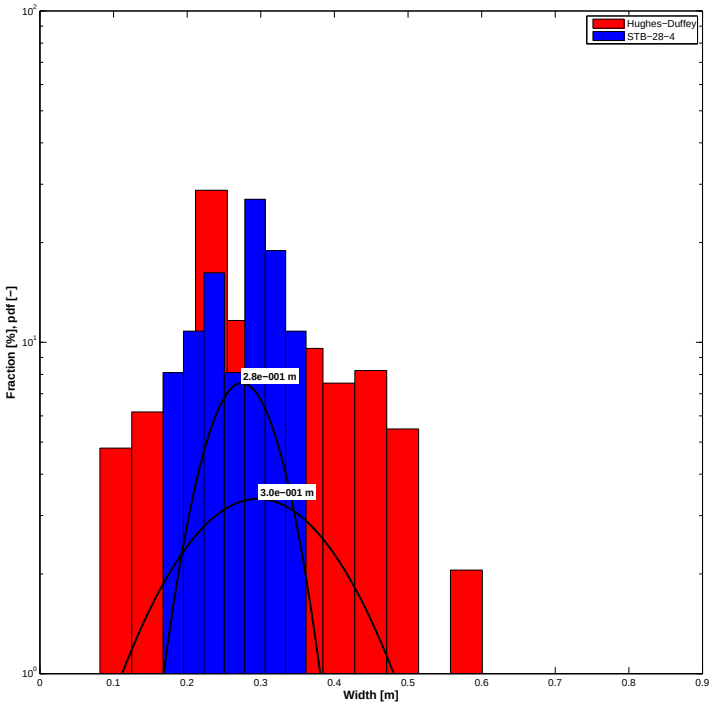

Figure 7.41. Bubble size distribution (maximum width) and the corresponding normal probability density function for the fully inflated ellipsoidal bubbles in the 2D-axisymmetric NEPTUNE_CFD simulation of the STB-28-4 experiment by using the Hughes-Duffey condensation model.

The maximum bubble width distribution of Figure 7.41 indicates that the bubble sizes are mostly in the correct range in the simulations. Despite this, there is still a large group of bubbles that are bigger than in the experiment. This basically indicates lower condensation rates than in the experiment. However, there is some uncertainty concerning the pattern recognition from the experimental video material. For example, the video material is only a 2-dimensional projection of the 3D bubbles, which may cause a certain number of miscalculated bubbles. That probably affects on the obtained distributions.

Figure 7.42 shows the bubble size distributions for the simulation with the Coste-Laviéville DCC model and the 'Large interface' drag model.

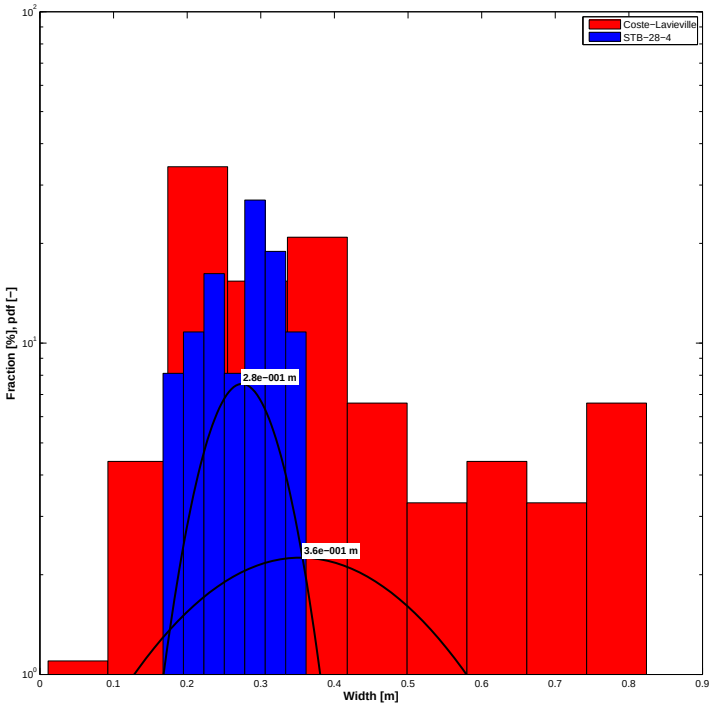

Figure 7.42. Bubble size distributions (maximum width) and the corresponding normal probability density function for the fully inflated ellipsoidal bubbles in the 2D-axisymmetric NEPTUNE_CFD simulation of the STB-28-4 experiment by using the Coste-Laviéville condensation model.

The maximum bubble width distribution of Figure 7.42 indicates that the bubble sizes are mostly in the correct range also in the simulations with the Coste-Laviéville model. Due to some very large bubbles, this result corresponds the distribution of the experimental video material slightly less than the one of the Hughes-Duffey DCC model.

Figure 7.43 shows the power spectrums from the FFT analysis of the bubble/jet $\sqrt{L_{\mathrm{Width}} L_{\mathrm{Height}}}$ in the simulations with the Hughes-Duffey and the Coste-Laviéville DCC models.

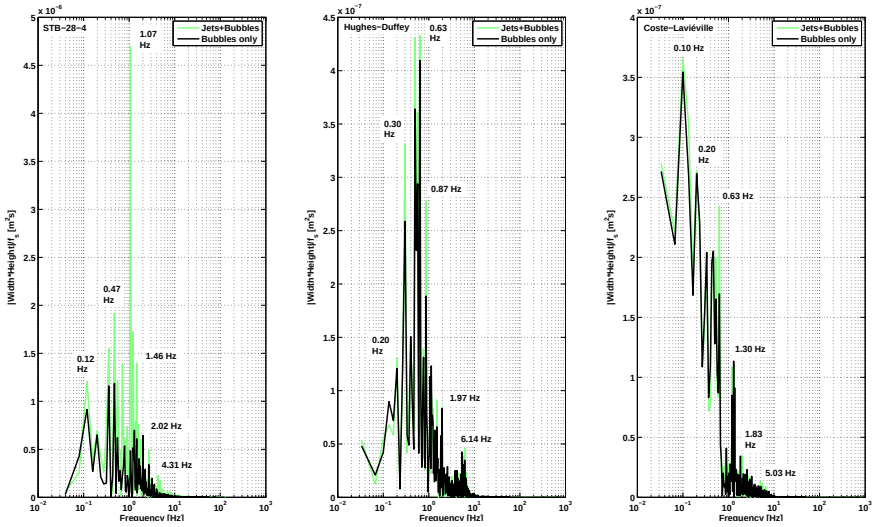

Figure 7.43. Power spectrums of the geometric mean of width and height $\sqrt{L_{\mathrm{Width}} L_{\mathrm{Height}}}$ of bubbles and jets in the 2D-axisymmetric NEPTUNE_CFD simulations of the STB-28-4 experiment by using the Hughes-Duffey and Coste-Laviéville condensation models.

As can be seen in Figure 7.43, the frequency of chugging at the exit of blowdown pipe is near the chugging rate of the experiment ($1\,\mathrm{Hz}$) in the case of the Hughes-Duffey model. In the Hughes-Duffey case, the frequency is slightly smaller than $1\,\mathrm{Hz}$ indicating a bit higher condensation rate (i.e interface often inside the blowdown pipe) than in the experiment. In the Coste-Laviéville case, the dominant chugging frequency is difficult to be marked out. There seems to be strong chugging around $0.1\,\mathrm{Hz}$, but there are also power peaks at $0.6\,\mathrm{Hz}$ and $1.3\,\mathrm{Hz}$. The low chugging frequencies could indicate very high condensation rates, but in this Coste-Laviéville case, it is not a likely explanation. The high powers at low frequencies seem to be caused instead by some very large, rarely occurring, and slowly condensing bubbles. The clear peak at $1.3\,\mathrm{Hz}$ is an indication of another chugging rate which is near the experimentally observed one. There is also a notable power peak at $6.1\,\mathrm{Hz}$ in the Hughes-Duffey case and a small peak at $5.03\,\mathrm{Hz}$ in the Coste-Laviéville case. An explanation for these frequencies can be obtained from Figure 7.44.

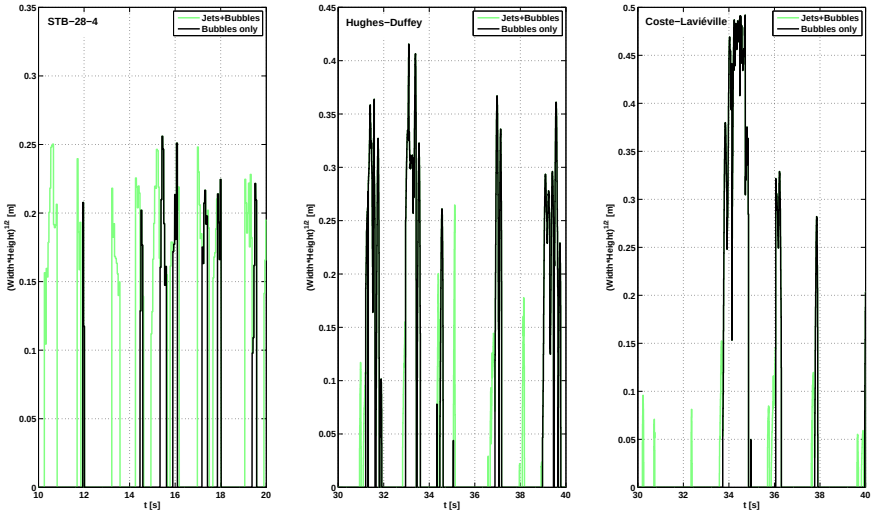

Figure 7.44. A sample of geometric mean of width and height $\sqrt{L_{\mathrm{Width}} L_{\mathrm{Height}}}$ data for bubbles and jets in the 2D-axisymmetric NEPTUNE_CFD simulations of the STB-28-4 blowdown experiment by using the Hughes-Duffey and Coste-Laviéville condensation models.

The sample of the bubble/jet data from the experiment show that the chugging cycle has a quite standard form: a jet appears first and it is often immediately followed by a bubble. The chugging cycles are not as uniform in the simulations; a small jet appears usually first and it is followed by a long-lived bubble or a series of successively appearing rapid bubbles. Although the frequency of the whole chugging cycle is near the experimental values, the flickering of long-lived or successive bubbles seems to occur at a higher frequency around $5\,\mathrm{Hz}$.

The condensation mass flow rates of the 2D-axisymmetric simulations with Hughes-Duffey and Coste-Laviéville DCC models are shown in Figure 7.45.

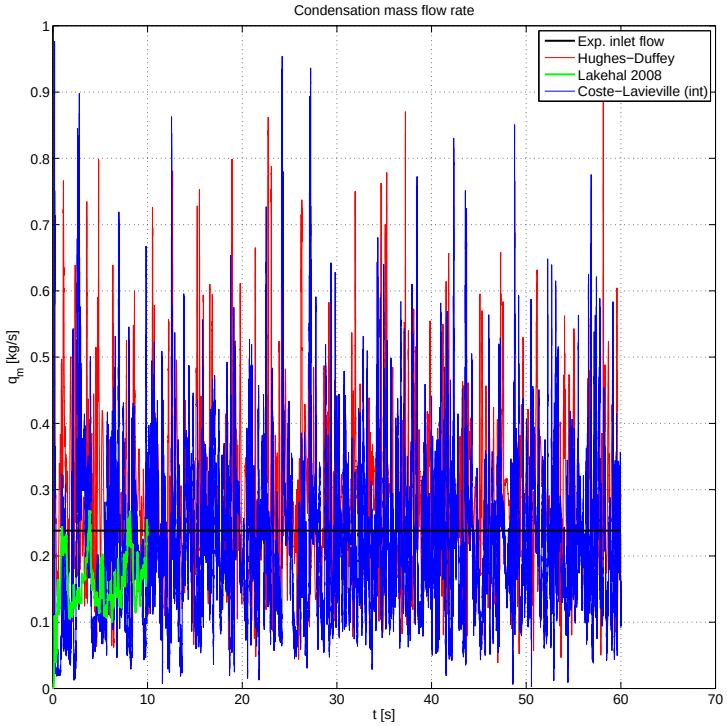

Figure 7.45. Condensation mass flow rate predictions of the Hughes-Duffey, Lakehal '08b, and Coste-Laviéville models. 2D-axisymmetric NEPTUNE_CFD simulations of the STB-28-4 experiment.

As can be seen in Figure 7.45, the Hughes-Duffey and Coste-Laviéville models predict quite similar DCC mass flow rates and are capable of condensating all the injected steam within the domain. Instead, the Lakehal '08b DCC model is not capable of condensing the steam within the domain. Figures 7.46 and 7.47 show the condensation mass fluxes and interfacial areas for these simulations.

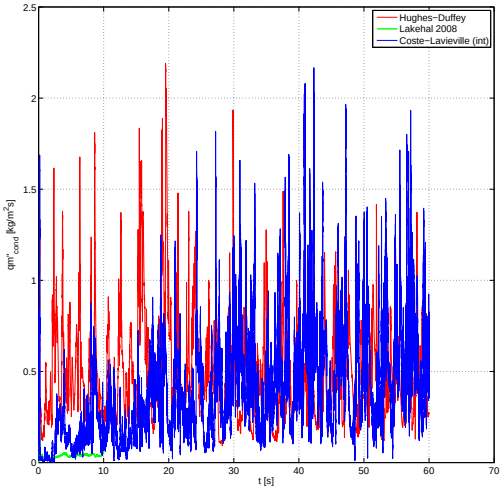

Figure 7.46. Condensation mass flux predictions of the Hughes-Duffey, Lakehal '08b, and Coste-Laviéville models. 2D-axisymmetric NEPTUNE_CFD simulations of the STB-28-4 experiment.

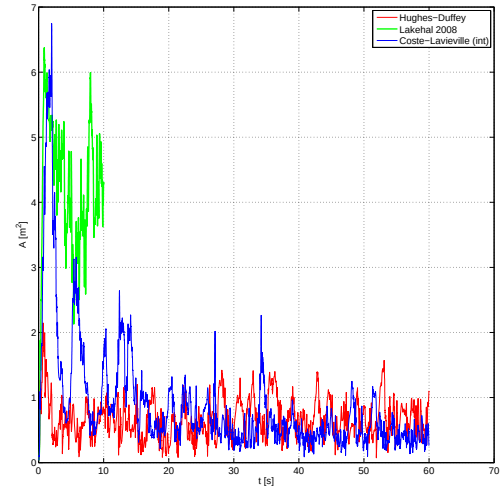

Figure 7.47. Total interfacial area in the simulations with Hughes-Duffey, Lakehal '08b, and Coste-Laviéville models. 2D-axisymmetric NEPTUNE_CFD simulations of the STB-28-4 experiment.

Figures 7.46 and 7.47 indicate the same as the qualitative observations and mass flow rates of Figure 7.45. The condensation rate of the Lakehal ’08b model is much smaller than the ones of the Hughes-Duffey and Coste-Laviéville models. This can be seen as an increased interfacial area. Figure 7.48 presents the HTCs for these cases.

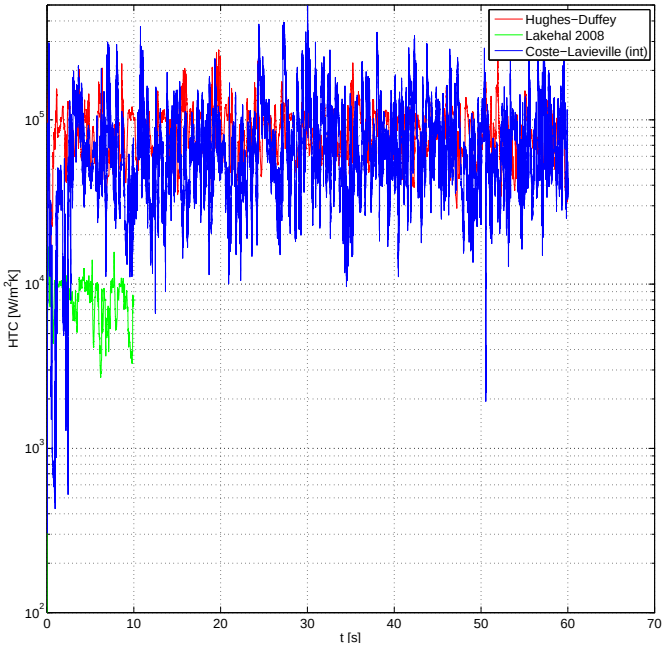

Figure 7.48. Average heat transfer coefficient of the Hughes-Duffey, Lakehal ’08b, and Coste-Laviéville models. 2D-axisymmetric NEPTUNE_CFD simulations of the STB-28-4 experiment.

There is an order of magnitude difference between the HTCs predicted by the DCC model of Lakehal ´08b and the models of Hughes-Duffey and Coste-Laviéville. The difference between the Lakehal ’08b model and the Hughes-Duffey model was similar also in the low-Re cases, i.e. in the STB-31 simulations. Concerning the Coste-Laviéville model, it seems to successfully select the different DCC correlations for the low-Re and high-Re condensation cases as it was meant to do. In the STB-31 case it, predicted low DCC rates (by choosing the Lakehal ’08 model), and in the STB-28 case, it predicted high DCC rates (by choosing the Coste ICMF ’04 model).

The pressure loads on the pool structures are an important parameter to be solved by the CFD and FSI simulations in the suppression pool cases. Some results of the pressure loads from the CFD simulations are presented next. For the 2D-axisymmetric simulation with the Hughes-Duffey DCC model, the pool bottom pressure below the blowdown pipe and the power spectrum of it are presented in Figure 7.49.

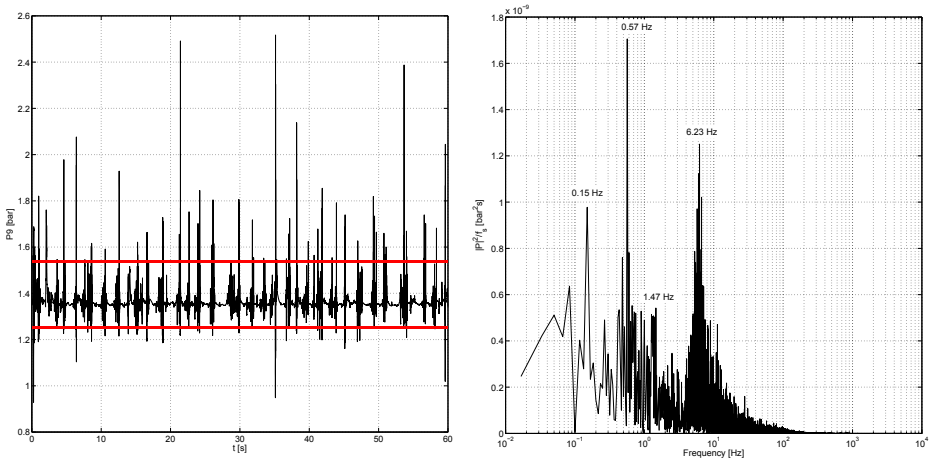

Figure 7.49. Pressure (P9) and the power spectrum of pressure pulse on the suppression pool bottom. The 2D-axisymmetric NEPTUNE_CFD simulation of the STB-28-4 experiment by using the Hughes-Duffey condensation model. The maximum pressure pulse level in the STB-28-4 experiment is marked with the red lines.

Figure 7.49 indicates that the amplitudes of the pressure pulses are clearly higher than in the experiment. This occurs probably due to many reasons. First of all, the simulation model assumes a rigid pool bottom, i.e. it does not absorb any portion of the pressure impulse. Secondly, the 2D-axisymmetric simulation geometry may enhance the pressure pulse due to the symmetric pool structures and symmetrically expanding and condensing bubbles. The Hughes-Duffey model seems to predict larger bubbles than seen in the experiment. Thus, thirdly, these larger bubbles probably lead also to larger pressure pulses if they appear to condense rapidly.

The power spectrum of the pressure signal of the Hughes-Duffey DCC model case corresponds well with the bubble/jet frequencies shown in Figure 7.43. The chugging frequency can probably be seen as a peak at $0.57\,\mathrm{Hz}$ and the bubble flickering can be seen at $6.23\,\mathrm{Hz}$, corresponding with the values of Figure 7.43.

For the 2D-axisymmetric simulation with the Lakehal '08b DCC model, the pool bottom pressure below the blowdown pipe and the power spectrum of it are presented in Figure 7.50.

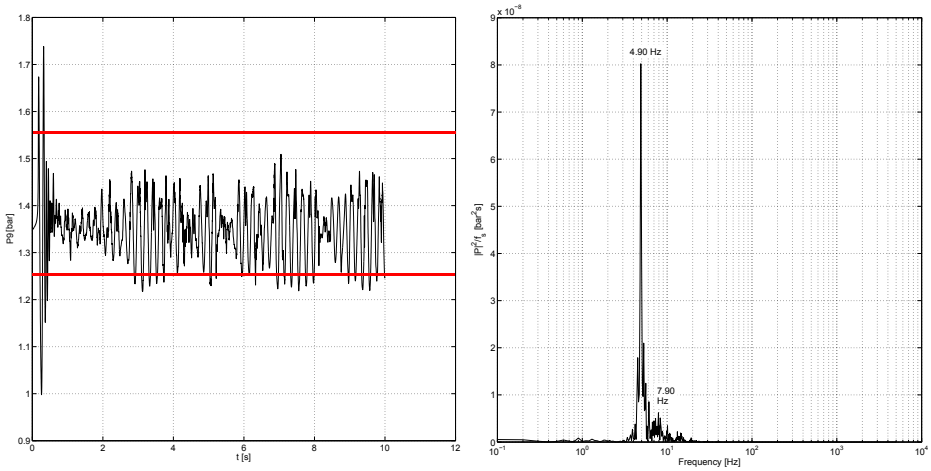

Figure 7.50. Pressure (P9) and the power spectrum of pressure pulse on the suppression pool bottom. The 2D-axisymmetric NEPTUNE_CFD simulation of the STB-28-4 experiment by using the Lakehal '08b condensation model. The maximum pressure pulse level in the STB-28-4 experiment is marked with the red lines.

Observable chugging did not occur in the STB-28 simulation cases in which the Lakehal '08b DCC model was used because the model underpredicted the condensation rate remarkably. That led to a constant presence of a flickering bubble at the mouth of the blowdown pipe. The pulsating motion of such bubbles is due to the fluid mechanical forces, i.e. buoyancy and drag forces, instead of the condensation induced collapses. This can be seen in the pressure results as a small amplitude fluctuation with the $4.9\,\mathrm{Hz}$ frequency which was also the frequency of the flickering bubbles at the pipe mouth in the Hughes-Duffey and Coste-Laviéville cases. This is an indication of that the frequency of approximately $5\,\mathrm{Hz}$ is an eigenfrequency of the non-condensing bubbling at the mouth of the blowdown pipe. Figure 7.51 shows the pressure results of the Coste-Laviéville DCC model.

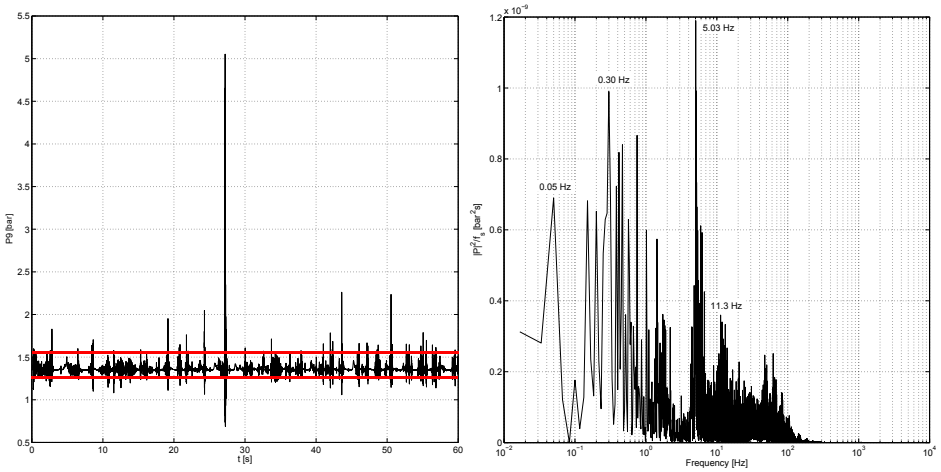

Figure 7.51. Pressure (P9) and the power spectrum of pressure pulse on the suppression pool bottom. The 2D-axisymmetric NEPTUNE_CFD simulation of the STB-28-4 experiment by using the Coste-Laviéville condensation model. The maximum pressure pulse level in the STB-28-4 experiment is marked with the red lines.

The Coste-Laviéville DCC model predicts fewer high pressure pulses on the pool bottom compared to the Hughes-Duffey model. Also the pressure signal seems to be more aperiodic as well, which can be seen as various peaks at low frequencies. These results correspond to the results from the pattern recognition process. It can be seen that a single exceptionally strong pressure peak is produced during the simulated period. It is a disputable result because such high bottom pressures seem to occur in the experiments typically only in the case of a water plug clearance at the beginning of the experiment (Laine and Puustinen, 2006b). The analysis of the field data of CFD indicates that this high pressure result is not due to a water plug. A collapse of a relatively small toroidal residual bubble causes this strong pressure pulse initiating in the vicinity of the blowdown pipe. An exceptionally high condensation rate cannot be seen in the CFD data at that point (e.g. in Figure 7.45). Therefore, it is possible that this occasional pressure pulse is only due to a recoverable numerical problem of the solver. In the STB-28 experiment, the highest peak was a $0.4\,\mathrm{bar}$ peak during the STB-28-7 phase which is far lower than the peak produced in the Coste-Laviéville simulation. Figure 7.52 shows the result of the pool bottom pressure in a short $8\,\mathrm{s}$ 3D simulation with the Hughes-Duffey DCC model.

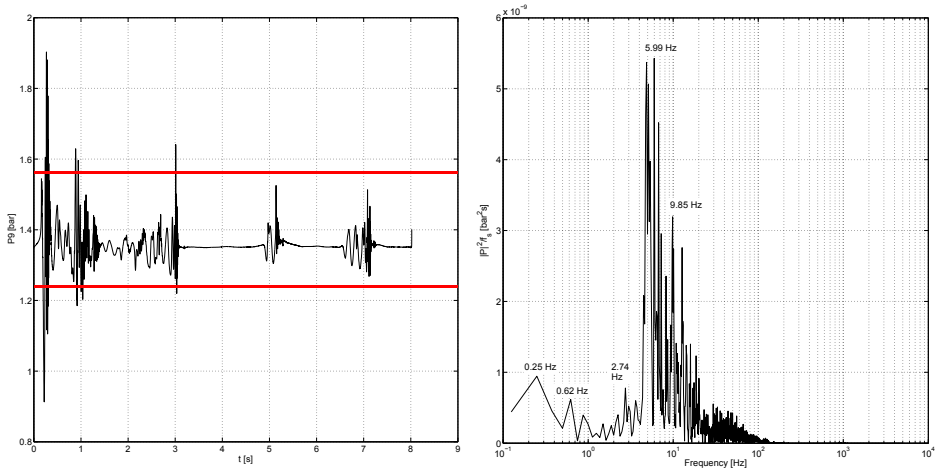

Figure 7.52. Pressure (P9) and the power spectrum of pressure pulse on the suppression pool bottom. A 3D NEPTUNE_CFD simulation of the STB-28-4 experiment by using the Hughes-Duffey condensation model. The maximum pressure pulse level in the STB-28-4 experiment is marked with red lines.

The pressure pulses that occurred in the 3D simulation seem to be smaller than the ones obtained in the 2D-axisymmetric simulations. Unfortunately, the simulated sample is much shorter, and this result is also biased by the initial transient towards the fully developed pool conditions. If the trend of the upcoming pressure pulses is the same as with the last two pressure pulses in the Figure 7.52, the 3D result is promising. The FFT analysis of the pressure signal in this 3D case is not sufficiently accurate because the length of the sample is short and the sample is affected by the initialization. The eigenfrequency of the flickering bubble can still be seen around $5\,\mathrm{Hz}$.

8 Stability, convergence and uncertainty of CFD simulations

The measurement inaccuracies and uncertainties due to non-measured quantities like non-condensable gases and wall condensation were discussed earlier in Chapters 3 to 6. The uncertainty and convergence of the CFD simulations is discussed briefly in this chapter. It should to be noticed that the simulations of this study are the first step in the application of separated flow DCC models in Eulerian suppression pool simulations, and a comprehensive sensitivity analysis work with various grids and parameters has not yet been carried out in this study.

STB-31 Simulations with interface tracking method of TransAT

A few simulations of the STB-31 case were run using DNS in TransAT, although in 2D axisymmetric geometry, however. To capture all the turbulence structures, i.e. eddies, the calculation grid has to be refined according to the Kolmogorov scales. The Kolmogorov scales for length, time, and velocity are defined as follows (Pope, 2009):

$$\eta \equiv \left(\frac{\nu^3}{\varepsilon}\right)^{1/4}, \tag{8.1}$$

$$\tau_\eta \equiv \left(\frac{\nu}{\varepsilon}\right)^{1/2}, \tag{8.2}$$

$$u_\eta \equiv (\nu\varepsilon)^{1/4}, \tag{8.3}$$

where η, τ_η, and u_η are the Kolmogorov scales for length, time, and velocity, respectively. The most important of these are the length and time scales because they define the grid size and time-step length. For the TransAT simulations, these parameters were estimated with the help of the best NEPTUNE_CFD simulation, i.e. the STB-31 simulation with the Lakehal et al. 2008b DCC model. The dissipation of the turbulence was recorded at four points near the phase interface, as shown in Figure 8.1.

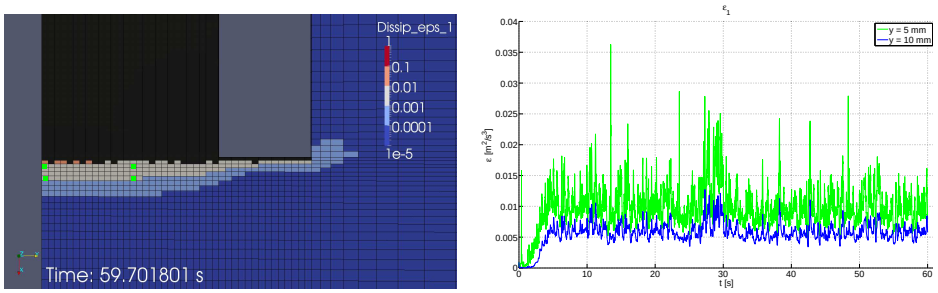

Figure 8.1. Dissipation of the turbulence near the steam/water interface in a 2D-axisymmetric NEPTUNE_CFD simulation of the STB-31 experiment. The Lakehal et al. 2008b condensation model used. Probe locations marked with green dots.

With the dissipation rate known, it is possible to calculate the Kolmogorov scales. The Kolmogorov scale for length is presented in Figure 8.2.

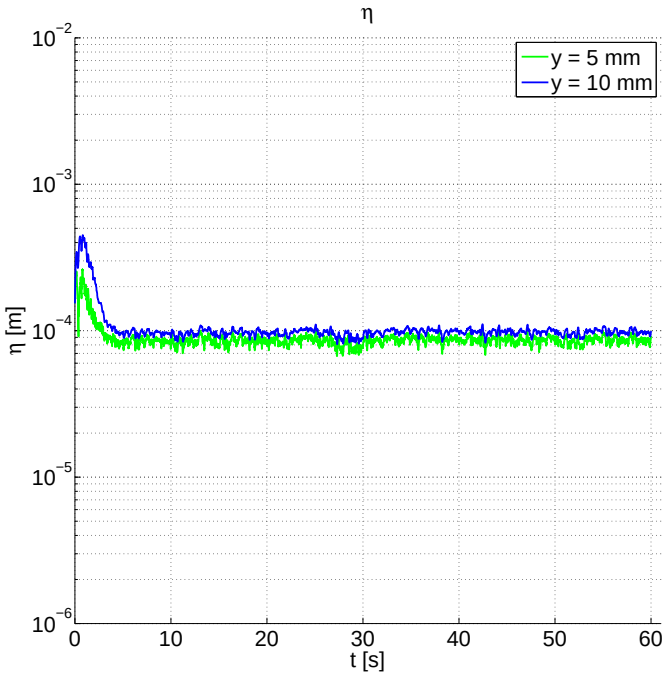

Figure 8.2. Kolmogorov scale for length near the steam/water interface in a 2D-axisymmetric NEPTUNE_CFD simulation of the STB-31 experiment. The Lakehal et al. 2008b condensation model used.

As can be seen in Figure 8.2, the Kolmogorov scale in the quasi-steady state of the STB-31 simulation is approximately $100\,\mu\mathrm{m}$, which indicates that the TransAT simulations with the denser circa $40\,\mu\mathrm{m}$ and circa $10\,\mu\mathrm{m}$ grids are feasible because in those cases, there are enough cells per eddy to capture its shape. The Kolmogorov scales for time and velocity are presented in Figure 8.3.

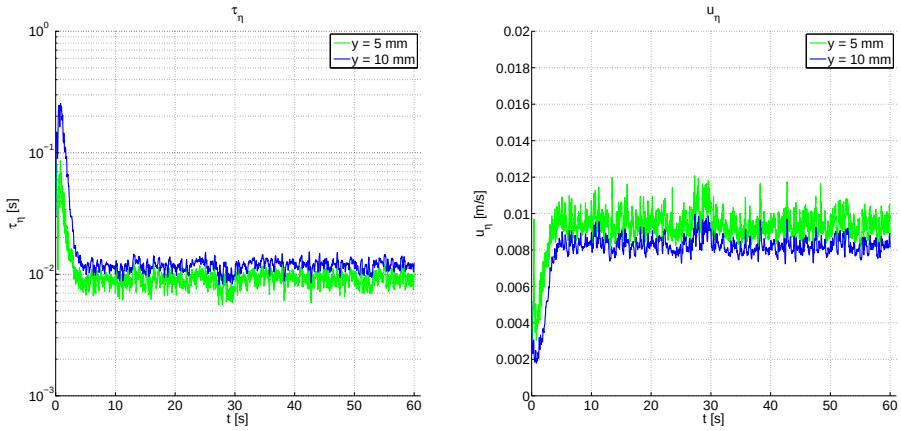

Figure 8.3. Kolmogorov scales for time and velocity near the steam/water interface in a 2D-axisymmetric NEPTUNE_CFD simulation of the STB-31 experiment. The Lakehal et al. 2008b condensation model used.

Figure 8.3 shows that the Kolmogorov time scale in the quasi-steady state of the STB-31 simulation is approximately $10\,000\,\mu\mathrm{s}$, which is much higher than the approximately 1–$5\,\mu\mathrm{s}$ time step used in the 2D-axisymmetric CFD simulations with TransAT. Thus, the time stepping in TransAT has also been valid in the sense of the Kolmogorov scales. The reason why the results of the DCC rate still change when refining the grid from circa SI40$\mu\mathrm{m}$ to circa $10\,\mu\mathrm{m}$ is probably the solution of the diffusive (viscous) sub-layer. The thickness of that layer can be very small, like $10\,\mathrm{nm}$, and the solution of the temperature gradient across it may require a higher grid resolution (Lakehal and Labois, 2011).

Figures 8.4 and 8.5 show examples of the residuals and Courant (CFL) numbers in the DNS simulations with TransAT.

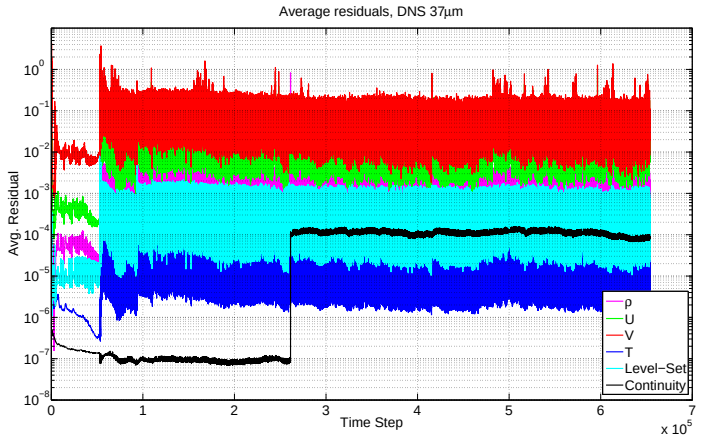

Figure 8.4. Residuals in a 2D-axisymmetric TransAT simulation of the STB-31 experiment. A DNS case with the $37\,\mu\mathrm{m}$ grid resolution.

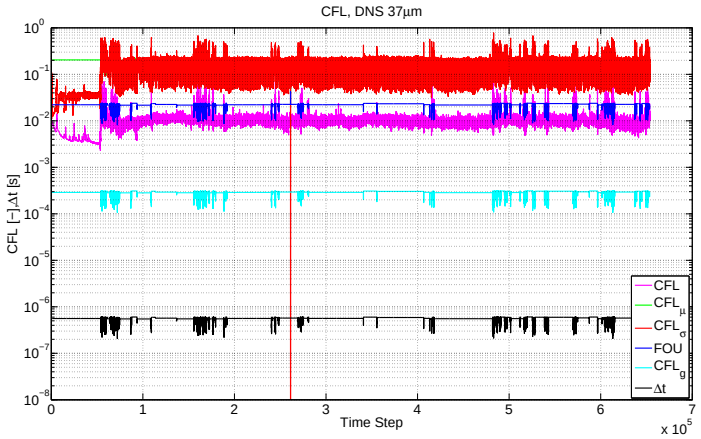

Figure 8.5. Courant numbers in a 2D-axisymmetric TransAT simulation of the STB-31 experiment. A DNS case with the $37\,\mu\mathrm{m}$ grid resolution.

As can be seen in Figures 8.4 and 8.5, the residuals are small and the CFL criteria are generally below 0.3 which is recommended for the explicit solver of TransAT. Tangential velocity residual 'V' is higher than the other residuals, which is caused by the coarser grid resolution in that direction. Figure 8.6 presents the mass (or volume) conservation information of this example simulation with the $37\,\mu\mathrm{m}$ grid resolution.

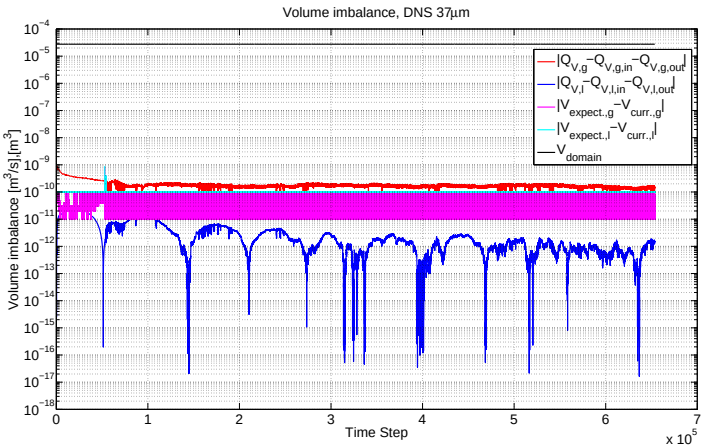

Figure 8.6. Mass balance in a 2D-axisymmetric TransAT simulation of the STB-31 experiment. A DNS case with the 37 µm grid resolution.

According to Figure 8.6, the mass balance is satisfied in this DNS simulation with dense grid. Although the Level Set method does not generally conserve mass accurately, the mass accuracy in this particular case is good. The other TransAT simulations with the explicit solver indicate similar results. Examples of the residuals and Courant criteria in TransAT RANS simulations are shown in Figures 8.7 and 8.8.

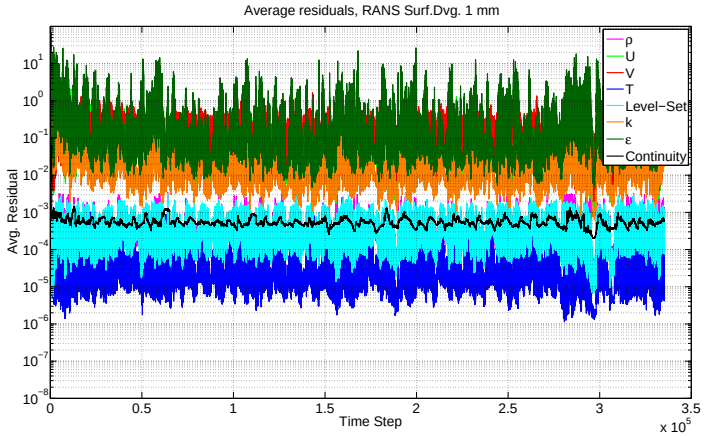

Figure 8.7. Residuals in a 2D-axisymmetric TransAT simulation of the STB-31 experiment. A URANS case with the 1 mm grid resolution and Lakehal '08b DCC model.

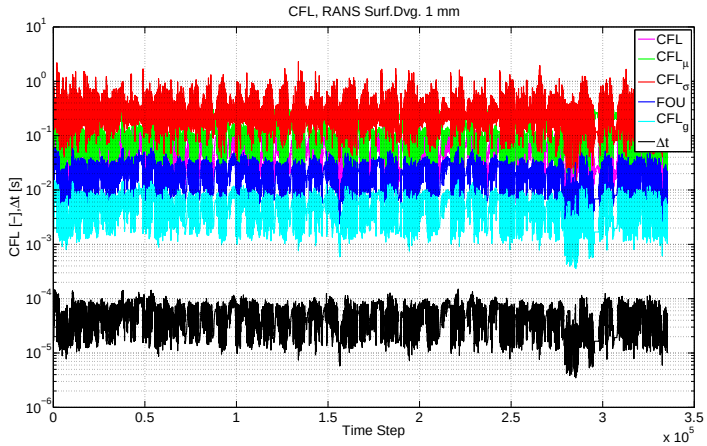

Figure 8.8. Courant numbers in a 2D-axisymmetric TransAT simulation of the STB-31 experiment. A URANS case with the $1\,\mathrm{mm}$ grid resolution and Lakehal '08b DCC model.

As can be seen in Figures 8.7 and 8.8, the residuals are small and the CFL criteria are generally below unity which is a good value for the implicit solver. It is not recommended to exceed $CFL_\sigma = 1$ for the surface tension. Thus, the CFL_σ criterion is maintained near unity. It can be seen that this criterion controls the time-stepping in this URANS case because the other CFLs are small compared to it. Figure 8.9 presents the mass (or volume) conservation information of this example of the URANS simulation.

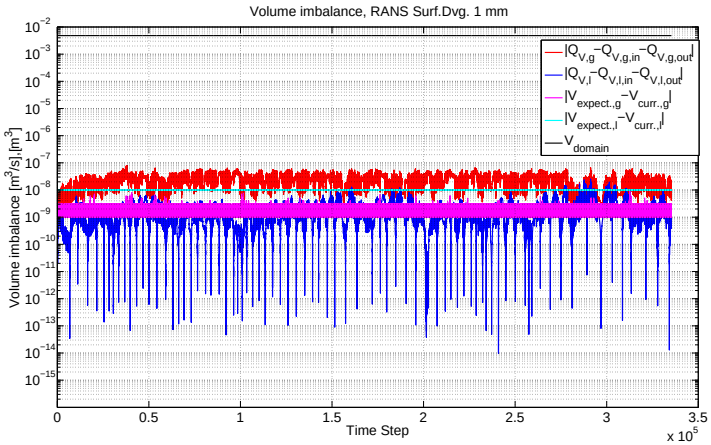

Figure 8.9. Mass balance in a 2D-axisymmetric TransAT simulation of the STB-31 experiment. A URANS case with the $1\,\mathrm{mm}$ grid resolution and Lakehal '08b DCC model.

Also in this TransAT URANS case, the mass conservation was satisfied.

STB-31 Simulations with Eulerian two-phase solver of NEPTUNE_CFD

Figure 8.10 shows examples of the volume fraction residuals and mass and energy imbalances in the two-phase simulations of the STB-31 experiment with NEPTUNE_CFD.

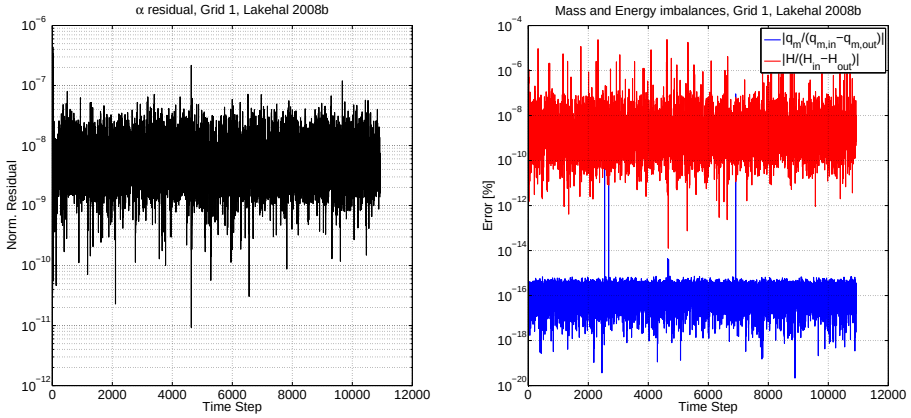

Figure 8.10. Volume fraction residual and mass and energy imbalance in a 2D-axisymmetric NEPTUNE_CFD simulation of the STB-31 experiment. The Lakehal et al. 2008b condensation model used.

As can be seen in Figure 8.10, the mass error is small in the NEPTUNE_CFD simulation. Figures 8.11 and 8.12 present the CFL numbers for this NEPTUNE_CFD simulation of the STB-31 experiment.

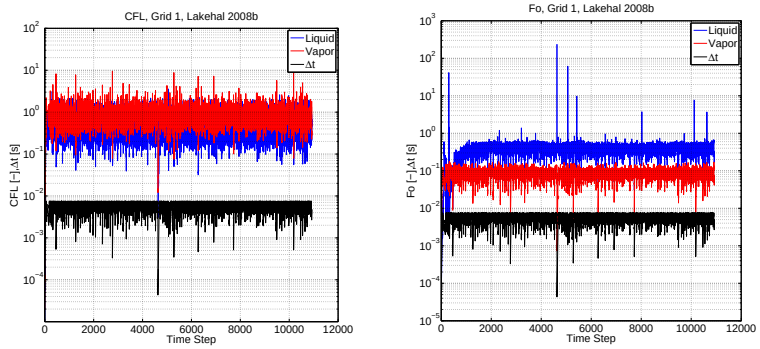

Figure 8.11. Courant and Fourier numbers in a 2D-axisymmetric NEPTUNE_CFD simulation of the STB-31 experiment. The Lakehal et al. 2008b condensation model used.

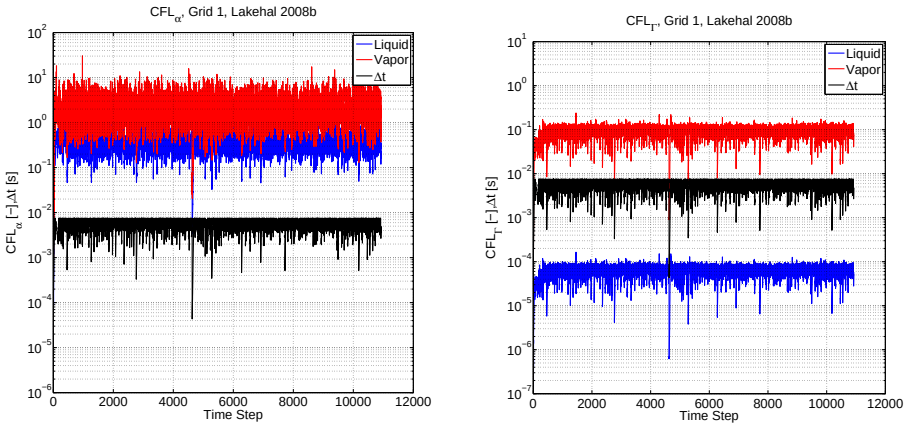

Figure 8.12. Courant (volume fraction and mass transfer) numbers in a 2D-axisymmetric NEPTUNE_CFD simulation of the STB-31 experiment. The Lakehal et al. 2008b condensation model used.

It can be seen from Figures 8.11 and 8.12 that the CFL values are in all cases below or around unity, as they should be.

STB-28 Simulations with Eulerian two-phase solver of NEPTUNE_CFD

Figure 8.13 shows examples of the residuals in the two-phase simulations of STB-28 experiment with NEPTUNE_CFD.

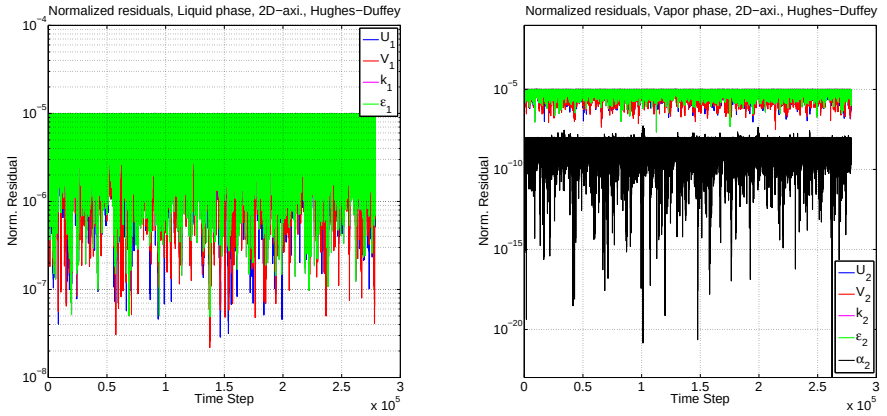

Figure 8.13. Normalized residuals in a 2D-axisymmetric NEPTUNE_CFD simulation of the STB-28 experiment. The Hughes-Duffey condensation model used.

As can be seen in Figure 8.13, the residuals seem to be small in this NEPTUNE_CFD simulation. Although it is not clear to analyse the convergence from these residuals, it is

quite clear that the simulation converges quite much from the initial state during a time-step. Figures 8.14 and 8.15 present the CFL numbers for this NEPTUNE_CFD simulation of the STB-28 experiment.

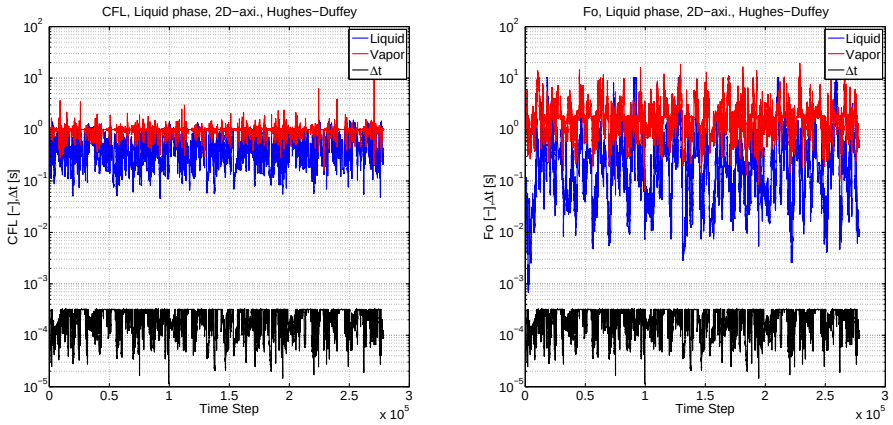

Figure 8.14. Courant and Fourier numbers in a 2D-axisymmetric NEPTUNE_CFD simulation of the STB-28 experiment. The Hughes-Duffey condensation model used.

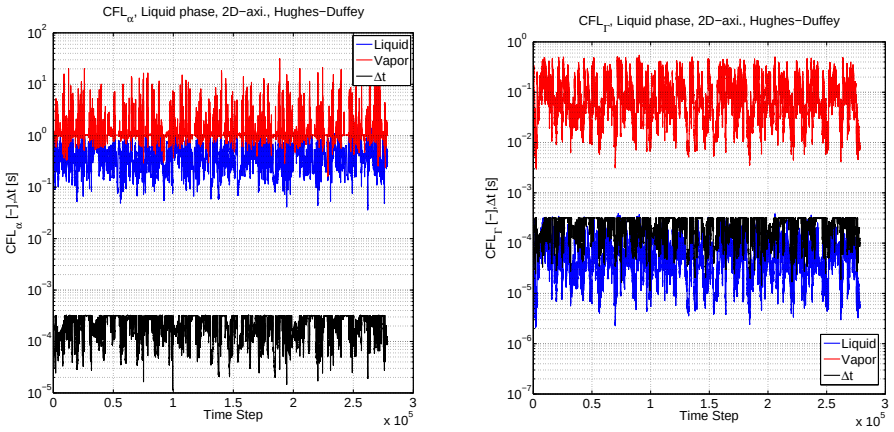

Figure 8.15. Courant (volume fraction and mass transfer) numbers in a 2D-axisymmetric NEPTUNE_CFD simulation of the STB-28 experiment. The Hughes-Duffey condensation model used.

It can be seen from Figures 8.14 and 8.15 that the CFL values are in all cases quite well below or around unity, as they should be. However, the vapor-side CFL_α criterion is near 10 occasionally. The rapid condensation is probably the reason for such high values for the volume fraction transportation. It does not seem to cause significant problems for the convergence and stability. That can be anticipated because the implicit solvers

are not very sensitive to high Courant numbers. Figure 8.16 shows the mass and energy imbalance in this chugging simulation.

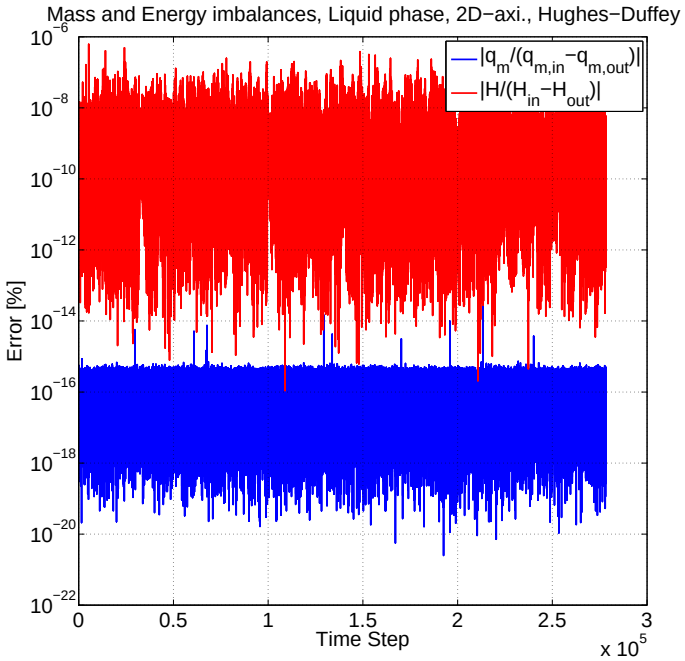

Figure 8.16. Mass and energy imbalance in a 2D-axisymmetric NEPTUNE_CFD simulation of the STB-28 experiment. The Hughes-Duffey condensation model used.

It can be seen in Figure 8.16, that the mass error is still small in this NEPTUNE_CFD simulation, despite the vigorous chugging that may cause challenges for the mass conservation.

9 Conclusions

The condensation rate has to be high in the safety pressure suppression pool systems of Boiling Water Reactors (BWR) in order to fulfill their safety function. Thus, the direct contact condensation phenomena turn out to be very challenging to be analysed in the suppression pool context either with experiments or numerical simulations. As to the experiments, the condensation induced pressure oscillations are often unfavourably violent for the delicate measurement instrumentation. As to the numerical (CFD) simulations, the pressure oscillations are violent for the pressure-velocity coupling algorithms of the CFD solvers. In this thesis, efforts have been made to increase the capability of Computational Fluid Dynamics (CFD) codes to successfully model and predict the rapid Direct Contact Condensation (DCC) in the BWR pressure suppression pools.

In this thesis, two of the condensation modes in the suppression pools were modelled by using the 2-phase CFD codes NEPTUNE_CFD and TransAT. The direct contact condensation models applied in this study were mostly the same as the ones that are currently being validated for Pressurized Thermal Shock (PTS) cases in the NURISP EU-project. These DCC models are typically used for separated flows, e.g. horizontal channel flow, and their applicability to the rapidly condensing flow in the condensation pool context had not been tested yet. The author tested some of these models in this study and participated into the development work of them. For example, the Coste and Laviéville (2009) model has been supported by the results of Tanskanen et al. (2008a).

Concerning the condensation modes in the suppression pools, a low Reynolds number case was considered first. The POOLEX experiment STB-31 was carried out in the conditions where the steam/water interface was flat and positioned quasi-steadily at the outlet of the blowdown pipe. Such a situation is a special case between the 'quasi-steady oscillatory interface condensation' mode and the 'condensation within the blowdown pipe' mode. As the experimental result was assumed to be affected by the non-condensable gases, the effect of them was estimated by using the Couette flow film model of Ghiaasiaan (2008). The effect of non-condensable gases was estimated small, although the uncertainty of the estimation remained high. The blowdown pipe was thermally insulated, and therefore the effect of the wall condensation was negligible during the experiment.

Simulations of the STB-31 case were conducted with various separated flow DCC models. It was found out in the NEPTUNE_CFD simulations that the condensation models of Lakehal et al. (2008b) and Coste and Laviéville (2009) predict the condensation rate quite accurately, while the other ones, like Hughes and Duffey (1991) and Coste (2004), overestimate it strongly. The TransAT simulations confirmed the NEPTUNE_CFD result of the Lakehal et al. (2008b) model and showed that the model of Banerjee et al. (1968) gives similar results. It was found out that the direct phase change solution and the surface renewal model of Lakehal et al. (2008a) need a very high grid resolution $(10 - 30\,\mu\mathrm{m})$ to correctly predict the condensation rate. However, they converged near to the measured values if the grid resolution was high enough. Such a convergence of the direct phase

change solution can be considered as partial validation of the STB-31 mass flow rate measurements and the applicability of the Lakehal et al. (2008a,b) models for that case.

The results obtained from these low-Reynolds number STB-31 simulations are in a good agreement with the results of the validation work in the PTS context; the Lakehal et al. (2008b) model gave better results in the low Reynolds number cases than the other ones (Coste and Laviéville, 2009). Also the result of the direct phase change solution was strongly dependent on the mesh refinement as assumed (Wu et al., 2007a). Concerning the low-Reynolds number cases in the suppression pool context, Thiele (2010) obtained results which are quite close to the low-Re results of the author.

After the promising results from the low-Reynolds number case, a high Reynolds number case corresponding the chugging condensation mode was considered. For that purpose, the earlier POOLEX experiment STB-28 was chosen as the reference. The STB-28 experiment was operated in the chugging mode, and during it, various standard and high-speed video samples of bubbles were recorded at different condensation pool temperatures. Because the pipe wall was not insulated as in the STB-31 case, the estimations of the wall condensation rates were calculated. The CFD simulations were conducted by using adiabatic boundary conditions for the pipe walls and taking the estimated wall condensation into account in the inlet mass flow rates. The effect of non-condensable gases was considered negligible in the STB-28 case.

In order to extract numerical information from the video material of the STB-28 experiment, a pattern recognition procedure was programmed in the MATLAB software environment. The bubble size distributions and the frequencies of chugging bubbles and jets were calculated with this procedure. As far as the author knows, this kind of a systematic recognition procedure has not been applied to the large bubble and jets in suppression pool cases elsewhere. Otherwise, the popularity of pattern recognition is increasing in the two phase flow analysis (Levy et al., 1992; Liebenberg et al., 2005). Despite its coarse and relatively simple nature, this procedure was a useful advancement in the analysis of the experimental chugging data. Due to its semi-automatic nature, it was possible to obtain statistical data of the bubble sizes and temporal data of the bubble/jet presence at the mouth of the blowdown pipe. With such data, it was possible to form quantitative data sets that could be compared to the corresponding CFD simulation data. This kind of a pattern recognition approach shall be an attractive option in the studies of chugging also in near future because the intrusive 2D measurement (e.g mesh sensors) are usually threatened by the water hammers, and the non-intrusive ones (e.g. tomography) turn out to be still too expensive or impractical.

The initial cartesian grid chugging simulations of the STB-28 case proved to be challenging (Tanskanen and Jordan, 2009). During this study, it was found out that a spherically curvilinear calculation grid at the exit region of the blowdown pipe improves the convergence. It decreases also the required cell count without increasing the diffusion of the interface. It was also found out that the initial level of the steam/water interface is an important factor for the initiation of chugging. If the interface was initialized to a level

high enough inside the pipe, the vigorous penetration of it into the pool water created a turbulent wake which invoked the chugging due to the improved heat transfer rate. The initiated chugging state seemed then to be self sustaining, as the mixed wake was renewed regularly by a new chugging jet. The renewal occurred often well before the turbulent kinetic energy of the previous jet was significantly dissipated.

Simulations of the STB-28 case were conducted with the separated flow DCC models of Hughes and Duffey (1991), Coste and Laviéville (2009), and Lakehal et al. (2008b) by using the Eulerian-Eulerian two-phase solver NEPTUNE_CFD. It was found out that the Hughes and Duffey (1991) model, and to some extent the Coste and Laviéville (2009) model, produced realistic chugging behavior, whereas the Lakehal et al. (2008b) model underpredicted the condensation rate by the amount that prevented the chugging to occur. The pressure loads on the pool bottom were found out to be overestimated in the 2D-axisymmetric simulations, but a 3D simulation provided quite promising results. In general, the 3D simulations with the suitable DCC models produced qualitatively very realistic shapes of the chugging bubbles and jets. It was found out that the comparative FFT analysis of the bubble size data (i.e. chugging data) and the pool bottom pressure signal can be a useful tool if one wishes to distinguish the eigenmodes of chugging, bubbling, and pool structure oscillations.

As far as the author knows, the chugging simulations by other authors are sparse, but not non-existent. Many of the studies by the other authors employ the interface tracking methods (VOF, Level Set) instead of the Eulerian-Eulerian set-up (e.g. Thiele (2010) and Yadigaroglu and Lakehal (2003)). It has been characteristic for many VOF studies, that the energy equation and the variable material properties were not available. For an example, Thiele (2010) tried to simulate a high velocity blowdown case with the flat plate condensation correlation with which he obtained the condensation rates that were approximately $35\,\%$ of the inlet mass flow rate. It is a significant underestimation, but taking into account the models used, it is not a poor result. A few authors have employed the Eulerian-Eulerian methodology as well (e.g. Pättikangas et al. (2011)) with moderate success. It is characteristic for the most of the studies, that the condensation rates were underestimated and aggressive chugging did not appear. One reason for this can be that the DCC models which would predict a high enough DCC rate are hard on the incompressible flow solvers even in the low-Re simulations. The author found out that the compressible flow solver with complete steam-tables (CATHARE steam tables in NEPTUNE_CFD) is beneficial for the numerical success of the chugging simulations.

Concerning the future work, development is needed both in the experimental field and in the modelling field. Concerning the experimental set-ups, Particle Image Velocimetry (PIV) and multiple high-speed video cameras would be useful measurement instruments. With PIV, a velocity field near the stable enough interface or in the bulk fluid near the bubbles could be solved. Such information would be useful for the model development work. With the multiple (2-3) high-speed video cameras, it would be possible to create a proper 3D representation of the steam bubbles and jets by using pattern recognition

methods. The accurate bubble dimension information could be compared to the corresponding volume fraction field data from the simulations. Concerning the modelling and also the experimental work, the interfacial area calculation for the Eulerian 2-phase flow modelling purposes should be developed further. When the two-phase flows and their challenging and vigorous condensation phenomena can be modelled with sufficient accuracy, also the Fluid Structure Interaction (FSI) modelling would be capable of solving the containment loads accurately without the need for over-conservative models.

It has long been a trend to increase the accuracy of modelling with the use of the best-estimate codes because the conservatism of the simpler models is ambiguous in complicated nuclear safety related cases (Wickett et al., 1998a,b). Due to that, e.g. the Radiation and Nuclear Safety Authority of Finland (STUK) requires that the best available modelling knowledge should be used in order to obtain results that are at the same time realistic and conservative. The use of the best-estimate software like the CFD codes is important in achieving accurate and reliable results required by the tightening safety criteria of the use of nuclear power. Due to the efforts done in this thesis, the two-phase CFD modelling of complex and numerically challenging phase change phenomena has taken a step forward to produce realistic results.

References

Ascomp (2011). *TransAT Handbook Series: Multiphase Flow Modelling*. Ascomp GmbH. Version 2.4.2, 2011.

Aust, E., Schultheiss, G.F., Seeliger, D., and McCauley, E.W. (1983). Experimental results about dynamic load mitigation for BWR-pressure suppression containments under LOCA-conditions. In: *7th Intern. Conf. on SMiRT, Chicago, Illinois*.

Aust, E. and Seeliger, D. (1982). Pool dynamics and dynamic loads in pressure suppression containment systems. *Transactions of the American Nuclear Society*, 41, pp. 696–699.

Banerjee, S. (1978). A Surface Renewal Model for Interfacial Heat and Mass Transfer in Transient Two-Phase Flow. *International Journal of Multiphase Flow*, 4, pp. 571–573.

Banerjee, S. (1990). Turbulence structure and transport mechanisms at interfaces. In: *9th International Heat Transfer Conference, Keynote Lectures*.

Banerjee, S., Lakehal, D., and Fulgosi, M. (2004). Surface Divergence Models for scalar exchange between Turbulent Streams. *International Journal of Multiphase Flow*, 30((7/8)), pp. 963–977.

Banerjee, S., Rhodes, S., and Scott, D. (1968). Mass transfer through falling wavy liquid films in turbulent flows. *Industrial & Engineering Chemistry of Fundamentals*, 7, p. 22.

Bejan, A. (1995). *Convection Heat Transfer*, 2nd edn. John Wiley & Sons, Inc. ISBN 9780471579724.

Brocchini, M. and Peregrine, D.H. (2001a). The dynamics of strong turbulence at free surfaces. Part 1. Description. *Journal of Fluid Mechanics*, 449, pp. 225–254.

Brocchini, M. and Peregrine, D.H. (2001b). The dynamics of strong turbulence at free surfaces. Part 2. Free-surface boundary conditions. *Journal of Fluid Mechanics*, 449, pp. 255–290.

Brumley, B. and Jirka, G. (1987). Near surface turbulence in a grid-stirred tank. *Journal of Fluid Mechanics*, 183, pp. 235–263.

Chan, C. and Lee, C. (1982). A regime map for direct contact condensation. *International Journal of Multiphase Flow*, 8(1), pp. 11–20.

Chen, C.L. and Dhir, V.K. (1982). Hydrodynamics of a bubble formed at vent pipe exit. *Int. J*, 8/2, pp. 147–163.

Chen, S., Gerner, F., and Tien, C. (1987). General film condensation correlations. *Exp. Heat Transfer*, 1, pp. 93–107.

Chuang, T.H. (1977). *Mark III one-third area scale submerged structure tests. [BWR]*. Technical report. General Electric Co., San Jose, CA (USA). Boiling Water Reactor Systems Dept.

Chun, M.H., Kim, Y.S., and Park, J.W. (1996). An Investigation of direct condensation of steam jet in subcooled water. *Int. Communications in Heat and Mass Transfer*, 23/7, p. 947.

Cooley, J.W. and Tukey, J.W. (1965). An Algorithm for the Machine Calculation of Complex Fourier Series. *Mathematics of Computation*, 19, pp. 297–301.

Coste, P. (2004). Computational Simulation of Multi-D Liquid-Vapor Thermal Shock with Condensation. In: *Proceedings of ICMF'04, Yokohama, Japan, May 30 - June 4*.

Coste, P. and Laviéville, J. (2009). A Wall Function-Like Approach for Two-Phase CFD Condensation Modelling of the Pressurized Thermal Shock. In: *The 13th International Topical Meeting on Nuclear Thermal Hydraulics (NURETH-13)*.

Coste, P., Pouvreau, J., Laviéville, J., and Boucker, M. (2008). Status of A Two-Phase CFD Approach to The PTS Issue. In: *XCFD4NRS, Grenoble, France*.

Coste, P., et al. (2007). Modeling Turbulence and Friction Around A Large Interface in Three-Dimension Two-Velocity Eulerian Code. In: *The 12th International Topical Meeting on Nuclear Reactor Thermal Hydraulics (NURETH-12), September 30-October 4*.

Davis, J. and Yadigaroglu, G. (2003). Direct contact condensation in Hiemenz flow boundary layers. *Int. Journal of Heat and Mass Transfer*, 47, pp. 1863–1875.

Driest, E.R.V. (1956). On turbulent flow near a wall. *Journal of Aeronautical Sciences*, 23, pp. 1007–1011.

Fortescue, G. and Pearson, J. (1967). On gas Absorption into a turbulent liquid. *Chemical Engineering Science*, 22, pp. 1163–1176.

Galyardt, D.L., Hayes, C.G., and Kushman, S.L. (1978). *Mark I Containment Program. 1/4 Scale Pressure Suppression Pool Swell Test Program: scaling evaluation.* Technical report. General Electric Co., San Jose, CA (USA). Nuclear Energy Engineering Div.

Ghiaasiaan, S. (2008). *Two-Phase Flow, Boiling, and Condensation in Conventional and Miniature Systems*, 1st edn. ISBN 978-0-521-88276-7: Cambridge University Press, New York.

Giencke, E. (1981). Pressure distribution due to a steam bubble collapse in a BWR pressure suppression pool. *Nuclear Engineering and Design*, 65, pp. 175–196.

Goldstein, R.J., Sparrow, E.M., and Jones, D.C. (1973). Natural Convection Mass Transfer Adjacent to Horizontal Plates. *International Journal of Heat and Mass Transfer*, 61, p. 1025.

Grafton, W.A., McIntyre, T.R., and Ross, M.A. (1977). *Mark II Pressure Suppression Test Program, Phase II and III tests*. Technical report. General Electric Co., San Jose, CA (USA). BWR Projects Dept.

Hart, J., et al. (2001). TEPSS–Technology enhancement for passive safety systems. *Nuclear Engineering and Design*, 209/1-3, pp. 243–252.

Higbie, R. (1935). The rate of absorption of a pure gas into a still liquid during short time periods of exposure. *Trans. AIChE*, 31, pp. 365–389.

Hinze, J. (1975). *Turbulence*, 2nd edn. McGraw-Hill series in mechanical engineering, McGraw-Hill Book Company.

Hughes, E.D. and Duffey, R.B. (1991). Direct Contact Condensation and Momentum Transfer in Turbulent Separated Flows. *International Journal of Multiphase Flow*, 17(5), pp. 599–619.

Hunt, J. and Graham, J. (1978). Free stream turbulence near plane boundaries. *Journal of Fluid Mechanics*, 84, pp. 209–235.

IAEA (2000). *Safety of Nuclear Power Plants: Design*. Technical report. NS-R-1. International Atomic Energy Agency.

Incropera, F.P. and Dewitt, D.P. (2002). *Fundamentals of Heat and Mass Transfer*, 5th edn. ISBN 0-471-38650-2: John Wiley & Sons, Inc.

Jensen, R. and Yuen, M. (1982). *Interphase Transport in Horizontal Stratified Cocurrent Flow*. NUREG Report. CR-2334. USNRC.

Karwat, H., Lewis, M., Mazzini, M., and Sandervaag, O. (1986). *Pressure Suppression System Containments: A state-of-the-art Report by a Group of Experts of the NEA/CSNI*. Restricted CSNI Report. 126. OECD-NEA/CSNI.

Kennedy, W., McGovern, D., Maraschin, R., and Wolfe, K. (1978). *Rigid and flexible vent header testing in the quarter scale test facility. Mark I Containment Program, Task 5. 3. 3*. Technical report. Acurex Corp., Mountain View, CA (USA). Alternate Energy Div.

Kerney, J., Feath, G.M., and Olson, D.R. (1972). Penetration characteristics of a submerged steam jet. *AIChE J.*, 18/3, pp. 584–553.

Kim, H. and Bankoff, S. (1983). Local heat transfer coefficient for condensation in stratified countercurrent steam-water stratified flow. *ASME J. Heat Transfer*, 105, pp. 706–713.

Kim, H., Lee, S., and Bankoff, S. (1985). Heat transfer and interfacial drag in countercurrent steam-water stratified flow. *International Journal of Multiphase Flow*, 11, pp. 593–606.

Kondo, S., Tobita, Y., Morita, K., and Shirakawa, N. (1992). SIMMERIII : An advanced computer program for LMFBR severe accident analysis. In: *Proceedings of the International Conference on Design and Safety of Advanced Nuclear Power Plants (ANP '92), Tokyo, Japan, October 1992*.

Kukita, Y., Namatame, K., and Shiba, M. (1984). LOCA air-injection loads in BWR MARK II pressure suppression containment systems. *Nuclear Engineering and Design*, 77/2, pp. 117–129.

Kukita, Y., Namatame, K., Takeshita, I., and Shiba, M. (1987). LOCA steam condensation loads in BWR MARK II pressure suppression containment system. *Nu*, 102/2, pp. 225–228.

Lahey, R. and Moody, F. (1993). *The Thermal-Hydraulics of a Boiling Water Reactor*, 2nd edn. American Nuclear Society.

Laine, J. (2002). *Condensation Pool Experiments with Non-Condensable Gas*. Technical report. Lappeenranta University of Technology, FINNUS Research Report TOKE-2/2002.

Laine, J. and Puustinen, M. (2003). *Preliminary Condensation Pool Experiments with Steam Using DN80 and DN100 Blowdown Pipes*. Research Report POOLEX 4/2003. Lappeenranta University of Technology.

Laine, J. and Puustinen, M. (2004). *Preliminary Condensation Pool Experiments with Steam Using DN200 Blowdown Pipe*. Research Report POOLEX 1/2005. Lappeenranta University of Technology.

Laine, J. and Puustinen, M. (2005). *Condensation Pool Experiments with Steam using DN200 Blowdown Pipe*. Research Report POOLEX 4/2004. Lappeenranta University of Technology.

Laine, J. and Puustinen, M. (2006a). *Condensation Pool Experiments with Steam using Insulated DN200 Blowdown Pipe*. Research Report POOLEX 3/2005. Lappeenranta University of Technology.

Laine, J. and Puustinen, M. (2006b). *Steam Blowdown Experiments on Chugging*. Research Report POOLEX 2/2005. Lappeenranta University of Technology.

Lakehal, D. (2007). *Deliverable D2.1.7.2: "Direct Numerical Simulation of Condensing Stratified Two-Phase Flow"*. Technical report. EUROPEAN COMMISSION, 6th EURATOM FRAMEWORK PROGRAMME 2005-2008, INTEGRATED PROJECT (IP): NURESIM Nuclear Reactor Simulations, SUB-PROJECT 2: Thermal Hydraulics.

Lakehal, D., Fulgosi, M., Banerjee, S., and Yadigaroglu, G. (2008a). Turbulence and Heat Exchange in Condensing Vapor-liquid flow. *Physics of Fluids*, 20, p. 065101.

Lakehal, D. and Labois, M. (2011). A New modelling strategy for phase-change heat transfer in turbulent interfacial two-phase flow. *International Journal of Multiphase Flow*, 37, pp. 627–639.

Lakehal, D., M.Fulgosi, and G.Yadigaroglu (2008b). DNS of Condensing Stratified Steam Water Flow. *ASME J. Heat Transfer*, 130, pp. 021501–10.

Lamont, J. and Scott, D. (1970). An eddy cell model of mass transfer into the surface of a turbulent liquid. *AIChE J.*, 16, pp. 513–519.

Laviéville, J., et al. (2006). *NEPTUNE CFD V1.0 theory manual*. Technical report. EDF.

Levy, E., Wagh, M., H.Sethu, and Pinarbasi, A. (1992). Pattern-Recognition Analysis of Bubbles Impacting on Tubes. *Powder Technology*, 70, pp. 175–181.

Li, H., Kudinov, P., and Villanueva, W. (2010). *Condensation, Stratification and Mixing in a BWR Suppression Pool*. NORTHNET Roadmap 3 Research Report. KTH.

Liebenberg, L., Thome, J.R., and Meyer, J.P. (2005). Flow Visualization and Flow Pattern Identification With power Spectral Density Distributions of Pressure Traces During Refrigerant Condensation in Smooth and Microfin Tubes. *Journal of Heat Transfer*, 127, pp. 209–220.

Lim, I., Tankin, R., and Yuen, M. (1984). Condensation measurement of horizontal concurrent steam-water flow. *Journal of Heat Transfer*, 106, pp. 425–432.

Lloyd, J.R. and Moran, W.R. (1974). Natural Convection Adjacent to Horizontal Surfaces of Various Planforms. *ASME Paper*, 74-WA/HT-66, pp. –.

Lu, Q. and Suryanarayana, N. (1995). Condensation of a Vapor Flowing Inside a Horizontal Rectangular Duct. *Journal of Heat Transfer*, 117/2, p. 418.

Magnaudet, J. and Calmet, I. (2006). Turbulent mass transfer through a flat shear-free surface. *Journal of Fluid Mechanics*, 553, pp. 155–185.

Mayinger, F. and Chen, Y. (1986). Heat Transfer at the Phase Interface of Condensing bubbles. In: *Proc. of the 8th Int. Heat Transfer Conf.*

McAdams, W. (1954). *Heat Transmission*, 3rd edn. McGraw-Hill.

McCready, J., et al. (1973). *Steam vent clearing phenomena and structural response of the BWR torus (Mark I containment)*. Technical Report. NEDO–10859. General Electric Co., San Jose, Calif. (USA). Atomic Products Equipment Dept.

McCready, M. and Hanratty, T. (1984). Concentration fluctuations close to a gas-liquid interface. *AIChE J.*, 30, pp. 816–817.

McIntyre, T.R., Myers, L.L., Torbeck, J.E., and Booker, R.J. (1975). *Mark III confirmatory test program: one third scale, three vent air tests*. Technical report. General Electric Co., San Jose, Calif. (USA). Boiling Water Reactor Systems Dept.

McIntyre, T.R., Ross, M.A., and Myers, L.L. (1976). *Mark II pressure suppression test program: Phase I tests. [BWR]*. Technical report. General Electric Co., San Jose, Calif. (USA). Boiling Water Reactor Systems Dept.

Meier, M. (1999). *Numerical and experimental study of large steam-air bubbles injected in a water pool*. Ph.D. thesis. ETH, Swiss Federal Institute of Technology, Zurich. DISS. ETH No. 13091.

Meier, M., Andreani, M., and Yadigaroglu, G. (1998). Experimental study of large steam-air bubbles condensing in a suppression pool. In: *IMECA'98, ASME, Anaheim*.

Moody, F.J. (1984). The Importance of Pools, Sprays, and Ice Beds in Fission Product Retention in Containment. In: *Proc. ANS Topical Meeting, Fission Product Behaviour and Source Term Research*.

Moody, F. (1977). *Analytical model for estimating drag forces on rigid submerged structures caused by LOCA and safety relief valve ramshead air discharges*. Technical report. NEDO-21471. San Jose, Calif. : General Electric Company.

Poikolainen, J. and Silde, A. (2008). *Validation of the Containment Water Pool Stratification Model of APROS Against The POOLEX Experiments STB-20 and STB-21*. Project Report. VTT Processes.

Pope, S.B. (2009). *Turbulent Flows*, 6th edn. Cambridge University Press, New York.

Pättikangas, T., Niemi, J., and Timperi, A. (2011). *Numerical modelling of pressure suppression pools with CFD and FEM codes*. Research Report. VTT-R-00927-11. VTT.

Pättikangas, T. and Pokela, H. (2003). *Wall-loadings caused by large air bubbles injected in water pool*. Project Report. PRO4/T7534/02. VTT Processes.

Pättikangas, T., Raussi, P., Pokela, H., and Huttunen, M. (2000). *Two-dimensional CFD simulation of water hammer in a pool*. Technical report. VTT Energy, Finland.

Pättikangas, T., et al. (2010). CFD modelling of condensation of vapour in the pressurized PPOOLEX facility. In: *CFD for Nuclear Reactor Safety Applications (CFD4NRS-3) Workshop, Bethesda, MD, USA, 14-16 September 2010*, p. 12.

Rayleigh, L. (1917). VIII. On the pressure developed in a liquid during the collapse of a spherical cavity. *Philosophical Magazine Series 6*, 34/200, pp. 94–98.

Riikonen, V. (2011). *Nuclear Safety Research Unit, Facilities*. url: `http://www.lut.fi/energy/et/yty`.

Robbins, C.H. (1960). *Tests of a Full Scale 1/48 Segment of the Humboldt Bay Pressure Suppression Containment*. Technical report. GEAP-3596. General Electric.

Räsänen, A. (2004). *Mittausjärjestelmä lauhtumisilmiöiden tutkimukseen*. Master's thesis. Lappeenranta University of Technology.

Sargis, D.A., Stuhmiller, J.H., and Wang, S.S. (1978). *A Fundamental Thermalhydraulic Model to Predict Steam Chugging Phenomena*. Technical report. Electric Power Reseach Institute.

Shimegi, N. and Suzuki, K. (1988). Analyses of pool swell tests by two-dimensional hydrodynamic computer code. *Journal of Nuclear Science and Technology*, 25/10, pp. 816–824.

Simpson, M.E. and Chan, C.K. (1982). Hydrodynamics of a subsonic vapor jet in subcooled liquid. *Journal of Heat Transfer*, 104/2, pp. 271–278.

Smith, B.L. (2007). A numerical investigation of three-dimensional flows in large volumes in the context of passive containment cooling in BWRs. *Nuclear Engineering and Design*, 237/11, pp. 1175–1184.

Sonin, A., Shimko, M., and Chun, J. (1986). Vapor condensation onto a turbulent liquid - I. The steady condensation rate as a function of the liquid-side turbulence. *International Journal of Heat and Mass Transfer*, 29, pp. 1319–1338.

Tanskanen, V. and Jordan, A. (2009). *Initialization of CFD Calculations of Steam Discharge Experiments*. SAFIR Research Report. CONDEX 4/2008. Lappeenranta University of Technology.

Tanskanen, V. and Jordan, A. (2010a). *CFD Simulation of STB-31 Experiment by Using Neptune-CFD and TransAT Codes*. SAFIR Research Report. CONDEX 3/2009. Lappeenranta University of Technology.

Tanskanen, V. and Jordan, A. (2010b). *Deliverable D2.3.4.15a, Validation of Condensation Models against POOLEX Condensation Pool Experiments*. Technical report. European Commission, 7th Euratom Framework Programme, Collaborative Project: NURISP: Nuclear Reactor Integrated Simulation Project.

Tanskanen, V. and Jordan, A. (2011). *3D CFD Simulation of STB-28 Steam Discharge Experiment*. SAFIR Research Report. CONDEX 3/2010. Lappeenranta University of Technology.

Tanskanen, V., Lakehal, D., and Puustinen, M. (2008a). Validation of Direct Contact Condensation CFD Models Against Condensation Pool Experiments. In: *XCFD4NRS, Grenoble, France*.

Tanskanen, V., Puustinen, M., and Laine, J. (2007). *Deliverable D2.1.15.2a: Validation of NURESIM-CFD Against POOLEX Condensation Pool Experiments: Progress report*. Technical report. European Commision, 6th Euratom Framework Programme 2005-2008, Integrated Project: NURESIM Nuclear Reactor Simulations Sub-Project 2: Thermal Hydraulics.

Tanskanen, V., Puustinen, M., and Laine, J. (2008b). *Deliverable D2.1.15.2b, Validation of NURESIM-CFD against POOLEX condensation pool experiment: Final Report, 6th Euratom Framework Program NURESIM*. Technical report. European Commission, 6th Euratom Framework Programme 2005-2008, Integrated Project (IP): NURESIM Nuclear Reactor Simulations Sub-Project 2: Thermal Hydraulics.

Tchen, C. (1947). *Mean value and correlation problems connected with the motion of small particles suspended in a turbulent fluid*. Ph.D. thesis. Martinus Nijhoff, The Hague.

Theofanous, T., Houze, R., and Brumfield, L. (1976). Turbulent mass transfer at free gas-liquid interfaces, with application to open channel, bubble and jet flows. *International Journal of Heat and Mass Transfer*, 19, pp. 613–624.

Thiele, R. (2010). *Modeling of Direct Contact Condensation With OpenFOAM*. Master thesis. KTH, Royal Institute of Technology, Division of Nuclear Reactor Technology, Royal Institute of Technology, Stockholm, Sweden. ISSN 0280-316X.

Timperi, A., Pättikangas, T., Niemi, J., and Ilvonen, M. (2006). *Fluid-Structure Interaction Analysis of a Water Pool under Loading Caused by Steam Injection*. Research Report. TUO72-056662. VTT.

Tuomainen, M. (2001). *Lauhdutusallaskokeiden suunnittelulaskuja Fluent-ohjelmalla*. Projektiraportti. ENE4-PR-12/01. VTT Energia.

Tuunanen, J., et al. (1998). *General description of the PACTEL test facility*. VTT Research Notes. 1929. VTT. ISBN 951-38-5338-1.

TVO (2007). *Ydinvoimalaitosyksiköt Olkiluoto 1 ja Olkiluoto 2*.

Varzaly, A.M. (1977). *Mark III small scale chugging tests: Test Series 5013. [BWR]*. Technical report. General Electric Co., San Jose, Calif. (USA). Boiling Water Reactor Systems Dept.

Varzaly, A.M., Grafton, W.A., Chang, H., and Mitchell, M.K. (1977). *Mark III Confirmatory Test Program: 1/root 3 scale condensation and stratification phenomena, Test Series 5807*. Technical report. General Electric Co., San Jose, Calif. (USA). Boiling Water Reactor Systems Dept.

White, F.M. (1999). *Fluid Mechanics*, 4th edn. WCB/McGraw-Hill. ISBN 0-07-069716-7.

Wickett, T., et al. (1998a). *Report of the Uncertainty Methods Study for Advanced Best Estimate Thermal Hydraulic Code Applications, Vol. 1*. Technical report. NEA/C-SNI/R(1997)35.

Wickett, T., et al. (1998b). *Report of the Uncertainty Methods Study for Advanced Best Estimate Thermal Hydraulic Code Applications, Vol. 2*. Technical report. NEA/C-SNI/R(1997)35/VOL2.

Wikdahl, C.E. (2007). *Marvikenreaktorn - ett industripolitiskt utvecklingsprojekt i otakt med tiden*. Technical report. SKI Rapport 2007:18. SKI.

Wu, J., Dhir, V., and Qian, J. (2007a). Numerical Simulation of Subcooled Nucleate Boiling by Coupling Level-Set Method with Moving-Mesh Method. *Numerical Heat Transfer, Part B*, 51, pp. 535–563. Copyright Taylor & Francis Group, LCC. ISSN:1040-7790 print/1521-0626 online.

Wu, X.Z., et al. (2007b). Experimental study on the condensation of supersonic steam jet submerged in quiescent subcooled water: steam plume shape and heat transfer. *Int. Journal of Multiphase Flow*, 33/12, pp. 1296–1307.

Yadigaroglu, G. and Lakehal, D. (2003). New challenges in computational thermal hydraulics. In: *NURETH-10, Seoul, Korea, October 5-9*.

Ylikauppila, M., Puustinen, M., and Tanskanen, V. (2009). *Blowdown Test Facilities: Literature Survey*.

Youn, D.H., et al. (2003). The direct contact condensation of steam in a pool at low mass flux. *Nuclear Science and Technology*, 40/10, pp. 881–885.

Yue, D.D. (1982). BWR Containment Failure Analysis during Degraded-Core Accidents. In: *1982 ANS Annual Meeting, Los Angeles, California. June 6-11, 1982.*

APPENDIX 1: The measurement instrumentation in POOLEX experiments

The pool test facility was originally scaled and constructed for the experiments with non-condensable gas (Laine, 2002). After some modifications, preliminary experiments with steam were executed by using the same pool test facility and DN80, DN100, and DN200 blowdown pipes (Laine and Puustinen, 2003, 2004). A new data acquisition system capable of measuring and recording a larger number of channels with adequate sampling rates than the system used in the pre-tests was installed. For more accurate observation of steam bubbles, the test rig was furnished with a digital high-speed video camera. After adding extra high-frequency instrumentation, particularly pressure transducers, the first detailed steam test series were executed with the modified pool test facility by using one DN200 blowdown pipe (Laine and Puustinen, 2005). A sketch of the test rig is presented in Figure A1.1. Table A1.1 shows the main dimensions of the test rig compared to the Olkiluoto plant conditions.

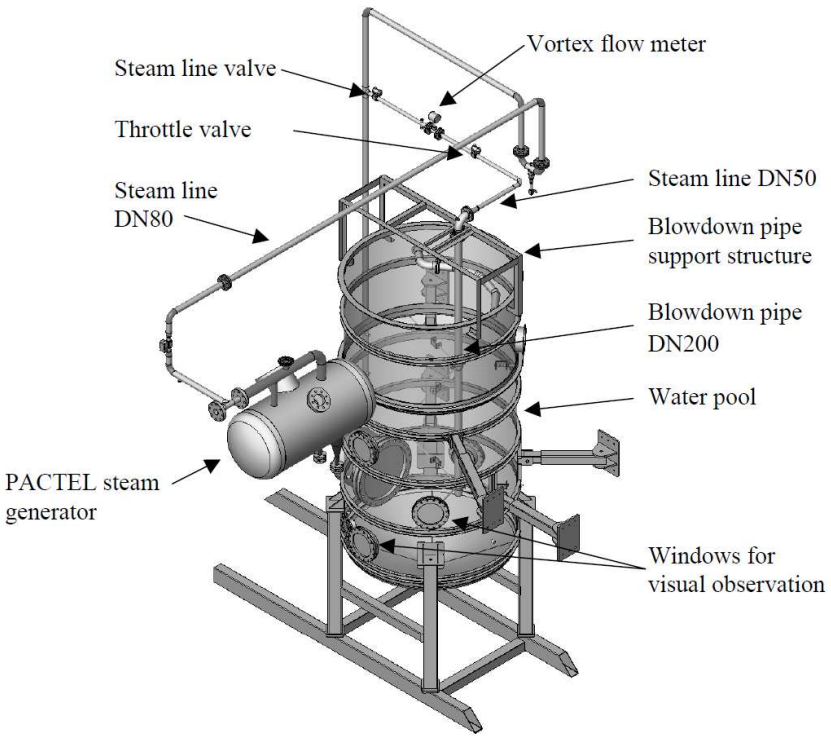

Figure A1.1. POOLEX test rig.

Table A1.1. Test rig vs. Olkiluoto 1 and 2 BWRs

	Test rig	Olkiluoto 1 and 2
Number of blowdown pipes	1	12
Inner diameter of blowdown pipe [mm]	214.1	600
Pool cross-sectional area [m^2]	4.5	287.5
Water level in the pool [m]	3.5	9.5
Pipes submerged [m]	2.0	6.5
Pool water volume [m^3]	15	2700
$\mathrm{A_{pipes}}/\mathrm{A_{pool}} \cdot 100\ \%$	0.8	1.6

Measurement instrumentation

The test facility was equipped with thermocouples for measuring steam and pool water temperatures (T), with pressure transducers (P) for observing pressure behavior in the blowdown pipe, in the steam line, and at the pool bottom, and with one pressure transducer (DP) for detecting the pool water level. Steam flow was measured with a vortex flow meter in the DN50 steam line in most of the experiments. Additional instrumentation includes six strain gauges (ST) on the pool outer wall, valve position sensors, and a high-speed video camera trigger. Figures 3.5, 3.6, 3.7, 3.10, 3.11, A1.2, and A1.3 show the exact measurement locations. Tables A1.2 and A1.3 lists the identification codes and error estimations of the measurements. The error estimations are calculated on the basis of variance analysis. The results agree with normal distributed data with a 95 % confidence interval.

Temperatures are measured by K-type thermocouples. In the pre-tests, $\varnothing\ 0.5\,\mathrm{mm}$ NiCrNi thermocouples proved to be fast enough for capturing the investigated phenomena with sufficient accuracy. The $3\,\mathrm{mm}$ NiCrNi thermocouples were used in the steam line (T13, T504) and at the pool bottom (T14).

In the STB-28 experiment, pressure oscillations in the blowdown pipe were measured by high-frequency pressure transducers (model Kyowa PVL-100K). Also the pressure transducer on the pool bottom was a high-frequency transducer (model Kyowa PVL-5K). Frequency response of the amplifier was $1\,\mathrm{kHz}$. In the STB-31 experiment, pressures were measured with pressure transducers (P9, model Kyowa PVL-5K; P7, model Rosemount 3051) and with differential pressure transmitters (P101,DP6, model Yokogawa EAJ 110).

Six uniaxial foil strain gauges (model Kyowa KFG-5-120-C1-11 L1M2R) were attached with glue onto the pool outside wall in the chugging experiments, see Figures A1.2 and A1.3. The gauge length and width were $5.0\,\mathrm{mm}$ and $1.4\,\mathrm{mm}$, respectively. The frequency response of the amplifier was $5\,\mathrm{kHz}$.

The steam flow rate (F) was measured with a rotameter (model Khrone H250) in the STB-31 experiment. The flow meter was installed in a vertical DN16 steam line, few meters

before the beginning of the blowdown pipe. Steam density was determined on the basis of the temperature measurement T13 and the pressure measurement P7 in the DN16 steam line. However, the temperature values of T13 were not accepted if they fell below the saturation temperature.

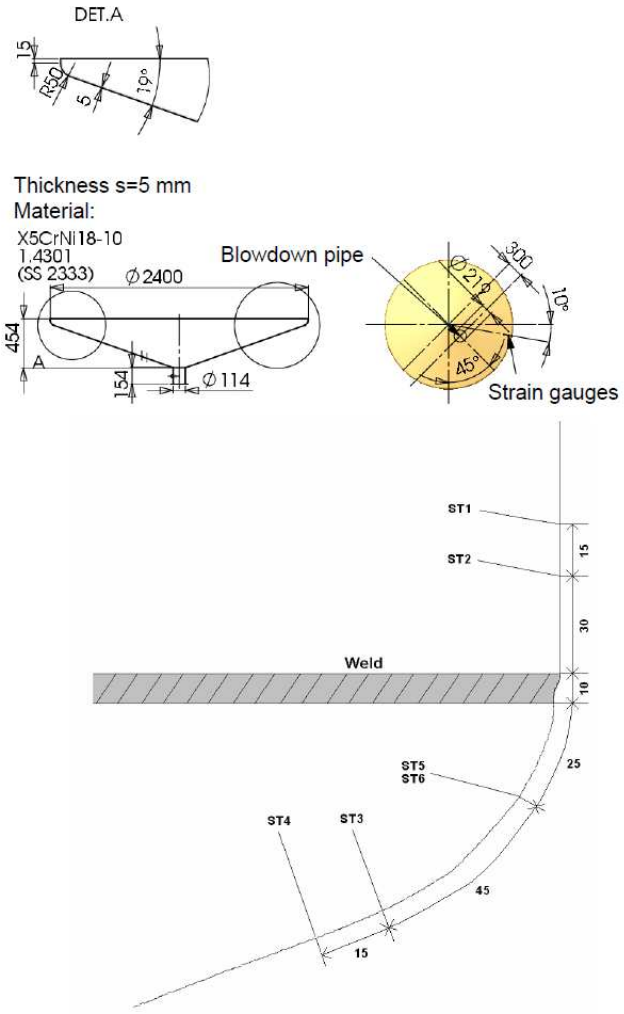

Figure A1.2. Strain gauges on the outer wall of the pool.

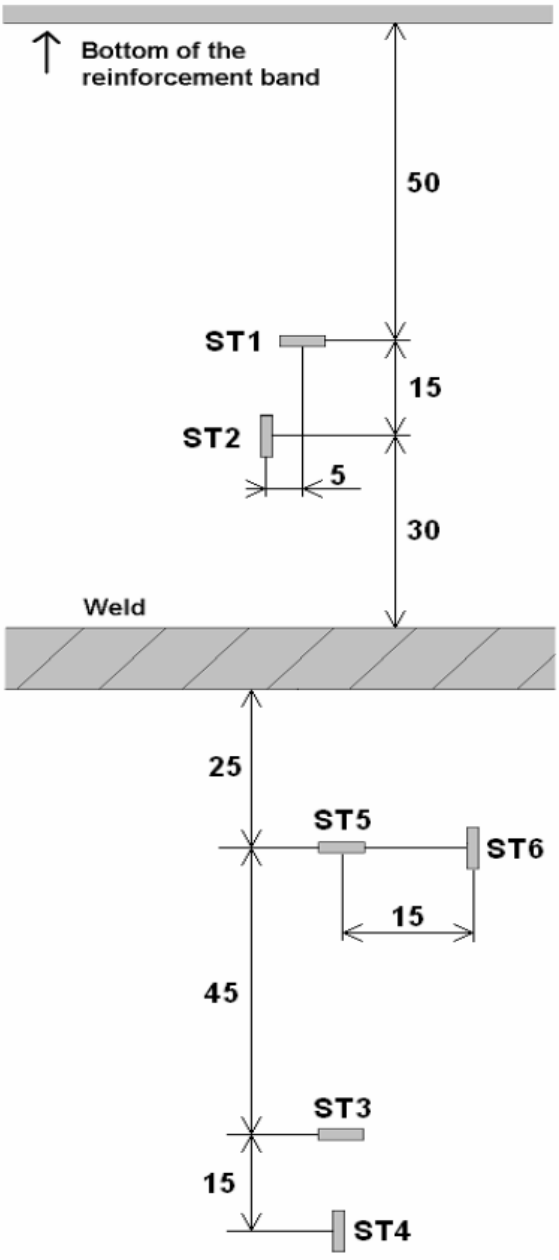

Figure A1.3. Strain gauges on the outer wall of the pool.

Table A1.2. Measurement instrumentation in the STB-28 experiment

Code	Measurement	Error estimation
T1 - T3	Temperatures in the blowdown pipe	$\pm$ 1.8 °C
T13	Temperature in the steam line	$\pm$ 3.5 °C
T14	Temperature in the pool	$\pm$ 2.7 °C
T15	Temperature at the pool bottom	$\pm$ 1.8 °C
T16	Temperature on the pool outer wall	$\pm$ 2.6 °C
T401	Temperature on the blowdown pipe outer wall	$\pm$ 1.8 °C
T504	Temperature in the steam line	$\pm$ 1.8 °C
P1	Pressure in the blowdown pipe (bottom)	$\pm$ 93 kPa
P2	Pressure in the blowdown pipe (middle)	$\pm$ 93 kPa
P3	Pressure in the blowdown pipe (top)	$\pm$ 93 kPa
DP6	Water level in the pool	$\pm$ 0.06 m
P7	Pressure in the steam line	$\pm$ 93 kPa
P8	Pressure in the steam generator	$\pm$ 60 kPa
P9	Pressure at the pool bottom	$\pm$ 5 kPa
F1	Volumetric flow rate in the steam line	$\pm$ 4.9 L/s
ST1 - ST6	Strains on the pool outer wall	$\pm$ 21 $\mu\varepsilon^*$
Trig	High speed camera trigger	Not defined
Valve	Valve position	Not defined

* The error estimates do not contain the effect of the strain gauge and the amplifier.

Table A1.3. Measurement instrumentation in the STB-31 experiment

Code	Measurement	Error estimation
T13	Temperature in the steam line	$\pm$ 3.6 °C
T14	Temperature in the pool	$\pm$ 2.7 °C
T15	Temperature at the pool bottom	$\pm$ 1.8 °C
T504	Temperature in the steam line	$\pm$ 1.8 °C
T701 - T711	Temperatures at the blowdown pipe outlet	$\pm$ 1.8 °C
T712	Temperature on the blowdown pipe outer wall	$\pm$ 1.8 °C
T713	Temperature of the insulation	$\pm$ 1.8 °C
T714	Temperature on the blowdown pipe inner wall	$\pm$ 1.8 °C
P101	Pressure in the blowdown pipe outlet	$\pm$ 4 kPa
DP6	Water level in the pool	$\pm$ 0.06 m
P7	Pressure in the steam line	$\pm$ 97 kPa
P8	Pressure in the steam generator	$\pm$ 62 kPa
P9	Pressure at the pool bottom	$\pm$ 5 kPa
F1	Steam mass flow rate	$\pm$ 1.3 g/s
Valve	Valve position	Not defined

Digital high-speed video camera

A Citius Imaging digital high-speed video camera (model C10) is used for the visual observation of the pool interior. The camera works in close co-operation with the PC which is used for controlling, display, and storage. The camera is a single unit and it is connected to the PC through a USB bus. Several cameras can be networked, e.g. for recording the same event from different angles simultaneously.

The video recording is at first stored to the RAM memory in the camera (in AVI format). From there it is transferred onto the PC hard disk. The camera is furnished with the maximum available amount of memory; 2 GB. The camera can achieve over 10000 frames/second (fps) recording speed and up to 652x496 pixels resolution with 256 shades of gray.

However, the speed and maximum recording time depend on the resolution used. During the experiments, a recording speed of approximately 220 fps with maximum available resolution (400x338) was used mostly. With these set-ups the maximum recording time is 73 seconds (29 MB/s). Table A1.4 shows more examples of resolution/speed/recording time combinations that can be attained with the camera.

Table A1.4. Examples of resolution, speed, and maximum recording time combinations of Citius Imaging high-speed digital video camera C10

Resolution [pixels]	Speed [fps]	Max. recording time [s]
640 x 480	99	70.9
340 x 256	330	74.7
172 x 128	1154	84.5
84 x 64	3551	112.5
40 x 20	10652	252

Data acquisition

National Instruments PCI-PXI-SCXI is a PC-driven multi-channel measurement system with a LabView user interface. The maximum number of measurement channels is 96 with additional eight channels for strain measurements. The maximum recording frequency depends on the number of measurements and is in the region of $300\,\mathrm{kHz}$ for all measured channels combined. The data acquisition system is discussed in more detail in reference Räsänen (2004).

Separate HPVee based software was used for monitoring and recording the essential measurements of the PACTEL facility producing steam (Tuunanen et al., 1998). Both data acquisition systems measured signals as volts. After the experiments, the voltage readings were converted to engineering units by using special conversion software.

Concerning the chugging experiments, the used data recording frequency of LabView was $10\,\mathrm{kHz}$ for measurements P1-P3, P9, and ST1-ST6. For temperature measurements T1-T3 and T16, the data recording frequency was $200\,\mathrm{Hz}$ (in the pre-tests, the $122\,\mathrm{Hz}$ data recording frequency was found to be fast enough for capturing the investigated phenomena). The temperature measurements are therefore averages of 50 measured points. In the STB-31 experiment, the data recording frequency of LabView was $1\,\mathrm{Hz}$. Residual measurements were recorded by HPVee software with the frequency of $1\,\mathrm{Hz}$ in both cases.

A separate measurement channel was used for steam line valve position information. Approximately $3.6\,\mathrm{V}$ means that the valve is fully open, and approximately $1.1\,\mathrm{V}$ that it is fully closed. Voltage under $1.1\,\mathrm{V}$ means that the valve is opening. Both HPVee and LabView record the channel.

A separate measurement channel was also used for the digital high-speed video camera triggering. When the camera got a signal from the trigger, it started to record. Depending on the adjustment, the camera either recorded the events from the triggering moment towards the future or from the past until the triggering moment. Boundary signal for the camera was approximately $3.5\,\mathrm{V}$. One additional channel recorded the exposure of the camera.

A high data recording frequency produced a large amount of measurement data. With the used data recording frequency and the number of measurement channels ($10\,\mathrm{kHz}$ / 16 channels and $200\,\mathrm{Hz}$ / 7 channels for temperature readings), LabView produced approximately $21\,\mathrm{MB}$ of data per a 10 second time interval. As a comparison, HPVee produced no more than approximately $1\,\mathrm{kB}$ of data / 10 seconds. The large amount of measurement data causes problems when processing and archiving the data.

APPENDIX 2: Error estimation, FFT, and Pattern Recognition Algorithms

The error estimation, FFT, and pattern recognition algorithms used in this thesis are described in this appendix. The error estimation and FFT algorithms are presented as MATLAB codes, and the pattern recognition algorithm is simplified to a pseudo-code presentation. The special MATLAB functions are also described briefly. The feasibility of the pattern recognition algorithm is briefly discussed.

Error estimation algorithm for the Couette flow film analysis

This MATLAB code contains the Couette flow film estimation of the effect of the non-condensable gases on the results of the STB-31 POOLEX experiment. The error estimation by means of total derivative is included as well. The MATLAB code of the algorithm is as follows:

```
function noncondensables()

close all;
load -ASCII STB31ML.csv
% Time [s] Tsat [K] T1bulk [K] T20 [K] T100 [K] p [bar] qm [g/s]
Am = pi * 0.10655^2;

Time = STB31ML(:,1);%[s]
Tsat = STB31ML(:,2) - 273.15; %[C]
DTsat = 1.8;
DT1bulk = 2.25;
DT20 = 1.8;
DT100 = 1.8;
Dp = 4000/10000;
DG = (1.3/1000)/Am;
T1bulk = STB31ML(:,3) - 273.15; %[C]
T20 = STB31ML(:,4) - 273.15; %[C]
T100 = STB31ML(:,5) - 273.15; %[C]
p = STB31ML(:,6); %[bar]
G = (STB31ML(:,7)./1000)./Am; %[kg/m^2s]

for i = 1:1:length(Time),
[h1d(i),dh1d_Tsat(i),dh1d_T1bulk(i)] = f_h1d(Tsat(i),T1bulk(i));
[TI(i),X0(i),dTI_T20(i),dTI_T100(i),dTI_p(i)] = f_TI(p(i),T20(i),T100(i));
[hfgTI(i), dhfg_TI(i)]= f_hfg(TI(i));
[h2I(i),dh2I_T20(i),dh2I_T100(i),dh2I_p(i),dh2I_G(i)] =
f_h2I(G(i),p(i),T20(i),T100(i),TI(i),dTI_T20(i),dTI_T100(i),dTI_p(i));
[hfgTsat(i),dhfg_Tsat(i)] = f_hfg(Tsat(i));

U(i) = (h1d(i).*(Tsat(i)-T1bulk(i)).*hfgTI(i).*G(i));
B(i) = ((h1d(i).*(TI(i)-T1bulk(i))-h2I(i).*(T100(i)-TI(i))).*hfgTsat(i));
```

```
Gwo(i) = U(i)./B(i);
qm(i) = G(i).*Am;
qmwo(i) = Gwo(i).*Am;

%---- Error estimation ------------
%--- Tsat ----
dU_Tsat(i) = hfgTI(i).*G(i).*(h1d(i)
+ (Tsat(i)-T1bulk(i)).*(dh1d_Tsat(i)));
dB_Tsat(i) = (TI(i)-T1bulk(i)).*(h1d(i).*dhfg_Tsat(i)
+ hfgTsat(i).*dh1d_Tsat(i)) - h2I(i).*(T100(i)-TI(i)).*dhfg_Tsat(i);

dGwo_Tsat(i) = (B(i).*dU_Tsat(i) - U(i).*dB_Tsat(i))./((B(i)).^2);
%---- Tsat End ----

%--- T1bulk ----
dU_T1bulk(i) = hfgTI(i).*G(i).*(h1d(i).*(-1) +
(Tsat(i)-T1bulk(i)).*(dh1d_T1bulk(i)));
dB_T1bulk(i) = hfgTsat(i).*(h1d(i).*(-1) +
(TI(i)-T1bulk(i)).*dh1d_T1bulk(i));

dGwo_T1bulk(i) = (B(i).*dU_T1bulk(i) - U(i).*dB_T1bulk(i))./((B(i)).^2);
%--- T1bulk End ----

%--- T20 ---
dU_T20(i) = h1d(i).*(Tsat(i)-T1bulk(i)).*G(i).*dhfg_TI(i).*dTI_T20(i);
dB_T20(i) = hfgTsat(i).*(h1d(i).*dTI_T20(i) - (h2I(i).*(-dTI_T20(i))
+ (T100(i)-TI(i)).*dh2I_T20(i)));

dGwo_T20(i) = (B(i).*dU_T20(i) - U(i).*dB_T20(i))./((B(i)).^2);
%--- T20 End ---

%--- T100 ---
dU_T100(i) = h1d(i).*(Tsat(i)-T1bulk(i)).*G(i).*dhfg_TI(i).*dTI_T100(i);
dB_T100(i) = hfgTsat(i).*(h1d(i).*dTI_T100(i) - (h2I(i).*(1-dTI_T100(i))
+ (T100(i)-TI(i)).*dh2I_T100(i)));

dGwo_T100(i) = (B(i).*dU_T100(i) - U(i).*dB_T100(i))./((B(i)).^2);
%--- T100 End---

%--- p ---
dU_p(i) = h1d(i).*(Tsat(i)-T1bulk(i)).*G(i).*dhfg_TI(i).*dTI_p(i);
dB_p(i) = hfgTsat(i).*(h1d(i).*dTI_p(i) - (h2I(i).*(-dTI_p(i))
+ (T100(i)-TI(i)).*dh2I_p(i)));

dGwo_p(i) = (B(i).*dU_p(i) - U(i).*dB_p(i))./((B(i)).^2);
%--- p End---

%--- G ---
dU_G(i) = h1d(i).*(Tsat(i)-T1bulk(i)).*hfgTI(i);
dB_G(i) = (-(T100(i)-TI(i)).*(dh2I_G(i))).*hfgTsat(i);
dGwo_G(i) = (B(i).*dU_G(i) - U(i).*dB_G(i))./((B(i)).^2);
%--- G End ---
```

```
%----- Total--------
DGwo(i) = abs(dGwo_Tsat(i)).*DTsat + abs(dGwo_T1bulk(i)).*DT1bulk
+ abs(dGwo_T20(i)).*DT20 + abs(dGwo_T100(i)).*DT100 + abs(dGwo_p(i)).*Dp
+ abs(dGwo_G(i)).*DG;

qmwoE(i) = DGwo(i).*Am;
%----------------------------------------
end

end

function [h1d,dh1d_Tsat,dh1d_T1bulk] = f_h1d(Tsat,T1bulk)
Tfilm = (Tsat+T1bulk)./2;
Pref = 119435/10000;
lambda = XSteam('tc_pT',Pref,Tfilm);
L = 0.053275;
g = 9.81;
beta = -1.0253486336e-12*(Tfilm+273.15).^4
+ 0.0000000017122263703*(Tfilm+273.15).^3 - 0.0000010594850174
*(Tfilm+273.15).^2 + 0.00029376443751*(Tfilm+273.15) - 0.030433697621;
muL = XSteam('my_pT',Pref,Tfilm);
rhoL = XSteam('rho_pT',Pref,Tfilm);
nuL = muL./rhoL;
cpL = XSteam('Cp_pT',Pref,Tfilm);
cpL = 1000*cpL;
alpL = (lambda.*nuL)./(cpL.*muL);

h1d = (0.27*lambda/L).*((g*beta*L^3)./(nuL.*alpL)).^(1/4)
.*(Tsat-T1bulk).^(1/4);
dh1d_Tsat = (0.27*lambda/L).*((g*beta*L^3)./(nuL.*alpL)).^(1/4)
.*(Tsat-T1bulk).^(-3/4).*(1/4);
dh1d_T1bulk = -1*dh1d_Tsat;
end

function [hfg,dhfg] = f_hfg(T)
hfg = (2239000-2252000)/(380-375)*(T-375)+2253000;
dhfg = (2239000-2252000)/(380-375);
end

function [TI,X0,dTI_T20,dTI_T100,dTI_p] = f_TI(p,T20,T100)
psatT20 = XSteam('psat_T',T20);
psatT100 = XSteam('psat_T',T100);

X0 = (psatT20./p + psatT100./p)./2 - ((log(20)+log(100))/2)
*((2*(log(20)*psatT20./p+log(100).*psatT100./p)-(psatT20./p+psatT100./p)
.*(log(20)+log(100))).(2*(log(20)^2+log(100)^2)-(log(20)+log(100))^2));

ppart = X0.*p;
TI = XSteam('Tsat_p',ppart);

%DpsatT
x1 = 0.23855557567849;
x2 = 650.17534844798;
```

```
x3 = 1167.0521452767;
x4 = 724213.16703206;
x5 = 17.073846940092;
x6 = 12020.82470247;
x7 = 3232555.0322333;
x8 = 14.91510861353;
x9 = 4823.2657361591;
x10 = 405113.40542057;
T = T20 + 273.15;% deg to K
dpsat_T20 = % a very long function of x1..x10. Not presented here.
T = T100 + 273.15;% deg to K
dpsat_T100 = % a very long function of x1..x10. Not presented here.
dpsat_T20 = dpsat_T20 * 10; %MPa to bars
dpsat_T100 = dpsat_T100 * 10; %MPa to bars

dX0_T20 = (1/(2*p))*dpsat_T20 - ((log(20)+log(100))/2)*(1/(2*(log(20)^2
+log(100)^2)-(log(20)+log(100))^2))*((2*log(20)/p)*dpsat_T20
- (log(20)+log(100))*(1/p)*dpsat_T20);
dX0_T100 = (1/(2*p))*dpsat_T100 - ((log(20)+log(100))/2)*(1/(2*(log(20)^2
+log(100)^2)-(log(20)+log(100))^2))*((2*log(100)/p)*dpsat_T100 - (log(20)
+log(100))*(1/p)*dpsat_T100);
dX0_p = (-1/(p^2))*((psatT20 + psatT100)/2) - ((log(20)+log(100))/2)
*(1/(2*(log(20)^2+log(100)^2)-(log(20)+log(100))^2))*((-2/(p^2))*(log(20)
*psatT20+log(100)*psatT100) + (1/(p^2))*(psatT20 + psatT100)
*(log(20)+log(100)));

dppart_X = p;

%DTsatp
y1 = 17.073846940092;
y2 = 14.91510861353;
y3 = 1167.0521452767;
y4 = 12020.82470247;
y5 = 4823.2657361591;
y6 = 724213.16703206;
y7 = 3232555.0322333;
y8 = 405113.40542057;
y9 = 650.17534844798;
y10 = 0.23855557567849;
P = ppart/10; %bar to MPa
dTsat_p = % a very long function of y1..y10. Not presented here.
dTsat_p = dTsat_p - 273.15;%K to deg

dTI_T20 = dTsat_p.*dppart_X.*dX0_T20;
dTI_T100 = dTsat_p.*dppart_X.*dX0_T100;
dTI_p = dTsat_p.*dppart_X.*dX0_p;
end

function [h2I,dh2I_T20,dh2I_T100,dh2I_p,dh2I_G] = f_h2I(G,p,T20,T100,TI,
dTI_T20,dTI_T100,dTI_p)

Mv = 18.0153;
Mn = 28.9647;
```

```
psatTI = XSteam('psat_T',TI);
psatT100 = XSteam('psat_T',T100);

mv2 = (Mv*psatT100./p)./(Mv*psatT100./p + Mn*(1-psatT100./p));
mvTI = (Mv*psatTI./p)./(Mv*psatTI./p + Mn*(1-psatTI./p));

rho2 = XSteam('rhoV_T',T100);
hm2I = (-G./rho2).*(log((1-mv2)./(1-mvTI))).^(-1);
cp2 = XSteam('CpV_T',T100);
cp2 = cp2*1000;
D12 = 0.000026*((T100+273.15)./298).^(3/2);
muG = XSteam('my_pT',p,T100);
nuG = muG./rho2;
lambdaG = XSteam('tcV_T',T100);
alpG = (lambdaG.*nuG)./(cp2.*muG);
Le = alpG./D12;

h2Id = rho2.*cp2.*Le.^(2/3).*hm2I;

h2I = (G.*cp2.*h2Id)./(1-exp(-G.*cp2./h2Id));

%-------Derivatives------
%dpsat_T*
x1 = 0.23855557567849;
x2 = 650.17534844798;
x3 = 1167.0521452767;
x4 = 724213.16703206;
x5 = 17.073846940092;
x6 = 12020.82470247;
x7 = 3232555.0322333;
x8 = 14.91510861353;
x9 = 4823.2657361591;
x10 = 405113.40542057;
T = TI + 273.15;% deg to K
dpsat_TI = % a very long function of x1..x10. Not presented here
T = T100 + 273.15;% deg to K
dpsat_T100 = % a very long function of x1..x10. Not presented here
dpsat_TI = dpsat_TI * 10; %MPa to bars
dpsat_T100 = dpsat_T100 * 10; %MPa to bars

%dmv*_T*
dmvI_TI = ((Mv*psatTI/p + Mn*(1-psatTI/p))*(Mv/p)*dpsat_TI - (Mv*psatTI/p)
*((Mv/p)*dpsat_TI - (Mn/p)*dpsat_TI))/((Mv*psatTI/p + Mn*(1-psatTI/p))^2);

dmv2_T100 = ((Mv*psatT100/p + Mn*(1-psatT100/p))*(Mv/p)*dpsat_T100
- (Mv*psatT100/p)*((Mv/p)*dpsat_T100 - (Mn/p)*dpsat_T100))/((Mv*psatT100/p
+ Mn*(1-psatT100/p))^2);

%dmv*_p
derp = (1/p)*dpsat_TI*dTI_p - (1/(p^2))*psatTI;

dmv2_p = (1/((Mv*psatT100/p + Mn*(1-psatT100/p))^2))*(-1*(Mv*psatT100/p
+ Mn*(1-psatT100/p))*(1/(p^2))*psatT100*Mv - (Mv*psatT100/p)*((-1/(p^2))
```

```
*psatT100*Mv + (1/(p^2))*psatT100*Mn));

%dhm2I_T*
dhm2I_T20 = (G./rho2)*(log((1-mv2)/(1-mvTI)))^(-2)*((1-mv2)/(1-mvTI))^(-1)
*-1*(1-mv2)*(1-mvTI)^(-2)*(-dmvI_TI*dTI_T20);
dhm2I_T100 = (G./rho2)*(log((1-mv2)/(1-mvTI)))^(-2)*((1-mv2)/(1-mvTI))^(-1)
*(1-mvTI)^(-2)*((1-mvTI)*(-dmv2_T100) - (1-mv2)*(-dmvI_TI*dTI_T100));

%dhm2I_p
dhm2I_p = (G./rho2)*(log((1-mv2)/(1-mvTI)))^(-2)*((1-mv2)/(1-mvTI))^(-1)
*(1-mvTI)^(-2)*((1-mvTI)*(-dmv2_p) - (1-mv2)*(-dmvI_TI*dTI_p));

%dhm2I_G
dhm2I_G = (-1/rho2)*(log((1-mv2)/(1-mvTI))).^(-1);

%dh2Id_T*
dh2Id_T20 = rho2*cp2*Le^(2/3)*dhm2I_T20;
dh2Id_T100 = rho2*cp2*Le^(2/3)*dhm2I_T100;

%dh2Id_p
dh2Id_p = rho2*cp2*Le^(2/3)*dhm2I_p;

%dh2Id_G
dh2Id_G = rho2*cp2*Le^(2/3)*dhm2I_G;

%dh2I_T*
dh2I_T20 = ((1-exp(-G*cp2/h2Id))*G*cp2*dh2Id_T20 - G*cp2*h2Id
*(-exp(-G*cp2/h2Id)*(G*cp2*(1/(h2Id^2))*dh2Id_T20)))
/((1-exp(-G*cp2/h2Id))^2);
dh2I_T100 = ((1-exp(-G*cp2/h2Id))*G*cp2*dh2Id_T100 - G*cp2*h2Id
*(-exp(-G*cp2/h2Id)*(G*cp2*(1/(h2Id^2))*dh2Id_T100)))
/((1-exp(-G*cp2/h2Id))^2);
%dh2I_p
dh2I_p = ((1-exp(-G*cp2/h2Id))*G*cp2*dh2Id_p - G*cp2*h2Id
*(-exp(-G*cp2/h2Id)*(G*cp2*(1/(h2Id^2))*dh2Id_p)))
/((1-exp(-G*cp2/h2Id))^2);
%dh2I_G
dh2I_G = ((1-exp(-G*cp2/h2Id))*cp2*(G*dh2Id_G + h2Id) - G*cp2*h2Id
*(-exp(-G*cp2/h2Id)*((-h2Id*cp2 + G*cp2*dh2Id_G)/(h2Id^2))))
/((1-exp(-G*cp2/h2Id))^2);
end
```

FFT algorithm for the time variant signals

This MATLAB code of the FFT algorithm is general and it should scale the power spectrum values correctly. The MATLAB code of the algorithm is as follows:

```
% t is the time vector and Data is the data versus it
T = t(2,1)-t(1,1);              % Sampling time
Fs = 1/T;                       % Sampling frequency
```

```
%L = 2^(nextpow2(length(t)));  % Length of signal (increased to
                               % the next power of 2)
L = length(t);                 % Length of signal as is. Slower in FFT,
                               % but it produces fewer anomal low frequencies
                               % An interpolated signal can be used to
                               % improve the visual appearance of the FFT

Dafft = fft(Data,L);           % Fast Fourier Transform function of MATLAB
NumUniquePts = ceil((L+1)/2);  % Only the half of the FFT'd data is unique
Dafft = Dafft(1:NumUniquePts); % Take the first half of the data vector
Pyy = abs(Dafft);               % Absolute values of the FFT data points
                               % (i.e. Complex numbers converted
                               % to their magnitudes)
Pyy = Pyy/L;                   % FTT output of MATLAB has to be divided by L
Pyy = Pyy.^2;                  % Power spectrum is fft'd Data^2
if rem(L, 2)                   % Odd L excludes the Nyquist point
  Pyy(2:end) = Pyy(2:end)*2;   % Data has to be multiplied by 2,
                               % because it was halved earlier
else                           % This necessary for conserving
                               % the total power of the signal
  Pyy(2:end-1) = Pyy(2:end-1)*2;
end
f = Fs/L*(0:NumUniquePts-1)';     % Build a frequency vector
power = Pyy;                       % Just rename. Not necessary.
                                   % Plot the power spectrum.
semilogx(f,power/Fs);              % Scale with the Sampling frequency.
                                   % (Not necessary, but a common habit)
hold on;
grid on;

% FFT Discrete Fourier transform.
%    FFT(X) is the discrete Fourier transform (DFT) of vector X.  For
%    matrices, the FFT operation is applied to each column. For N-D
%    arrays, the FFT operation operates on the first non-singleton
%    dimension.
%
%    FFT(X,N) is the N-point FFT, padded with zeros if X has less
%    than N points and truncated if it has more.
%
%    FFT(X,[],DIM) or FFT(X,N,DIM) applies the FFT operation across the
%    dimension DIM.
%
%    For length N input vector x, the DFT is a length N vector X,
%    with elements
%                     N
%       X(k) =       sum  x(n)*exp(-j*2*pi*(k-1)*(n-1)/N), 1 <= k <= N.
%                    n=1
%    The inverse DFT (computed by IFFT) is given by
%                     N
%       x(n) = (1/N) sum  X(k)*exp( j*2*pi*(k-1)*(n-1)/N), 1 <= n <= N.
%                    k=1
```

Pattern recognition algorithm for large steam bubbles and jets

This algorithm can be applied to a series of frames that are numbered in ascending order. This algorithm is only applicable to cases where a single blowdown pipe is submerged vertically into a pool. The blowdown pipe radius is needed as a spatial scaling parameter and the frame rate of the film is needed as a temporal scaling parameter. Other case dependent configuration parameters are usually needed to be adjusted as well. The user has a limited possibility to alter the Region of Interest (ROI) assumptions during the code run. For example, Graphical User Interface (GUI) can be used to manually set the ROI limits for elliptic shapes. The pseudo-code of the algorithm is presented below, in the following order: the main program procedure, large subroutine functions, and miscellaneous rules/formulas/comments. The other functions in the code are MATLAB functions and they are introduced in the next chapter.

procedure RECOGNIZER() ▷ Main program

****Initial parameters and set-up****

Input: $f \leftarrow$ Frame rate
Input: $R \leftarrow$ Radius of the pipe
Input: $Color \leftarrow$ 0 for monochrome, 1 for color
Input: $Query \leftarrow$ 1 for extra user intervention, else 0
Input: $i_{\mathrm{refS}} \leftarrow$ N:o of the reference figure ▷ Needed for masking and scaling
Input: $\{i_{\mathrm{refL}}\} \leftarrow$ N:o/list of the ref. figure(s) for lighting ▷ Needed for lighting level
Input: $\{figs\} \leftarrow$ Full list of the figure files

Input: $\epsilon_{\mathrm{obj}} \leftarrow$ Pixel tolerance for small objects ▷ e.g. Small bubbles
Input: $\epsilon_{\mathrm{hole}} \leftarrow$ Pixel tolerance for ROI holes ▷ e.g. Shadows on the bubble
Input: $Fl_{\mathrm{crop}} \leftarrow$ Crop filter from the GUI ▷ To remove frame boundary anomalies
Input: $\{M\} \leftarrow$ Masks from the GUI ▷ To remove shiny structures
Input: $\{X, Y\}_{\mathrm{mouth}} \leftarrow$ Pipe mouth vertices from the GUI ▷ To calculate aspect angle

$[x_{\mathrm{c}}, y_{\mathrm{c}}, m_{\mathrm{m}}, n_{\mathrm{m}}] \leftarrow$FITELLIPSE($\{X, Y\}_{\mathrm{mouth}}$) ▷ Fit an ellipse
$scale \leftarrow R/m_{\mathrm{m}}$ ▷ Meter/pixel scaling
$\alpha \leftarrow$ ARCSIN($n_{\mathrm{m}}/m_{\mathrm{m}}$) ▷ Vertical aspect angle
$F_{\mathrm{light}} \leftarrow$ AVEFIG($\{figs\}(\{i_{\mathrm{refL}}\}), Color, Fl_{\mathrm{crop}}, \{M\}$) ▷ Mean of lighting figures
$[Fl_{\mathrm{L1}}, Fl_{\mathrm{L2}}] \leftarrow$BACKGROUNDLIGHT($F_{\mathrm{light}}$) ▷ Background lighting filters

Output: SAVE the solver state

****Start The Pattern Recognition Loop****

for $i_{\mathrm{fig}} \leftarrow$1:LENGTH($\{figs\}$) **do** ▷ Loop through all the frames

Process the frame

$F \leftarrow$IMREAD($\{figs\}(i_{\mathrm{fig}})$) ▷ Read the frame
$Time(i_{\mathrm{fig}}) \leftarrow (i_{\mathrm{fig}} - 1)/f$ ▷ Current time

if $Color == 1$ **then**
$F \leftarrow$RGB2GRAY(F) ▷ Convert to monochrome
end if
$F \leftarrow$IMCROP(F, Fl_{crop}) ▷ Crop the boundary
$F \leftarrow$ROIFILL($F, \{M\}$) ▷ Apply the masks
$F \leftarrow$IMSUBTRACT(F, Fl_{L1}) ▷ Remove background light
($F \leftarrow$IMADD(F, Fl_{L2})) ▷ Add light to shadows, optional
$F \leftarrow$IMADJUST(F) ▷ Enhance contrast
$Gtr \leftarrow$GRAYTRESH(F) ▷ Obtain gray threshold
$F_{\text{bw}} \leftarrow$IM2BW(F, Gtr) ▷ Convert to black-white
$F_{\text{bw}} \leftarrow$BWAREAOPEN($F_{\text{bw}}, \epsilon_{\text{obj}}$) ▷ Removing small (white) objects
$Se \leftarrow$STREL('disk',ϵ_{hole}) ▷ Build patching element
$F_{\text{bw}} \leftarrow$IMCLOSE(F_{bw}, Se) ▷ Remove large (black) holes
$F_{\text{bw}} \leftarrow$IMFILL(F_{bw},'holes') ▷ Remove small (black) holes if any

Find the ROI(s)

$[\{B\}, \{L\}] \leftarrow$BWBOUNDARIES($F_{\text{bw}}$,'noholes') ▷ Obtain the boundaries and ▷ labels of recognized objects
$[B_{\text{big}}, Stats_{\text{big}}, B_{\text{2big}}, Stats_{\text{2big}}] \leftarrow$FINDROIS($\{B\}$,$\{L\}$,$x_{\text{c}}$,$m_{\text{m}}$) ▷ Find the two ▷ largest objects

Output: DISPLAY the objects in GUI

$B_{\text{ROI}} \leftarrow B_{\text{big}}$ ▷ Default assumption
if <**Rule-1**> is met **then**
Input: $B_{\text{ROI}} \leftarrow$GUI proposes B_{2big} ▷ Ask if user wish to swap
end if

Analyze the shape of the ROI

$iselli(i_{\text{fig}}) \leftarrow 0$ for jet (default), 1 for elliptic bubble if <**Rule-2**> is met
if $Query == 1$ **then**
Input: $iselli(i_{\text{fig}}) \leftarrow$ 0,1 or 2 from GUI. ▷ '2' means elliptic, but the ▷ GUI is used to crop the ROI
end if
($iselli(i_{\text{fig}}) \leftarrow$SECUCHECK($B_{\text{ROI}}$,$iselli(i_{\text{fig}})$) ▷ Swap to elliptic, if jet ▷ leads to NaNs)

Procedure for elliptic ROIs

if $iselli(i_{\text{fig}}) == 1$ or 2 **then**
$B_{\text{ROI}} \leftarrow$DATARIPPER($B_{\text{ROI}}$,$iselli(i_{\text{fig}})$,$F_{\text{bw}}$) ▷ Removal of biased points
$[x_{\text{Bc}}, y_{\text{Bc}}, m_{\text{B}}, n_{\text{B}}] \leftarrow$FITELLIPSE($\{B_{\text{ROI}}\}$) ▷ Fit an ellipse
Output: DISPLAY the result, SAVE the GUI window as figure
$Width(i_{\text{fig}}) \leftarrow 2 * m_{\text{B}} * scale$ ▷ Width of ellipse
$Height(i_{\text{fig}}) \leftarrow$COS($\alpha$)$*2 * n_{\text{B}} * scale$ ▷ Height of ellipse
$Area(i_{\text{fig}}) \leftarrow$ from <**Formula-1**> ▷ Area from analytical formula
$Volume(i_{\text{fig}}) \leftarrow$ from <**Formula-2**> ▷ Volume from analytical formula

end if

Procedure for jet-type ROIs

if $iselli(i_{\text{fig}}) == 0$ **then**

Output: DISPLAY the result, SAVE the GUI window as figure

$[x_{\max}, y_{\max}] \leftarrow$SIZE($F_{\text{bw}}$) ▷ Resolution of the frame

$rect_1 \leftarrow [1, 1, x_{\text{c}}, y_{\max}]$ ▷ Cropping bound 1

$rect_2 \leftarrow [x_{\text{c}}, 1, x_{\max}, y_{\max}]$ ▷ Cropping bound 2

$F_{\text{bw1}} \leftarrow$IMCROP($F_{\text{bw}}, rect_1$) ▷ Split the frame

$F_{\text{bw2}} \leftarrow$IMCROP($F_{\text{bw}}, rect_2$) ▷ with the pipe axis

$[\{B1\}, \{L1\}] \leftarrow$BWBOUNDARIES($F_{\text{bw1}}$,'noholes') ▷ Obtain boundaries

$[\{B2\}, \{L2\}] \leftarrow$BWBOUNDARIES($F_{\text{bw2}}$,'noholes') ▷ and labels of objects ▷ in halved frames

$[B(1)_{\text{ROI}}, Stats(1)_{\text{ROI}}, \sim, \sim] \leftarrow$FINDROIS($\{B1\}$,$\{L1\}$,$x_{\text{c}}$,$m_{\text{m}}$) ▷ Find the

$[B(2)_{\text{ROI}}, Stats(2)_{\text{ROI}}, \sim, \sim] \leftarrow$FINDROIS($\{B2\}$,$\{L2\}$,$x_{\text{c}}$,$m_{\text{m}}$) ▷ largest ▷ object

for $i \leftarrow 1 : 2$ **do** ▷ Do for the both ROIs

$B_{\text{sc}} \leftarrow [B(i)_{\text{ROI}}[\text{all}, 1] * \text{COS}(\alpha), B(i)_{\text{ROI}}[\text{all}, 2]]$ ▷ Straighten the ▷ aspect angle

$[x_{\text{Jc}}, y_{\text{Jc}}] \leftarrow Stats(i)_{\text{ROI}}.\text{Centroid}$ ▷ Obtain the centroid coords.

$C_{\text{sc}} \leftarrow [x_{\text{Jc}}, y_{\text{Jc}} * \text{COS}(\alpha)]$ ▷ Straighten the aspect angle

$A \leftarrow Stats(i)_{\text{ROI}}.\text{Area}$ ▷ Obtain the area of ROI

$A_{\text{sc}} \leftarrow Area * \text{COS}(\alpha)$ ▷ Straighten the aspect angle

$\{\Delta^2\} \leftarrow (\text{DIFF}(B_{\text{sc}}))^2$ ▷ Square of difference of data points

$S_P \leftarrow \Sigma(\text{SQRT}(\Sigma(\{\Delta^2\}(2))))$ ▷ Perimeter of the ROI

if $i == 1$ **then** ▷ for the left hand side half-frame

$x_{\text{Jlim}} \leftarrow$MAX($B_{\text{sc}}[\text{all}, 2]$) ▷ Pixels on the axis boundary

$[x1max, \sim] \leftarrow$SIZE(F_{bw1})

$r \leftarrow x1max - C_{\text{sc}}[1]$ ▷ Axis-centroid distance

else ▷ for the right hand side half-frame

$x_{\text{Jlim}} \leftarrow$MIN($B_{\text{sc}}[\text{all}, 2]$) ▷ Pixels on the axis boundary

$r \leftarrow C_{\text{sc}}[1]$ ▷ Axis-centroid distance

end if

$B_B \leftarrow B_{\text{sc}}[@(B_{\text{sc}}[\text{all}, 2] = x_{\text{Jlim}}), \text{all}]$ ▷ Points laying on the axis

$\{\Delta_B^2\} \leftarrow (\text{DIFF}(B_B))^2$

$S_B \leftarrow \Sigma(\text{SQRT}(\Sigma(\{\Delta_B^2\})))$ ▷ Length of the curve on the axis

$S \leftarrow S_P - S_B$ ▷ Length of the curve w/o axis

$Areaj(i) \leftarrow S * 2 * \pi * r$ ▷ Guldin's rule

$Volj(i) \leftarrow A_{\text{sc}} * 2 * \pi * r$ ▷ Guldin's rule

end for

$Area(i_{\text{fig}}) \leftarrow \Sigma(Areaj(i))/i * scale^2$ ▷ Area as mean of the ▷ bodies of rotation

$Volume(i_{\text{fig}}) \leftarrow \Sigma(Volj(i))/i * scale^3$ ▷ Volume as mean of the ▷ bodies of rotation

$Width(i_{\text{fig}}) \leftarrow$see <**Comment-1**> ▷ Width of the jet

$Height(i_{\text{fig}})$ ←see <**Comment-1**> ▷ Height of the jet
end if

if <**Rule-3**> **then**
Output: SAVE the solver state
end if

end for

****End The Pattern Recognition Loop****
****Save the RESULT array****

Output: $RESULT \leftarrow [Time, Volume, Area, Width, Height, iselli]$

end procedure

function AVEFIG($\{figs\}(\{i_{\text{refL}}\}), Color, Fl_{\text{crop}}, \{M\}$)
*** This function calculates an average figure ***
*** Crop and mask filters are applied at the end ***
for $i \leftarrow 1$:LENGTH($\{figs\}(\{i_{\text{refL}}\})$) **do**
Fr_L ←IMREAD($\{figs\}(i)$) ▷ Read the frame
if $Color == 1$ **then**
Fr_L ←double(RGB2GRAY(Fr_L)) ▷ Convert to monochrome
else
Fr_L ←double(Fr_L)
end if
$F_{\text{light}} \leftarrow F_{\text{light}} + Fr_L$ ▷ Sum the frames
end for
F_{light} ←uint8(F_{light}/i) ▷ Calculate the average figure

F_{light} ←IMCROP($F_{\text{light}}, Fl_{\text{crop}}$) ▷ Crop the boundary
F_{light} ←ROIFILL($F_{\text{light}}, \{M\}$) ▷ Apply the masks
return F_{light}
end function

function BACKGROUNDLIGHT(F_{light})
*** This function 'opens' the figure with a structuring element blurring it a bit ***
*** The opened figure can be used as background lighting filter ***
*** The opened figure can be modified to create another lighting filter ***
Se ←STREL('disk',1)
Fl_{L1} ←IMOPEN(F_{light}, Se)
$[end1, end2]$ ←SIZE(Fl_{L1}) ▷ Size of the frame
for $co1 \leftarrow 1 : end1$ **do**
for $co2 \leftarrow 1 : end2$ **do**
** An example of the second lighting filter **
** to add light to another side of a frame **
$I \leftarrow Fl_{\text{L1}}(co1, co2)$

```
            Fl_L2(co1, end2 − (co2 − 1)) ← I/4
        end for
    end for
    return Fl_L1, Fl_L2
end function

function FINDROIS({B},{L},x_c,m_m)
    *** This function searches the largest (two) recognized regions ***
    *** And returns their 'Stats' i.e. Area and Centroid ***
    stats ←REGIONPROPS(L,'Area','Centroid')
    area_1 ← area_2 ← 0
    big ← big_previous ← 1
    for i ← 1 :LENGTH({B}) do
        area ← stats(i).Area
        **An Example of optional modifications to straight away neglect**
        **the regions laterally too far from the mouth.**
        **Suitable for a full frame case.**
        centroid ← stats(i).Centroid
        xdist ←ABS(centroid(1,1) − x_c)
        if xdist >= m_m then
            area ← 0
        end if
        if area > area_2 then
            if area > area_1 then
                bigprev ← big
                big ← i
                area_2 ← area_1
                area_1 ← area
            else
                bigprev ← i
                area_2 ← area
            end if
        end if
    end for
    B_big ← {B}(big)
    B_2big ← {B}(bigprev)
    Stats_big ← stats(big)
    Stats_2big ← stats(bigprev)
    return B_big, Stats_big, B_2big, Stats_2big
end function

function SECUCHECK(B_ROI,iselli(i_fig)
    *** This function changes 'iselli' to 1, if 'iselli' leads ***
    *** to NaNs when the jet region is splitted to two pieces ***
    *** Current, somehow functional, version is old and messy and ***
    *** thus not presented here. ***
    *** The basic idea is to split the region and check NaNs, ***
```

*** same way the jet is divided later in the main algorithm. ***
*** After splitting, the half-ROIs can be checked by: ***
$s \leftarrow \max(\max([\text{ISNAN}(B_{\text{left}}),\text{ISNAN}(B_{\text{right}})]))$
if $s! = 0$ **then**
$iselli(i_{\text{fig}}) \leftarrow 1$
end if
return $iselli(i_{\text{fig}})$
end function

function DATARIPPER(B_{ROI},$iselli(i_{\text{fig}})$,F_{bw})
*** This function is for elliptic ROIs only. ***
*** This function removes data points from ***
*** the twilight zone of the ROI. ***
*** This function executes the GUI intervention, ***
*** if $iselli == 2$. ***

$xmin_{\text{bu}} \leftarrow \min(B_{\text{ROI}}(all, 2))$
$xmax_{\text{bu}} \leftarrow \max(B_{\text{ROI}}(all, 2))$
$ymin_{\text{bu}} \leftarrow \min(B_{\text{ROI}}(all, 1))$
$ymax_{\text{bu}} \leftarrow \max(B_{\text{ROI}}(all, 1))$

if $iselli(i_{\text{fig}} == 2$ **then**
** User picks y-limits in GUI **

$[\sim, \sim, \sim, \sim, xi, yi] \leftarrow$BWSELECT($F_{\text{bw}}$)
$ymin_{\text{bu}} \leftarrow \min(yi)$
$ymax_{\text{bu}} \leftarrow \max(yi)$

** User draw a box around the shadow region in GUI **

$[\sim, C_{\text{rect}}] \leftarrow$IMCROP($F_{\text{bw}}$)
$x_{\text{crmin}} \leftarrow C_{\text{rect}}(1)$
$y_{\text{crmin}} \leftarrow C_{\text{rect}}(2)$
$x_{\text{crmax}} \leftarrow x_{\text{crmin}} + C_{\text{rect}}(3)$
$y_{\text{crmax}} \leftarrow y_{\text{crmin}} + C_{\text{rect}}(4)$
end if
$xmean_{\text{bu}} \leftarrow (xmin_{\text{bu}} + xmax_{\text{bu}})/2$
$ymean_{\text{bu}} \leftarrow (ymin_{\text{bu}} + ymax_{\text{bu}})/2$

** Build a bounding ellipse **

$fact \leftarrow 0.9$ ▷ < 1 if the ellipse crops shadow ($iselli == 1$)
if $iselli(i_{\text{fig}} == 2$ **then**
$fact \leftarrow 1$ ▷ ≥ 1 if the ellipse crops appendices ($iselli == 2$)
end if
$m_{\text{t}} \leftarrow fact * (xmax_{\text{bu}} - xmin_{\text{bu}})/2$
$n_{\text{t}} \leftarrow fact * (ymax_{\text{bu}} - ymin_{\text{bu}})/2$

** Removal algorithm of data points **
** Complicated boolean structures not presented in this pseudo-code**

* 1. Remove points at the upper bound of the frame, if any.*
* This is needed if the bubble is crossing the boundary. *

$B_{\mathrm{ROI}} \leftarrow B_{\mathrm{ROI}}(@(B_{\mathrm{ROI}}(all, 1)! = 1), all)$

if $iselli(i_{\mathrm{fig}} == 2)$ **then**
* 2a. Remove the appendices with the bounding ellipse *

$B_{\mathrm{ROI}} \leftarrow B_{\mathrm{ROI}}(\text{"}At\, points\, inside\, the\, bounding\, ellipse\text{"})$

* 3. Remove the shadow bounding points inside the cropping box *

$B_{\mathrm{ROI}} \leftarrow B_{\mathrm{ROI}}(\text{"}At\, points\, outside\, the\, crop\, box\text{"})$
else
* 2b. Remove the shadow bounding points inside the bounding ellipse *

$B_{\mathrm{ROI}} \leftarrow B_{\mathrm{ROI}}(\text{"}At\, points\, outside\, the\, bounding\, ellipse\text{"})$
end if
return B_{ROI}
end function

<**Rule-1**>:
Usually the largest object is the desired ROI, if the frame is filtered successfully. However, two or more bubbles may be present in the frame occasionally, e.g. a new bubble starts to inflate before the residues of previous bubbles or jets have been condensed. Remaining anomalies may also be recognized as large regions some times. Thus, a query is initiated, if the largest recognized shape is not near the pipe mouth anymore. For example, a useful criterion for that can be:

$xdist \leftarrow |x_{\mathrm{cROI}} - x_c|$
$ydist \leftarrow y_{\mathrm{cROI}} - y_c$
if $xdist \geq m_m$ **or** $ydist > 1.2 * m_m$ **or** $ydist < -m_m$ **then**
Ask user if he wish to choose the 2nd largest region instead
end if

<**Rule-2**>:
If one wishes to be certain about the type of the ROI (jet/ellipse), he uses GUI query to tell it to the algorithm. In the later versions (not documented in this thesis) of the algorithm that query is made more practical, i.e. user does not need to tell the assumption separately for every frame. However, it is possible to make the algorithm to guess the shape (usually) correctly with some rules. For example;

$ydist \leftarrow y_{\mathrm{cROI}} - y_c$
if $ydist > 2 * n_m$ **then**

Shape is not bubble (i.e. ellipse)
end if,

because the centroid of bubble is rarely much below the mouth of the blowdown pipe (note that positive y-axis points here downwards). The centroid of jet can usually be clearly below the blowdown pipe mouth instead.

<**Rule-3**>:
A rule for backup save during the run. For example, save after any elliptic bubble or save at every N^{th} frame.

<**Formula-1**>:
The surface area has not been used in this study. However, it can be calculated analytically for an oblate ellipsoid of rotation:

$Area = 2\pi m^2(1 + ((1 - e_c^2)/e_c)\mathrm{arctanh}(e_c))$,
where $e_c^2 = 1 - n^2/m^2$.

<**Formula-2**>:
The volume can be calculated analytically for an oblate ellipsoid of rotation:

$Volume = 4/3\pi m^2 n$,

<**Comment-1**>:
The width and height of jet type ROIs are estimated in the algorithm with mean values obtained from a quite complicated calculation process. As the width and height for jets are not used in this study, the calculation of them is not explained further. In future, the jet penetration depth (i.e. its height) may be of interest and could be analysed in detail. The width of a jet is quite irrelevant to be presented instead, because such a mean value does not provide more useful information of the (arbitrary) shape of a jet.

Special functions of MATLAB

The introductions of the special functions of MATLAB are presented in this chapter. The functions are presented in the order of their appearance in the pseudo-code.

```
% FITELLIPSE  Least-squares fit of ellipse to 2D points.
%        A = FITELLIPSE(X,Y) returns the parameters of the best-fit
%        ellipse to 2D points (X,Y).
%        The returned vector A contains the center, radii, and orientation
%        of the ellipse, stored as (Cx, Cy, Rx, Ry, theta_radians)
%
% Authors: Andrew Fitzgibbon, Maurizio Pilu, Bob Fisher
% Reference: "Direct Least Squares Fitting of Ellipses", IEEE T-PAMI, 1999
%
%  @Article{Fitzgibbon99,
%   author = "Fitzgibbon, A.¬W.and Pilu, M. and Fisher, R.¬B.",
%   title = "Direct least-squares fitting of ellipses",
%   journal = pami,
%   year = 1999,
```

```
%   volume = 21,
%   number = 5,
%   month = may,
%   pages = "476--480"
%  }
%
% This is a more bulletproof version than that in the paper, incorporating
% scaling to reduce roundoff error, correction of behaviour when the input
% data are on a perfect hyperbola, and returns the geometric parameters
% of the ellipse, rather than the coefficients of the quadratic form.


%IMREAD Read image from graphics file.
%    A = IMREAD(FILENAME,FMT) reads a grayscale or color image from the file
%    specified by the string FILENAME...
% The text string FMT specifies the format of the file by its standard
%    file extension...If IMREAD cannot find a file
%    named FILENAME, it looks for a file named FILENAME.FMT.


% RGB2GRAY Convert RGB image or colormap to grayscale.
%    RGB2GRAY converts RGB images to grayscale by eliminating the
%    hue and saturation information while retaining the
%    luminance.
%
%    I = RGB2GRAY(RGB) converts the truecolor image RGB to the
%    grayscale intensity image I.


% IMCROP Crop image.
%    I = IMCROP creates an interactive image cropping tool, associated with
%    the image displayed in the current figure, called the target image. The
%    tool is a moveable, resizable rectangle that is interactively placed
%    and manipulated using the mouse.  After positioning the tool, the user
%    crops the target image by either double clicking on the tool or
%    choosing 'Crop Image' from the tool's context menu...
%    I2 = IMCROP(I) displays the image I in a figure window and creates a
%    cropping tool associated with that image...  The cropped image returned, I2, is
%    of the same type as I.

%   You can also specify the cropping rectangle non-interactively, using
%    these syntaxes:

%       I2 = IMCROP(I,RECT)
%       X2 = IMCROP(X,MAP,RECT)

%    RECT is a 4-element vector with the form [XMIN YMIN WIDTH HEIGHT];
%    these values are specified in spatial coordinates.


% ROIFILL Fill in specified polygon in grayscale image.
%    Use ROIFILL to fill in a specified polygon in a grayscale
%    image. ROIFILL smoothly interpolates inward from the pixel values on the
```

```
%    boundary of the polygon by solving Laplace's equation. ROIFILL can be
%    used, for example, to erase objects in an image...
%    J = ROIFILL(I) displays the image I and creates an interactive polygon
%    tool associated with that image.
%    J = ROIFILL(I,BW) uses BW (a binary image the same size as I) as a
%    mask.
%    [J,BW] = ROIFILL(I) returns the binary mask used to determine which
%    pixels in I get filled.


% IMSUBTRACT Subtract two images or subtract constant from image.
%    Z = IMSUBTRACT(X,Y) subtracts each element in array Y from the
%    corresponding element in array X and returns the difference in the
%    corresponding element of the output array Z.  X and Y are real,
%    nonsparse, numeric or logical arrays of the same size and class, or Y
%    is a double scalar.  The output array, Z, has the same size and class
%    as X unless X is logical, in which case Z is double.


% IMADD Add two images or add constant to image.
%    Z = IMADD(X,Y) adds each element in array X to the corresponding
%    element in array Y and returns the sum in the corresponding element
%    of the output array Z.  X and Y are real, nonsparse, numeric arrays
%    or logical arrays with the same size and class, or Y is a scalar
%    double.  Z has the same size and class as X unless X is logical, in
%    which case Z is double.


% IMADJUST Adjust image intensity values or colormap.
%    J = IMADJUST(I) maps the values in intensity image I to new values in J
%    such that 1% of data is saturated at low and high intensities of I.
%    This increases the contrast of the output image J...


% GRAYTHRESH Global image threshold using Otsu's method.
%    LEVEL = GRAYTHRESH(I) computes a global threshold (LEVEL) that can be
%    used to convert an intensity image to a binary image with IM2BW. LEVEL
%    is a normalized intensity value that lies in the range [0, 1].
%    GRAYTHRESH uses Otsu's method, which chooses the threshold to minimize
%    the intraclass variance of the thresholded black and white pixels.


% IM2BW Convert image to binary image by thresholding.
%    IM2BW produces binary images from indexed, intensity, or RGB images. To do
%    this, it converts the input image to grayscale format (if it is not already
%    an intensity image), and then converts this grayscale image to binary by
%    thresholding. The output binary image BW has values of 1 (white) for all
%    pixels in the input image with luminance greater than LEVEL and 0 (black)
%    for all other pixels. (Note that you specify LEVEL in the range [0,1],
%    regardless of the class of the input image.)
%
%    BW = IM2BW(I,LEVEL) converts the intensity image I to black and white.
```

```
% BWAREAOPEN Morphologically open binary image (remove small objects).
%    BW2 = BWAREAOPEN(BW,P) removes from a binary image all connected
%    components (objects) that have fewer than P pixels, producing another
%    binary image BW2.  The default connectivity is 8 for two dimensions,
%    26 for three dimensions, and CONNDEF(NDIMS(BW),'maximal') for higher
%    dimensions.


%STREL Create morphological structuring element.
%...
%    SE = STREL('disk',R,N) creates a flat disk-shaped structuring element
%    with the specified radius, R.  R must be a nonnegative integer.  N must
%    be 0, 4, 6, or 8.  When N is greater than 0, the disk-shaped structuring
%    element is approximated by a sequence of N (or sometimes N+2)
%    periodic-line structuring elements.  When N is 0, no approximation is
%    used, and the structuring element members comprise all pixels whose
%    centers are no greater than R away from the origin.  N can be omitted,
%    in which case its default value is 4.  Note: Morphological operations
%    using disk approximations (N>0) run much faster than when N=0.  Also,
%    the structuring elements resulting from choosing N>0 are suitable for
%    computing granulometries, which is not the case for N=0.


% IMCLOSE Morphologically close image.
%    IM2 = IMCLOSE(IM,SE) performs morphological closing on the
%    grayscale or binary image IM with the structuring element SE.  SE
%    must be a single structuring element object, as opposed to an array
%    of objects...
%     The morphological close operation is a dilation followed by an erosion,
%    using the same structuring element for both operations.


% IMFILL Fill image regions and holes.
%    BW2 = IMFILL(BW1,LOCATIONS) performs a flood-fill operation on
%    background pixels of the input binary image BW1, starting from the
%    points specified in LOCATIONS...
%
%    BW2 = IMFILL(BW1,'holes') fills holes in the input image.  A hole is
%    a set of background pixels that cannot be reached by filling in the
%    background from the edge of the image.


% BWBOUNDARIES Trace region boundaries in binary image.
%    B = BWBOUNDARIES(BW) traces the exterior boundary of objects, as well
%    as boundaries of holes inside these objects. It also descends into the
%    outermost objects (parents) and traces their children (objects
%    completely enclosed by the parents). BW must be a binary image where
%    nonzero pixels belong to an object and 0-pixels constitute the
%    background. B is a P-by-1 cell array, where P is the number of objects
%    and holes. Each cell contains a Q-by-2 matrix, where Q is the number of
%    boundary pixels for the corresponding region. Each row of these Q-by-2
%    matrices contains the row and column coordinates of a boundary pixel.
%    The coordinates are ordered in a clockwise direction...
```

```
%
%     B = BWBOUNDARIES(...,OPTIONS) provides an optional string input. String
%    'noholes' speeds up the operation of the algorithm by having it search
%    only for object (parent and child) boundaries.  By default, or when
%    'holes' string is specified, the algorithm searches for both object and
%    hole boundaries.
%
%    [B,L] = BWBOUNDARIES(...) returns the label matrix, L, as the second
%    output argument. Objects and holes are labeled. L is a two-dimensional
%    array of nonnegative integers that represent contiguous regions...


% DIFF Difference and approximate derivative.
%    DIFF(X), for a vector X, is [X(2)-X(1)  X(3)-X(2) ... X(n)-X(n-1)].
%    DIFF(X), for a matrix X, is the matrix of row differences,
%       [X(2:n,:) - X(1:n-1,:)].


% IMOPEN Morphologically open image.
%    IM2 = IMOPEN(IM,SE) performs morphological opening on the grayscale
%    or binary image IM with the structuring element SE.  SE must be a
%    single structuring element object, as opposed to an array of
%    objects...
%    The morphological open operation is an erosion followed by a dilation,
%    using the same structuring element for both operations.


% REGIONPROPS Measure properties of image regions.
%    STATS = REGIONPROPS(BW,PROPERTIES) measures a set of properties for
%    each connected component (object) in the binary image BW, which must be
%    a logical array; it can have any dimension...
%    STATS = REGIONPROPS(L,PROPERTIES) measures a set of properties for each
%    labeled region in the label matrix L. Positive integer elements of L
%    correspond to different regions...
%    PROPERTIES can be a comma-separated list of strings, a cell array
%    containing strings, the string 'all', or the string 'basic'


% BWSELECT Select objects in binary image.
% ...
%     BW2 = BWSELECT(BW1,N) displays the image BW1 on the screen
%    and lets you select the (R,C) coordinates using the mouse...
%    N can have a value of either 4 or 8 (the
%    default), where 4 specifies 4-connected objects and 8
%    specifies 8-connected objects...
%    [X,Y,BW2,IDX,Xi,Yi] = BWSELECT(...) returns the XData and
%    YData in X and Y; the output image in BW2; linear indices of
%    the pixels belonging to the selected objects in IDX; and the
%    specified spatial coordinates Xi and Yi.
```

Feasibility of the algorithm

The feasibility of this algorithm was originally tested with a high-speed video clip of the POOLEX /STB-28-4 experiment. When the algorithm was applied to other video clips, it was found out that the feasibility of this algorithm should be ensured separately for each clip because various conditions of the pattern recognition may change when the conditions in the experiment change. Especially, the lighting conditions change depending on the camera location and the amount of dispersed small bubbles in the bulk water. The shape, size, and the behaviour of the large steam bubbles change when the subcooling of the pool water changes, which may lead to different needs of user intervention when distinguishing the regions of interest. Due to that, it is recommended to test and adjust the script every time it is applied to a new video clip.
The pattern recognition algorithm presented in this study is an ad-hoc script to be used in the cases where a pipe is submerged vertically into a pool filled with water. The outlet of the pipe is assumed to be facing downwards with zero inclination, and the outlet (mouth) of the pipe has to have a circular design. This script is made for the cases where a single camera is positioned normal to the pipe mouth plane. Mathematically, an aspect angle of $0°$-$90°$ is accepted, in which the $0°$ case means that the pipe mouth plane is normal to the camera lens and the $90°$ case means that the mouth plane is aligned with the camera lens (i.e. camera observes the mouth right below it). However, the idea of the script is to solve the bubble as a volume of rotation in respect to the pipe axis. Thus, the scaling error of the vertical radii of an ellipse should increase rapidly with the increasing aspect angle. Only moderate aspect angles $0°$-$15°$ have been used in this study, which should make the errors due to the aspect angle relatively small.

The main purpose of this script is to capture the widths and volumes of the large bubbles and estimate the volumes of the jets that inflate and collapse around the mouth of the blowdown pipe. Only the bubbles whose width is the same or larger than the radius of the blowdown pipe should be accepted in manual postprocessing because the smaller ones do not represent the type of the bubble that this script is meant to capture. All the jets accepted by the script can be instead accepted also in the postprocessing if they are not just artefacts of noise captured by the script. The script itself is very sensitive to capture smaller bubbles or noise from the frames where any larger bubbles/jets are not available. However, if any real large bubble/jet is present, the script adapts better, and the effect of small bubbles and noise reduces remarkably. This happens because of the increased contrast due to the real bright steam region.

Concerning the obtained widths and volumes, the width of a bubble is the most accurate dimension obtained by this script. The width is independent of the aspect angle, and it is obtained by fitting an ellipse which decreases the effect of nonphysical appendices or gaps possibly remaining after the pattern recognition process. The volume of the bubble is subjected to errors due to the aspect angle and limited knowledge of its real shape in the depth dimension. Furthermore, the toroidicity of the bubble is not analysed during the run of the script. Even the most perfectly ellipsoidal bubbles have often an axial hole in the middle which adds systematic error to all of the recognized bubble volumes. In the case of jets, the recognized volume of a jet cannot be considered as an absolute volume-of-void at all because the void fraction of the photographed jet is not necessarily near unity, unlike in the case of an expanding bubble. Many of the recognized jets are just bursts of a varying amount of small bubbles. The recognized volume of a jet can still be used e.g. in the FFT analysis to analyse the rate of chugging.